Université de Strasbourg

UNIVERSITÉ DE STRASBOURG

EDSC École Doctorale des Sciences Chimiques

ÉCOLE DOCTORALE 222
UMR 7006

THÈSE présentée par :
Jorge Leira-Iglesias

Soutenue le : **06 Octobre 2017**

Pour obtenir le grade de : **Docteur de l'université de Strasbourg**
Discipline/Spécialité : Chimie

Dissipative supramolecular polymerization mediated by chemical fuels

THÈSE dirigée par :
Mr. Thomas Hermans Docteur, Université de Strasbourg (UMR7006)

RAPPORTEURS :
Mr. Job Boekhoven Professeur, Technische Universität München
Mme. Beatriu Escuder Gil Professeur, Universitat Jaume I

AUTRES MEMBRES DU JURY :
Mme. Anja Palmans Professeur, Technische Universiteit Eindhoven

Brief Contents

Contents

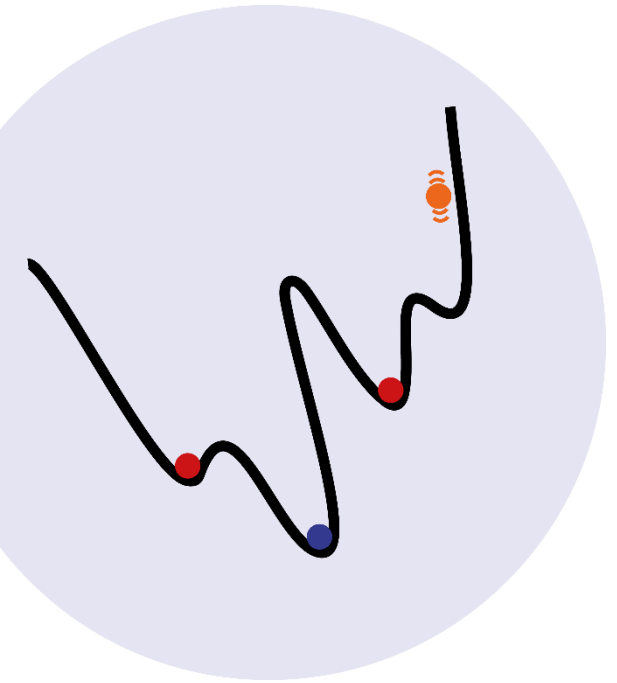

1

Introduction: Molecular self-assembly inspired by nature

Abstract: Self-assembly systems are ubiquitous in living organisms performing complex functions. Supramolecular chemistry aims to develop complex functional materials through non-covalent interactions. In the last two decades, supramolecular chemists have developed systems that can self-assemble into distinct structures in their most stable configuration (thermodynamic equilibrium). However, supramolecular structures can also exist as kinetically trapped or metastable states (local minima). Different preparation protocols can be applied to tune the final outcome of the self-assembly. As a step further, supramolecular chemists have developed different dissipative supramolecular systems that can perform a transient formation of self-assembled structures upon the addition of a chemical fuel mimicking the different self-assembly processes in the cell. In this chapter, we introduce a range of these systems, and a way to classify them.

Parts of this chapter have been published:
* Sorrenti, A., Leira-Iglesias, J., Markvoort, A. J., de Greef, T. F., & Hermans, T. M. Non-equilibrium supramolecular polymerization. *Chemical Society Reviews*, **46**, 5476-5490 (2017).

1.1. Thermodynamic States

Supramolecular chemistry has been defined by Jean-Marie Lehn as "the chemistry beyond the molecule" aiming to develop complex chemical systems through non-covalent intermolecular interactions.[1,2] In addition, supramolecular systems are ubiquitous in living systems and they are involved in complex functions such as translation, replication, signalling and cellular transport.[3,4] Inspired by nature, supramolecular chemistry has first focused on the design of molecular components that can spontaneously self-organized into more complex structures.[5,6] For example, providing a new way for chemical synthesis. The self-organization process is guided by the molecular information encoded in the building-block.[7–9] The information stored in the component is amplified to the supramolecular level through specific interaction and recognition patterns leading to functional supramolecular materials such as supramolecular polymers, liquid crystals and so on.[5,10] As an example, Fujita a co-workers,[11] inspired by the self-assembly of virus capsids, have designed a giant spherical metal complex formed by 90 components (30 Pd^{2+} ions and 60 bent ligands). The flexibility of the ligand permits the molecules to adjust themselves and reach the desired structure.[11] In addition, many of these examples have been designed to respond to a stimuli such as pH, ionic strength, light, temperature, etc. leading to adaptable functional materials.[12] In this chapter, we will show and explain the theory behind the different supramolecular polymerization mechanisms. In addition, we will expose different preparation protocols that allow to guide the system through the energy landscape. Afterwards, we will show the state-of-the-art in supramolecular chemistry in which a transient formation of self-assembly structures can be achieved upon the addition of a chemical fuel. Finally, the general self-assembly behaviour of perylene diimide derivative (PDIs) is introduced. PDIs are well-known building-block in supramolecular chemistry, which multiple applications.

Self-assembly is intrinsically dynamic, non-covalent bonds may form and break permitting the continuous exchange and reorganization of the building-block into the supramolecular structures leading the system to the most stable configuration[1,8], that is, the thermodynamic equilibrium state (#1 in Figure 1.1A).[13,14] However, unexpected configurations or structures can be achieved when the system cannot adjust itself. In other words, strong non-covalent interactions are involved in the self-assembly process hampering the formation of the most stable configuration.[15] The system is guided to local free energy minima in which kinetically trapped or metastable states can be found (#2 and #3 in Figure 1.1A) meaning that the self-assembly process is governed by the kinetics of the systems and thus, the final structure depends on the sample preparation protocol due to non-linear processes such as nucleation effects or multiple competitive growth pathways. Sample preparation can be used to control the supramolecular polymerization process and obtain different supramolecular assemblies at the same final conditions, just by tuning the preparation methodologies (see section 1.3). This can be used to develop different materials with optimized functional properties.

Molecular chaperones are used in living systems to assist in protein folding and also, to control the self-assembly of flagellae (long filaments that act as propellers in cell motility).[16] Chaperones assist the self-assembly of each filament, consisting of 20.000 monomers polymerized at a precisely defined position. Specifically, chaperones bind to the filament impeding the incorrect polymerization of the monomers and thus, avoiding the formation of kinetically trapped states and permitting the correct self-assembly pathway.

Afterwards, chaperones drive the filament to dock at the exact position of the cell surface. Artificial supramolecular chaperones have not been invented so far, but they would be of great interest to control the final outcome of distinct supramolecular aggregates in trapped or metastable states.

In contrast, living cells continuously consume energy in order to keep supramolecular structures in so called dissipative non-equilibrium states (#4 in figure 1.1A, see section 1.4). In the cytoskeleton (i.e., a network of dynamic structures) three different kind of dissipative supramolecular systems are constantly polymerizing and depolymerizing: microtubules, actin filaments and the intermediate filaments. Constant consumption of a chemical fuel, e.g. guanosine triphosphate (GTP) for microtubules and adenosine triphosphate (ATP) for actin filaments, allows spatiotemporal control over the self-assembly permitting the cell to divide, move, transport and organize internal organelles.[3] Obviously, we are far from fully understanding this kind of complexity, however, few examples of dissipative supramolecular systems have been reported in which transient self-assembly formation of supramolecular structures was shown.[17–21]

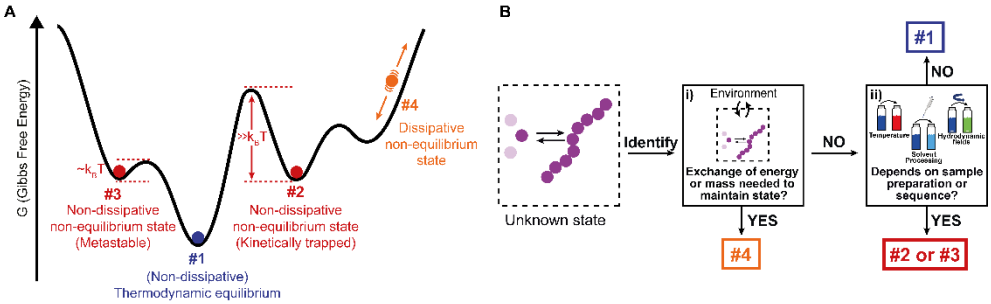

Figure 1.1. Identifying the different thermodynamic states in supramolecular self-assembly. (A) Schematic Gibbs free energy landscape. (B) Decision tree to identify the different states shown in (A). Reproduced from ref. * (see page 1) with permission from the Royal Society of Chemistry.

So far, we have briefly introduced four different supramolecular thermodynamic states (#1, #2, #3 and #4 in figure 1.1A). However, in literature a clear definition was lacking. Recently, we have provided a general classification and description of the different states and how, they can be identified:

- *Thermodynamic equilibrium*: the system resides in the global minimum of the free energy landscape (state #1 in Fig. 1.1A). No external energy inputs are required to maintain the system, and on average no changes are observed in time. Note that dissipation, usually in the form of heat release, does occur during the downhill self-assembly process from the monomers to the assembly. Once the equilibrium is reached, however, no further dissipation occurs.[22] Equilibrium structures are still dynamic, meaning that the monomers continuously exchange with the solution, and their reversibility is crucial for the system to find and remain in its most stable configuration.[10] It has to be stressed that, for a given molecular design (chemical information), the shape of the energy landscape depends on parameters such as temperature, solvent composition and salt concentrations. As a result, the morphology of the most stable aggregate (i.e., the position of the global minimum) can change for different sets of these parameters (see Section 1.2). Nearby free

energy minima—often observed in experiment as polymorphic structures—can also be populated according to the Boltzmann distribution if the activation barrier is low.[23]

- *Non-dissipative non-equilibrium states (kinetically trapped or metastable states)*: the self-assembled system is confined in a local minimum of the energy landscape (states #2 and #3 in Fig. 1.1A). Its time evolution depends on the shape of the energy landscape around the minimum, and two situations can be envisaged. If the energy barrier for a pathway leading to the thermodynamic equilibrium is low enough, that is, on the same order of magnitude as k_BT (where k_B is the Boltzmann constant, and T temperature), the system will slowly relax to a more stable structure. Such a system is in a so-called metastable state (#3 in Fig. 1.1A). Note that multiple metastable configurations can exist along the pathway to the global minimum. On the other hand, when the energy barrier is much higher than k_BT, the system will remain captured in the local minimum for a period much longer than the experimental observation. This state is commonly referred to as a kinetically trapped state (#2 in Fig. 1.1A). In the latter case, suitable experimental procedures have to be undertaken to ''help'' the system to escape its trap (see Section 1.3).

- *Dissipative non-equilibrium state*: dissipative self-assembled systems require a constant influx of energy or matter (e.g., a chemical fuel or light), and removal of waste products, to be kept steadily in a dissipative non-equilibrium state (state #4 in Fig. 1.1A). If the energy supply stops, the system relaxes spontaneously to the thermodynamic state or to a non-dissipative non-equilibrium state encountered on the way. The terminology of ''dissipative structures'' as formulated by Prigogine, refers to emergent structures or patterns that are formed on length scales much larger than the individual molecules, the latter of which at equilibrium do not form such structures or patterns. Instabilities occurring far from equilibrium, such as those due to reaction–diffusion phenomena, can lead to dissipative structures even on the mm scale, that is, far beyond the length scale of typical intermolecular interactions (e.g., hydrogen bonding, ionic interactions, π–π stacking, etc.).[24] In contrast, in supramolecular chemistry well-ordered structures often already exist in non-dissipative states, and to this day it is unclear how dissipation in self-assembly has to be related to dissipative structures in the Prigogine-sense. What is clear, is that dissipative self-assembly is a very exciting new direction[17–21] where challenges, such as obtaining non-equilibrium steady states (NESS) or oscillations, are abundant (see section 1.4).

Decision tree to identify thermodynamic states

In Fig. 1.1B, we provide a decision tree to assign a given self-assembled system to one of the states discussed above.

i) Does the system need to exchange energy and/or matter with the environment to maintain its structure over prolonged times?
YES: it is a dissipative non-equilibrium state (#4, Fig. 1.1A).
NO: ↵

ii) Does the obtained supramolecular structure depend on the preparation protocol, that is, on parameters such as rate of cooling, solvent processing, order of addition, etc.?

YES: it is a non-dissipative non-equilibrium state, either metastable (#3, Fig. 1.1A), if it evolves slowly with time to a more stable state, or kinetically trapped if it remains indefinitely (#2, Fig. 1.1A).

NO: the same structure is obtained independently of the history of the sample. It is the thermodynamic equilibrium (#1, Fig. 1.1A).

So far, we have provided new definitions for the four different thermodynamic states (#1, #2, #3 and #4 in Figure 1.1A) and a guide to how a supramolecular system can be identified. In the next section we provide a mechanistic insight of the different supramolecular polymerization processes.

1.2. Supramolecular polymerization mechanisms

Molecular self-assembly of small molecules can be described as the stepwise reversible addition of monomers into dimensional assemblies at the thermodynamic equilibrium (so far, supramolecular chemists have focussed on the description of one-dimensional polymerization), each step is characterized by a decrease/increase in the Gibbs free energy.[13] The first model is based on the isodesmic equilibrium in which polymers grow stepwise, each monomer addition can be described by a single equilibrium constant that depends on the chemical information provided by the monomer, the temperature and the solvent. The Gibbs free energy is equal for all the steps and therefore, independent of the polymer length. On the other hand, cooperative (nucleated) polymerization can be defined by two equilibrium constants in which a first non-favourable thermodynamic step occurs (formation of small oligomer or nuclei) followed by an energetically favoured elongation step, both equilibria are described by the reversible addition of monomers to the pre-nucleus and post-nucleus oligomers. Studying spectroscopic techniques (i.e. UV-Vis, fluorescence or CD spectroscopy) as a function of temperature or total concentration can be used to determine the supramolecular polymerization process (Figure 1.2A).[25,26]

In the last years, different examples have shown that supramolecular polymerization at thermodynamic equilibrium can result in multiple assemblies with different morphologies. In other words, the free energy landscape can be modified (affording different thermodynamic equilibria with different morphologies) depending on the final conditions such as monomer concentration, temperature, ionic strength or solvent composition.[15] For example, one structure can be the most thermodynamically favoured at certain temperature, solvent composition or salt concentration and maybe, a different morphology can be reached under different conditions. Recently, Stupp and co-workers studied the aggregation of a peptide amphiphile under different conditions.[15] The study shows that short fibrils are formed at low ionic strength with a random coil structure. However, the peptide amphiphile self-assembled into long fibrils with a β-sheet structure at higher amounts of salt concentration. The latter clearly shows different assembly morphologies that depend on the final concentration, indicating that equilibrium structures depend only on the final conditions and not on how the assembly it was reached.

While thermodynamic insights are well established in the field of supramolecular chemistry, kinetic characterization of supramolecular polymerization is mostly lacking in the field. Kinetic models can also be explained by the stepwise monomeric growth of a

supramolecular polymer. Isodesmic polymerization can be described with two rate constants (addition and dissociation of monomers to a growing assembly) where the aggregation constant and the mean length as a function of time can be obtained. Cooperative polymerization is also based on association/dissociation of monomers in a growing assembly in which different rate constants are used for pre-nucleus and post-nucleus oligomers formation.[27,28] This model shows that the time evolution of the assemblies is characterized by a lag time at lower concentrations followed by a promptly increase in the aggregation constant upon increasing concentration (Figure 1.2B).

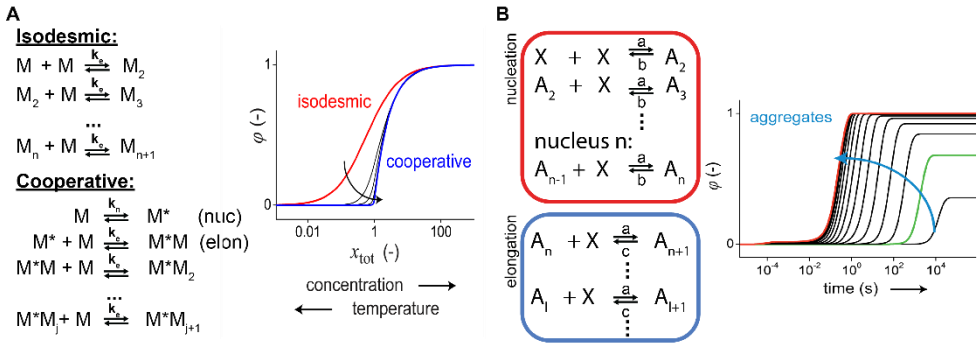

Figure 1.2. Supramolecular polymerization. (A) Schematic representation of a one-dimensional supramolecular polymerization in which aggregates, Ai, grow exclusively by monomer addition. When the association equilibrium constants are equal (Kn = Ke) aggregate growth occurs via an isodesmic self-assembly mechanism, and when Kn < Ke, a cooperative nucleation–elongation mechanism is followed. The exact mechanism has a profound influence on the fraction of aggregation, φ (-), as a function of temperature or concentration. (B) Kinetic nucleation–elongation model of a single-pathway supramolecular polymerization based on monomer association and dissociation. Simulations performed (a = 10^4 M^{-1} s^{-1}, b = 1 s^{-1}, c = 0.01 s^{-1}, n = 5) reveal faster growth at higher total monomer concentration. Reproduced from ref. * (see page 1) with permission from the Royal Society of Chemistry.

Typically, kinetics of the supramolecular polymerization is studied by performing heating and cooling experiments in which the fraction of aggregation changes with temperature. In some cases, hysteresis can be detected, that is to say, heating and cooling measurements do not coincide, meaning that opposite reactions (equilibrium between monomers and aggregates) do not relax on the time scale of the experiment.[13] The latter occurs when large kinetic barriers are involved in the assembly or disassembly process (i.e. #2 in Figure 1.1A). Hysteresis can be enhanced (in addition, can be quantified by measuring the area below the curves) when multiple self-assembly pathways are involved in the polymerization.[29] Korevaar and co-workers analysed the supramolecular polymerization of S-chiral oligo(p-phenylenevinylene).[30] They demonstrated that S-OPV can self-assemble into left-handed helical aggregates in apolar solvents under thermodynamic control. However, right-handed helical aggregates can be formed when the self-assembly process is initiated from the monomeric state, which later on are converted to left-handed aggregates. In order to explain the two different pathway formation, they developed a kinetic model where multiple pathways compete for the same monomer leading to metastable (kinetically controlled) or stable pathways (thermodynamically controlled). Recently, Markvoort et al. studied the effect of fragmentation and coagulation processes in the self-assembly process. They demonstrated that fragmentation and coagulation events delay the formation of thermodynamic products.[28]

Competition between two different pathways (metastable and stable pathways) can be used to control the final assembled structure.[30,31] This strongly affects the self-assembly dynamics (which is enhanced when off-pathways become kinetically trapped) depending on the available amount of monomer. Based on the last phenomenon, Takeuchi et al. designed a living supramolecular polymerization system.[32] They synthetized a porphyrin dye that can self-assemble via cooperative polymerization into thermodynamically stable H-aggregates, and also assemble into kinetically trapped J-aggregates via an isodesmic mechanism (Figure 1.3A). J-aggregates (kinetically trapped) were formed upon cooling a monomeric solution. The assemblies could be converted (overcoming the energy barrier) upon addition of H-aggregates seeds (previously prepared separately). This can be explained as the monomer retention in the J-aggregate assemblies which impedes the formation of nuclei and as a consequence also the thermodynamically favoured H-aggregates. Living supramolecular polymerization is analogous to conventional polymer growth and can yield aggregates with controlled length and narrow dispersity. Repeated addition of stock solution results in longer H-aggregates assemblies and shorter growth rates (i.e. initial seeds are more diluted) with the same low dispersity.

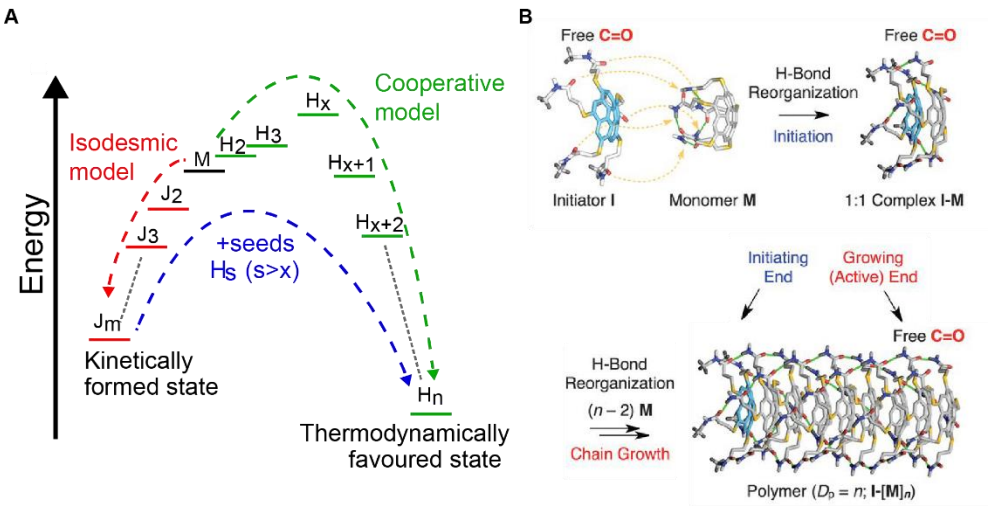

Figure 1.3. Living supramolecular polymerizations. (A) Energy landscape of two competing supramolecular polymerization pathways, where the formation of H-aggregates needs to overcome an energetic barrier corresponding to the appearance of critical nuclei. Reproduced from ref. * (see page 1) with permission from the Royal Society of Chemistry. (B) Homochiral assemblies of curannulene derivatives were obtained. Spontaneous supramolecular polymerization occurs upon addition of an initiator. Reprinted from ref. 33 with permission from AAAS.

Aida et al. have shown another fantastic example of living supramolecular polymerization in which monomers of curannulene derivatives are kinetically trapped due to the formation of intramolecular hydrogen bonding between five amide units. The latter leads the monomer to adopt a cage-like closed conformation.[33] In this way, spontaneous supramolecular polymerization was prevented by including conformational restrictions in the monomer. Upon the addition of an initiator (modified by incorporating N-methylated amide units hampering their own polymerization) polymers grow via a cooperative mechanism (Figure 1.3B). The initiator decreases the energy of the transition state for self-

opening the closed conformation. In addition, the H-bonding amide network (5 intermolecular bonds per molecule) provides directionality and causes the formation of homochiral assemblies. The latter was used to obtain optical resolution of a racemic mixture by using a chiral initiator molecule.

So far, we have seen that thermodynamic parameters as well as kinetic parameters are of key importance to understand the different supramolecular polymerization mechanisms. Two different mechanism can be distinguished (i.e., isodesmic and cooperative). Both methods are based on the continuous exchange of monomers in solution, that is to say, association and dissociation of monomers into the assemblies. Different techniques such as stopped-flow (dilution/co-solvation) or temperature jump have been used in the field, in order to study the insights of each mechanism in full detail. In addition, the incorporation of new techniques has helped to understand and find many undetectable metastable and off-pathways processes. All this together has led to better control over supramolecular structures and dispersity. That is to say, kinetic trapping can be used to get more monodisperse supramolecular polymers (dispersity is close to 1.0), while the dispersity tends to 2 at the thermodynamic equilibrium. In the next section, we focus on how different methodologies can be used to control the self-assembly process yielding different non-dissipative non-equilibrium states (#2 and #3 in Figure 1.1A).

1.3. Non-dissipative non-equilibrium states

Supramolecular chemists have used different preparation methodologies to guide the system through the energy landscape in order to reach or avoid different supramolecular structures, that is, non-dissipative non-equilibrium states, #2 and #3 in Figure 1.1A. The latter can be done by using the same building-block under the same final conditions (e.g., temperature, pH, ionic strength, solvent compositions, etc.), in other words, different final structures can be obtained depending on the preparation protocol (i.e., the final energy landscape is not modified) by which monomers aggregate into different assemblies. On the other hand, regarding the thermodynamic states (#1 in Figure 1.1A), the final outcome is independent of the preparation protocol and thus, the final energy landscape only depends on the final conditions of the system as mentioned in section 1.2. Different examples in which different preparation protocols such as modulating temperature, solvent processing (see section 1.5), order of addition, multi-step non covalent synthesis, controlled diffusion, hydrodynamic fields, template assisted self-assembly and chemical fuels (see chapter 2) are described below.

1.3.1. Modulating temperature

Building-blocks tend to self-assemble spontaneously in non-aqueous solution. This process is usually exothermic and is enhanced a lower temperatures. Therefore, self-assembly can be induced by cooling down monomeric solutions of the building-blocks. The cooling rate and temperature profile can be modulated yielding different supramolecular structures at the same final temperature. Meijer and co-workers[26,30] have shown an example where a monomeric solution of S-OPV (70 °C in MCH) was slowly cooled down (1 °C min^{-1}) to 0 °C leading the system to the most stable configuration, left-handed helical assemblies (thermodynamic equilibrium state, #1 in Figure 1.1A). In contrast, when a monomeric solution was quickly cooled down, right-handed helical assemblies were

obtained (kinetically trapped state, #2 in Figure 1.1A), see figure 1.4A,B. Afterwards, the solution was heated up to 25 °C resulting in the left-handed assemblies (equilibrium state) and indicating the formation of metastable assemblies (#3 in Figure 1.1A) at this temperature. In another example, Schmidt and Meijer[34] could selectively obtain different self-assembled states of a chiral carbonyl-bridged triarylamine trisamides (CBT) at the same final conditions depending on the temperature profile performed (Figure 1.4C,D). Kinetically trapped assemblies (state #2 in figure 1.1A) could be obtained via isodesmic polymerization upon cooling down a monomeric solution (from 80 °C to 7 °C), the final assemblies were stable for more than 5 h. However, the thermodynamic equilibrium state could be obtained via cooperative polymerization after cooling down a monomeric solution (80 °C) to –5 °C followed by an increase of the temperature up to 7 °C (i.e., the temperature sequence is: 80 °C → –5 °C → 7 °C). Seeding experiments (mixed of both assemblies in solution with 1:1 ratio) showed that the kinetically trapped state was rapidly converted to the thermodynamic state, in other words, self-nucleation of the kinetically trapped state was not possible due to the high energy barrier between both states. In addition, control over the self-assembly could be performed when nuclei were pre-formed in solution. Interestingly, self-assembly only occurs when both assemblies, thermodynamic and kinetically trapped state, possess the same chirality.

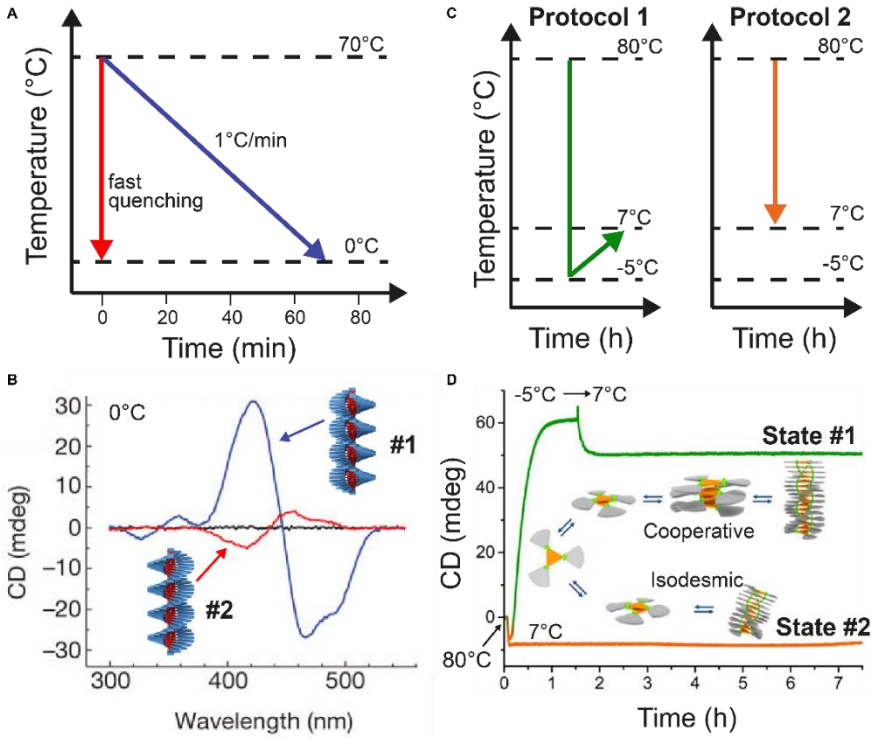

Figure 1.4. Modulating temperature to control self-assembly. (A) Schematic representation of different cooling rates from the molecularly dissolved state at 70 °C in MCH to the self-assembled state at 0 °C. (B) CD spectra of the thermodynamic (#1, blue line) and kinetic (#2, red line) S-OPV assemblies formed respectively by slow cooling (1 °C min^{-1}) and fast quenching. (C) Different cooling protocols. (D) Two different CBT assemblies (#1 or #2) selectively obtained by using the cooling protocols reported in (C). The self-assembly process was monitored over time by following the CD signal at 490 nm. Reproduced from ref. * (see page 1) with permission from the Royal Society of Chemistry.

1.3.2. Order of addition

Addition of salts or protons to a monomeric solution or even co-aggregation (two or more building-blocks that self-assemble together) are common strategies to induce self-assembly. The order of addition of the different components can guide supramolecular structures to different non-dissipative states (#1, #2 and #3 in figure 1.1A). Purrello and Ribó have widely studied the self-assembly of ionic porphyrins like meso-(4-sulfonatophenyl) porphyrin, H_2TPPS_4.[35,36] The final structure of the H_2TPPS_4 assemblies strongly depends on experimental conditions, such as ionic strength, concentration and ageing of the stock solution, concentration of the final solution, pH, etc. One nice example shows that the aggregation of H_2TPPS_4 depends on the order of addition of protons and NaCl.[35] J-aggregates could be obtained when a solution of H_2TPPS_4 was added to an acid aqueous solution (pH 3) containing NaCl. The protonated porphyrin H_4TPPS_4, which is the assembling unit, was obtained. However, when NaCl was added to a solution of H_4TPPS_4 (protonated porphyrin), only monomeric protonated porphyrins were observed under conditions where normally aggregation occurs (see figure 1.5A). This was explained due to the presence of pre-nuclei of protonated porphyrin in solution, which upon addition of salt rapidly elongate yielding J-aggregates. The latter was confirmed by working in a more diluted range in which J-aggregates could not be obtained independently of the protocol performed. Heteroaggregation of H_2TPPS_4 porphyrin with a chiral cationic surfactant results in the formation of different supramolecular assemblies depending on the order of addition of the components (Figure 1.5B).[36] Namely, when a solution of surfactant (above the critical micellar concentration) was added into a diluted porphyrin solution, micellized monomeric porphyrins were obtained. On the other hand, the addition of a concentrated porphyrin solution to a micellar surfactant solution yielded heteroaggregates in solution (Figure 1.5B). Both kind of assemblies did not interconvert in each other indicating the importance of the preparation protocol which allows to selectively choose different kind of aggregates at the same final composition.

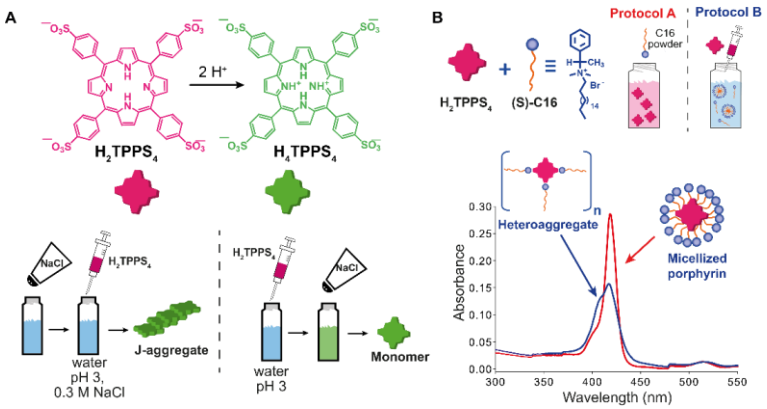

Figure 1.5. Effect of the order of addition on self-assembly. (A) Structure of H_2TPPS_4 and of its protonated form H4TPPS4, and schematic illustration of the effect of adding H_2TPPS_4 before or after NaCl to a pH 3 citrate buffer solution. (B) Two 1 mM H_2TPPS_4 solutions containing the chiral surfactant C_{16} at $[C_{16}]/[H_2TPPS]$ ratio 2500:1 were prepared either by dissolving the surfactant powder in a 1 mM H_2TPPS_4 solution (protocol A), or by adding a stock 1 mM porphyrin solution to the surfactant solution (protocol B), yielding respectively monomeric micellized porphyrin (red line in the UV-Vis spectrum), or surfactant/porphyrin heteroaggregates (blue line). Reproduced from ref. * (see page 1) with permission from the Royal Society of Chemistry.

1.3.3. Multi-step non-covalent synthesis

Stepwise addition of multiple components could be used to build complex supramolecular structures. The latter is usually performed by stabilizing kinetically trapped intermediate assemblies (#2 in Figure 1.1A). Interestingly, this can be used to obtain aggregates in solution in which the individual components are not soluble. An example is the formation of liposomes (natural non-dissipative non-equilibrium structures) consisting on different steps. First, the lipid is dissolved in a good solvent (promoting molecularly dissolved solutions of the building-block). Then, hydration of the film is performed giving a suspension of large multilamellar vesicles. Finally, freeze-thaw cycles to form large unilamellar vesicles and extrusion were performed to get the desired size.[37] Hermans et al. have shown the multi-step formation of dendrimer-based patchy nanoparticles in water.[38,39] Such particles are based on guest-host interactions where the hydrophobic dendritic core (host) interacts at its periphery with water soluble hydrophilic guest molecules (figure 1.6A). The host dendrimer is only soluble in water due to its strong hydrophobic character. For this reason, guest and host molecules were first dissolved in chloroform, and afterwards transferred to water via the neat state overcoming the energy barrier for core solvation (figure 1.6B). The final outcome depends on the ratio between the guest and host molecules. When the number of guest molecules exceeds the number of binding sites per host molecule, truly patchy particles were obtained (a single host molecule is surrounded by multiple guest molecules). On the other hand, if the number of guest molecules is lower than the binding sites, kinetically trapped particles (cluster of host molecules) were obtained. Interestingly, dilution induced assembly of molecules because of the increase of hydrophobic domains exposed to water leading to destabilization of the particles that finally precipitate (see figure 1.6B).

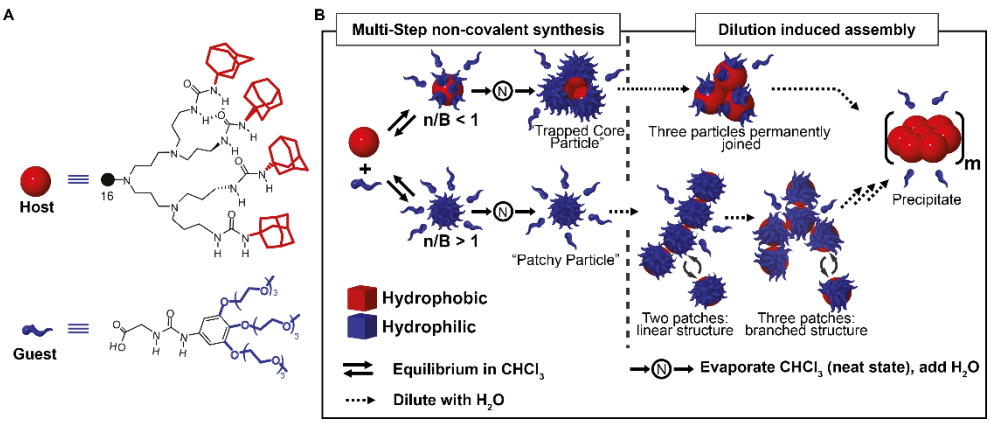

Figure 1.6. Multi-step non-covalent synthesis. (A) Molecular structure of the urea-adamantyl poly(propylene imine) dendrimeric host, and of the ureido acetic acid guest. (B) Host and guest are mixed in chloroform to form a pre-complex, which is later transferred to water via the neat state. Depending on the ratio of guest molecules and binding sites (n/B), either a small complex with three host molecules trapped in the core (for n/B o 1), or a patchy particle (for n/B 4 1) are obtained. Dilution with water induces aggregation due to the dissociation of the host molecules which leaves hydrophobic patches exposed. Reproduced from ref. * (see page 1) with permission from the Royal Society of Chemistry.

1.3.4. Controlled diffusion

Another preparation protocol that is commonly utilized by supramolecular chemist to induce self-assembly consist in the addition of a bad solvent (the building-block tends to spontaneously self-assemble in the solvent) to a molecular dispersed solution of the building-block (see example in section 1.5). The latter can lead to local gradients in reactant concentration or different solvent composition and thus, heterogeneous solutions are obtained impeding the reproducibility of the final structure. The latter occurs when cooperative (nucleated) polymerization is involved in the self-assembly and the diffusion of molecules is similar to the nucleation rate. In addition, control over reactant/solvent diffusion can be used to perform pathway selection and selectively prepare different non-dissipative non-equilibrium structures (#2 and #3 in Figure 1.1A). As an example, microfluidic mixing can be used to control the outcome of the self-assembly. By varying different parameters, such as total flow rate, flow focusing, and the chip geometry, it is possible to precisely define the reaction-diffusion zone, i.e., the concentration gradients and solvent compositions in space, and the interfaces at which nucleation occurs. Numata and co-workers[40] prepared porphyrin assemblies (from nano to micro scale) under kinetically control in a microfluidic chip. They enhanced the formation of H_2TPPS J-aggregates upon the addition of protons in a microfluidic chip. This permitted to obtain assemblies at final conditions where for example, polymerization cannot occur in a flask (Figure 1.7A). Moreover, different flow rates (i.e. affecting the local proton concentration and controlling the nucleation step) could be used to modulate the final size (degree of aggregation) and length of the assemblies (Figure 1.7B-D).

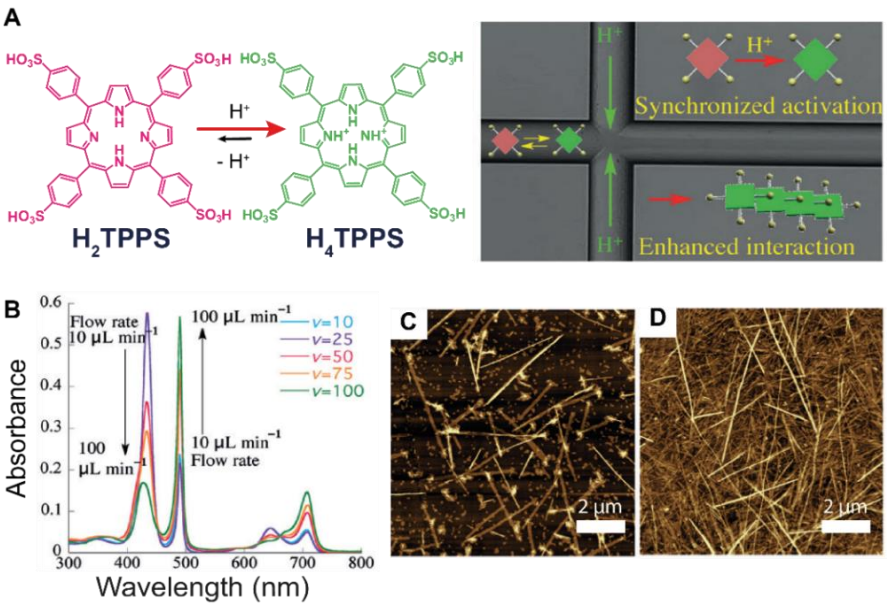

Figure 1.7. Effect of controlled diffusion on supramolecular polymerization. (A) Schematic representation of the concept of synchronized activation of H_2TPPS (i.e., protonation to H4TPPS) in a microfluidic chip yielding enhanced formation of J-aggregates. (B) UV-Vis spectra recorded for various flow rates (pH 3): J-aggregates absorb at 490 and 700 nm, monomeric H_4TPPS at 434 nm. (C and D) AFM images of the J-aggregates prepared at pH 3.0 under microfluidic synthesis at flow rates 50 and 100 mL min^{-1} respectively. Reproduced from ref. * (see page 1) with permission from the Royal Society of Chemistry.

1.3.5. Hydrodynamic fields

Hydrodynamic flows have been another tool used to induce self-assembly and control the final outcome of the assembly. The structures can be selectively prepared by different mechanism[41] such as alignment of the particles in the flow, deformation due to the torque generated by the gradient of flow velocity or shear-induced breaking. In one example, Ribó et al.[42] have shown that vortex stirring induces the formation of J-aggregates of non-chiral diprotonated porphyrin H_4TPPS_3, the final chirality of the assemblies is determined by the direction of rotation (Figure 1.8A,B). Recently, Micali and co-workers[43] showed a similar example. The nucleation polymerization step of the same porphyrin (H_4TPPS_3) is controlled by applying a combination of rotating and magnetic forces. Vortex stirring can favour the formation (e.g., by a weak torque) of one enantiomeric nucleus, which is amplified in the elongation step resulting in a selection of the chiral sign due to the symmetry breaking. In conclusion, hydrodynamic fields can be used to control the final outcome of the self-assembly and to induce chirality of different non-chiral building blocks. These can be used as a strategy to obtain tuneable smart materials.

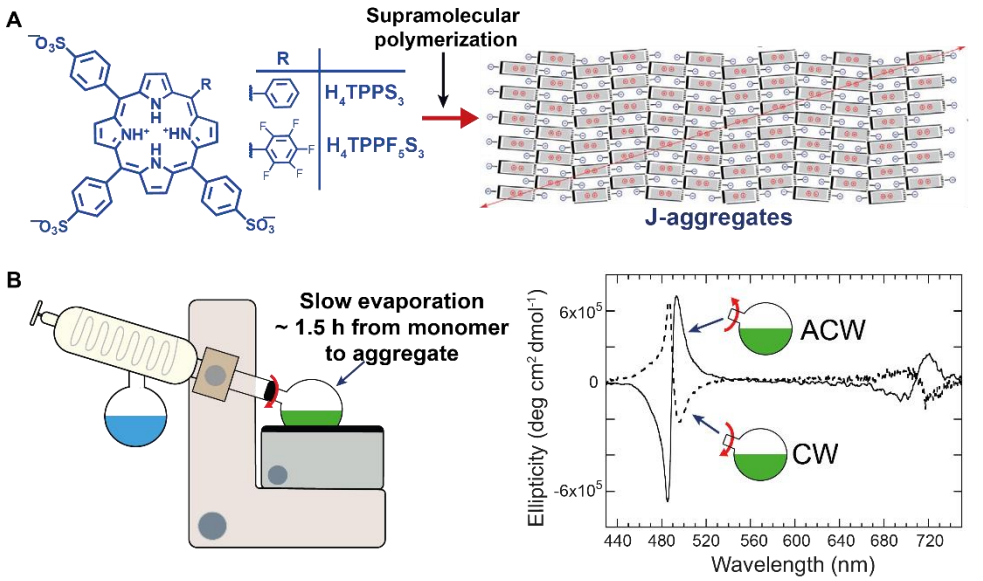

Figure 1.8. Pathway selection via hydrodynamic fields. (A) Diprotonated 4-sulfonatophenyl meso-substituted porphyrins self-assemble hierarchically to give J-aggregates. This aggregates are based on an intrinsically chiral 2D sheet structure, that depending on the porphyrin meso-substitution pattern, and on the preparation protocol can assemble further to give bi- or multi-layered structures. (B) Chiral sign selection in H_4TPPS_3 J-aggregation depending on the direction of stirring during the rotary evaporation of diluted monomeric solutions to assembled ones. Reproduced from ref. * (see page 1) with permission from the Royal Society of Chemistry.

1.3.6. Template assisted self-assembly

Templates have been used by supramolecular chemist as a tool to assist in the construction of different structures. They allow to obtain non-dissipative non-equilibrium assemblies (#2 and #3 in Figure 1.1A) that cannot be formed spontaneously without templating (the template decrease the energy barrier of a specific pathway). The latter

allows control over size, shape and length of the structure. Once the template is removed, the structure is preserved residing in a deep energy valley (i.e., if it is a state #2). One example performed by Purrello and co-workers[44] showed the formation of chiral structures made by two different non-chiral porphyrin building-blocks which assemble stepwise on a template. Specifically, a tetracationic porphyrin was assembled on an anionic polyglutamate template. Then, the tetraanionic porphyrin was incorporated in the pre-template (Figure 1.9). The supramolecular chirality and structure was conserved By removing the template due to the high kinetic stability of the structure in water (i.e. slow dynamics). Once formed, the chiral information is stored in the structure providing enough information to act itself as a template upon the addition of freshly monomer species. In another example, Meijer and co-workers combined the sergeant-and-soldier approach with removal of the sergeant to obtain well-defined chiral assemblies.[45]

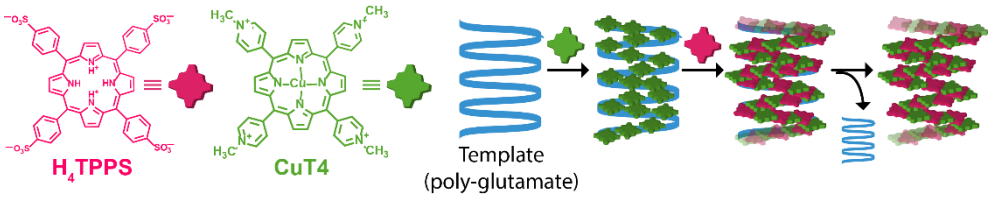

Figure 1.9. Template assisted self-assembly. A tetracationic porphyrin (CuT4) is assembled on a polyglutamate template, afterwards, a tetraanionic porphyrin (H_4TPPS_4) is assembled in the pre-templated aggregates. Removing the template, the formed assemblies were retained. Reproduced from ref. * (see page 1) with permission from the Royal Society of Chemistry.

1.4. Dissipative non-equilibrium states

So far, we have seen how different thermodynamic states can be obtained depending on the preparation protocol and also, how to identify a given self-assembly system. Thermodynamic and kinetic insights are of key importance to understand the mechanism that lead the system to different non-dissipative states (#1, #2 and #3 in Figure 1.1A). As a consequence, different protocols can be used to control the outcome of the self-assembly yielding non-dissipative non-equilibrium states (#2 and #3 in Figure 1.1A). The latter points out the importance of the experimental conditions. In this section, we will show different examples of dissipative natural systems and also the state-of-the-art in artificial dissipative supramolecular systems.

Living cells are constantly contracting, dividing, generating protrusions, moving and organizing internal organelles where the instructions are provided by internal or external signals.[3] All these functions rely on out-of-equilibrium supramolecular systems, all of these are sustained by chemical fuels and constantly dissipating energy.[46] Spatiotemporal control of these supramolecular systems is of key importance in biological complexity. Spatiotemporal control is orchestrated by constant inflow of chemical fuels, network reactions and feedback loops which regulate the precise and temporal occurrence of the self-assembly process.[47] Specifically, chemically fueled processes, network reactions and feedback loops occur in a network of supramolecular assemblies so-called the cytoskeleton where the elements are in constant communication, coordination and synchronization in order to perform complex functions.[3]

The cytoskeleton is a complex network of supramolecular structures which are constantly polymerizing and depolymerizing. For example, it provides control over the cell

shape, drives materials from one side of the cell to the other, and enables some cells to swim, and others to creep across surfaces. Three main kind of filaments (supramolecular assemblies) are fundamental in the behaviour of the cytoskeleton: microtubules, actin filaments and the intermediate filaments.[48] Microtubules (the largest structures) are involved in cellular transport and determine the position of organelles (one side is attached to the centrosome, Figure 1.10A). Actin filaments are important for cell locomotion and determine the surface cellular shape (highly concentrated in the cortex, Figure 1.10B). Intermediate filaments provide mechanical strength and resistance to shear stress (extended along across the cytoplasm, Figure 1.10C).

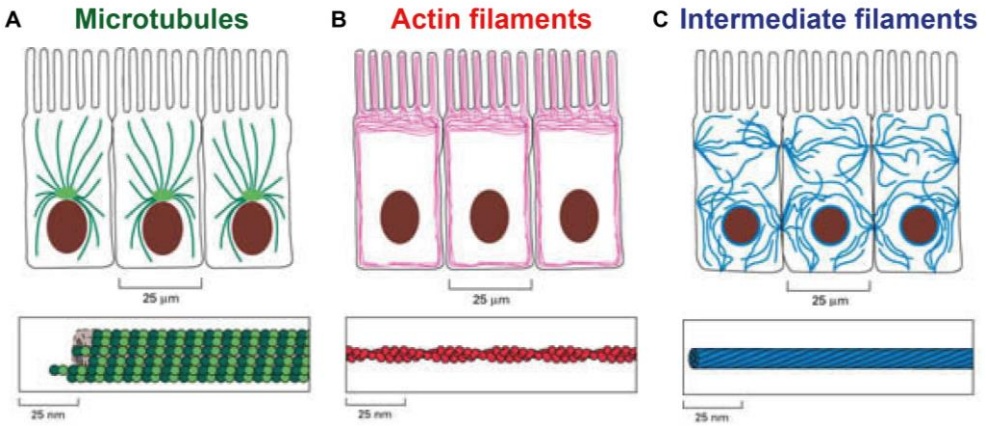

Figure 1.10. Biological supramolecular assemblies (A) Microtubule are the largest structures and are involved in the cellular transport. (B) Actin filaments are important cell motion. (C) Intermediate filaments provide mechanical strength to the cell. Reproduced from ref. 3.

Microtubules are archetypal of dissipative energy driven supramolecular systems with adaptive properties. Stable supramolecular polymerization and fast depolymerization is mediated by Guanosine triphosphate (GTP) which provides mechanically stiff and highly dynamic properties to the structure.[47] Microtubules are formed via polymerization of α/β tubulin hetero-dimers incorporated at the + end of the microtubule, tubulin is activated after bounding to GTP (chemical fuel). Depolymerization occurs promptly via hydrolysis of GTP-tubulin to guanosine diphosphate (GDP), see figure 1.11. Microtubule polymerization and depolymerization are constantly occurring, the latter is known as dynamic instabilities in the microtubule growth which can lead to obtain oscillations or patterns in the microtubule structure.[49] This highly dynamic process allows for the reorientation of the microtubule in order to search for free cellular space.[50,51] In addition, organelles emit signals to stabilize microtubules growth and their reorientation, for example, they serve as tracks for molecular motor proteins to transport cellular components.[48] Importantly, GTP drives microtubule polymerization but once is consumed, no further formation of microtubules can be observed, in other words, dissipative states cannot be sustained once the energy provided stops (the systems relaxes to the thermodynamic equilibrium). Another dissipative system in living cells is made up of actin filament, the polymerization occurs in a similar way as for microtubules, in this case, the system is fueled by adenosine triphosphate (ATP).[48] Polymerization occurs as soon as ATP binds to actin proteins and depolymerization is driven

by the hydrolysis of ATP to adenosine diphosphate (ADP). The unidirectional growth of the filaments provides an adaptable network for the deformation of the cell membrane.

Pursuing analogs of natural dissipative supramolecular systems is one of the key approaches to obtain smart life-like materials with complex functionalities such as self-healing, adaptability, motility and self-replication. In addition, emergent behaviour can be observed by keeping the system out-of-equilibrium such as oscillations and Turing patterns.[46,52] Nevertheless, mimicking biological systems and its behaviour still is a major challenge in the field.

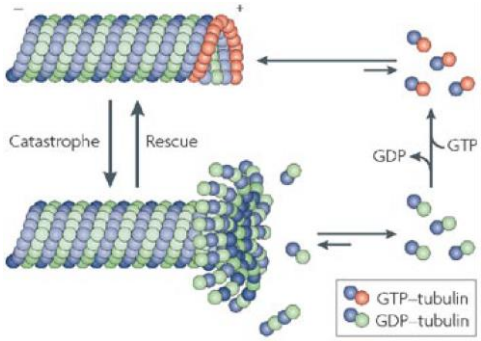

Figure 1.11. Microtubule self-assembly process. The polymerization is led by fueling of GTP, depolymerization occurs after hydrolysis of GTP to GDP. Reproduced from ref. 4 with permission from the Royal Society of Chemistry.

In recent years, supramolecular chemists have focussed on the design of dissipative self-assembly systems. So far, transient formation of assemblies has been shown upon activation of a specific building block where the monomer can be switched from assembling to non-assembling, in other words, the addition of an aliquot of chemical fuel (pipette in Figure 1.12A) lead to transient formation of assemblies (i.e. monomer → assemblies → monomer, figure 1.12A).[17,46] Interestingly, constant addition of chemical fuel (tap in Figure 1.12B) allows to keep the system out-of-equilibrium, this may lead to observe emergent behaviour such as steady states, supramolecular oscillations or Turing patters (figure 1.12B). Different strategies to get dissipative self-assembly systems have been performed such as: directed chemical modification of the building block,[18,19] enzymes mediated reactions[20] or stabilization of charges[21,53–55].

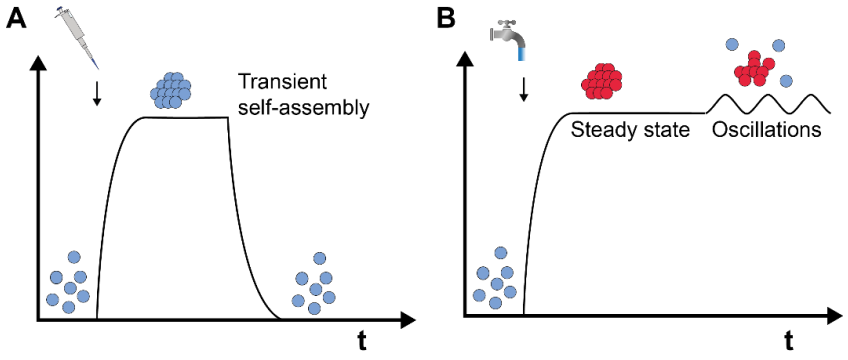

Figure 1.12. Dissipative self-assembly systems. (A) Addition of an equivalent of chemical fuel leads to transient formation of assembled species. (B) Emergent behaviour can be observed upon constant addition of the chemical fuel, the system constantly dissipates energy by keeping it under out-of-equilibrium conditions.

1.4.1. Directed chemical modification

Boekhoven et al.[18,19] performed the first synthetic example of a transient self-assembly system. A molecular hydrogelator was switched between assembling and non-assembling. The assembled state is reached upon activation of the building-block with a methylating agent (dimethyl sulphate, DMS) at basic conditions. Over time, the building-block is hydrolysed back leading the system to the initial non-assembled state (Figure 1.13A,B). The study[19] shows that the hydrolysis rate depends on the pH at which the experiment was performed (higher pH values increased the rate of hydrolysis). Moreover, hydrolysis was not observed at lower pH values (below pH 9). Interestingly, a gel formed at pH 11 has a lifetime of 10 h (Figure 1.13B). However, lifetimes of less than 4 h can be obtained when the amount of chemical fuel added is reduced indicating that the lifetime and dissolution of the gel strongly depend on the experimental conditions. Therefore, stiff hydrogels can be obtained upon the addition of chemical fuel at lower pH values since hydrolysis does not occur or is too slow hampering the dissolution of the gel. On the other hand, less stiff hydrogels were obtained at higher pH values. Specifically, different mechanical properties of the hydrogel (i.e., weaker or stronger hydrogels with different lifetimes) can be obtained by changing the concentration of chemical fuel. This was confirmed by a kinetic model. In addition, the material also showed self-regenerating behaviour after applying mechanical perturbations when high amounts of gels were present (Figure 1.13C).

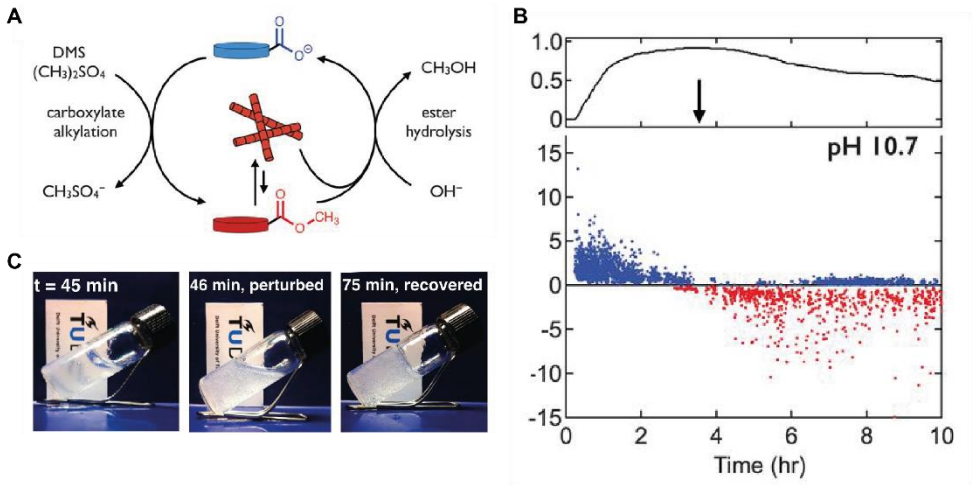

Figure 1.13. Chemical modification. (A) The building-block is activated upon addition of dimethyl sulphate, over time the building-block is hydrolysed leading the system to the initial non-assembled state. (B) Transient assembly formation at pH 10.7. The red dots and the blue dots indicate assembled state and non-assembled state, respectively. (C) The system self-regenerates after applying a mechanical perturbation. Reprinted from ref. 19 with permission from AAAS.

1.4.2. Enzymes mediated reactions

Enzymes are highly interesting due to their abundance in living systems. They are used to create fast responses of natural systems. Recently, biosynthetic supramolecular systems mediated by different enzymatic reactions have been developed. Ulijn and co-

workers[20] developed a biocatalytic dissipative self-assembly system where the self-assembly process is switched on and off by different irreversible enzymatic pathways. The system is based on a naphthalene-peptide gelator that tends to self-assemble upon catalytic incorporation of a hydrophobic amino acid (trans-acylation was mediated by α-chymotrypsin). The same enzyme also catalyses the hydrolysis of the building-block yielding the starting materials (i.e., deactivated building-block and amino acid). Over time, both reactions start to compete leading to an equilibrium situation in which the final assembled state depends on the assembly character of the naphthalene-peptide derivative employed (Figure 1.14A). Transient gel formation was performed by using thermolysin that performs direct condensation of free acids and amides. It was shown that the hydrogel lifetime can be tuned by changing the pH. In addition, the system could be refueled up to three times indicating that waste accumulation impedes further repetition of assembling/disassembling cycles (Figure 1.14B).

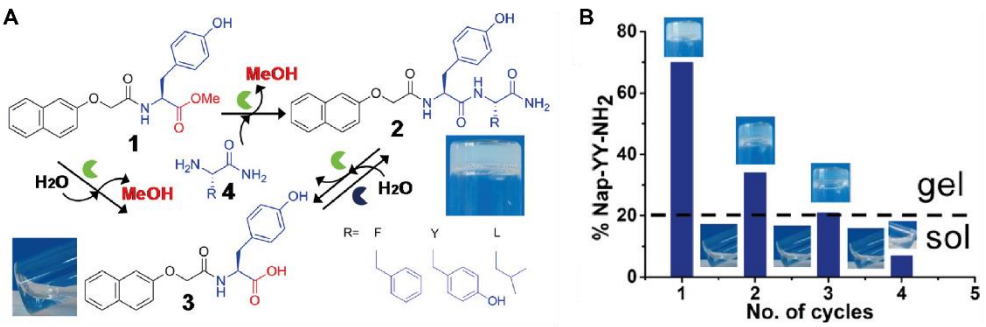

Figure 1.14. Biosynthetic dissipative systems. (A) The catalytic incorporation of a hydrophobic amino acid is performed by α-chymotrypsin yielding **2**. The same enzyme can hydrolyse **2** leading to compound **3**. Thermolysin was incorporated into the network to carry out the condensation of the free amino acid. (B) The system can be refueled up to three times, waste accumulation impedes further repetition of the cycles. Reproduced from ref. 20 with permission from American Chemical Society.

1.4.3. Stabilization of charges

Recently, George and co-workers[53] demonstrated transient helical conformation of a naphthalene diimide derivative (NDPA) upon the addition of adenosine triphosphate (ATP, chemical fuel). Once NDPA binds to ATP, P-helical assemblies were obtained. ATP is hydrolysed to ADP by hexokinase enzyme yielding M-helical assemblies. Transient formation of the assemblies was performed by introducing into the network creatine phosphokinase, an enzyme that forms ATP upon the addition of sacrificial reactant phosphocreatine and ADP (Figure 1.15A,B). On the other hand, hexokinase transfers a phosphate group from ATP to glucose yielding ADP and glucose-2-phosphate. Different lifetimes and frequency of the assemblies were obtained by changing enzyme compositions and the concentration of all the species in solution. The latter allows to control the rates of P→ M conversion. In another recent example, Prins and co-workers[21,54,55] demonstrated transient stabilization of vesicular assemblies. ATP (chemical fuel) stabilized vesicle formed by C_{16}TACN·Zn^{2+} surfactant. Dissipative transient formation of vesicular assemblies was achieved by incorporating an extra pathway. ATP is hydrolysed by potato apyrase enzyme to adenosine monophosphate (AMP) and two molecules of orthophosphate (Pi), see Figure 1.15C. Aggregation studies showed that AMP and P_i did not induce formation of vesicles by

themselves. The process could be cycled 7 times, then waste accumulation impedes further formation of vesicular assemblies (Figure 1.15D). Interestingly, the system was used to perform a chemical reaction. They demonstrated that product formation is controlled by the lifetime of the vesicular assembly. This approach can be used to control reactions under non-equilibrium conditions.

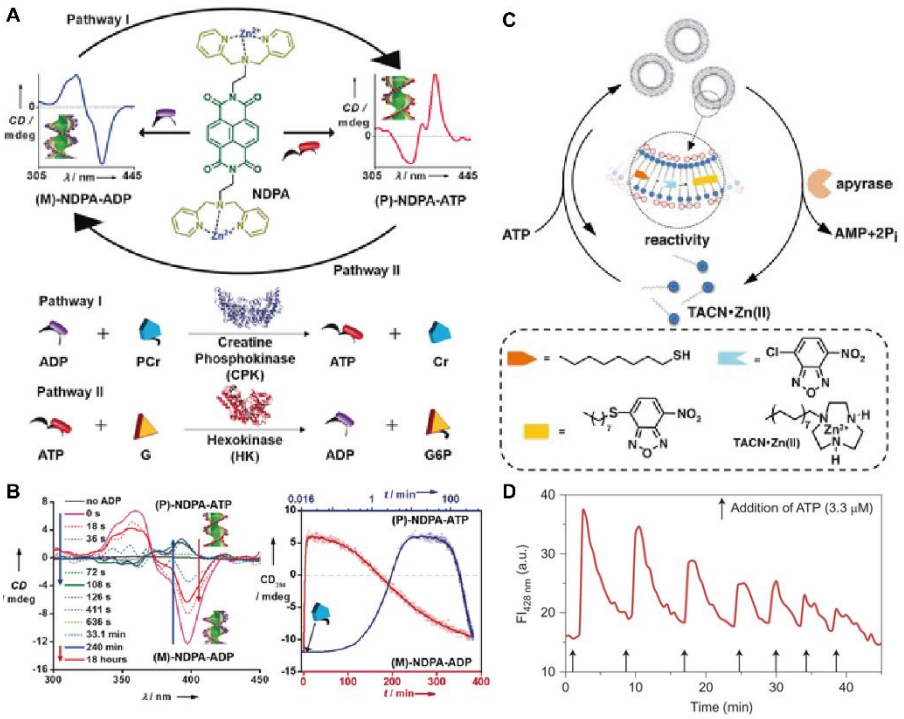

Figure 1.15. Stabilization of charges (A) NDPA can interact with ATP and ADP yielding P-helix or M-Helix assemblies, respectively. (B) Transient formation of M-Helix assemblies can be observed upon addition of an equivalent of the chemical fuel (ATP). Reproduced from ref. 53 with permission from Wiley. (C) Vesicular assemblies can be formed upon addition of ATP, non-assembled state can be obtained after hydrolysis of ATP. (D) The system can be refueled 7 times, afterwards, accumulation of waste inhibits further vesicle formation. Reproduced from ref. 21 with permission from Nature Research.

1.5. Perylene diimide derivatives as a building-block

Perylene diimide derivative derived from perylene-3,4,9,10-tetracarboxylic acid diimide (PDIs) are widely-used building-blocks in supramolecular chemistry as its self-assembly can be controlled through π-π stacking, electrostatic interactions and the hydrophobic effect.[56] The core consists of a rigid polycyclic scaffold substituted with two imide groups at the 3,4- and 9,10- positions, which makes a flat and rigid π-conjugated system (Figure 1.16A). When imide groups are incorporated into the chromophore, the strong conjugation between the imide groups with perylene core (acceptor-donor-acceptor type interaction) shifts the absorption peak from 400 to 520 nm. The HOMO and LUMO orbitals from quantum chemical calculations showed nodes at the imide nitrogen, which electronically isolates the perylene diimide from various imide substituents (Figure 1.16B).[56,57] As a result, the core can be regarded as a closed chromophoric system whose

photophysical property is not affected by varying the imide substituents. Another advantage of the rigid PDIs is that they show little solvatochromism as solvent molecules do not affect their conformation. While the photo-physical and chemical property of a monomer is robust, those of aggregates are sensitive to the packing motifs of monomers.[56] Namely, aggregation can be followed by spectroscopic techniques due to the change in the vibronic progression upon stacking of consecutive cores (Figure 1.16C).[56–59]

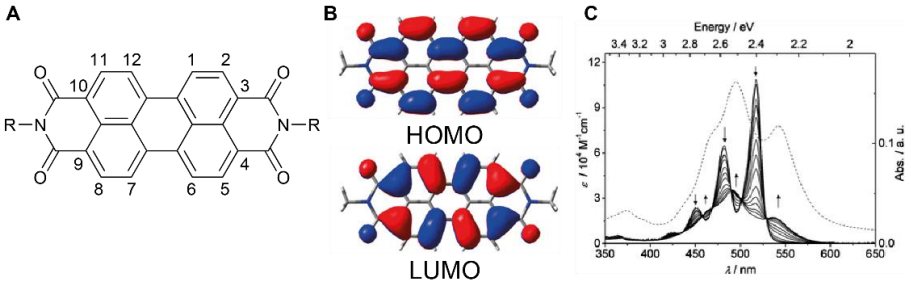

Figure 1.16. Perylene diimide derivatives. (A) Chemical structure of Perylene Diimide derivatives (PDIs). (B) HOMO and LUMO orbitals show the closed chromophoric character of the core. (C) UV-Vis spectroscopy can be used to follow the aggregation of PDIs, aggregation induces changes in the vibronic progression. The arrows indicate the direction of the self-assembly. Dashed line spectrum belongs to a spin-coated PDI derivative. Reproduced from ref. 56 with permission from American Chemical Society.

PDIs show strong absorption in the visible range with maxima between 500 and 570 nm due to the S0 → S1 transitions of the perylene core. Upon self-assembly broader and (hypsochromically or bathochromically) shifted bands are obtained. In addition, the variation between the 0-0 and 0-1 transitions ($A_{0\text{-}1}/A_{0\text{-}0}$) is used to elucidate the self-assembly process (an increase of the ratio indicates further aggregation of assemblies, e.g., the value for monomeric species in solution is about 0.65).[56,60] PDIs show strong assembling properties that are intrinsic of its molecular structure. The polymerization occurs through the extended π-surface of the core. Especially in water where the self-assembly constant is two orders of magnitude higher than in any other solvent (the hydrophobic effect play an important role).[61] In addition, PDIs have been used for multiple applications in organic electronics, photovoltaics or as smart materials.[56,62] All this together makes PDI an interesting and attractive platform to use in supramolecular chemistry.

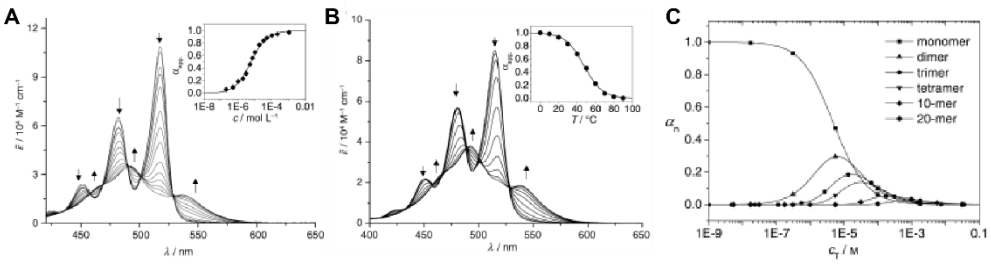

Figure 1.17. General spectroscopic behaviour of PDIs. (A) Concentration dependent UV-Vis spectroscopy shows the evolution of the polymerization. Dilution promotes formation of non-assembled species. Arrows indicates the direction of the self-assembly. (B) Temperature dependent UV-Vis spectroscopy shows the evolution of the self-assembly. Polymerization is induced by cooling down a solution. Arrows indicates the direction of the self-assembly. (C) Molar fraction of the aggregates at different concentrations based on the isodesmic model. Reproduced from ref. 60 with permission from Wiley.

PDIs tend to self-assemble into columnar structures (cofacial polymerization). Different models have been used to elucidate the mechanism of the polymerization. Würthner and co-workers extensively studied the aggregation of different perylene diimide derivatives in organic and aqueous solutions.[56,61] In one example, a trialkylphenyl-functionalized perylene diimide was studied by different techniques such as UV-Vis, fluorescence and NMR spectroscopy.[60] The supramolecular polymerization was followed by performing concentration and temperature dependent UV-Vis absorption spectra. PDI was not assembled at low concentrations showing the characteristic vibronic progression of molecularly dissolved PDIs chromophores with absorption bands between 400 and 550 nm. Aggregation was induced by increasing the concentration. This yielded broader and less structured spectra due to the electronic coupling between consecutive cores showing an increase of the ratio between the bands (increase in the degree of aggregation), see Figure 1.17A. Temperature-dependent UV-Vis experiments showed comparable variations of the spectra as observed for concentration dependent experiments (Figure 1.17B). Lower temperatures promote the supramolecular polymerization. The molar fraction of the aggregates was obtained by fitting the data with an isodesmic polymerization model (Figure 1.17C).

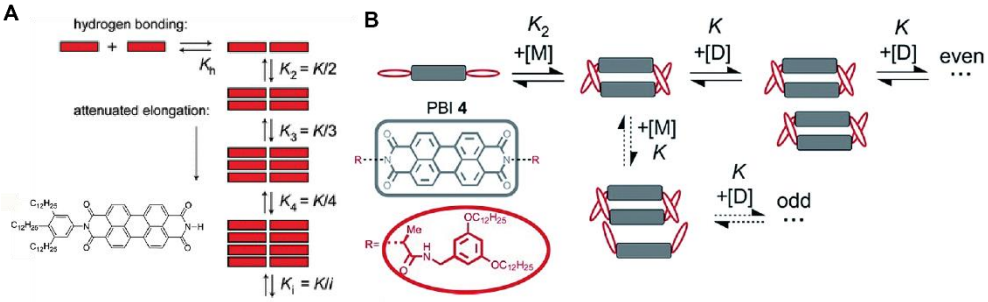

Figure 1.18. New polymerization models. (A) Attenuated elongation was initiated after dimer formation. The polymer grows via dimer-dimer interaction. Reproduced from ref. 63 with permission from the Royal Society of Chemistry. (B) Oligomers were formed after dimer formation via hydrogen bonding. The model takes into account the formation of even and odd oligomers. Reproduced from ref. 64 with permission from the Royal Society of Chemistry.

In addition, the self-assembly behaviour of different PDI derivatives has led to develop new polymerization models where the self-assembly behaviour cannot be explained by basic isodesmic or cooperative polymerization models.[63,64] As an example, Meijer and co-workers[63] studied the polymerization of an asymmetric PDI. Temperature dependent UV-Vis absorption spectra showed a non-sigmoidal shape suggesting that assemblies grow via a cooperative mechanism. Surprisingly, smaller assemblies were found by small angle X-ray scattering (SAXS) experiments (not expected for a cooperative growth). They developed a thermodynamic self-assembly model that can explain the observed behaviour. In the model, an attenuated elongation was initiated after unfavourable dimer formation (steric hindrance impedes the formation of long polymers), once dimer is formed the polymer grows via dimer-dimer interaction (Figure 1.18A). In a recent example, Würthner and co-workers[64] developed a new K_2-K_1 anti-cooperative polymerization model to explain the self-assembly polymerization of a symmetric PDI derivative (Figure 1.18B). Specifically, the dimer was formed via hydrogen bonding. Then, assemblies can grow by consecutive additions of dimers into the assemblies (even oligomers) or by consecutive

additions of monomeric species into the assemblies (odd oligomers). Moreover, the model permits to obtain the ratio between even and odd oligomers (Figure 1.18B). All these studies have served to elucidate new polymerization models that can be extended to other systems in which oligomers or assemblies grow via dimer formation.

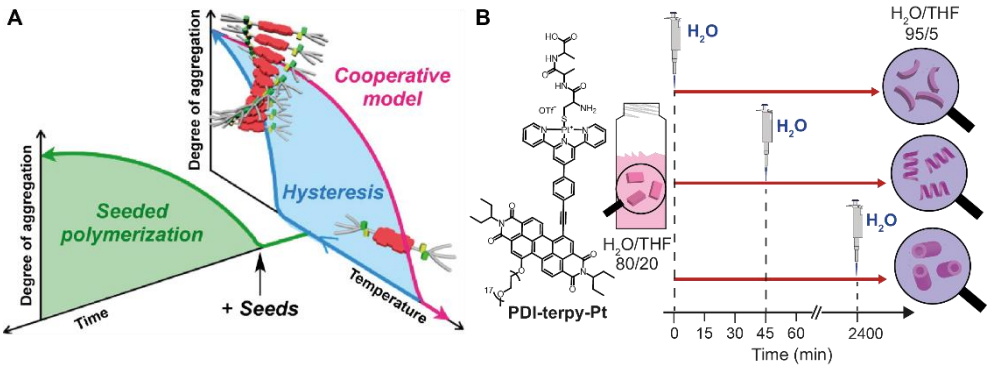

Figure 1.19. Kinetically trapped and metastable PDIs. (A) A living supramolecular polymerization obtained by the addition of seeds to kinetically trapped monomers in a thermal hysteresis. (B) Schematic illustration of different kinetic assemblies of PDI-Pt obtained by diluting with water a water/THF = 80/20 mixture to 95/5 at different evolution times during self-assembly (0, 45, and 2400 min). Reproduced from ref. * (see page 1) with permission from the Royal Society of Chemistry.

PDIs have been used to selectively tune the final supramolecular structure. Sample preparation leads to different metastable or kinetically trapped states.[65,66] As an example, Ogi et al.[65] designed a symmetric PDI derivative building block in which monomeric species were kinetically trapped via hydrogen intramolecular bonding formation. Specifically, upon cooling a monomeric solution, a mixture of non-assembling monomers and assembling monomers was obtained delaying the nucleation step with lag times of more than 1 hour. Thermodynamically favourable seeded supramolecular assemblies with low dispersity were obtained by adding existing pre-assembled supramolecular seeds. Seeding experiments allow to control the supramolecular polymerization. This approach can be used to control not only the nanostructures but also the distinct properties of the materials (Figure 1.19A). In another example, kinetically trapped PDI states were used to control the final structures. Rybtchinsky and co-workers[66] showed pathway selection by kinetically trapping a perylene diimide terpyridine platinum complex, PDI-Pt (Figure 1.19B). PDI assemblies were obtained by using a good solvent (THF, molecularly dispersed solution can be obtained) and a bad solvent (aggregation is induced in water). In water, the hydrophobic effect was enhanced resulting in slow assembly/disassembly dynamics and strong kinetic trapping. On the other hand, solvophobicity can be diminished upon addition of THF, which leads to metastable assemblies that could equilibrate over time. Disordered curved fiber assemblies were obtained in solution mixtures of water/THF = 95/5 giving a small CD signal that did not change over time. However, when THF is increased the system evolves for 3 days yielding straight fiber assemblies with higher CD signals. This approach has been used to kinetically trap different metastable assemblies. The same final composition was adjusted at different time points. PDI-Pt was dissolved in water/THF = 80/20 solution. Then, the system was adjusted up to 5% of THF content at different time evolution (0 min, 45 min and 2400 min) leading to completely different assemblies. Therefore, short curved fibers with 3.0 nm diameter, longer fibers with 3.2 nm diameter and nanotubes with 4.5 nm diameter were

obtained respectively. Interestingly, the assemblies did not interconvert over long times indicating the formation of kinetically trapped states.

So far, we have seen that PDIs have been widely used in supramolecular chemistry leading to different supramolecular structures and novel polymerization mechanism. In addition, the strong aggregation properties of PDIs can be used to tune the outcome of the self-assembly. Along this thesis, we will show different PDI derivatives examples where non-dissipative equilibrium states, kinetically trapped states and dissipative states are involved. Interestingly, emergent behaviour is obtained under non-equilibrium conditions.

1.6. Aim and outline of this thesis

Living cells use dissipative self-assembly polymerization to quickly adapt and perform different functions (translation, mass transport, etc.). We are far from mimicking such systems. Thermodynamic and kinetic insights are important in order to elucidate the self-assembly behaviour of the different supramolecular systems. Different techniques and methodologies have been used to tune and control the self-assembly process leading to different structures. So far, only transient dissipative systems have been demonstrated. The design of new methodologies and techniques to bring and keep the system out of equilibrium are needed.

The aim of this thesis is to develop new strategies and methodologies to tune, control and understand dissipative self-assembly. Constant influx of energy by chemical fuels or thermal gradients allows to keep the system under non-equilibrium conditions. This can lead to emergent behaviour such as oscillations or waves.

To this end, in **chapter 2** assembly/disassembly cycles of a symmetric perylene diimide derivative containing solubilizing oligoethyleneglycol chains were performed in aqueous solutions by using reducing ($Na_2S_2O_4$) and oxidizing agents (O_2) as chemical fuels. This approach can be used to perform pathway selection and overcome kinetically trapped states. The frequency and number of redox cycles provides control over the nucleation, growth process, size and internal order of the assembled structures. **Chapter 3** shows oscillating behaviour of the system under continuous influx of chemical fuel (reducing agent) in a semi-batch reactor. Depending on the flow rate and the history of the system, different kinds of oscillatory behaviour can be found. Kinetic studies show a size-dependent reduction rate, which acts as a negative feedback in the oscillatory network. In order to explain the oscillatory behaviour, a mathematical model (based on chemical kinetics) is developed. In addition, reaction-diffusion processes in non-stirred media are also studied. Interestingly, a trigger supramolecular wave is obtained upon addition of seeds (assembled structures) to a thin layer of non-assembled structures.

In **chapter 4** a novel technique to sustain a supramolecular system under non-equilibrium conditions is developed. A peptide perylene diimide derivative is designed in order to perform assembly/disassembly cycles upon the addition of the chemical fuel (ATP) by phosphorylation and dephosphorylation, respectively. Waste accumulation leads to inhibition of the system impeding the repetition of multiple transient self-assembly cycles. The latter can be solved by designing a membrane reactor (open system) that allows the

inflow of ATP and removal of the waste leading to sustain non-equilibrium steady states (NESS) where assembly/disassembly cycles are continuously occurring.

In **chapter 5**, microscale thermophoresis (MST) is used to study the supramolecular polymerization of a symmetric perylene diimide derivative containing tryptophan moieties. MST is a technique that relies on the directed migration of molecules in a temperature gradient. MST technique is used to study a model supramolecular polymerization system under non-equilibrium conditions.

The epilogue provides a broader perspective of the work done in this thesis. The different techniques and methodologies that have been used to obtain different dissipative supramolecular systems. We believe that these could eventually be applied to obtain more life-like synthetic materials.

1.7. References

1. Lehn, J.-M. Toward complex matter: Supramolecular chemistry and self-organization. *Proc. Natl. Acad. Sci.* **99,** 4763–4768 (2002).
2. Lehn, J.-M. Toward self-organization and complex matter. *Science* **295,** 2400–2403 (2002).
3. Alberts, B. *et al. Molecular Biology of the Cell*. (Garland Science, 2002).
4. Merindol, R. & Walther, A. Materials learning from life: concepts for active, adaptive and autonomous molecular systems. *Chem. Soc. Rev.* (2017). DOI: 10.1039/C6CS00738D
5. Lehn, J.-M. From supramolecular chemistry towards constitutional dynamic chemistry and adaptive chemistry. *Chem. Soc. Rev.* **36,** 151–160 (2007).
6. Lehn, J.-M. From Molecular to Supramolecular Chemistry. in *Supramolecular Chemistry* 1–9 (Wiley-VCH Verlag GmbH & Co., 1995).
7. Lehn, J.-M. Supramolecular Chemistry—Scope and Perspectives Molecules, Supermolecules, and Molecular Devices (Nobel Lecture). *Angew. Chem. Int. Ed. Engl.* **27,** 89–112 (1988).
8. Lehn, J.-M. *Supramolecular Chemistry: Concepts and Perspectives*. (John Wiley & Sons, 2011).
9. Aida, T., Meijer, E. W. & Stupp, S. I. Functional Supramolecular Polymers. *Science* **335,** 813–817 (2012).
10. Steed, J. W. & Atwood, J. L. *Supramolecular Chemistry*. (John Wiley & Sons, 2013).
11. Fujita, D. *et al.* Self-Assembly of M30L60 Icosidodecahedron. *Chem* **1,** 91–101 (2016).
12. Urban, M. W. *Handbook of Stimuli-Responsive Materials*. (John Wiley & Sons, 2011).
13. De Greef, T. F. A. *et al.* Supramolecular Polymerization. *Chem. Rev.* **109,** 5687–5754 (2009).
14. Ciferri, A. *Supramolecular Polymers, Second Edition*. (CRC Press, 2005).
15. Tantakitti, F. *et al.* Energy landscapes and functions of supramolecular systems. *Nat. Mater.* **15,** 469–476 (2016).
16. Evans, L. D., Stafford, G. P., Ahmed, S., Fraser, G. M. & Hughes, C. An escort mechanism for cycling of export chaperones during flagellum assembly. *Proc. Natl. Acad. Sci.* **103,** 17474–17479 (2006).
17. Mattia, E. & Otto, S. Supramolecular systems chemistry. *Nat. Nanotechnol.* **10,** 111–119 (2015).
18. Boekhoven, J. *et al.* Dissipative Self-Assembly of a Molecular Gelator by Using a Chemical Fuel. *Angew. Chem.* **122,** 4935–4938 (2010).
19. Boekhoven, J., Hendriksen, W. E., Koper, G. J. M., Eelkema, R. & Esch, J. H. van. Transient assembly of active materials fueled by a chemical reaction. *Science* **349,** 1075–1079 (2015).
20. Debnath, S., Roy, S. & Ulijn, R. V. Peptide Nanofibers with Dynamic Instability through Nonequilibrium Biocatalytic Assembly. *J. Am. Chem. Soc.* **135,** 16789–16792 (2013).
21. Maiti, S., Fortunati, I., Ferrante, C., Scrimin, P. & Prins, L. J. Dissipative self-assembly of vesicular nanoreactors. *Nat. Chem.* **8,** 725–731 (2016).
22. Kondepudi, D. & Prigogine, I. *Modern Thermodynamics: From Heat Engines to Dissipative Structures*. (Wiley, 2014).
23. Atkins, P. & Paula, J. de. *Atkins' Physical Chemistry*. (OUP Oxford, 2014).
24. Nicolis, G. & Prigogine, I. *Self-organization in nonequilibrium systems: from dissipative structures to order through fluctuations*. (Wiley, 1977).
25. Smulders, M. M. J. *et al.* How to Distinguish Isodesmic from Cooperative Supramolecular Polymerisation. *Chem. – Eur. J.* **16,** 362–367 (2010).
26. Korevaar, P. A., de Greef, T. F. A. & Meijer, E. W. Pathway Complexity in π-Conjugated Materials. *Chem. Mater.* **26,** 576–586 (2014).
27. van der Zwaag, D. *et al.* Kinetic Analysis as a Tool to Distinguish Pathway Complexity in Molecular Assembly: An Unexpected Outcome of Structures in Competition. *J. Am. Chem. Soc.* **137,** 12677–12688 (2015).
28. Markvoort, A. J., Eikelder, H. M. M. ten, Hilbers, P. A. J. & de Greef, T. F. A. Fragmentation and Coagulation in Supramolecular (Co)polymerization Kinetics. *ACS Cent. Sci.* **2,** 232–241 (2016).
29. D. van der Zwaag, P. A. Korevaar, A. J. Markvoort, T. F. A. de Greef, Internal communication. Internal communication.

30. Korevaar, P. A. *et al.* Pathway complexity in supramolecular polymerization. *Nature* **481,** 492–496 (2012).
31. Powers, E. T. & Powers, D. L. Mechanisms of Protein Fibril Formation: Nucleated Polymerization with Competing Off-Pathway Aggregation. *Biophys. J.* **94,** 379–391 (2008).
32. Ogi, S., Sugiyasu, K., Manna, S., Samitsu, S. & Takeuchi, M. Living supramolecular polymerization realized through a biomimetic approach. *Nat. Chem.* **6,** 188–195 (2014).
33. Kang, J. *et al.* A rational strategy for the realization of chain-growth supramolecular polymerization. *Science* **347,** 646–651 (2015).
34. Haedler, A. T. *et al.* Pathway Complexity in the Enantioselective Self-Assembly of Functional Carbonyl-Bridged Triarylamine Trisamides. *J. Am. Chem. Soc.* **138,** 10539–10545 (2016).
35. Escudero, C. *et al.* Hierarchical dependence of porphyrin self-aggregation: controlling and exploiting the complexity. *J. Porphyr. Phthalocyanines* **14,** 708–712 (2010).
36. El-Hachemi, Z., Mancini, G., Ribó, J. M. & Sorrenti, A. Role of the Hydrophobic Effect in the Transfer of Chirality from Molecules to Complex Systems: From Chiral Surfactants to Porphyrin/Surfactant Aggregates. *J. Am. Chem. Soc.* **130,** 15176–15184 (2008).
37. Akbarzadeh, A. *et al*. Liposome: classification, preparation, and applications. *Nanoscale Res. Lett.* **8,** 102 (2013).
38. Hermans, T. M. *et al.* Stepwise Noncovalent Synthesis Leading to Dendrimer-Based Assemblies in Water. *J. Am. Chem. Soc.* **129,** 15631–15638 (2007).
39. Hermans, T. M. *et al.* Self-assembly of soft nanoparticles with tunable patchiness. *Nat. Nanotechnol.* **4,** 721–726 (2009).
40. Numata, M. Supramolecular Chemistry in Microflow Fields: Toward a New Material World of Precise Kinetic Control. *Chem. - Asian J.* **10,** 2574–2588 (2015).
41. Ribó, J. M., El-Hachemi, Z. & Crusats, J. Effects of flows in auto-organization, self-assembly, and emergence of chirality. *Rendiconti Lincei* **24,** 197–211 (2013).
42. Ribó, J. M., Crusats, J., Sagués, F., Claret, J. & Rubires, R. Chiral Sign Induction by Vortices During the Formation of Mesophases in Stirred Solutions. *Science* **292,** 2063–2066 (2001).
43. Micali, N. *et al.* Selection of supramolecular chirality by application of rotational and magnetic forces. *Nat. Chem.* **4,** 201–207 (2012).
44. D'Urso, A., Fragalà, M. E. & Purrello, R. From self-assembly to noncovalent synthesis of programmable porphyrins' arrays in aqueous solution. *Chem. Commun.* **48,** 8165 (2012).
45. Helmich, F., Lee, C. C., Schenning, A. P. H. J. & Meijer, E. W. Chiral Memory via Chiral Amplification and Selective Depolymerization of Porphyrin Aggregates. *J. Am. Chem. Soc.* **132,** 16753–16755 (2010).
46. Ashkenasy, G., M. Hermans, T., Otto, S. & F. Taylor, A. Systems chemistry. *Chem. Soc. Rev.* **46,** 2543–2554 (2017).
47. Heinen, L. & Walther, A. Celebrating Soft Matter's 10th Anniversary: Approaches to program the time domain of self-assemblies. *Soft Matter* **11,** 7857–7866 (2015).
48. D.), R. A. H. (Ph, Harvey, R. A. & Ferrier, D. R. *Biochemistry*. (Lippincott Williams & Wilkins, 2011).
49. Obermann, H., Mandelkow, E. M., Lange, G. & Mandelkow, E. Microtubule oscillations. Role of nucleation and microtubule number concentration. *J. Biol. Chem.* **265,** 4382–4388 (1990).
50. Drechsel, D. N., Hyman, A. A., Cobb, M. H. & Kirschner, M. W. Modulation of the dynamic instability of tubulin assembly by the microtubule-associated protein tau. *Mol. Biol. Cell* **3,** 1141–1154 (1992).
51. Ernster, L. & Schatz, G. Mitochondria: a historical review. *J. Cell Biol.* **91,** 227s–255s (1981).
52. Epstein, I. R. & Pojman, J. A. *An Introduction to Nonlinear Chemical Dynamics: Oscillations, Waves, Patterns, and Chaos*. (Oxford University Press, 1998).
53. Dhiman, S., Jain, A. & George, S. J. Transient Helicity: Fuel-Driven Temporal Control over Conformational Switching in a Supramolecular Polymer. *Angew. Chem.* **129,** 1349–1353 (2017).
54. Chen, J., Maiti, S., Fortunati, I., Ferrante, C. & Prins, L. J. Temporal Control over Transient Chemical Systems using Structurally Diverse Chemical Fuels. *Chem. - Eur. J.* (2017). DOI: 10.1002/chem.201701533

55. Pezzato, C. & Prins, L. J. Transient signal generation in a self-assembled nanosystem fueled by ATP. *Nat. Commun.* **6,** 7790 (2015).
56. Würthner, F. *et al.* Perylene Bisimide Dye Assemblies as Archetype Functional Supramolecular Materials. *Chem. Rev.* **116,** 962–1052 (2016).
57. Würthner, F. Perylene bisimide dyes as versatile building blocks for functional supramolecular architectures. *Chem. Commun.* **0,** 1564–1579 (2004).
58. Würthner, F., Chen, Z., Dehm, V. & Stepanenko, V. One-dimensional luminescent nanoaggregates of perylene bisimides. *Chem. Commun.* **0,** 1188–1190 (2006).
59. Chen, Z. *et al.* Photoluminescence and Conductivity of Self-Assembled π–π Stacks of Perylene Bisimide Dyes. *Chem. – Eur. J.* **13,** 436–449 (2007).
60. Würthner, F., Thalacker, C., Diele, S. & Tschierske, C. Fluorescent J-type Aggregates and Thermotropic Columnar Mesophases of Perylene Bisimide Dyes. *Chem. – Eur. J.* **7,** 2245–2253 (2001).
61. Görl, D., Zhang, X. & Würthner, F. Molecular Assemblies of Perylene Bisimide Dyes in Water. *Angew. Chem. Int. Ed.* **51,** 6328–6348 (2012).
62. van Herrikhuyzen, J., Syamakumari, A., Schenning, A. P. H. J. & Meijer, E. W. Synthesis of n-Type Perylene Bisimide Derivatives and Their Orthogonal Self-Assembly with p-Type Oligo(p-phenylene vinylene)s. *J. Am. Chem. Soc.* **126,** 10021–10027 (2004).
63. Weegen, R. van der *et al.* Small sized perylene-bisimide assemblies controlled by both cooperative and anti-cooperative assembly processes. *Chem. Commun.* **49,** 5532–5534 (2013).
64. Gershberg, J., Fennel, F., H. Rehm, T., Lochbrunner, S. & Würthner, F. Anti-cooperative supramolecular polymerization: a new K 2 – K model applied to the self-assembly of perylene bisimide dye proceeding via well-defined hydrogen-bonded dimers. *Chem. Sci.* **7,** 1729–1737 (2016).
65. Ogi, S., Stepanenko, V., Sugiyasu, K., Takeuchi, M. & Würthner, F. Mechanism of Self-Assembly Process and Seeded Supramolecular Polymerization of Perylene Bisimide Organogelator. *J. Am. Chem. Soc.* **137,** 3300–3307 (2015).
66. Tidhar, Y., Weissman, H., Wolf, S. G., Gulino, A. & Rybtchinski, B. Pathway-Dependent Self-Assembly of Perylene Diimide/Peptide Conjugates in Aqueous Medium. *Chem. – Eur. J.* **17,** 6068–6075 (2011).

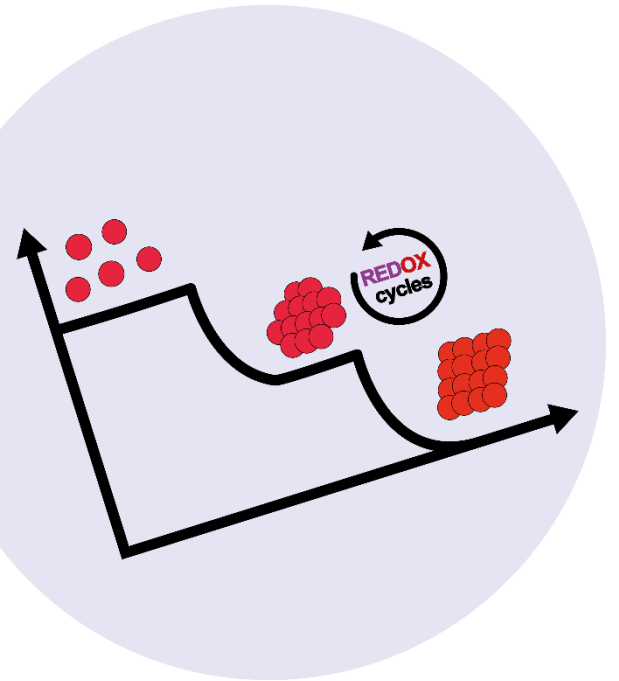
REDOX
cycles

2

Supramolecular pathway selection mediated by chemical fuels

Abstract: In this chapter we develop a new approach to achieve supramolecular pathway selection of a perylenediimide derivative in aqueous solution mediated by chemical fuels. Redox reactions control assembly/disassembly cycles. The number and frequency of cycles affect the nucleation and growth process, providing control over the size and internal order of the resulting self-assembled structures.

This work has been published:
Leira-Iglesias, J., Sorrenti, A., Sato, A., Dunne, P. A., & Hermans, T. M. Supramolecular pathway selection of perylenediimides mediated by chemical fuels. *Chemical Communications,* **52, 9009-9012 (2016).

2.1. Introduction

In Chapter 1 we have shown the importance of studying the kinetics of a supramolecular system in order to completely understand its behaviour. In addition, the incorporation of techniques such as stopped-flow or temperature-jump has helped to find previously undetectable metastable states and off-pathways processes. Kinetic studies have brought new mechanistic insights such as nucleation effects or the presence of multiple pathways, which has led to the development of new tools for non-covalent synthesis. The latter is used to guide the system through the energy landscape in order to reach the desired structure. Different preparation protocols (e.g. solvent processing, modulating temperature, order of addition, etc.) can be used to reach the target assembled state. The latter is relevant in aqueous environments where the assembly can be governed by the hydrophobic effect and thus, enhancing the appearance of high kinetic barriers and slow exchange dynamics.[1] The high free energy of the polymerization of perylene diimide (PDI) in water with respect to any of the other solvents indicates that the core is strongly assembled. This diminishes the exchange of monomers into polymers and thus, the exchange dynamics (Figure 2.1A). As we have explained in chapter 1 (section 1.3), pathway selection can be used to obtain different supramolecular structures. Most of the protocols involve heating/cooling steps to control kinetics.[2–5] However, the hydrophobic effect can hamper such control of the system in aqueous media leading to precipitation of the system or further aggregation upon heating due to entropic effects.[6–8]

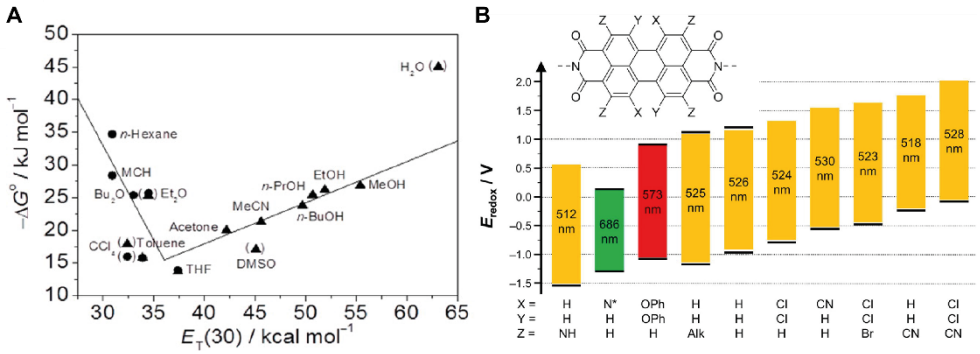

Figure 2.1. Perylene diimide derivatives. (A) Standard Gibbs free energy for isodesmic polymerization vs solvent polarity of different PDIs assemblies (B) Substituents in the bay position of different PDIs highly influenced the photophysical and redox properties. Reproduced from ref. 1 with permission from American Chemical Society.

As mentioned in chapter 1, PDIs are well-known building blocks with strong absorption, long fluorescence lifetimes and high quantum yields.[1,9] They are highly used in organic electronics, photovoltaics or smart materials because of its high thermal, chemical and photochemical stability.[1,9–11] The stability of the core is attributed to the poor electronic character, which makes PDIs resistive to oxidative degradation or other decomposition processes.[1] In addition, due to their electron-deficient character, PDIs can be easily stepwise reduced to the radical anion and the dianion species. Different studies have shown that both species (radical anion and dianion) are stable for long times under inert atmospheres (oxygen free).[1,9] Namely, stable water soluble PDI dianions have been used for dyeing of cotton.[12] Quantum chemical calculations revealed that reduction processes, as well as $S_0 \rightarrow S_1$ transitions can be explained in a simple way as an electron

transition from the HOMO to the LUMO orbital.[1] Moreover, variations on the imide substituents do not affect the photophysical properties or redox potentials of the core as we have seen in chapter 1, section 1.5 (Figure 2.1B). In contrast, the photophysical and redox properties can be highly influenced by including some substituents in the bay positions (i.e., substituents at the core positions). [9] The latter can also affect the aggregation of PDIs by enhancing or diminishing the self-assembly character of the core. These redox properties can be used to switch on and off the properties of the material by performing assembly and disassembly cycles, in addition, morphology, size and length are crucial for the good performance of some materials. The latter can be done by tuning the self-assembly behaviour of each material, redox cycles could be an interesting tool to perform pathway selection and control the outcome of the self-assembly. Interestingly, PDIs can be reduced by sodium dithionite ($Na_2S_2O_4$) in aqueous solutions yielding stable radical anion and dianion species that can be oxidized back to the neutral state upon exposure to air.[13–15] Reduction of PDIs has been previously used to obtain a reversible hydrogel,[16] or crystalline nanobelts.[17]

In this chapter, a new approach to perform pathway selection over the self-assembly of a perylene diimide derivative was demonstrated. Assembly/Disassembly cycles were performed by two redox agents. The latter can be used to overcome kinetic trapped states and control the self-assembly of a perylene diimide derivative (balance between colloidal stability and precipitation), which is determined by the number and frequency of redox cycles.

2.2. Model system: redox switchable perylene diimide derivative (PDI-1)

We designed a symmetric water soluble perylene diimide derivative (**PDI-1**, see Scheme 2.2) containing solubilizing oligoethyleneglycol chains and amide moieties that can form H-bonding. **PDI-1** was synthetized following the next synthetic route (Scheme 2.1). First, the preparation of an oligoethyleneglycol derivative of the gallic acid moiety was done. Tosylation was performed on a commercially available triethyleneglycol monomethylether yielding the corresponding tosyl oligoethyleneglycol derivative (**2**). Afterwards, nucleophilic substitution was carried out to obtain the methyl gallate derivative (**3**), followed by hydrolysis of the methyl gallate yielding the corresponding gallic acid derivative (**4**), see Scheme 2.1.

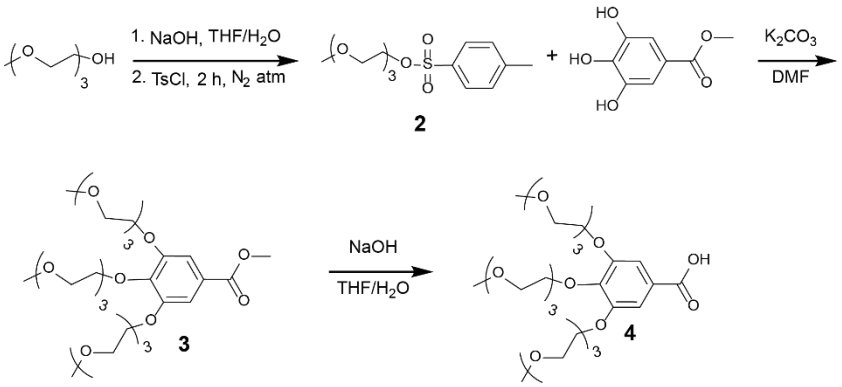

Scheme 2.1. Synthesis of the gallic derivative. Synthesis of the oligoethyleneglycol gallic acid solubilizing moiety (**4**). Reproduced from ref. ** (see page 29) with permission from the Royal Society of Chemistry.

Next, the target molecule was prepared by imidization of perylene-3,4,9,10-tetracarboxylic acid dianhydride with ethylenediamine followed by addition of formic acid in order to obtain the corresponding perylene diimide salt (**5**). Finally, an amide coupling between the perylene diimide derivative and oligoethyleneglycol derived from gallic acid was performed yielding the target compound **PDI-1** (Scheme 2.2). The detailed synthesis is described in section 2.7.

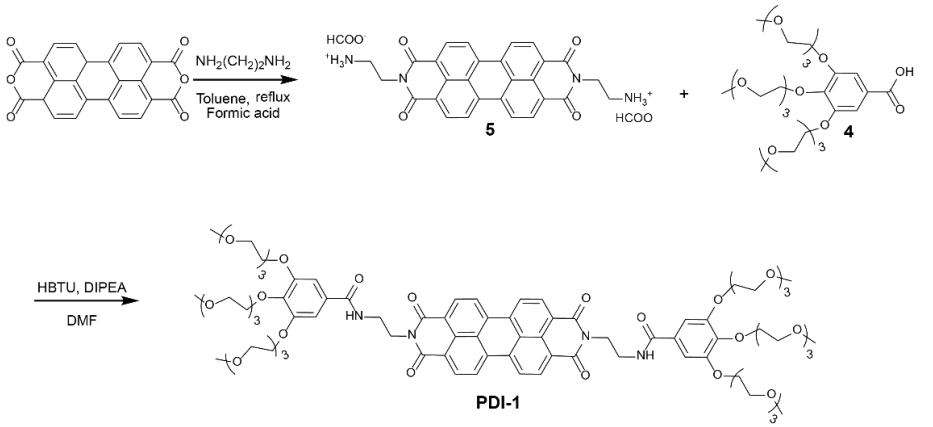

Scheme 2.2. Synthesis of PDI-1. Once **PDI-1** core and oligoethyleneglycol moiety were prepared, amide coupling was performed yielding the target **PDI-1**. Reproduced from ref. ** (see page 29) with permission from the Royal Society of Chemistry.

The self-assembly behaviour of our chromophore **PDI-1** was studied. A cherry red colour solution (characteristic of assembled PDIs) was obtained upon dissolving **PDI-1** in aqueous borate 50 mM buffer solution (pH 8). **PDI-1** can be promptly dissolved up to a concentration of 100 μM. However, precipitation was observed after overnight ageing. In addition, heating and cooling procedures (used as a tool to yield monomeric solution of different building blocks, see chapter 1),[3,4,18] led to rapid irreversible precipitation. Next, we decided to study the UV-Vis spectroscopic properties of **PDI-1** in order to better understand the self-assembly behaviour. Freshly prepared **PDI-1** solution showed a broad absorption band from 400 to 650 nm due to the S0 → S1 electronic transitions with maxima at 505, 528 and 560 nm (Figure 2.2A, pink). In addition, the characteristic vibronic progression of monomeric solutions is lacking. The latter strongly indicates the formation of H-aggregates due to π-π stacking.[19–21] To further support this, monomeric **PDI-1** solution could be obtained in acetonitrile at lower concentrations (5 μM), where the UV-Vis and fluorescence spectra show the characteristic vibronic pattern of the S0 → S1 transitions for typical monomeric PDIs solution with absorption from 400 to 600 nm and maxima at 455, 485 and 521 nm that belong to the 0 → 2, 0 → 1, 0 → 0 electronic transitions, respectively. Moreover, the mirror image emission shows the same characteristic bands (between 500 nm and 650 nm), see Figure 2.2B. The absence of **PDI-1** monomers in aqueous solution was confirmed by fluorescence spectroscopy, which shows emission from 570 to 750 nm (Figure 2.2C), a markedly red shifted spectrum indicates the formation of cofacial stacked **PDI-1**.[1,22] In addition, large red emissive **PDI-1** aggregates were detected by confocal microscopy adapted with a spectral detector in order to observe emissive species. The assemblies have a wide size distribution (between 1 to 10 μm) centered around 5 μm (Figure 2.4A,C).

Therefore, freshly prepared **PDI-1** solution in borate buffer results into large colloidal π-π stacked assemblies that are cofacially packed and precipitate slowly overnight.

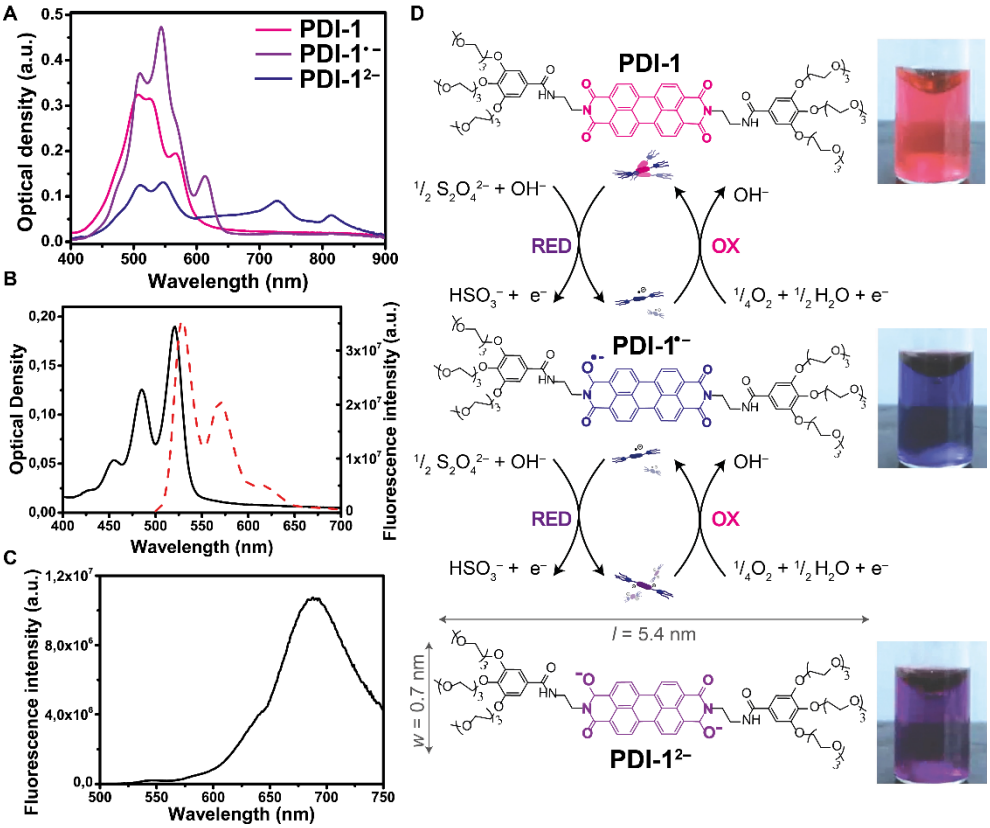

Figure 2.2. Model system PDI-1. (A) UV-Vis spectroscopy of 100 μM **PDI-1** (pink line), **PDI-1**$^{\bullet-}$ (blue line) and **PDI-1**$^{2-}$ (violet line) solutions in 50 mM borate buffer pH 8 (optical path 2 mm). (B) UV-Vis (black line) and fluorescence (red dashed line) spectra of 5 mM **PDI-1** in acetonitrile (optical path 1 cm) show the characteristic vibronic progression of the PDI scaffold and the mirror image emission. (C) Fluorescence emission spectra of freshly prepared **PDI-1** in 50 mM borate buffer pH 8 shows the absence of monomeric **PDI-1**. (D) Redox cycle of **PDI-1**. The neutral **PDI-1** is reduced to **PDI-1**$^{\bullet-}$ upon addition of 1 eq. of $Na_2S_2O_4$, further addition of $Na_2S_2O_4$ yields **PDI-1**$^{2-}$,which can be oxidized back by O_2, via radical anion. Reproduced from ref. ** (see page 29) with permission from the Royal Society of Chemistry.

The reduction of **PDI-1** was studied once its assembled state was well characterized. **PDI-1**$^{2-}$ was obtained upon the addition of 2 eq. of $Na_2S_2O_4$ to a freshly prepared **PDI-1** solution. A rapid colour change from red to purple was observed due to the formation of **PDI-1**$^{2-}$ (Figure 2.2D). The latter was confirmed by UV-Vis spectroscopy, a hyperchromic shifted intense band with a partially resolved vibronic pattern (maxima at 509 and 543 nm) together with a new band at 614 nm (Figure 2.2A, purple line spectrum), indicates the formation of PDI dianion species in aqueous solutions.[13,14] Interestingly, the partially resolved vibronic structure, together with the ratio of the peak intensities I_{509nm}/I_{543nm} for **PDI-1**$^{2-}$ (0.78) suggest that 100 μM **PDI-1**$^{2-}$ solutions are partially assembled in borate buffer solution. Specifically, the ratio for **PDI-1**$^{2-}$ in borate buffer solution is higher as compared with previous reported[13,14] monomeric aqueous PDI dianion solutions (0.55).

The latter was confirmed by concentration dependent UV-Vis experiments (from 0.5 μM to 100 μM) performed under N_2 atmosphere (in order to avoid the expontaneous oxidation of **PDI-1**$^{2-}$).The I_{509nm}/I_{543nm} ratio shows a progressive decrease upon dilution indicating that **PDI-1**$^{2-}$ is assembled at 100 μM (Figure 2.3A). The formation of **PDI-1**$^{2-}$ assemblies can be described by isodesmic model in which all monomer association/dissociation steps (see Chapter 1, section 1.2) are explained by the equilibrium constant (K_{eq}). Based on this model, the degree of aggregation (α) and the molar fraction of monomer can be explained by equation (1) and (2), respectively.[23–25] Both equations together can be used to calculate equation (3) permitting to obtain the equilibrium constant by plotting the ratio of the peak intensities I_{509nm}/I_{543nm} of all spectra against the concentration of **PDI-1**$^{2-}$ (Figure 2.3B).

$$\alpha = 1 - \alpha_{mon} = \frac{R(C) - R_{mon}}{R_{pol} - R_{mon}} \quad (1)$$

$$\alpha_{mon} = \frac{2K_{eq}C + 1 - \sqrt{4K_{eq}C + 1}}{2K_{eq}^2 C^2} \quad (2)$$

$$R(C) = \left[1 - \left(\frac{2K_{eq}C + 1 - \sqrt{4K_{eq}C + 1}}{2K_{eq}^2 C^2}\right)\right] \times \left(R_{pol} - R_{mon}\right) + R_{mon} \quad (3)$$

where $R(C)$ = I_{509nm}/I_{543nm} at a given concentration; C is the total concentration; R_{pol} corresponds to the ratio (I_{509nm}/I_{543nm}) for the fully aggregated state of **PDI-1**$^{2-}$; and R_{mon} corresponds to the ratio (I_{509nm}/I_{543nm}) for monomeric **PDI-1**$^{2-}$ species. The self-assembly equilibrium constant obtained from the fitting was K_{eq} = 2.0 x 10^4 ± 3 x 10^3 M^{-1}, with an adjusted R^2 > 0.999. The latter indicates that **PDI-1**$^{2-}$ assemblies grow via isodesmic polymerization mechanism. However, further studies are needed to confirm the exact supramolecular polymerization mechanism. In addition, **PDI-1**$^{2-}$ assemblies could be detected by dynamic light scattering (DLS) with a corresponding size of 96 ± 28 nm at 100 μM (Figure 2.10C).

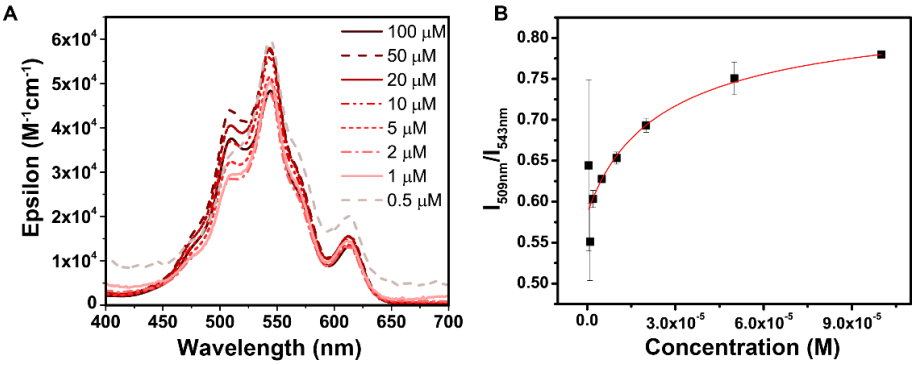

Figure 2.3. Supramolecular polymerization of PDI-1^{2-}. (A) UV-Vis spectra recorded at 25 °C for different concentrations of **PDI-1**$^{2-}$ (from 0.5 μM to 100 μM, optical path 0.2 – 1 cm) in 50 mM borate buffer (spectra normalized to show the molar extinction coefficient). (B) Ratio of peak intensities at 509 nm and 543 nm (I_{509nm}/I_{543nm}), relative to the absorption spectra of in panel (A), as a function of **PDI-1**$^{2-}$ concentration (black squares). Error bars show standard deviations. The red solid line corresponds to the fitting with a concentration-dependent isodesmic (Equal K model)[23], from which a $K_{eq.}$ = 2.0 x 10^4 ± 3 x10^3 M^{-1} was obtained. Reproduced from ref. ** (see page 29) with permission from the Royal Society of Chemistry.

PDI-1^{2-} was oxidized back to the neutral **PDI-1** under spontaneous oxidation to air (Figure 2.2D). Moreover, electrochemical studies were performed in order to know the redox potential of **PDI-1** (see appendix). In agreement with previous studies, reduction and oxidation cycles can be reversibly repeated more than 10 times without **PDI-1** decomposition. The latter was also confirmed spectroscopically. Interestingly, a transient blue colour was observed due to the radical anion formation **PDI-1$^{\bullet-}$** (Figure 2.2D). Transient formation of the radical anion **PDI-1$^{\bullet-}$** could be followed by UV-Vis spectroscopy, a red shifted spectra with characteristic bands at 727 and 813 nm indicates the transient formation of **PDI-1$^{\bullet-}$** species as mentioned previously in literature (Figure 2.2A, blue line spectrum).[13,14]

Therefore, **PDI-1** colloidal assemblies were reduced to the radical anion **PDI-1$^{\bullet-}$** upon addition of $Na_2S_2O_4$ and then to **PDI-1^{2-}** species. These reduction steps promote the partial disassembly of **PDI-1^{2-}**. Two additional negative charges per core appear upon complete reduction of **PDI-1** inducing electrostatic repulsions between consecutive cores and thus, disassembly of the structures. This results in an equilibrium between small **PDI-1^{2-}** assemblies and monomeric **PDI-1^{2-}** species in borate buffer solution. **PDI-1^{2-}** is oxidized back within minutes upon oxidation with air (i.e., **PDI-1^{2-} → PDI-1$^{\bullet-}$ → PDI-1**, see Figure 2.2D). The latter oxidation and reduction steps will be referred to as a redox cycle. In addition, the oxidation time (the total time in which **PDI-1$^{\bullet-}$** and **PDI-1^{2-}** species are maintained) was controlled by the amount of $Na_2S_2O_4$ added and the stirring rate. For example, higher $Na_2S_2O_4$ amounts and lower stirring rates lead to longer oxidation times.

So far, we have seen that **PDI-1** assembled into red emissive large aggregates due to π-π stacking and H-bonding. Moreover, they are reversibly reduced to **PDI-1^{2-}** via transient radical anion **PDI-1$^{\bullet-}$** formation upon addition of $Na_2S_2O_4$. The reduction of **PDI-1** leads to small **PDI-1^{2-}** assemblies in borate buffer, in equilibrium with **PDI-1^{2-}** monomers. **PDI-1^{2-}** can be oxidized back to the neutral **PDI-1** state. In the next section we will show how a single redox cycle (referring to consecutive reduction and oxidation) affects the aggregation of **PDI-1**.

2.3. Effect on the self-assembly of PDI-1 after one redox cycle

As mentioned in section 2.2, confocal micrographs showed the presence of large red emissive **PDI-1** assemblies (100 μM) with an average size of 5 μm (Figure 2.4A). **PDI-1^{2-}** assemblies could not be detected by confocal microscopy just after reduction of **PDI-1** since the size of **PDI-1^{2-}** assemblies (96 ± 28 nm) is below the detection limit of the confocal microscope (data not shown). Immediately after the spontaneous oxidation of **PDI-1^{2-}** assemblies, red emissive aggregates were observed again by confocal microscopy. Interestingly, particle analysis shows that the size of the assemblies evolved from ~ 400 nm to 1-2 μm in about 20 min (Figure 2.4B,C). Specifically, assemblies grow for 20 min. Cycled **PDI-1** solutions show smaller size of assemblies (constant after 20 min) and has a narrower size distribution as compared with freshly prepared **PDI-1** solution (Figure 2.4A-C). The assembly process after oxidation back to **PDI-1** was further studied by UV-Vis spectroscopy and atomic force microscopy (AFM).

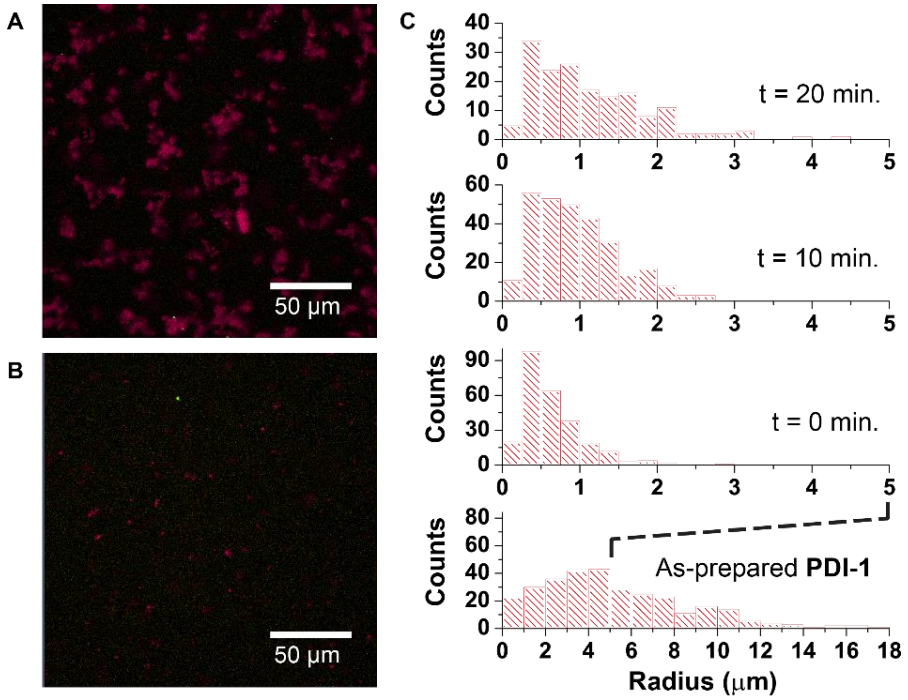

Figure 2.4. Confocal measurements of fresh prepared and cycled PDI-1 solutions. (A,B) True colour confocal micrographs (using spectral detector) of 100 μM **PDI-1** borate buffer solution: (A) as-prepared, (B) 20 min after 1 redox cycle. (C) Size distribution of freshly prepared **PDI-1** aggregates (bottom) and at t = 0, 10, 20 min after 1 redox cycle (by particle analysis of micrographs). Reproduced from ref. ** (see page 29) with permission from the Royal Society of Chemistry.

UV-Vis spectroscopy after 1 redox cycle (reduction and oxidation steps) showed a blue-shifted and less intense absorption spectra with respect to the freshly prepared **PDI-1** solution (Figure 2.5A). This indicates that cycled **PDI-1** assembled into stacks where the chromophore is 30° rotated with respect to the next one.[1,19–21] The latter shows that **PDI-1** forms helical assemblies, as was recently demonstrated by high-resolution TEM.[22] Interestingly, the UV-Vis spectra evolves while the self-assembly process is going on (Figure 2.5A). The overall optical density increased and a red-shifted spectra was observed. Specifically, 502 and 548 nm bands were shifted to 508 and 567 nm respectively, and a new band appeared at 528 nm (Figure 2.5A). We decided to use the term of optical density (OD) since there is a significant contribution of light scattering to the UV-Vis spectra. OD is the sum of scattering and absorption. After 20 min the UV-Vis spectrum looks like the freshly **PDI-1** one with the characteristics maxima at 505, 528 and 560 nm and lacking the vibronic progression of monomeric **PDI-1** in aqueous solutions. This indicates that the self-assembly process was completely finished.

In addition, AFM was studied to elucidate the morphology of **PDI-1** assemblies just after 1 redox cycle (Figure 2.5B) and after 20 min ageing (Figure 2.5C). Immediately after 1 redox cycle, fibrous assemblies were found with a regular height of 1.5 ± 0.1 nm (Figure 2.5B), which is twice the width of the **PDI-1** chromophore (see Figure 2.2D). However, when a cycled **PDI-1** solution was left for 20 min and then spin coated on mica, assemblies of fused smaller rigid rods with a regular height of 2.1 ± 0.2 nm can be observed (Figure 2.5C), corresponding with three times the width of the **PDI-1** chromophore (see Figure 2.1D). UV-

Vis spectra and AFM studies suggest that there is a hierarchical growth process where the initial 1D columnar assemblies interact side-to-side yielding fused **PDI-1** bundles in agreement with previous reports on structurally similar PDIs in water.[22] The side-to-side fusion of the assemblies would affect the internal order of the chromophores resulting in a different building-block arrangement. The latter may enhance the changes in the UV-Vis spectra (Figure 2.5A) and specifically, the red-shift and new band at 528 nm. Namely, it has been demonstrated that the spectral features and the exciton coupling are very sensitive to minimal changes in the internal order of the chromophores (e.g. distance or rotational offset).[21,22]

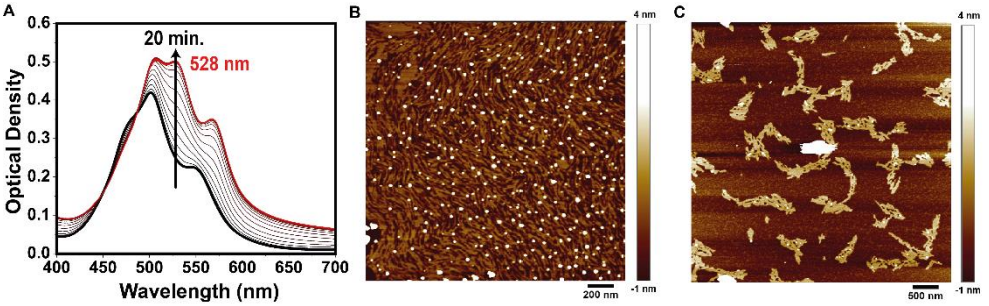

Figure 2.5. PDI-1 after a redox cycled. (A) UV-Vis spectra of a 100 μM **PDI-1** solution (optical path 2 mm) immediately after 1 redox cycle. (B,C) AFM images of a 100 μM **PDI-1** solution in 50 mM borate buffer spin-coated on mica (B) immediately after 1 redox cycle and (C) after 20 min ageing following 1 redox cycle. Reproduced from ref. ** (see page 29) with permission from the Royal Society of Chemistry.

To completely understand the self-assembly process that occurs after 1 redox cycle, the time evolution of the assemblies was studied. Interestingly, the evolution of the OD intensity at 528 nm during the self-assembly process was S-shaped (Figure 2.6A). The latter suggests that assemblies were formed under an autocatalytic process. In other words, **PDI-1** grows via a nucleated polymerization (cooperative). The time evolution of the assemblies was followed after 1 redox cycle (reduction and oxidation steps) at different **PDI-1** concentrations (i.e, between 10 to 50 μM) in order to confirm the presence of the autocatalytic process (Figure 2.6A). In fact, the rate growth of the assemblies changes with **PDI-1** concentration (Figure 2.6A). The nucleation step is delayed at lower concentration when fewer nuclei are present in solution. In addition, the presence of a lag time before starting the polymerization (e.g., plateau at 10 mM **PDI-1** concentration in Figure 2.6A) indicates that the assemblies grow via cooperative polymerization. In order to get more insights on the autocatalytic nucleation of **PDI-1**, the time evolution of the assemblies was fitted using a minimal 2-step autocatalytic model, which was first proposed by Watzky and Finke.[26] This model has been used to analyse the self-assembly kinetics of different proteins.[27] The model has two steps that are determined by two different equations (4) and (5):

$$A \overset{k_1}{\rightarrow} B \tag{4}$$

$$A + B \overset{k_2}{\rightarrow} 2B \tag{5}$$

specifically, the model describes two pseudoelementary steps where equation (4) is the nucleation step, which is determined by the rate constant k_1 and equation (5) is the elongation/growth step, determined by the rate constant k_2. Both steps are irreversible meaning that they can be used in our system since there is no monomer after completion of the self-assembly process. In addition, *A* refers to species, with concentration smaller than the critical size for nucleation (pre-nuclei), and *B* refers to the concentration of catalytic species that grow exponentially.

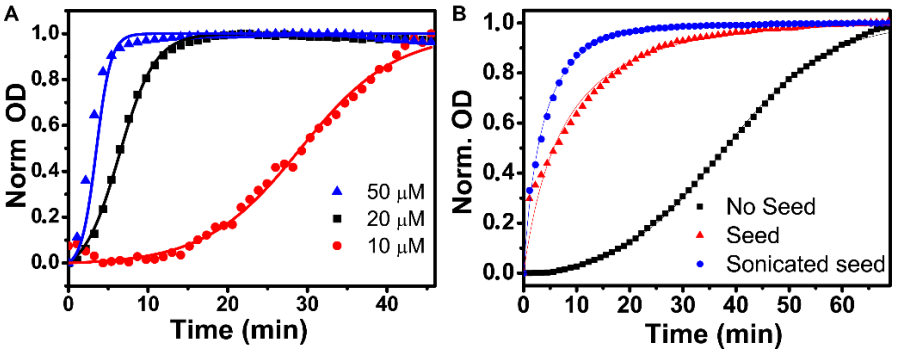

Figure 2.6. Time evolution of PDI-1. (A) Time evolution of the normalized optical density (OD) at 528 nm immediately after 1 redox cycle for **PDI-1** solutions at different concentrations (symbols). The solid lines correspond to the fitting of the experimental data using the minimal 2-step model described above. (B) Normalized optical density (OD) at 528 nm vs. time after 1 redox cycle for 10 μM **PDI-1** (black squares) and for 10 μM **PDI-1** seeded with 1h aged **PDI-1** seeds (red triangles), or sonicated seeds (blue circles). The S-shape indicates autocatalytic growth. Reproduced from ref. ** (see page 29) with permission from the Royal Society of Chemistry.

The assembly kinetics of **PDI-1** was measured just after 1 redox cycle at 50, 20 and 10 μM (Figure 2.6A, symbols for all the concentrations). We assumed that species *B* is the one that contributes most to the OD signal (the OD intensity was normalized between 0 and 1), the analytical expression of the 2-step model[27] was used to obtain equation (6). The latter was utilized to fit the data that was obtained for the different kinetic concentrations (Figure 2.6A, solid lines).

$$B = \left(A_0 - \frac{\frac{k_1}{k_2} + A_0}{1 + \frac{k_1}{k_2 A_0} e^{(k_1 + k_2 A_0)t}} \right) / A_0 \qquad (6)$$

The experiments at 50 and 20 μM could be fitted with the same constants k_1 and k_2 0.02442 ± 0.003 min^{-1} and 0.02112 ± 0.0008 μM^{-1} min^{-1}, respectively. In addition, the experiments at lower concentration (i.e., 10 μM) gave a slower nucleation step (close to 20 times slower) with a constant k_1 value of 0.00128 ± 0.0002 min^{-1}. The fitting gave a $R^2 > 0.99$ for all the curves. However, this model includes all the possible self-assembly events into a nucleation phase (i.e., first step, equation 4) and elongation phase together (i.e., second step, equation 5). The model could explain the autocatalytic behaviour of a cycled **PDI-1** (i.e., just after 1 redox cycle) but perhaps it is a bit too simplistic. Further kinetic studies are needed to confirm the exact growth mechanism and an extended cooperative model is developed in order to fully understand the nucleated polymerization of **PDI-1** in chapter 3.

In addition, seeding experiments provide strong evidence that **PDI-1** grows via nucleated/cooperative supramolecular polymerization (i.e., autocatalytic growth). Seeding

experiments have been previously used as initiators in the living polymerization of block-copolymers[28,29] or π-conjugated[30] systems, moreover, seeds have been used to selectively convert H-aggregates that are kinetically trapped into J-aggregates.[31] Seeds were prepared by performing 1 redox cycle on a 10 μM freshly prepared **PDI-1** solution and let **PDI-1** assemblies grow for 1 h. Seeds were added to a just cycled 10 μM **PDI-1** solution (immediately after 1 redox cycle). The total time to complete the supramolecular polymerization was about 70 min. As mentioned above, the presence of a long lag phase of ~ 10 min at 10 μM **PDI-1** solution was observed (Figure 2.6A). On the other hand, the supramolecular polymerization starts immediately upon addition of seeds (i.e., indicated by the increase of OD the intensity). The plateau in OD (indicating the end of the process) is reached much faster (~ 40 min), see Figure 2.6B. In addition, when 1 h old seeds were sonicated for 5 min and then added to a cycled **PDI-1** solution, the process ends in a shorter time (plateau is reached before) indicating that the growth of **PDI-1** assemblies is even faster. Our results confirm the autocatalytic growth of **PDI-1** after performing 1 redox cycle. Interestingly, seeding experiments could be used to control the growth rate and also to control the polydispersity of the assemblies as previous studies have shown.[28–31] The latter can be used as an approach to obtain interesting materials with different properties depending on the **PDI-1** concentration and amount of seeds added.

So far, we have seen that a freshly prepared **PDI-1** solution results into large red emissive colloidal assemblies (i.e., π-π cofacially stacked), which precipitate overnight. **PDI-1**$^{2-}$ was formed upon reduction of **PDI-1** with $Na_2S_2O_4$ (step vi in Figure 2.7), via radical anion **PDI-1**$^{\bullet-}$. In addition, we have found that there is an equilibrium between **PDI-1**$^{2-}$ assemblies and **PDI-1**$^{2-}$ monomeric species in solution (i in Figure 2.7). The supramolecular polymerization of **PDI-1**$^{2-}$ could be explained with an isodesmic model. The oxidation of **PDI-1**$^{2-}$ assemblies leads promptly to the formation of small **PDI-1** assemblies with a different molecular packing (e.g. showed by UV-Vis spectroscopy and AFM, step ii in Figure 2.7). Afterwards, cycled **PDI-1** assemblies grow via a cooperative supramolecular polymerization (i.e., autocatalytic process) in which side-to-side fusion of 1D stacks lead to the precipitation of **PDI-1** overnight (steps iii, iv and v in Figure 2.7). In the next section, the effect of multiple consecutive redox cycles is studied.

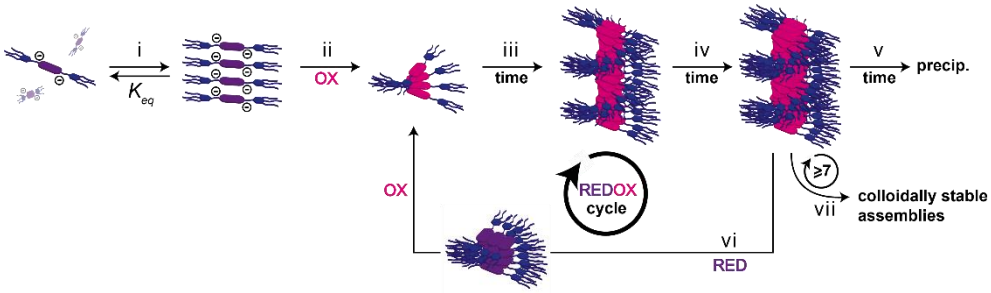

Figure 2.7. Pathway selection of PDI-1. Schematic representation of pathway selection with the following steps: i) equilibrium between monomeric and assembled **PDI-1**$^{2-}$, ii) oxidation followed by internal structural rearrangement, iii–iv) nucleation and growth of side–to–side fused assemblies, v) precipitation (overnight), vi) reduction by $Na_2S_2O_4$ followed by O_2 oxidation, resulting in 1 redox cycle, vii) alternative pathway yielding colloidally stable aggregates by 7 or more redox cycles at a suitable frequency (see section 2.4). Reproduced from ref. ** (see page 29) with permission from the Royal Society of Chemistry.

2.4. Effect of multiple redox cycles

Interestingly, we found that **PDI-1** assemblies could be selectively tuned when more than one redox cycle was performed. In other words, **PDI-1** assemblies progressively change after consecutive redox cycles. Specifically, the total number and frequency of the redox cycles determine the final outcome of **PDI-1** assemblies. We studied the effect on the self-assembly after performing 7 redox cycles at two different frequencies. In the first place, 7 consecutive cycles were done at 3 min intervals, i.e., reduction to **PDI-1**$^{2-}$ was performed as soon as **PDI-1** was oxidized back (as soon as the red solution was observed). The amount of $Na_2S_2O_4$ added to **PDI-1** solution was optimized in order to obtain 1 redox cycle every 3 min. Concretely, the hierarchical growth was not allowed to occur (i.e., the latter takes around 10 min at 100 μM **PDI-1** solutions), leading to precipitation of colloidal **PDI-1** assemblies just after overnight (i.e., pathway i-v in Figure 2.7) as was also observed for freshly prepared **PDI-1** assemblies (step i-ii in Figure 2.9A). On the other hand, if 7 redox cycles were performed at regular intervals of 20 min, the hierarchical process occurred permitting the growth of **PDI-1** assemblies. This resulted in only partial precipitation of **PDI-1** assemblies. A visible pink supernatant was observed after the 7 redox cycles. The solution was centrifuged for 20 min yielding a pinkish solution in which the colloidal **PDI-1** assemblies were stable for months (step iii in Figure 2.9). Specifically, a concentration series was prepared (i.e., from 100 μM to 1 μM **PDI-1** solution, see Figure 2.8A), in which the maxima OD intensity at 503 nm was followed (solid dots in Figure 2.8B). A linear fitting of the experimental data was performed yielding the linear expression: OD = 0.01811·[C] – 0.01431 and a $R^2 > 0.99$. The measured optical density spectrum of the supernatant (Figure 2.9C) gave a concentration of 10 μM that was stable for months.

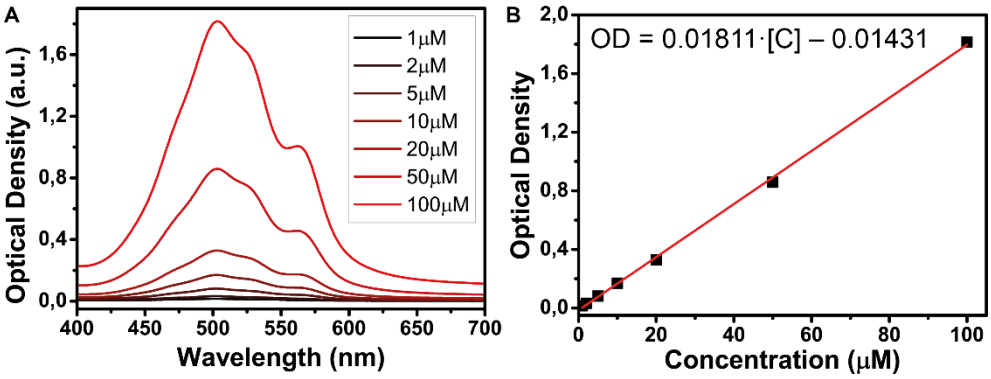

Figure 2.8. PDI-1 concentration series. (A) UV-Vis spectroscopy of **PDI-1** solution at different concentrations (i.e., from 1 to 100 μM). (B) The maxima OD intensity (i.e., 509 nm) was followed represented by the black dots. The experimental is fitted with a linear expression in order to know the exact concentration of the supernatant 100 μM **PDI-1** solution. The solid line represents the fitting which gave the next linear expression: OD = 0.01811·[C] – 0.01431 and a $R^2 > 0.99$. Reproduced from ref. ** (see page 29) with permission from the Royal Society of Chemistry.

To dismiss that 10 μM **PDI-1** solution was simply the solubility limit of assemblies in solution, we prepared a freshly 10 μM **PDI-1** solution (step iv in Figure 2.9B), which also precipitates overnight as observed for 100 μM **PDI-1** solution (step v in Figure 2.9B). Precipitation was confirmed by UV-Vis spectroscopy (blue spectra in Figure 2.9C). Cycling experiments (at intervals of 20 min) also led to 10 μM **PDI-1** colloidally stable assemblies

(step vi in Figure 2.9B). Interestingly, the OD spectrum has the same maximum at 508 nm as compared with the 100 μM supernatant solution (Figure 2.9 C). However, both solutions show different OD spectra suggesting that both assemblies have different morphologies and packing of the chromophores. In addition, dynamic light scattering experiments show that 10 μM **PDI-1** solution vs the supernatant solution are different in size. Smaller assemblies were found for 10 μM **PDI-1** solution (Figure 2.9D). Therefore, the nucleation step depends on the initial **PDI-1** concentration, which can explain the difference between both colloidally assembled structures. In fact, we can confirm that the importance steps for pathway selection are frequency of the cycles, time (e.g. could be tuned by adding different amounts of $Na_2S_2O_4$ into the system) and number of cycles.

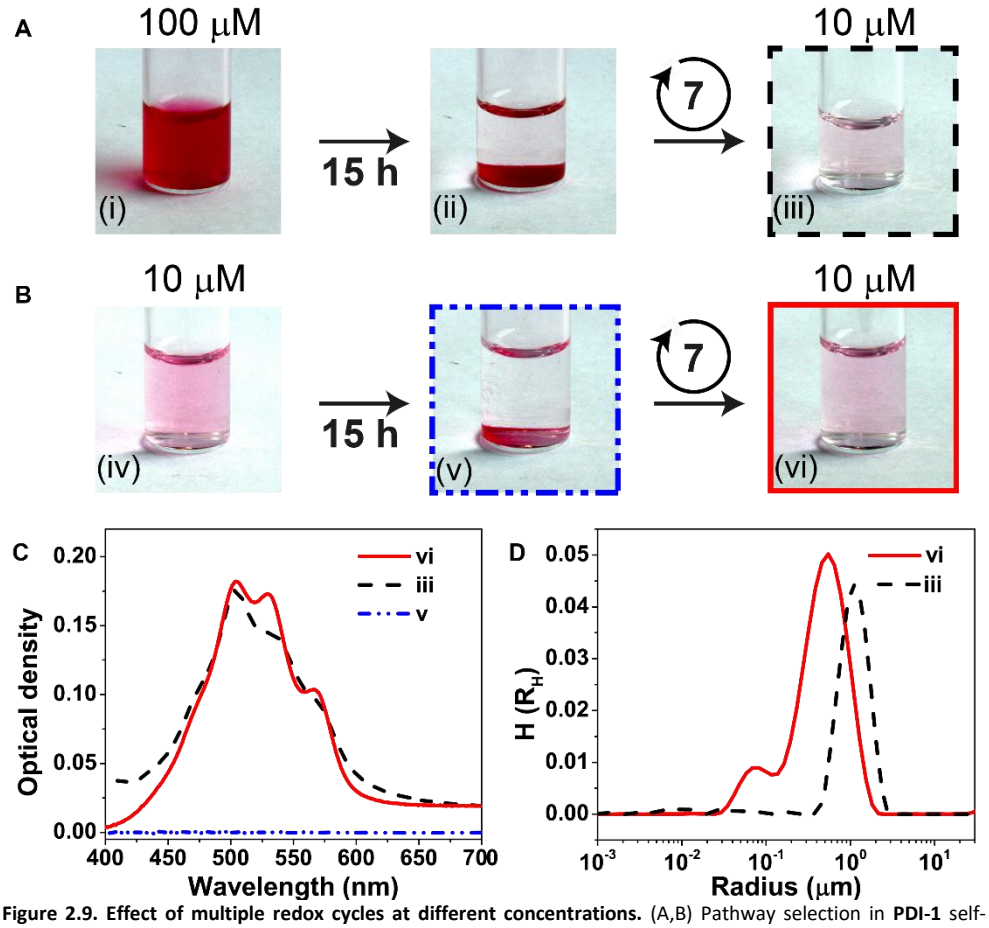

Figure 2.9. Effect of multiple redox cycles at different concentrations. (A,B) Pathway selection in **PDI-1** self-assembly starting at 100 μM and 10 μM, respectively: (i, iv) freshly prepared solutions; (ii, v) overnight precipitation; (iii, vi) colloidally stable assemblies after redox cycling (7 times at 20 min intervals). (C,D) UV-Vis spectra and hydrodynamic radii obtained for soluble assemblies (i.e., 10 μM) corresponding to iii (red solid line) and vi (dashed black line). The dash-dot blue line in (C) is the UV-Vis spectrum of v, confirming complete precipitation overnight. Reproduced from ref. ** (see page 29) with permission from the Royal Society of Chemistry.

To study more in detail the system, the autocatalytic process/growth of **PDI-1** assemblies was followed by dynamic light scattering and UV-Vis spectroscopy after each redox cycle (i.e., 7 cycles at 20 min intervals). An increase of the scattering intensity R_{vv}/c in DLS was observed on cycled **PDI-1** solutions (red dark squares in Figure 2.10A) as compared to freshly **PDI-1** solutions suggesting that more assemblies species can be found in solution. In addition, upon further cycling a progressive decrease of the scattering intensity (plateaus in Figures 2.10A) and an overall decrease of the hydrodynamic radii (Figure 2.10C) suggest progressive structural changes. In fact, the continuous increase in the OD intensity indicates a real rearrangement of the chromophore (Figure 2.10D). Moreover, the increase in the lag phase shows that nucleation is affected by multiple cycles (Figure 2.10B) On the other hand, when the size and the polydispersity of the assemblies were measured, it was observed that the hydrodynamic radii (R_H ~ 628 ± 83 nm) and the distribution of the assemblies stayed approximately constant after the third or fourth redox cycle.

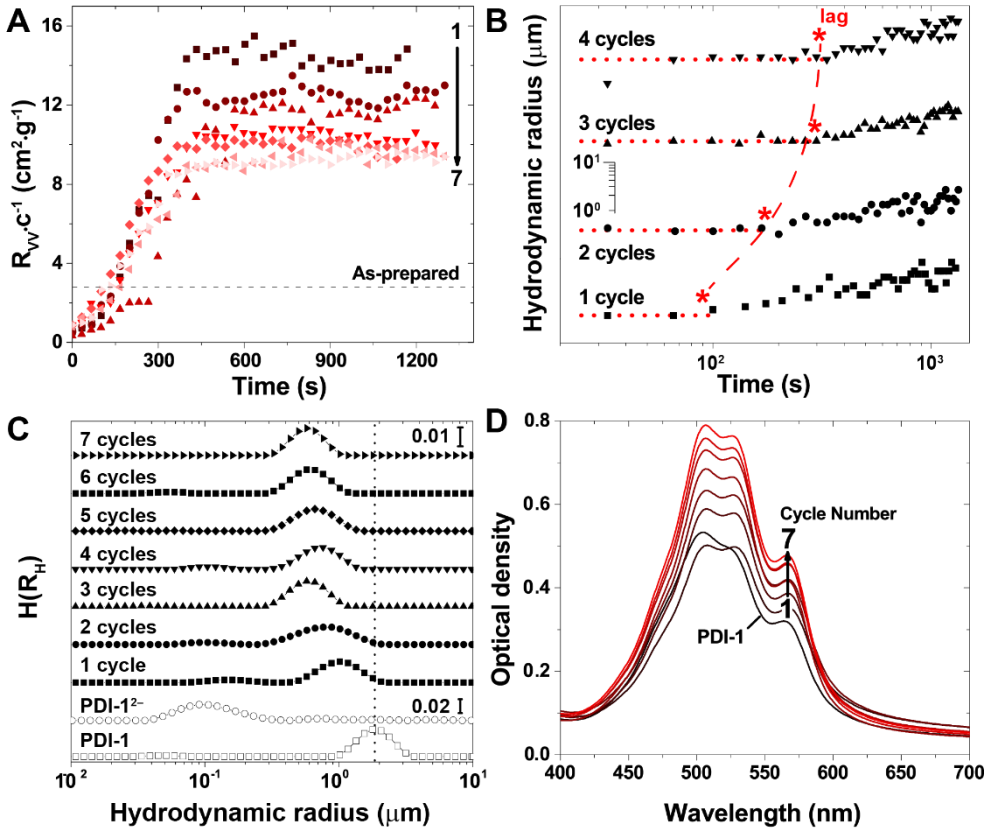

Figure 2.10. **Multiple redox cycle experiments.** (A) Absolute scattering intensity R_{vv}/c vs time immediately after oxidation. The decreasing plateau indicates denser assemblies upon cycling (1 → 7). (B) Hydrodynamic radius R_H (from dynamic light scattering) vs. time. Red stars (and dashed line) show increasing lag times upon cycling. (C) R_H measured for freshly prepared 100 μM **PDI-1** (empty squares), **PDI-1**$^{2-}$ (empty circles) and for **PDI-1** (filled symbols) for up to 7 redox cycles show that after ~3 cycles the size of the assemblies remains constant. (D) UV-Vis spectra of **PDI-1** (each recorded 20 min after oxidation) increase upon cycling, showing internal structural changes in the **PDI-1** assemblies. Reproduced from ref. ** (see page 29) with permission from the Royal Society of Chemistry.

All these observations clearly indicate that outcome of **PDI-1** assemblies could be selectively chosen upon cycling in which the frequency between the cycles and total number of cycles will determine the final **PDI-1** structure. The decrease in the scattering intensity R_{vv}/c (i.e., after the second redox cycle, see Figure 2.10A) and the increase in the OD intensity indicates a progressive structural evolution of **PDI-1** assemblies after each redox cycle. In addition, both UV and DLS confirm that there is a real rearrangement of the chromophores since the changes in the OD intensity (observed in Figure 2.4A) are not only due to scattering. In other words, if the contribution is coming only from scattering, a decrease in the scattering intensity R_{vv}/c should lead to a decrease of the OD intensity. In addition, the delay in the nucleation step after each redox cycle could be due to the changes in the structure of the nuclei or the number of nucleating species. Finally, the decrease of the scattering intensity R_{vv}/c and the constant size (R_H) of the **PDI-1** assemblies after each redox cycle indicate that the density of the assemblies increases after each cycle.

We can conclude that **PDI-1** molecules can be kept in solution (i.e., cycled faster than precipitation) depending on the frequency at which the redox cycles are performed. The latter also designates whether nucleation and growth of **PDI-1** assemblies can occur permitting to control the final outcome of the assemblies. The key importance of the system to reach cycle-dependent pathway selection is that the equilibrium between **PDI-1**$^{2-}$ assemblies and **PDI-1**$^{2-}$ monomers in solution provides some memory effect to the system that depends on previous redox cycles. Longer times in the reduced state would reset the system and erase the memory of the previous cycles.

2.5. Conclusions

In this chapter we have shown a new approach in which reducing ($Na_2S_2O_4$) and oxidizing (O_2) agents are used as chemical fuels to drive assembly and disassembly cycles in order to tune and control the resulting assemblies and thus, control pathway selection. The frequency, number of cycles and redox cycling time (i.e., total time to perform reduction and oxidation steps) are of key importance to balance the system and reach the target. In addition, chemically fuelled self-assembly can be used as a new approach to overcome strong kinetic barriers guiding the system through the energy landscape to reach target supramolecular structures. The latter may allow the use of other PDI derivatives or hydrophobic self-assembling moieties in aqueous environments.

In the next chapter, we show how the same system can be pushed out of equilibrium by constantly adding a chemical fuel (i.e., reducing and oxidizing agents) to a **PDI-1** solution, resulting in emergent behaviour of **PDI-1** assemblies. In addition, the seeding approach is used to obtain a supramolecular wave in a thin layer of just cycled **PDI-1** assemblies.

2.6. Experimental section

Electrochemical measurements. Electrochemical measurements were performed with an Autolab type III μ-potentiostat using a 3-electrode setup consisting of a 2 mm glassy carbon working electrode, Pt foil counter electrode and either a Ag/AgCl reference electrode for aqueous baths or a Pt wire quasi-reference electrode for non-aqueous ones. Ferrocene was used as an internal reference and a method to determine the solution resistance in DCM (dichloromethane). Before each measurement, the working electrode was successively polished using 1 μm, 0.25 μm and 0.1 μm paste followed by ultrasonication in water, and for the non-aqeous bath a further sonication in DCM. The baths consisted of 0.1 M tetra-n-butylammonium hexafluorophosphate ($TBAPF_6$) and 0.1 mM **PDI-1** in DCM, and 2 mM gallic acid and 0.1 M KCl in water. All solutions were nitrogen purged for 1 hour prior to use, and all electrochemical measurements were carried out under a nitrogen blanket.

Sample preparation for 1 redox cycle. A solution was prepared by dissolving **PDI-1** (0.33 mg, 0.20 μmol) in 50 mM borate buffer, pH 8. Next, **PDI-1** was reduced (2 mL of 100 μM solution) adding 1 μL of a 400 mM $Na_2S_2O_4$ solution (in borate buffer) under stirring (note: the colour changes from cherry red to purple). The stirring in air caused the **PDI-1**$^{2-}$ to oxidize back to the neutral **PDI-1** in 2–3 minutes due to atmospheric oxygen.

Sample preparation for multicycle experiments. Samples of **PDI-1** (2 mL, 100 μM) in 50 mM borate buffer were prepared analogously to the 1 cycle preparation (see paragraph above). Multiple redox cycles of **PDI-1** were performed by repeated additions of 1 μL of a $Na_2S_2O_4$ solution (400 mM in borate buffer) under stirring at time intervals of 20 min., in the "slow cycling", (i.e., allowing time for hierarchical growth, leading to colloidally stable solutions of 10 μM) or 3 min., in the "fast cycling", (i.e., leading to complete precipitation). The redox cycles do not change the pH measurably (verified up to 7 cycles).

Seeding experiments. An aliquot (0.5 mL) of 100 μM **PDI-1** (aged for 10 min. after one redox cycle) was added to 2 mL of just oxidized 100 μM **PDI-1** solution (prepared as described above).

Confocal measurements. Confocal micrographs were taken by using Zeiss LSM 710 confocal microscope system with 63x magnification, numerical aperture, NA, 1.3 of Zeiss LCI Plan-NEOFLUAR immersion objective lens (Zeiss GmbH). The samples were excited by continuous-wave laser at 488 nm. The emission was measured from 500 nm to 700 nm using a spectral detector. Measurements were performed on as-prepared a 100 μM **PDI-1** and at different time intervals after oxidation (1 redox cycle).

UV-Vis measurements. UV-Vis spectra were taken by using a JASCO V-670 spectrometer equipped with a Peltier system as a temperature controller. When not otherwise specified, spectra were recorded in a 0.2 cm quartz cuvette at 25 ºC.

Fluorescence measurements. Emission spectra were recorded with a Fluorolog®-3 spectrofluorometer by exciting at 488 nm and recording between 500 nm and 750 nm.

Dynamic light scattering (DLS). The intensity autocorrelation functions $g^{(2)}(q,\tau) \equiv \langle I(q,0)I(q,\tau)\rangle / \langle I(q,0)^2\rangle$ were measured on a home-built light scattering setup with an ALV7002 digital correlator using a laser diode at λ = 639 nm at a wavevector *q = 0.0185 nm^{-1}* (90° scattering angle). Measurements were performed on freshly 100 μM **PDI-1**, its reduced form **PDI-1^{2-}**, and every 30 s or 60 s for 20 min. immediately after oxidation (for each redox cycle). The relaxation dynamics were analysed by the inverse Laplace transformation $g^{(1)}(\tau) = \int_0^\infty H(\Gamma)e^{-\Gamma t}d\Gamma$ where $g^{(1)} = \sqrt{g^{(2)} - 1}$. Hydrodynamic radii R_H were then calculated using the Stokes-Einstein relation $R_H = k_B T/(6\pi\eta D)$ where $D = 1/(\tau q^2)$.

Atomic force microscopy (AFM). Measurements were performed under ambient condition using a Bruker Veeco Dimension 3100 AFM microscope with Nanoscope IV controller, operating in tapping mode. Silica probes Bruker TESPAW-V2 with a resonance frequency of ~360 kHz and a spring constant of ~80 Nm^{-1} were used. The samples were prepared by spin-coating (3000 rpm, 1 min.) on freshly cleaved Mica surfaces 100 μM **PDI-1** solutions soon after oxidation (1 redox cycle) and after further 20 min. ageing. The height of the **PDI-1** assemblies in the different samples was determined by cross section analysis of at least 50 fibers.

2.7. Synthesis of PDI-1

Synthesis general. Methyl gallate was purchased from TCI chemicals. Triethyleneglycol monomethylether and perylene-3,4,9,10-tetracarboxylic dianhydride were purchased from Sigma-Aldrich. All other chemicals and solvents were purchased from Sigma-Aldrich and VWR. Purification of the reaction mixtures was performed by column flash chromatography using Geduran Si 60 silica gel (230-400 mesh). NMR spectra were recorded on a NMR Bruker AVANCE 400 MHz.

[2-[2-(2-Methoxyethoxy)ethoxy]ethoxy]p-toluenesulfonate (2). To a solution of triethyleneglycol monomethylether (10 g, 0.061 mol, 1 eq) in 20 mL THF, a solution of NaOH (5 g, 0.125 mol, 2 eq) in H_2O (20 mL) was added under stirring at 0 ºC. To this mixture, a solution of tosyl chloride (15 g, 0.078 mol, 1.3 eq) dissolved in 20 mL THF was added dropwise under inert atmosphere. Then, the reaction was allowed to warm to rt and stirred for 2 hours. Afterwards, 120 mL of diethyl ether were added and the organic layer was washed with 1 M NaOH (3 x 100 mL), water (2 x 100 mL), and dried over anhydrous $MgSO_4$. After evaporation and drying under vacuum, the tile product was obtained as a yellowish oil (18.53 g, 95%). ^{1}H NMR (400 MHz, $CDCl_3$) δ 7.84 (d, J = 8.3 Hz, 2H), 7.39 (d, J = 8.5 Hz, 2H), 4.25 –4.16 (m, 2H), 3.75 – 3.70 (m, 2H), 3.69 – 3.61 (m, 6H), 3.57 (dd, J = 5.8, 3.3 Hz, 2H), 3.41 (s, 3H), 2.49 (s, 3H).

Methyl 3,4,5-tris[2-[2-(2-Methoxyethoxy)ethoxy]ethoxy]benzoate (3). Methyl gallate (2 g, 10.8 mmol, 1 eq) and potassium carbonate (15 g, 108 mmol, 10 eq) were added to a solution of **2** (13.7 g, 43.2 mmol, 4 eq) in DMF (50 mL). The reaction mixture was heated at 80 ºC overnight under inert atmosphere. Then, the solvent was removed under vacuum and CH_2Cl_2 (100 mL) was added to the solid residue. The obtained solution was collected in a separatory funnel and washed with saturated $NaHCO_3$ (50 mL) and brine (50 mL). The organic layer was dried over anhydrous $MgSO_4$, followed by evaporation and drying under vacuum. Purification by flash chromatography using hexane/ethyl acetate (1:5) as eluent afforded **3** (6.02 g ,90%) as a yellow oil. ^{1}H NMR (400 MHz, $CDCl_3$) δ 7.31 (s, 2H), 4.23 – 4.19 (m, 6H), 3.88 (dd, J = 8.8, 3.6 Hz, 9H), 3.77 –3.70 (m, 6H), 3.70 – 3.62 (m, 12H), 3.56 (dd, J = 5.9, 3.2 Hz, 6H), 3.39 (s, 9H).

3,4,5-tris[2-[2-(2-Methoxyethoxy)ethoxy]ethoxy]benzoic acid (4). To a solution of **3** (6.02 g, 10.61 mmol, 1 eq) in 50 mL of a THF/H_2O 1.5:1 mixture at 0 °C, 10 mL of a 10.6 M solution of NaOH (100.61 mmol, 10 eq) were added. The reaction mixture was allowed to warm to rt and stirred overnight, after that, it was acidified to pH 2 with HCl (1 M) and extracted with CH_2Cl_2 (3 x 70 mL). The collected organic phase was dried over anhydrous $MgSO_4$, concentrated and dried under vacuum to give **4** (6.35 g, 98%) as a yellow oil. ^{1}H NMR (400 MHz, DMSO-d_6) δ 7.22 (s, 2H), 4.18 – 4.12 (m, 6H), 3.80 – 3.72 (m, 6H), 3.56 (m, 18H), 3.43 – 3.39 (m, 6H), 3.23 (s, 9H).

N,N'-bis(aminoethyl) perylene-3,4,9,10-tetracarboxylic diimide (5). To a suspension of perylene-3,4,9,10-tetracarboxylic acid dianhydride (0.25 g, 0.64 mmol, 1 eq) in 20 mL of toluene, 0.56 mL of ethylenediamine (8.9 mmol, 13 eq) were added in 10 min. The reaction mixture was refluxed overnight under inert atmosphere. After cooling down to rt, the obtained dark red precipitate was collected by filtration and then re-dispersed in

10 mL of aqueous KOH (5 M) and stirred overnight. Then, the red solid was filtered again, washed with H_2O, and dissolved in 10mL of formic acid. The insoluble fraction was filtered off, and 200 mL of isopropanol were added to the filtrate giving after precipitation, centrifugation and drying diimide **5** (0.12 g, 33%). ^{1}H NMR (400 MHz, D_2O) δ 7.98 (8H), 4.35 (4H), 3.33 (4H).

N,N'-Di[3,4,5-tris[2-[2-(2-Methoxyethoxy)ethoxy]ethoxy]benzoylaminoethyl]-perylene-3,4,9,10-tetracarboxylic diimide (PDI-1). Carboxylic acid **4** (0.157 g, 0.26 mmol, 2.4 eq) was dissolved in 20 mL of DMF. To this solution, HBTU (0.098 g, 0.26 mmol, 2.4 eq) and DIPEA (190 μL, 1.07 mmol, 10 eq) were added under inert atmosphere. After 5 min., diimide **5** (0.061 g, 0.11 mmol, 1 eq) was added and the reaction mixture was stirred at rt for 48 hours, after which 50 mL of CH_2Cl_2 were added. The organic phase was washed with saturated $NaHCO_3$ (2 x 50 mL) and brine, dried over anhydrous $MgSO_4$, and the solvent was evaporated under vacuum. Crude **PDI-1** was purified by flash chromatography using CH_2Cl_2/MeOH (gradient from 100:0 to 80:20) as eluent, followed by redissolution in CH_2Cl_2 (50 mL) and washes with 6 M HCl (3 x 50 mL) and brine, to remove traces of unwanted monosubstituted product. The organic phase was then dried over anhydrous $MgSO_4$ and concentrated to give pure **PDI-1** (0.112 g, 63%) as a red solid. ^{1}H NMR (400 MHz, DMSO) δ 8.70 (s, 4H), 8.48 (s, 2H), 8.39 (s, 4H), 7.00 (s, 4H), 4.55 (s, 12H), 4.28 (s, 4H), 4.03 (s, 16H), 3.78 – 3.40 (m, 68H), 3.19 (s, 18H). ^{13}C NMR (101 MHz, DMSO) δ 166.53, 163.38, 152.13, 140.20, 134.16, 130.05, 124.37, 123.12, 106.68, 72.30, 71.68, 70.29, 70.01, 69.31, 68.73, 63.49, 58.45. HRMS (ESI+) Calculated Mass for $C_{84}H_{112}N_4O_{30}Na_2$ [M+2Na$^+$]: 851.3573. Found: 851.3539.

2.8. References

1. Würthner, F. *et al.* Perylene Bisimide Dye Assemblies as Archetype Functional Supramolecular Materials. *Chem. Rev.* **116,** 962–1052 (2016).
2. Tidhar, Y., Weissman, H., Wolf, S. G., Gulino, A. & Rybtchinski, B. Pathway-Dependent Self-Assembly of Perylene Diimide/Peptide Conjugates in Aqueous Medium. *Chem. – Eur. J.* **17,** 6068–6075 (2011).
3. Korevaar, P. A. *et al.* Pathway complexity in supramolecular polymerization. *Nature* **481,** 492–496 (2012).
4. Korevaar, P. A., de Greef, T. F. A. & Meijer, E. W. Pathway Complexity in π-Conjugated Materials. *Chem. Mater.* **26,** 576–586 (2014).
5. Ogi, S., Stepanenko, V., Sugiyasu, K., Takeuchi, M. & Würthner, F. Mechanism of Self-Assembly Process and Seeded Supramolecular Polymerization of Perylene Bisimide Organogelator. *J. Am. Chem. Soc.* **137,** 3300–3307 (2015).
6. Görl, D., Zhang, X., Stepanenko, V. & Würthner, F. Supramolecular block copolymers by kinetically controlled co-self-assembly of planar and core-twisted perylene bisimides. *Nat. Commun.* **6,** ncomms8009 (2015).
7. El-Hachemi, Z., Mancini, G., Ribó, J. M. & Sorrenti, A. Role of the Hydrophobic Effect in the Transfer of Chirality from Molecules to Complex Systems: From Chiral Surfactants to Porphyrin/Surfactant Aggregates. *J. Am. Chem. Soc.* **130,** 15176–15184 (2008).
8. Chandler, D. Interfaces and the driving force of hydrophobic assembly. *Nature* **437,** 640–647 (2005).
9. Würthner, F. Perylene bisimide dyes as versatile building blocks for functional supramolecular architectures. *Chem. Commun.* **0,** 1564–1579 (2004).
10. Würthner, F., Chen, Z., Dehm, V. & Stepanenko, V. One-dimensional luminescent nanoaggregates of perylene bisimides. *Chem. Commun.* **0,** 1188–1190 (2006).
11. R. Draper, E. *et al.* Air-stable photoconductive films formed from perylene bisimide gelators. *J. Mater. Chem. C* **2,** 5570–5575 (2014).
12. P, S. M. & Neugebauer, W. Manufacture of vat dyestuffs. (1929).
13. Shirman, E. *et al.* Stable Aromatic Dianion in Water. *J. Phys. Chem. B* **112,** 8855–8858 (2008).
14. Marcon, R. O. & Brochsztain, S. Aggregation of 3,4,9,10-Perylenediimide Radical Anions and Dianions Generated by Reduction with Dithionite in Aqueous Solutions. *J. Phys. Chem. A* **113,** 1747–1752 (2009).
15. Iron, M. A., Cohen, R. & Rybtchinski, B. On the Unexpected Stability of the Dianion of Perylene Diimide in Water—A Computational Study. *J. Phys. Chem. A* **115,** 2047–2056 (2011).
16. Krieg, E. *et al.* Supramolecular Gel Based on a Perylene Diimide Dye: Multiple Stimuli Responsiveness, Robustness, and Photofunction. *J. Am. Chem. Soc.* **131,** 14365–14373 (2009).
17. Cao, X., Wu, Y., Fu, H. & Yao, J. Self-Assembly of Perylenediimide Nanobelts and Their Size-Tunable Exciton Dynamic Properties. *J. Phys. Chem. Lett.* **2,** 2163–2167 (2011).
18. Haedler, A. T. *et al.* Pathway Complexity in the Enantioselective Self-Assembly of Functional Carbonyl-Bridged Triarylamine Trisamides. *J. Am. Chem. Soc.* **138,** 10539–10545 (2016).
19. Görl, D., Zhang, X. & Würthner, F. Molecular Assemblies of Perylene Bisimide Dyes in Water. *Angew. Chem. Int. Ed.* **51,** 6328–6348 (2012).
20. Chen, Z. *et al.* Photoluminescence and Conductivity of Self-Assembled π–π Stacks of Perylene Bisimide Dyes. *Chem. – Eur. J.* **13,** 436–449 (2007).
21. Seibt, J. *et al.* On the geometry dependence of molecular dimer spectra with an application to aggregates of perylene bisimide. *Chem. Phys.* **328,** 354–362 (2006).
22. Zhang, X., Görl, D., Stepanenko, V. & Würthner, F. Hierarchical Growth of Fluorescent Dye Aggregates in Water by Fusion of Segmented Nanostructures. *Angew. Chem. Int. Ed.* **53,** 1270–1274 (2014).
23. Martin, R. B. Comparisons of Indefinite Self-Association Models. *Chem. Rev.* **96,** 3043–3064 (1996).
24. Smulders, M. M. J. *et al.* How to Distinguish Isodesmic from Cooperative Supramolecular Polymerisation. *Chem. – Eur. J.* **16,** 362–367 (2010).
25. De Greef, T. F. A. *et al.* Supramolecular Polymerization. *Chem. Rev.* **109,** 5687–5754 (2009).

26. Watzky, M. A. & Finke, R. G. Transition Metal Nanocluster Formation Kinetic and Mechanistic Studies. A New Mechanism When Hydrogen Is the Reductant: Slow, Continuous Nucleation and Fast Autocatalytic Surface Growth. *J. Am. Chem. Soc.* **119,** 10382–10400 (1997).
27. Morris, A. M., Watzky, M. A. & Finke, R. G. Protein aggregation kinetics, mechanism, and curve-fitting: A review of the literature. *Biochim. Biophys. Acta BBA - Proteins Proteomics* **1794,** 375–397 (2009).
28. Gädt, T., Ieong, N. S., Cambridge, G., Winnik, M. A. & Manners, I. Complex and hierarchical micelle architectures from diblock copolymers using living, crystallization-driven polymerizations. *Nat. Mater.* **8,** 144–150 (2009).
29. Wang, X. *et al.* Cylindrical Block Copolymer Micelles and Co-Micelles of Controlled Length and Architecture. *Science* **317,** 644–647 (2007).
30. Zhang, W. *et al.* Supramolecular Linear Heterojunction Composed of Graphite-Like Semiconducting Nanotubular Segments. *Science* **334,** 340–343 (2011).
31. Ogi, S., Sugiyasu, K., Manna, S., Samitsu, S. & Takeuchi, M. Living supramolecular polymerization realized through a biomimetic approach. *Nat. Chem.* **6,** 188–195 (2014).
32. Carter, M. K. Correlation of electronic transitions and redox potentials measured for pyrocatechol, resorcinol, hydroquinone, pyrogallol, and gallic acid with results of semi-empirical molecular orbital computations – A useful interpretation tool. *J. Mol. Struct.* **831,** 26–36 (2007).

2.9. Appendix

2.9.1. Electrochemical analysis of PDI-1

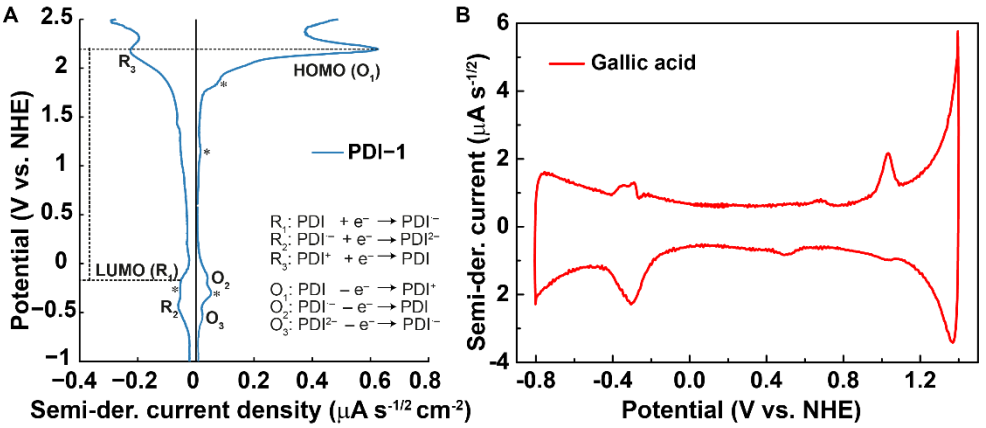

Figure 2.11. Electrochemical measurements. A) Semi-derivative cyclic voltammogram of 200 μM **PDI-1** in 0.1 M $TBAPF_6$ in DCM at 100 mV/s. The HOMO and LUMO levels are marked by the first oxidation and reduction peaks respectively. The redox peaks due to the gallic moiety are marked by *. (B) Semi-derivative cyclic voltammogram of 2 mM gallic acid in 0.1 M KCl in water at 100 mV/s. Reproduced from ref. ** (see page 29) with permission from the Royal Society of Chemistry.

The HOMO-LUMO levels of **PDI-1** can be related to the standard potentials of reduction and oxidation of the molecule.[2] From the semiderivative of a cyclic voltammogram at 100 mV/s, and a concentration of 200 μM (Fig. 2.11), we observed two reduction peaks from the PDI core at -0.20 V (the LUMO) and -0.42 V, and their corresponding re-oxidation peaks at -0.54 V for the return of the dianion to the radical, and -0.14 V for the radical returning to the neutral molecule. This difference in the forward and reverse sweeps decreased with lower scan rates as expected for a quasi-reversible system. There is a coupled, reversible redox peak at -0.25 V with the return (positive) peak at -0.3 V which is due to the reduction of the gallic moiety of **PDI-1**, as can be seen in Fig 2.11 for the semiderivative of a cyclic voltammogram of 2 mM gallic acid in water. At positive potentials, the molecule undergoes quasi-reversible oxidation at 2.20 V (HOMO), and we observe two further irreversible oxidation peaks of two of the hydroxyl groups from the gallic ligands[32] at 1.16 V, and 1.84 V. We can only detect the first gallic acid oxidation peak in water at 1.03 V, as at higher potentials the peaks are masked by the decomposition of water. The HOMO-LUMO redox gap for **PDI-1** is 2.40 V, or equivalently 517 nm, in agreement with the UV-Vis absorption spectra.

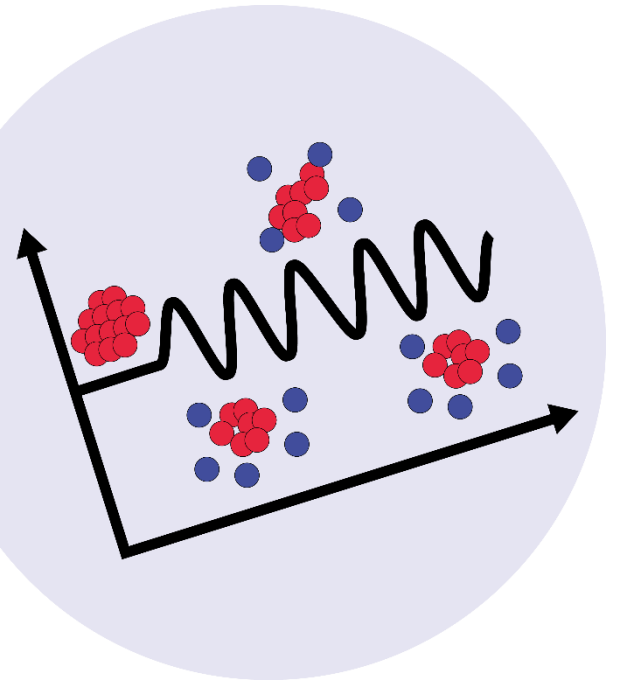

Supramolecular oscillations and waves

3

Abstract: In this chapter we demonstrate that the presence of positive and negative feedback loops in supramolecular polymerization can lead to different supramolecular oscillating behaviours. In addition, a supramolecular wave can be obtained in a thin layer of solution due to (non-covalent) reaction-diffusion processes in non-stirred media. In parallel, we develop a (polymer) length-dependent analytical model that can qualitatively reproduce the observed oscillations. We believe that our studies serve as a stepping-stone to develop adaptable life-like materials.

3.1. Introduction

Living organisms operate for long periods of time under far-from-equilibrium conditions and rely on non-linear chemical dynamic processes permitting the spatiotemporal control of different systems such as microtubules.[1] They consist of thousands of (dis)connected time-regulated reaction networks and functions involving the self-assembly of different structures.[2] The self-assembly is orchestrated by constant energy dissipation, regulatory networks, kinetic control, and feedback loops.[3,4] In addition, living organisms are highly dynamic and present non-linear behaviour with emergent properties that are not predictable by looking only at the molecular information.[5,6] Emergent behaviour can be achieved by coupling feedback loops and diffusion.[6] Namely, the presence of an autocatalytic process (i.e., positive feedback) can lead to global bistabilities and thus, the system can exist in two different stable steady-states. Figure 3.1A shows different autocatalytic networks and Figure 3.1B shows bistabilities, which can be induced by applying different stimuli. In addition, the incorporation of a negative feedback into the chemical network can lead to oscillatory behaviour.[7] Therefore, the presence of positive and negative feedback loops are required in the dynamic network of the system to observe emergent behaviour under far-from-equilibrium conditions where the system constantly dissipates energy. The emergent behaviour cannot be sustained anymore once the system stops dissipating energy.[6]

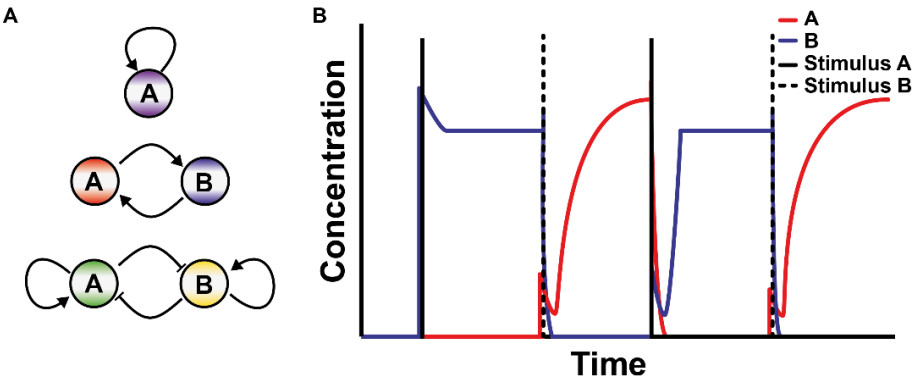

Figure 3.1. Feedback loops and bistabilities. (A) Different autocatalytic networks: (top) direct autocatalysis, (middle) indirect autocatalysis and (bottom) mutual inhibition with autocatalysis. (B) An autocatalytic network can coexist in two different steady states A (red) and B (blue). Switching between the two states can be performed by applying different stimuli. Reproduced from ref. 7 with permission from the Royal Society of Chemistry.

Natural systems possess multiple time-regulated functions.[8] Cells alternate growth and division, and many metabolic functions are synchronized with solar time cycle. These networks consists of individual oscillators that communicate at different time scales.[4] As an example, the circadian clock (or so called master clock) oscillates with a period related to solar time (i.e., 24 hours) in order to regulate functions such as sleep cycles, glucose metabolism, and cell-replication. Several transcription-translation feedback loops with a crucial delay between stimuli and response regulate the oscillatory behaviour.[9] The circadian clock can be regulated by phosphorylation, methylation, or acetylation reactions (Figure 3.2A-C). In mammals, dimerization of CLOCK and BMAL1 proteins (transcription factors) induces the expression of multiple genes resulting in positive feedback. On the

other hand, CLOCK-BMAL1 complex also activates the expression of their own inhibitor/negative regulator PER and CRY proteins leading to negative feedback. Transcription is favoured by the first half of the circadian day until newly synthetized PER and CRY proteins accumulate and inhibit transcription. In order to restart the circadian cycle, PER and CRY proteins must be removed by post-translational phosphorylation.[9,10] In parallel, the CLOCK-BMAL1 complex enhances the expression of ROR and REV-ERB genes that activate and repress, respectively, the formation of BMAL1, and thus stabilizing the oscillatory behaviour (Figure 3.2C).[10,11] The circadian oscillator couples to peripheral oscillators (e.g., found in the liver, pancreas, etc.) to drive further macroscopic functions (Figure 3.2A).[12] These core and peripheral oscillators could keep their periods for days even when they were removed from the organism (Figure 3.2B).[13,14]

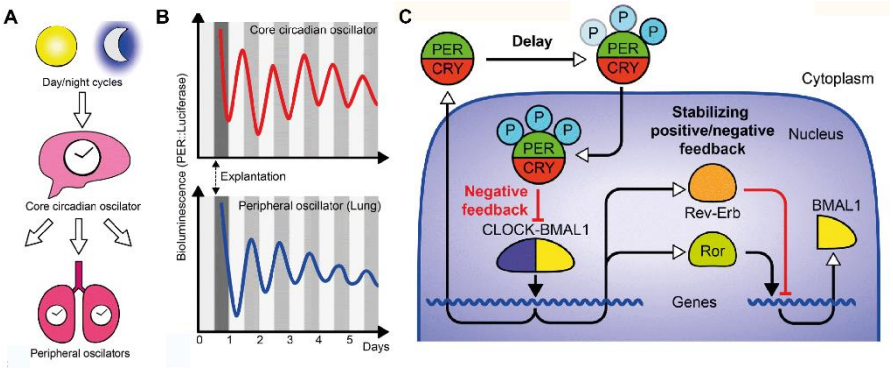

Figure 3.2. Biological oscillations. (A) The core clock of the hierarchical circadian network synchronizes the metabolic clock in the lungs while being regulated by the solar cycle. (B) Real time PER expression in the core circadian oscillator and in the peripheral oscillators (i.e., lungs) in mice. White and dark regions refers to day and night cycles. (C) Feedback loops into the network controls the circadian oscillations. Reproduced from ref. 4 with permission from the Royal Society of Chemistry.

Microtubules (MTs) are a great biological example of a dissipative supramolecular system kept out-of-equilibrium by constant addition of chemical fuel. Specifically, MTs grow via cooperative polymerization upon activation of tubulin with GTP (chemical fuel) where the growth rate increases linearly with tubulin concentration. In addition, MTs depolymerize promptly upon hydrolysis of GTP-tubulin to GDP-tubulin. Interestingly, MTs show periods of slow growth and fast shortening (i.e., length fluctuations), known as dynamic instabilities.[15–19] The latter depends on 4 different parameters: the growth rate, shortening rate, frequency of switching from growth to shrinkage (catastrophe frequency), and the reverse process known as rescue frequency (Figure 3.3A).[20] Hydrolysis occurs when GTP-tubulin is incorporated into the microtubule structure[21] leading to fast depolymerization of MTs since the dissociation rate of GDP-tubulin is almost 3000 times higher than the one for GTP-tubulin.[20,22] This leads to highly robust structures when fuelled by GTP. However, MTs are highly dynamic when GTP is converted to GDP. The latter behaviour could not be achieved under thermodynamic conditions where high association constants (K_a) will lead to strong robust polymers but with low dynamics, whereas, low K_a will lead to fast dynamics and poor mechanical properties. Especially, dynamic instabilities allows the quick adaption and reorientation of MTs.[16,19] In addition, dynamic instabilities are also regulated by microtubule-associated proteins (MAPs) in the cell where for example, microtubule polymerases increase the growth rate (10 times) and microtubule

depolymerases promotes the catastrophe. This means that MT polymerization/ depolymerization is controlled by the chemical network and feedback loops. Interestingly, the dynamic instabilities can lead to oscillations or even pattern formation (in non-stirred media). The latter has attracted many scientist in the last years. As a result, oscillatory behaviour has been observed for *in vitro* and *in vivo* experiments (Figure 3.3B). Moreover, different models have been developed to explain the oscillatory behaviour of MTs.[18,19] Mandelkow and co-workers[16] developed a model in which the microtubules grow via cooperative polymerization (i.e., positive feedback). Then, the hydrolysis of GTP to GDP occurs leading to the catastrophe of MTs (i.e., depolymerization) and the formation of oligomers. The slow dissolution of the oligomers acts as the required negative feedback in order to yield oscillatory behaviour. Finally, tubulin-GDP may exchange the nucleotide (GDP to GTP) to restart the polymerization. In addition, MTs can form spatial patterns in thin liquid layers. Mandelkow et al. observed the formation of linear or circular waves depending on the boundary conditions under non-stirred conditions.[16] The periods on the waves are on the order of minutes in which wave velocities are around 1 mm/min. The oscillations appears as a result of the coupling between diffusion and oscillatory reactions.[16]

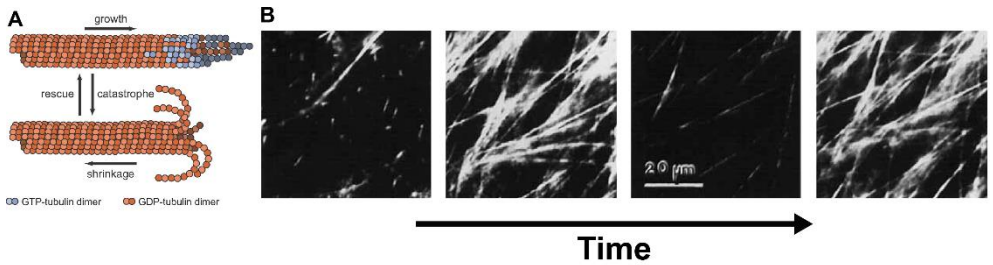

Figure 3.3. Microtubule oscillations. (A) Microtubules show short periods of growth and shrinkage, which depends on the growth rate, the shrinkage rate, rescue frequency and catastrophe frequency. Reproduced from ref. 21 with permission from Wiley. (B) Dark field video microscopy allows to follow microtubules oscillations in time. Reproduced from ref. 17 with permission from Wiley.

Non-linear chemical dynamics and feedback controlled chemical reactions have been studied since the discovery of the most famous oscillating reaction, the Belousov-Zhabotinsky (BZ) reaction.[23,24] The system involves more than 10 individual reactions that are used to periodically reduce and oxidize a metal catalyst (i.e., cerium or ruthenium).[5] The oscillatory behaviour can be easily followed since the colour of the catalyst is different in the different oxidation states. Oscillations occurs due to the autocatalytic formation of bromous acid ($HBrO_2$) that is inhibited by the formation of bromide (Br^-), i.e., delayed negative feedback (Figure 3.4A). Interestingly, the catalytic amount of the metal limits the formation of the autocatalytic species yielding oscillations even in closed reactors.[5] In addition, spatiotemporal waves were observed in thin layers after perturbation of the medium (Figure 3.4B).[5,24,25]

Encouraged by the discovery of the BZ oscillator, scientists have developed novel chemical oscillators.[5] The use of open reactors has led to the development of novel synthetic oscillator, such a pH or redox oscillators.[5,26–29] In most cases, open reactors are required since oscillatory behaviour is driven by constant exchange of reactants and products. In other words, the oscillatory behaviour decays if the system is not fed with reactants.[5] Interestingly, Taylor and co-workers have shown that sustained oscillations can be obtained in a continuous stirring tank reactor (CSTR, i.e., open reactor) using only a

positive feedback loop.[28] However, the oscillatory behaviour is irregular and difficult to control. The addition of a delayed negative feedback to the same system leads to robust and regular oscillations,[29] demonstrating the importance of positive and negative feedback in the network reactions. Very recently, Whitesides and co-workers[30] have developed an oscillator based on biologically relevant organic reactions. Oscillations emerged from the interaction of 3 different reactions: the autocatalytic formation of thiols and amides, a trigger that controls the autocatalytic growth, and an inhibitory process that removes thiol species. This system open a new avenue to develop dynamic networks relevant to life.

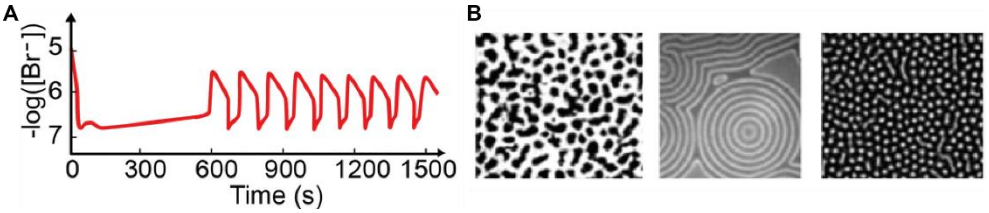

Figure 3.4. BZ oscillations and patterns. (A) BZ oscillations of one of the chemical network are shown in a well stirred reactor. (B) Different spatiotemporal patterns can be observed in thin (non-stirred) layers for the BZ reaction. Reproduced from ref. 26 with permission from Nature Research.

In recent years, BZ and other chemical oscillators have been combined with stimuli-responsive[31] materials (e.g., redox or pH switchable) leading to oscillating gels[32,33], vesicles/micelles[34,35], nanoparticles[36] and block-copolymers[37,38]. For example, Yoshida and co-workers designed a poly(*N*-isopropyl acrylamide) hydrogel (PNIPAM) covalently bound to a Ruthenium catalyst that oscillates between Ru^{2+} and Ru^{3+} in the presence of the BZ reaction mixture (Figure 3.5A). The latter promotes shrinking and swelling of the hydrogel due to charge modification of the Ru catalyst. Synchronous oscillations were obtained in well-stirred microgel suspension media. In addition, reaction/diffusion fronts were obtained in non-stirred media permitting to perform mass transport due to volume changes in the hydrogel layer.[39,40] Based on this, Ueki et al.[35] developed novel block-copolymers that can be switched between micelle and unimer states, structural oscillations were obtained when the system was coupled to BZ reactions (Figure 3.5B).

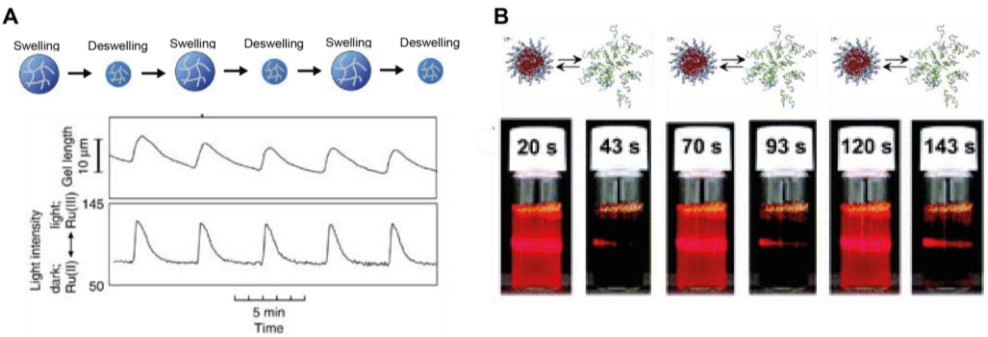

Figure 3.5. Synthetic oscillators. (A) BZ reactions are coupling to PNIPAM hydrogel. Oscillations in the chemical network produce shrinking and swelling of the hydrogel. Reproduced from ref. 33 with permission from Wiley. (B) Structural oscillations of block-copolymers (micelle-unimer) were observed when the system was coupled to BZ reactions. Reproduced from ref. 36 with permission from the Royal Society of Chemistry.

So far, no examples have been provided of a self-oscillating artificial supramolecular system in solution, where the dynamics of the assembled structure itself produces the oscillatory behaviour without the presence of a chemical oscillator. The latter may occur if the system is kept far-from-equilibrium under constant addition of a chemical fuel and positive and negative feedbacks stem from the supramolecular polymerization.

In this chapter, we show the first artificial supramolecular oscillator. Our redox-switchable supramolecular system (see chapter 2) was kept far-from-equilibrium under constant influx of the chemical fuel in a well-stirred media leading to supramolecular oscillations. In addition, a supramolecular wave was obtained when the system was studied in non-stirred media.

3.2. Kinetics of the redox switchable system (PDI-1)

We have investigated our redox switchable **PDI-1** system (see chapter 2) under continuous influx of chemical fuel ($Na_2S_2O_4$) in a well-stirred semi batch reactor. As mentioned in chapter 2, **PDI-1** assemblies can be reduced to **PDI-1**$^{2-}$ upon the addition of 2 eq. of $Na_2S_2O_4$ via radical anion (**PDI-1**$^{\bullet-}$) formation (Figure 3.6A). Reduction of **PDI-1** promotes disassembly and leads to an equilibrium between monomeric **PDI-1**$^{2-}$ species and small **PDI-1**$^{2-}$ assemblies (96 ± 28 nm at 100 μM) in borate buffer solution. **PDI-1**$^{2-}$ spontaneously oxidizes back to **PDI-1** by air (O_2), again via the radical anion **PDI-1**$^{\bullet-}$ (Figure 3.6A). After one redox cycle, **PDI-1** grows hierarchically via a cooperative polymerization. The OD intensity at 528 nm was followed at different **PDI-1** concentrations and previously fitted with a minimal 2-step autocatalytic model (chapter 2). This model could explain the autocatalytic behaviour of **PDI-1** assemblies phenomenologically, but the model is too simplistic to understand oscillations (as we will show below).

The nucleated growth of **PDI-1** assemblies after one redox cycle was followed at different concentrations, using different amounts of seeds or different stirring rates in order to fully study the **PDI-1** kinetics polymerization (Figure 3.6B-D). The growth rate varies with concentration at the same stirring rate (i.e., 500 rpm, see Figure 3.6B). That is to say, the minimum nuclei concentration is reached faster at higher **PDI-1** concentrations inducing the elongation of **PDI-1** assemblies. In addition, the final state (i.e., the plateau in the OD intensity) is also reached sooner at higher **PDI-1** concentrations (i.e., plateau at 45 min and 120 min at 100 and 25 μM, respectively). At lower concentrations the absence of pre-nuclei delays the elongation step, and a characteristic lag phase can be observed, which is longer at lower concentrations (Figure 3.6B, around 30 min at 25 μM). In addition, the autocatalytic growth of **PDI-1** could be accelerated by seeding a freshly cycled **PDI-1** solution using 1 h old seeds (Figure 3.6C). Different amount of seeds (from 5 to 15 % v/v) were added to a freshly cycled **PDI-1** solution (Figure 3.6C), after which the lag phase disappeared for all amounts of seeds added to the 100 μM **PDI-1** solution. That is to say, seeds trigger the elongation step since they act as nuclei. As expected, higher amounts of **PDI-1** seeds lead to faster elongation.

In addition, the lag phase was decreased three times (compared the different starting plateaus in Figure 3.6D) by increasing the stirring rate (i.e., from 500 to 1000 rpm) indicating that higher stirring rates enhance the formation of nuclei and thus, the growth of **PDI-1** assemblies (Figure 3.6D). This could be due to the mechanical forces of stirring resulting in fragmentation of existing nuclei resulting in more smaller nuclei.[41,42] In short,

the concentration, amount of seeds and stirring rates can be used to control the growth rate of **PDI-1** assemblies.

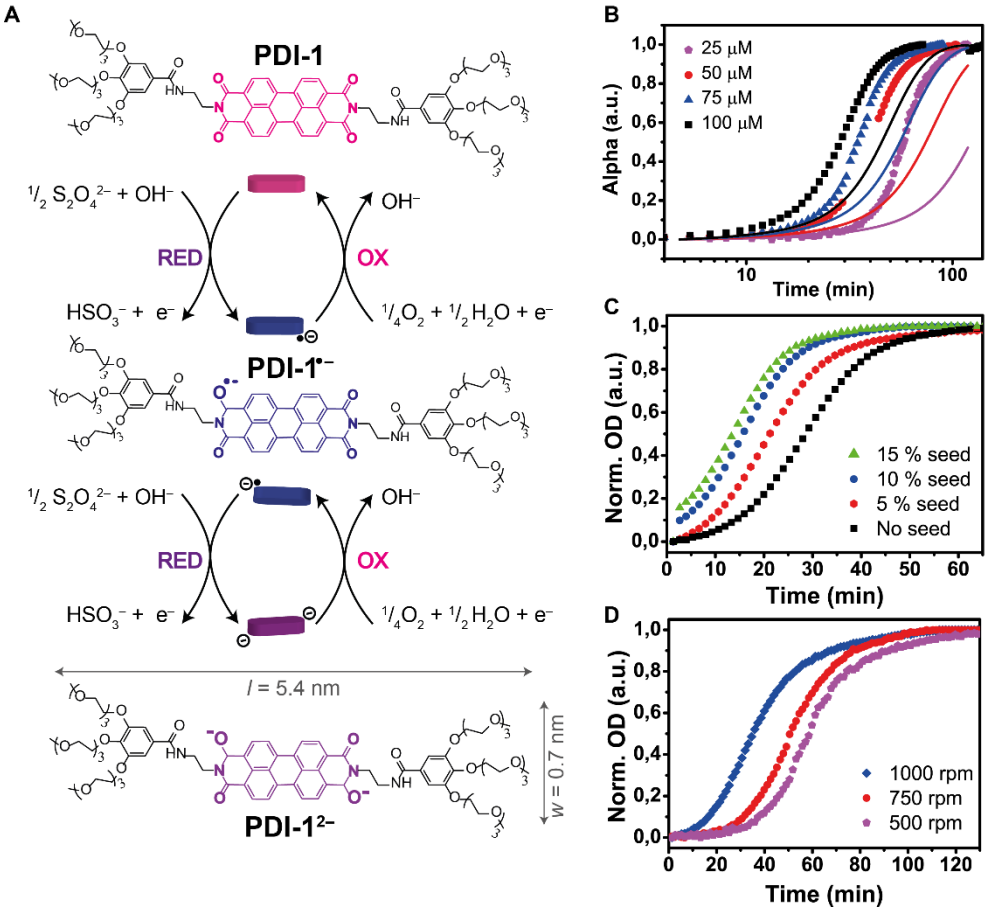

Figure 3.6. Kinetics of the model PDI-1 system. (A) Redox cycle of **PDI-1**. The neutral **PDI-1** is reduced to **PDI-1**$^{\bullet-}$ upon addition of 1 eq. of $Na_2S_2O_4$, further addition of $Na_2S_2O_4$ yields **PDI-1**$^{2-}$,which can be oxidized back by O_2, via radical anion. (B-D) Kinetic studies performed after 1 redox cycle (B) at different **PDI-1** concentrations (solid lines come are fitted using a 1D cooperative model), (C) adding different amounts of **PDI-1** seeds (100 μM cycled **PDI-1** solutions and 1 h old seeds) and (D) at different stirring rates at 25 μM.

To better understand the kinetics of our **PDI-1** system we used a cooperative model in which assemblies grow into two distinct stages.[43,44] A first non-favourable step occurs in which polymers grow up to a critical size. Afterwards the elongation of polymers becomes thermodynamically favourable, and the assemblies grow rapidly.[43,45] Both steps are based on the association and dissociation of monomers into pre-nucleus (k_{fn}, k_{rn}; where subscript f is "forward" and r "reverse" for the "nucleation" n) or post-nucleus (k_{fe}, k_{re}; where e is "elongation") oligomers (see appendix for the set of differential equations and matlab code). To fit our experimental data (Figure 3.6B), we assume the optical density is proportional to the degree of aggregation α.[46] The experimental data at different concentrations and different amount of seeds was fitted in order to get the kinetic constants and also the critical size of the nucleus (Figure 3.6B, solid lines indicate the fitting

curve). The fitted curves give a k_{fn} = 50 M^{-1} s^{-1}, k_{rn} = 0 s^{-1}, k_{fe} = 10^5 M^{-1} s^{-1}, k_{re} = 0 s^{-1}, nucleus size equals 3, and the maximal polymer length 4000. The curves were not perfectly fitted, this may be due to our model that only takes into account the formation of 1D polymers. Specifically, the elongation phase proceeds more rapidly in the experiments as compared to the model (even when k_{fe} > 10^{10} M^{-1} s^{-1}). As we know, **PDI-1** forms colloidally side-to-side fused assemblies, which may increase the elongation rate. This initial cooperative model does, however, provide some rough estimates for the kinetic constants, which were used as a starting point for a more advanced model (see below) section 3.4.

Next we studied the kinetics of the reduction of **PDI-1** to **PDI-1**$^{2-}$ by stopped flow experiments. Two solutions are rapidly mixed and then, injected into an observation cell. The mixing occurs on the milliseconds time scale (Figure 3.8A).[47] Stopped-flow is usually coupled to UV-Vis, fluorescence or CD spectrophotometers in order to follow the fast kinetics of self-assembled systems[48] or the rapid unfolding/refolding of proteins[49]. In our case, the stopped-flow device was coupled to a UV-Vis spectrophotometer to measure the reduction rate of a freshly prepared **PDI-1** solution and the reduction rates of a cycled **PDI-1** solution while the assemblies were growing.

One syringe was loaded with just cycled **PDI-1** solution, whereas the second syringe was loaded with $Na_2S_2O_4$ solution. Next, both solutions were rapidly mixed and then, injected into the observation cell. Specifically, cycled **PDI-1** solution was kept for 90 min inside the syringe. $Na_2S_2O_4$ solution and cycled solution were injected every one minute in order to follow the reduction kinetics while **PDI-1** assemblies were growing inside the syringe (i.e., after a redox cycle **PDI-1** assemblies grow for 90 min, see Figure 3.6B). Said more simply, the aim of these experiments was to determine whether there was a relation between the reduction rate and the size of **PDI-1** assemblies.

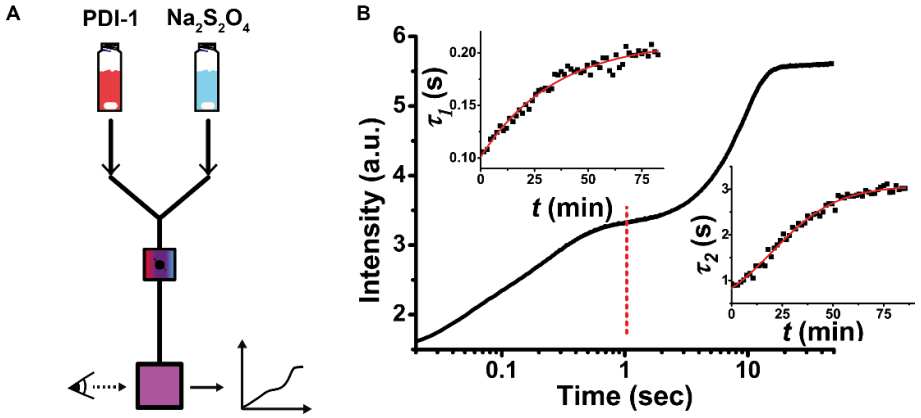

Figure 3.8. Stopped-flow measurements. (A) General scheme of the stopped-flow experiment. Kinetics are measured by quickly mixing two solutions (i.e., **PDI-1** and $Na_2S_2O_4$) and injecting them in an observation chamber. (B) General kinetic measurement for **PDI-1** at 612 nm. Two processes, one exponential (< 1 s) and one sigmoidal (> 1s), can be observed upon reduction of **PDI-1**. The top left inset shows the evolution of the time constant τ_1 obtained from the fitting I = A.exp(τ_1/t) (red line to guide the eye). The bottom right inset shows the evolution of time constant τ_2 obtained by fitting y = A_2+(A_1-A_2)/(1 + exp((t-t_0)/τ_2)) (red line to guide the eye).

The reduction kinetics (from **PDI-1** to **PDI-1**$^{2-}$) was followed at 612 and 727 nm (i.e., characteristic OD bands for dianion and radical anion species, respectively). Interestingly, two distinct kinetic processes were observed (Figure 3.8), where there is a fast exponential increase (1-2 s), followed by a slower sigmoidal process. We observed that both processes

slowed down when more time passed, suggesting that the growth of **PDI-1** assemblies (in the syringe) indeed affects the reduction kinetics. Specifically, the decay time was obtained from the fitting of both processes with general exponential and sigmoidal expressions, respectively. The insets in Figure 3.8B show the evolution of the decay times for the exponential and sigmoidal processes, respectively. So, larger assemblies lead to longer decay times and thus slower reduction kinetics. Moreover, when the growth of **PDI-1** assemblies has finished, the reduction rate is constant as well. The latter matches well with UV-Vis spectroscopy data where **PDI-1** assemblies (100 μM **PDI-1** solution) grow for up to 1 hour (Figure 3.6B).

Surface erosion is a well-known process in polymer (and colloidal) chemistry where degradable particles degrade at different rates depending on the surface area that is exposed to the solvent.[50–52] We believe that the first fast exponential process is due to the initial contact of $Na_2S_2O_4$ with the **PDI-**1 assemblies, following ordinary reaction kinetics. Next, the aqueous $Na_2S_2O_4$ solution has to penetrate inside the colloid, which is hampered by its hydrophobic environment. Therefore, reaction and dissolution only occur at the outer exposed surface resulting in typical surface erosion with a characteristic sigmoidal release profile.

So far, we have shown that **PDI-1** assemblies can be reduced to **PDI-1**$^{2-}$ (k_{red} in Figure 3.9) upon addition of $Na_2S_2O_4$ via radical anion formation. **PDI-1**$^{2-}$ exhibits an equilibrium between monomeric and small assemblies in solution. After oxidation by O_2 (k_{ox} in Figure 3.9), **PDI-1** assemblies grow via cooperative polymerization (positive feedback). The reduction rate depends on size of **PDI-1** assemblies (different in Figure 3.9), that is to say, bigger assemblies have slower reduction rates and smaller assemblies reduce faster.

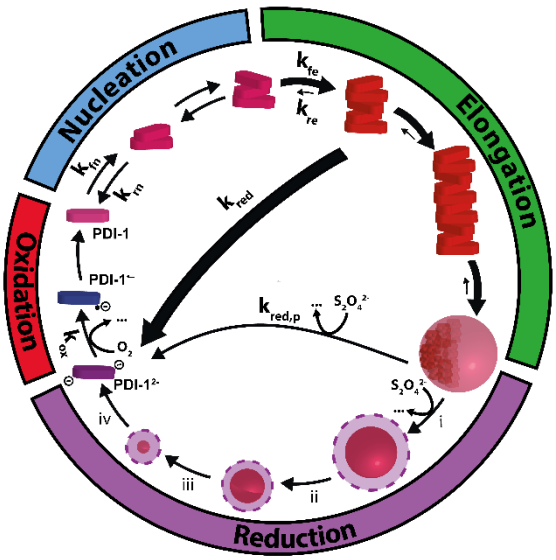

Figure 3.9. Processes important in supramolecular oscillations of PDI-1 assemblies. Freshly prepared **PDI-1** solution can be reduced to **PDI-1**$^{2-}$ upon addition of $Na_2S_2O_4$ (k_{red}, reduction step). **PDI-1**$^{2-}$ can be spontaneously oxidized back to **PDI-1** via radical anion **PDI-1**$^{\bullet-}$ formation (k_{ox}, oxidation step). Just cycled **PDI-1** grow via cooperative polymerization in which small assemblies are formed first (k_n, nucleation step), afterwards assemblies grow rapidly (k_e, elongation step). **PDI-1** assemblies can be reduced back upon addition of $Na_2S_2O_4$. The reduction rate depends on the size of the assemblies ($k_{red,p}$). The latter can be due to the surface erosion of colloidal **PDI-1** assemblies in which the surface of the assemblies is degraded layer by layer (i-iv).

3.3. Supramolecular oscillator

Encouraged by our findings on the autocatalytic growth of **PDI-1** assemblies (positive feedback) and size dependent reduction reaction (negative feedback), we decided to study the system under continuous non-equilibrium conditions. Therefore, we added a constant influx of chemical fuel ($Na_2S_2O_4$) to a **PDI-1** solution in a well-stirred semi-batch reactor. The assembly process was followed by UV-Vis and fluorescence spectroscopy, dynamic and static light scattering (DLS and SLS, respectively) and colorimetric measurements (CCD camera).

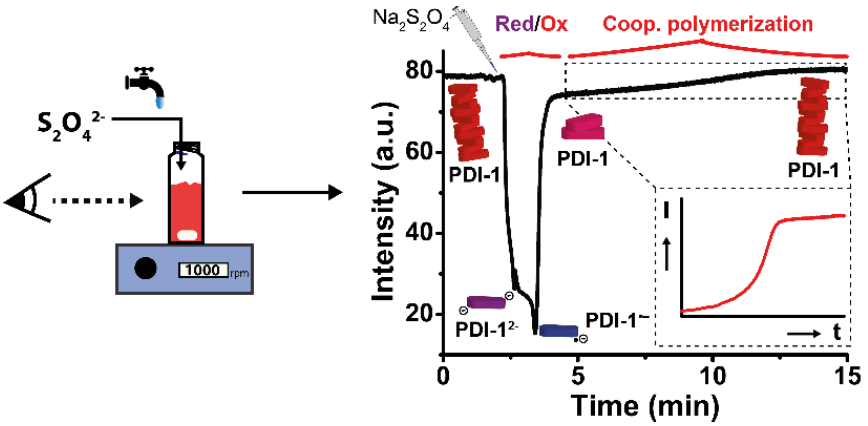

Figure 3.10. Experimental setup and colorimetric measurement technique. The system is measured in a semi-batch reaction under constant stirring with a CCD camera and a diode array. **PDI-1** is reduced to **PDI-1**$^{2-}$ upon addition of $Na_2S_2O_4$ (pipette icon). Afterwards, the system is oxidized back through the radical anion **PDI-1**$^{\bullet-}$ (*Ox* process in Figure) to the **PDI-1**. Then, **PDI-1** assemblies grow via cooperative polymerization (inset shows the magnified cooperative growth of **PDI-1** assemblies).

The system was followed in real time by a CCD camera and a photodiode array, which allows spectra to be collected every few seconds (Figure 3.10A). The CCD camera outputs red, green and blue (RGB) components at each frame (10 fps). The colours permit to distinguish **PDI-1** (red colour), radical anion **PDI-1**$^{\bullet-}$ (blue colour) and **PDI-1**$^{2-}$ (violet colour) species in solution when one redox cycle was performed in a semi-batch reactor under constant stirring rate (Figure 3.10). We decided to follow the red channel, since it is the most sensitive and shows the largest changes between the different species. The red channel intensity drops upon reduction to **PDI-1**$^{2-}$ by adding $Na_2S_2O_4$ solution (intensity goes from 80 to 30, Figure 3.10). When the system is oxidized back to **PDI-1**, first the intensity signal decreases even more due to the formation of radical anion **PDI-1**$^{\bullet-}$, afterwards the signal quickly increases indicating the formation of just cycled **PDI-1** assemblies (Ox in Figure 3.10). Next, a gradual sigmoidal increase of the intensity could be observed due to the autocatalytic growth of **PDI-1** assemblies (coop. polymerization in Figure 3.10).

In addition, a photodiode array was coupled to the setup to measure the entire UV-Vis spectrum (400 to 900 nm). The latter was again used to identify the composition of species present at each specific time, since **PDI-1**, **PDI-1**$^{\bullet-}$ and **PDI-1**$^{2-}$ species have different characteristic UV-Vis peaks (see Chapter 2). In particular, we decided to focus on one of the characteristic bands of **PDI-1**$^{\bullet-}$ radical anion (727 nm) and dianion **PDI-1**$^{2-}$ (612 nm) species.

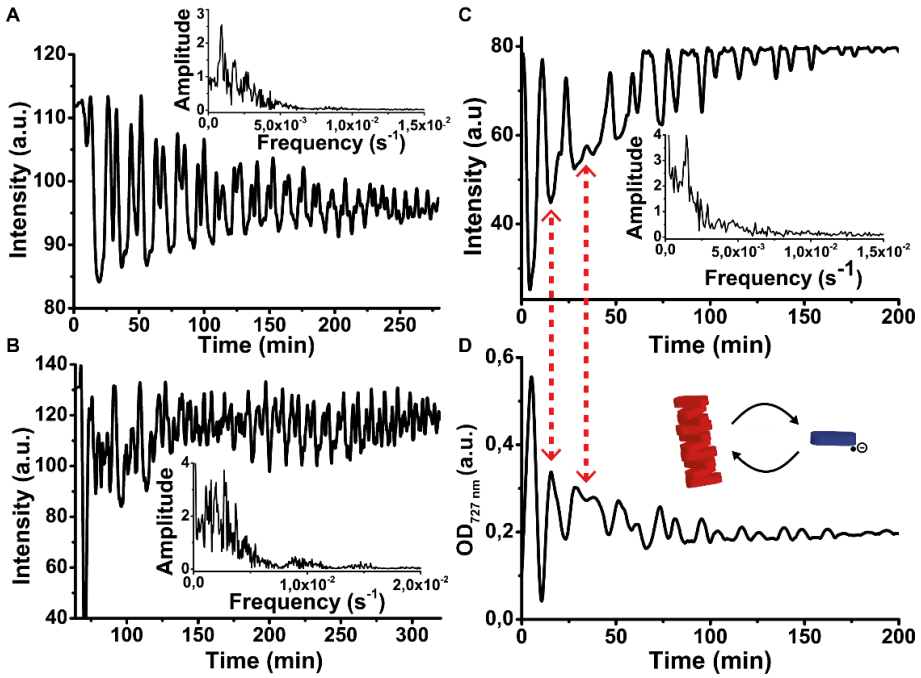

Figure 3.11. Supramolecular oscillations. Different supramolecular oscillating behaviours for **PDI-1** in a stirred semi-batch reactor for continuous addition of $Na_2S_2O_4$ solution (at a flowrate of 0.75 µL/min). Different types of oscillations were found (A,C) period-two oscillations, or (B) irregular oscillations. The insets shows the Fourier transformed frequency and amplitude of each oscillation. (D) UV-Vis spectroscopy of the same experiment shown in panel C, which indicates that oscillations occur between **PDI-1** and **PDI-1**$^{\bullet-}$ (red arrows indicate the formation of **PDI-1**$^{\bullet-}$).

Next, we performed continuous influx experiments. A round vial containing **PDI-1** solution was constantly fed with aqueous $Na_2S_2O_4$ solution (0.4 M) at a constant stirring rate of 1000 rpm (Figure 3.12A). In all cases, **PDI-1** assemblies were "reset" by performing one redox cycle in order to obtain more homogeneous **PDI-1** solutions (cf. chapter 2, where more uniform colloidal **PDI-1** assemblies were obtained after one cycle). Once the neutral state of **PDI-1** was reached again, we proceed to constantly fuel the system. The system was enclosed in a photography studio (a box with white LED lights) to avoid fluctuations of the light and therefore, changes in the overall colour. Ventilators were incorporated into the setup in order to fix the temperature and keep oxygen levels constant.

Interestingly, we found that **PDI-1** shows different oscillating behaviours. Depending on the flow rate, we have observed irregular oscillations (Figure 3.11B) and also, period-two damped oscillations (Figure 3.11A,C). Specifically, oscillations were detected where the intensity of the red channel continuously drops and recovers for more than 200 minutes (Figure 3.11A-C). The experimental data was smoothed with a second order Savitzky-Golay filter with a window of 2500 points. Then, a Fourier transform was applied to obtain the periodicity of the oscillations yielding a period of 7-10 min for the period-2 oscillations (inset in Figure 3.11A,C) and three different periods of 7, 2 and 1 min for the irregular oscillations (inset in Figure 3.11B) confirming the different oscillating behaviours of the system. In addition, the OD intensity of the characteristic band (at 727 nm) of the radical anion **PDI-1**$^{\bullet-}$ shows an oscillating increase and decrease of the intensity (i.e.,

smoothed with a second order Savitzky-Golay filter with a window of 150 points, see Figure 3.11D), which coincides with the oscillating behaviour observed by the CCD camera (red arrows in Figure 3.10). The latter suggests that oscillations occur between the neutral **PDI-1** and radical anion **PDI-1$^{\bullet-}$**. However, there is a significant contribution of scattering in the UV spectra (baseline shifts with time) that can hinder the detection of **PDI-1^{2-}** species. Further studies are needed to know the exact composition of all the species that are involved in our oscillator.

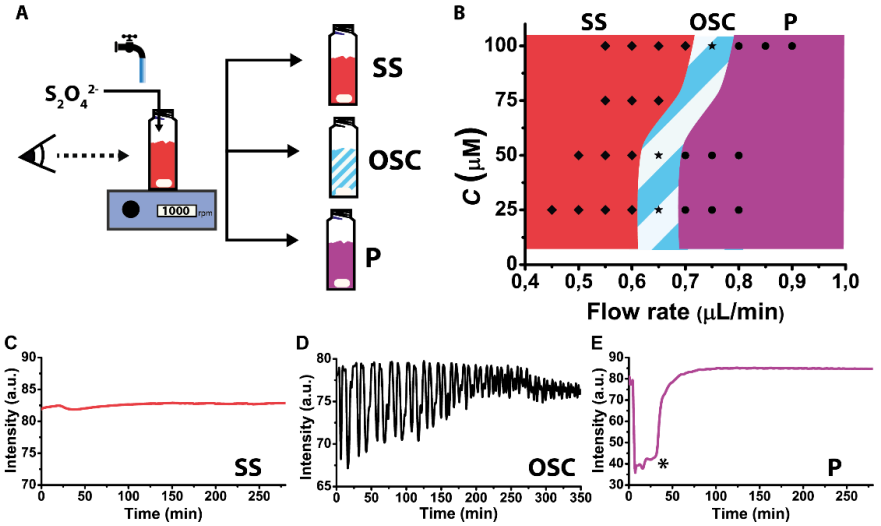

Figure 3.12. Phase Space of the different PDI-1 behaviours. (A) The phase space was mapped in a semi-batch reactor under constant influx of $Na_2S_2O_4$ and constant stirring rate. (B) The phase space was studied at different **PDI-1** concentrations and $Na_2S_2O_4$ flow rates. Three different behaviour were found: (C) steady state (red zone in B), (D) oscillations (blue/white zone in B) and (E) precipitation (purple zone in B).

The phase space of the supramolecular oscillator was studied by varying the concentration of **PDI-1** and the influx of chemical fuel (Figure 3.12B). Interestingly, three different steady-states were found (*SS*, *OSC* and *P* in Figure 3.12B). The first steady-state *SS* was observed at lower flow rates, where the colour intensity suggests that **PDI-1** assemblies are the predominant species in solution (Figure 3.12C and red zone in Figure 3.12B). We believe the oxidation rate to be higher than the reduction rate, so disassembly is not possible, and therefore no oscillations are observed.

An oscillating window *OSC* in the phase space was found when the flow rate was increased. At this higher flow rate there is enough $Na_2S_2O_4$ to disassemble **PDI-1** assemblies. For higher **PDI-1** concentrations the oscillatory behaviour is found at higher $Na_2S_2O_4$ flow rates (Figure 3.12D and blue/white zone in Figure 3.12B), which make sense since more reductant is required to reduce more molecules. The last steady-state *P* was reached by increasing the flow rate even more. In this region, the more reduced species **PDI-1$^{\bullet-}$** and **PDI-1^{2-}** predominate (Figure 3.12E and violet zone in Figure 3.12B). Surprisingly, the system precipitates after some minutes (asterisk in Figure 3.12E). At this point it is not clear what causes the precipitation. One explanation could be that **PDI-1$^{\bullet-}$** species form a new type of assemblies that grow faster as compared to **PDI-1** neutral species.[53]

As far as we know this is the first example of an artificial supramolecular oscillator in solution. Of great interest is the fact that the self-assembly itself affects the chemical

(reduction) kinetics, which creates a feedback mechanism leading to different oscillating behaviours. The oscillations depends on the **PDI-1** concentration and the $Na_2S_2O_4$ flow rate.

3.4. General Supramolecular oscillator model

In order to understand the observed oscillating behaviour, we developed a mathematical model based on mass action kinetics of the system in collaboration with Dr. Michael Stich (Aston University). The model assumes (cf. Figure 3.13A):

1. Assemblies grow via an irreversible cooperative polymerization mechanism. That is, only the forward nucleation k_{fn} and elongation k_{fe} rates are considered.
2. Supramolecular polymers can fragment into two (un)equal pieces with rate k_{frag}.
3. There is a length-dependent reduction rate with a linear decrease in the overall rate $k_{red,p}$ (subscript p for "polymer") with polymer length j. This is as if one molecule of dithionite reacts with the polymer, releasing one reduced monomer r.
4. The reduced monomer r can be oxidized by oxygen (implicitly considered) back to the neutral monomer m.

Based on the laws of mass action for these processes we can derive the overall model, but this is not solvable analytically. We therefore consider only the first moment (i.e., the total number of polymers P), and the second moment (i.e., the total mass of polymers M). The reduced monomer concentration r (i.e., **PDI-1**$^{2-}$) and oxidized monomer concentration m (**PDI-1**) are explicitly considered. This leads to the following set of ordinary differential equations (ODEs):

$$\frac{dP}{dt} = -(3k_{frag} - 2k_{32})P + k_{frag}M + k_{nf}m^2$$

$$\frac{dM}{dt} = 4k_{32}M - 2(k_{frag} + (k_{31} - k_{32}))P + 2k_{fe}Pm + 2k_{nf}m^2$$

$$\frac{dr}{dt} = k_{31}P - k_{32}M - k_{ox,m}r$$

$$m = m_{tot} - M - r$$

The equations reduce to the previously derived model by Cohen et al.[54], when no length dependence is considered (i.e., k_{32} = 0). The coupled ODEs were analysed using continuation analysis using MatCont 5.1 in MATLAB (using the built-in ODE45 solver).

Preliminary analyses on the model have shown a sizable region in the phase space containing damped oscillations, even in the absence of length dependence. This means that it is likely that damped oscillations can be found in any cooperative polymerization system, when it is coupled to a fuel-driven disassembly step.

Since sustained oscillations have not been found yet, the solutions we find are dependent on the initial conditions (cf. caption Figure 3.13C). For the phase plot in Figure 3.13C, only the fuelled rates of oxidation $k_{ox,m}$ and reduction $k_{red,p}$ were changed, leading to a wide region where at least 3 oscillations with an amplitude of at least 50% of the value at

steady state were observed. The phase space needs to be explored more thoroughly to see if regions of sustained oscillations exist. The latter makes further studies easier, because the dependence on initial conditions would vanish. Preliminary simulations with a small k_{32} value (k_{32}/k_{31} = 1/50; i.e., slight length dependent reduction rate, which is slower for larger supramolecular polymers) showed a factor ~2.1 increase in oscillation amplitude. This is promising, since it indeed indicates that additional negative feedback increases the oscillations.

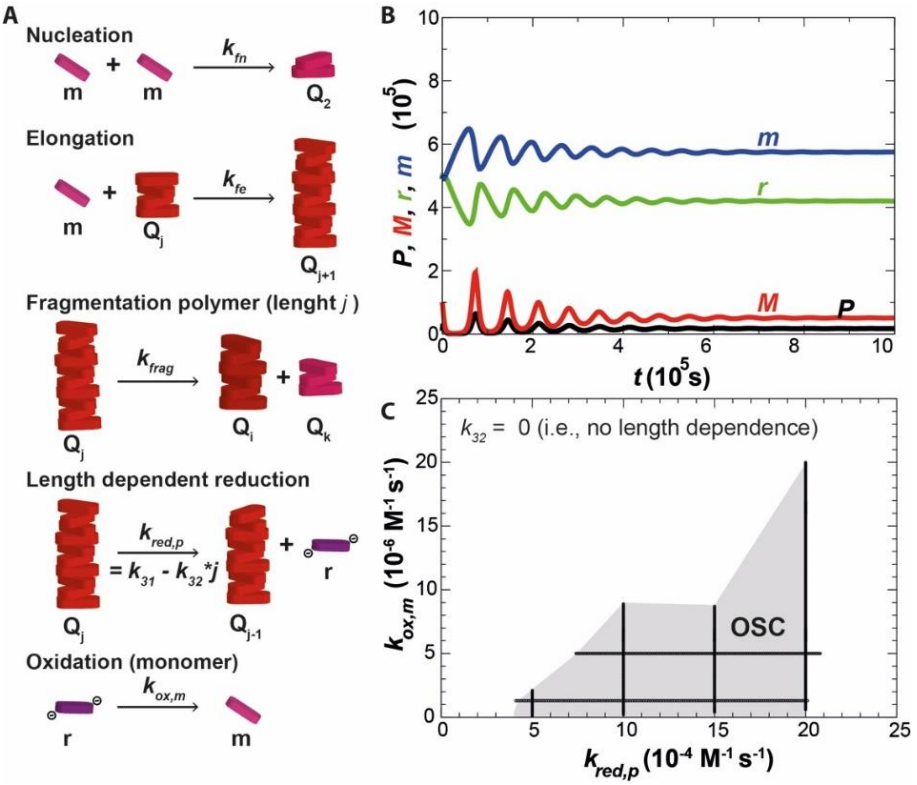

Figure 3.13. Supramolecular oscillator model. (A) Reactions considered in the model: nucleation, elongation, reduction, fragmentation, length dependent reduction, and oxidation. (B) Typical damped oscillations observed in all species. C) Phase space indicating the (dark shaded) region labelled "OSC", where damped oscillations are observed (for a length independent reduction rate). The initial conditions are $P_0 = 10^{-8}$, $M_0 = 10^{-7}$, m_0 = 10-5, r_0 = 0, k_{nf} = 0.0004, k_{ef} = 400, k_{frag} = 0.0003. The reduction rate $k_{red,p} = k_{31}$ (x-axis), and oxidation rate $k_{ox,m}$ are varied.

This arguably oversimplified model needs to be explored in more detail to provide definitive answers. However, a damped oscillating regime has already been found. We are not sure at this point whether the damped oscillations in the experiments and simulations have similar origins. Further studies, where perturbations to the oscillating state (e.g., adding seeds during oscillation) could shed more light on the latter, and are ongoing.

3.5. Supramolecular waves

Reaction-diffusion processes are ubiquitous in living system in which transport properties are coupled with the chemical kinetics of the reactions.[55,56] These intracellular processes regulate the cell proliferation and the formation of self-assembled structures such as microtubules and actin filaments.[25,57] Many of these processes rely on temporal oscillations and waves in the concentration of Ca^{2+}. External signals regulate the concentration of Ca^{2+} in the cell that cause regular variations in its concentration and for example, enhance the gene expression.[58] In addition, Ca^{2+} waves propagate from different geometries and bind to distinct kinds of calcium binding sites (e.g., ATPase and phospholipases) and synchronize intracellular and extracellular events.[59] So far, chemists have used reaction-diffusion processes that employ inorganic reactions to obtain spatial patterns such as Liesegang rings, spiral waves, stationary or Turing patterns.[25,59] Bishop and Grzybowsky[60] showed how chemical waves can be emitted in different ways from selective points in a star shape geometry. Specifically, they patterned spatially chemical oscillations (i.e., BZ system) in a star geometry. Afterwards, oscillations were coupled to an excitable medium to obtain travelling chemical waves. The wave was initiated in different parts of the geometry depending on how it was triggered (i.e., formaldehyde or methanol), and also shows different modes of emission.

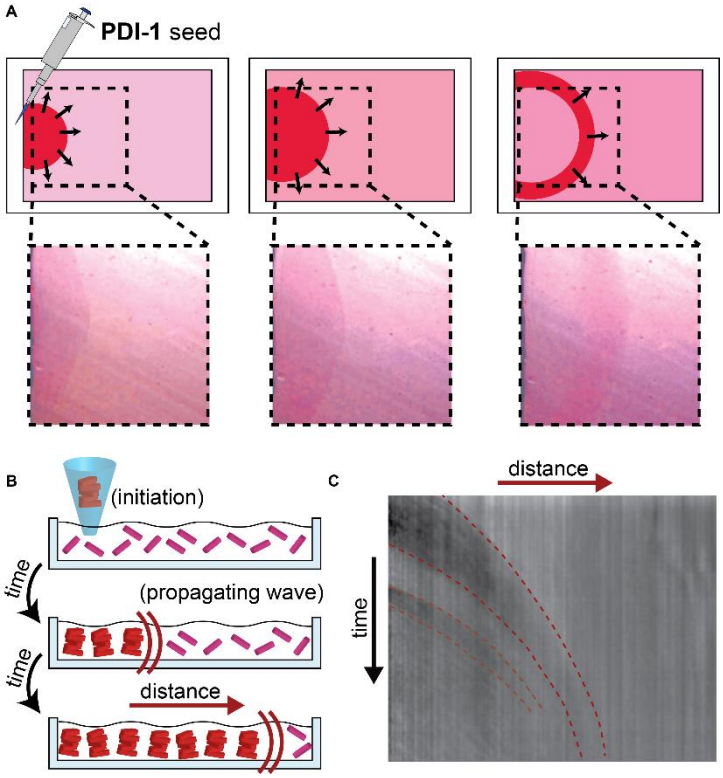

Figure 3.14. Supramolecular waves in non-stirred excitable thin liquid layers. (A,B) Just redox cycled **PDI-1** solution was poured in a 3D printed chip. Afterwards, **PDI-1** seeds (aged for 1 h) were injected in one of the edges of the chip. A wave of supramolecular assemblies was found. (C) The kymograph (extracted from the data obtained) shows that the wave constant was not constant. Moreover, a second wave was found after some time.

Van Esch and co-workers[57] used reaction-diffusion processes in order to obtain different self-assembling structures. Specifically, two different reactants (i.e., hydrazide and aldehyde) can react with one another leading to the formation of a supramolecular gelator (i.e., trishydrazone). Both reactants were placed at opposite sides of a diffusive matrix (alginate) leading to a supramolecular gel line within the matrix. In addition, the authors could obtained different pattern and shapes by placing the reactants in different places of the diffusive matrix. This example shows an approach to obtain different patterns by combining reaction-diffusion processes with self-assembling species in which the reactions take place in a diffusive matrix.

However, artificial trigger waves in supramolecular systems are lacking in the field in which reaction-diffusion process occurs in an excitable media guiding the self-assembly process. The latter has intrigued us since our **PDI-1** system has all the requirements to observe reaction-diffusion processes. For this reason, we decided to use our **PDI-1** system as an excitable medium. A just cycled **PDI-1** solution was poured immediately after oxidation in a 3D printed square chip where two glass cover slips are separated 1 mm (i.e., to avoid convection and solvent evaporation). Imaging of the solution was possible through the top glass wall with the help of a stereoscope. Next, a small amount of 1 h old **PDI-1** seeds was added at one of the edges of the square chip (Figure 3.14A-B). As mentioned above, just cycled **PDI-1** solution and older seeds have slightly different colours, which allows visualization of what is occurring inside the cassette (Figure 3.14B). Interestingly, in preliminary experiments we observed a dark pinkish band moving from the initial zone to the other edge of the chip (Figure 3.14A-B) suggesting auto-amplification of **PDI-1** assemblies and thus, a propagating wave of supramolecular **PDI-1** assemblies. Just cycled **PDI-1** solution is nucleated by **PDI-1** seeds at the edge of the band inducing the formation of new **PDI-1** assemblies that propagate to the other part of the chip (Figure 3.14A-B). Surprisingly, in the same experiment a second trigger wave that travels from the initial seeding point was observed after some minutes. However, these studies have to be repeated in order to confirm this process. The presence of a second wave does, however, show that it is not simply convective transport of seeds. The progression of the wave was studied with the help of ImageJ (Figure 3.14C). Surprisingly, we found that the wave front did not propagate at constant speed (dashed red line in Figure 3.14C). Previous studies have shown that front waves travel at linear speed in excitable media when diffusion is coupled to an autocatalytic process.[56,61–63] The fact that we did not observe a linear speed in the front wave could be due to nucleation and elongation processes occurring in the background, which diminishes the amount of molecules that can participate in the wave. In addition, a lag phase was also found before the wave starts indicating that nucleation and elongation steps of **PDI-1** assemblies play an important role in the propagation of the wave. Moreover, we found that the speed of the wave is two order of magnitude bigger than diffusion of **PDI-1** assemblies indicating that the propagation of the wave is not due to pure mass transport of assembled species.

A model to describe the wave propagation is being developed. As far as we know, this is the first example of an artificial supramolecular wave and we believe that our studies will open the avenue to understand and find more examples. We hope that in the near future we can find supramolecular patterns that can be modified by nucleation and elongation events and negative feedback.

3.6. Conclusions

In this chapter, we have shown that dissipative self-assembly systems can show emergent behaviour when positive and negative feedback are found in the chemical kinetics of the system. **PDI-1** shows different oscillating behaviours under constant influx of chemical fuel in well-stirred media. The autocatalytic growth of the assemblies (positive feedback) and the size dependent reduction (negative feedback) present in the chemical kinetic lead to supramolecular oscillations. In addition, a supramolecular wave was also found in a thin layer of solution. The speed of the wave was not constant since **PDI-1** undergoes homogenous nucleation in all the parts of the cassette and the growth of the assemblies is sigmoidal. In addition, we have developed a minimal analytical mathematical model that explains when supramolecular oscillations can be expected. Damped oscillations were found in a region of the phase space when the system crosses a bifurcation point. We hope that our simplified mathematical model can be applied to find and understand supramolecular oscillating systems in more general terms.

In the next chapter, we show a new approach to work in an open system where a dissipative supramolecular system is kept out-of-equilibrium by constantly adding a chemical fuel and removing the chemical waste.

3.7. Experimental section

Kinetic studies at different concentrations. A 100 μM mother solution was prepared by dissolving **PDI-1** (0.33 mg, 0.20 μmol) in 50 mM borate buffer, pH 8. Next, **PDI-1** mother solution was diluted with borate buffer yielding 75, 50 and 25 μM **PDI-1** solution. Afterwards, 2 mL of the different concentration **PDI-1** solutions were redox cycled (reduction and oxidation steps) adding 1 μL of a 400 mM $Na_2S_2O_4$ solution (in borate buffer) under constant stirring (500 rpm).

Kinetic studies at different seeding concentrations. A 100 μM solution was prepared by dissolving **PDI-1** (0.33 mg, 0.20 μmol) in 50 mM borate buffer, pH 8. Next, 15, 10 and 5 % (0.3, 0.2 and 0.1 mL) of 100 μM **PDI-1** seeds (100 μM **PDI-1** solution aged for 60 min. after one redox cycle, prepared analogously to the one at kinetic studies at different concentrations) were added to 2 mL of just oxidized 100 μM **PDI-1** solution (just cycled solution) under constant stirring (500 rpm).

Kinetic studies at different stirring rates. A 100 μM solution was prepared by dissolving **PDI-1** (0.33 mg, 0.20 μmol) in 50 mM borate buffer, pH 8. Afterwards, 2mL of **PDI-1** was redox cycled (reduction and oxidation steps) adding 1 μL of a 400 mM $Na_2S_2O_4$ solution (in borate buffer) at different stirring rates (1000, 750 and 500 rpm).

UV-Vis measurements. UV-Vis spectra were taken by using a JASCO V-670 spectrometer equipped with a Peltier system as a temperature controller. Spectra were recorded in a 1 cm quartz cuvette at 25 ºC.

Stopped-flow experiments. The reduction kinetics of **PDI-1** was monitored using a stopped- flow apparatus (SFM-3, Bio-Logic, Claix, France). The OD intensity was followed at 612 and 727 nm (characteristic band for **PDI-1**$^{2-}$ and **PDI-1**$^{\bullet-}$, respectively). Freshly prepared 100 μM solution was prepared by dissolving **PDI-1** (0.33 mg, 0.20 μmol) in 50 mM borate buffer, pH 8. Just redox cycled 100 μM solutions were prepared by dissolving **PDI-1** in borate buffer, afterwards, **PDI-1** solution was redox cycled adding 1 mL of a 400 mM $Na_2S_2O_4$ solution (in borate buffer) under constant stirring rate (1000 rpm). The reduction kinetic was recorded after fast mixing of 80 μL of **PDI-1** solution (freshly prepared or redox cycled solutions) and 80 mL of $Na_2S_2O_4$ solution. Specifically, just redox cycled **PDI-1** solution was measured for 90 min injecting **PDI-1** and $Na_2S_2O_4$ solutions every one minute. The data recording frequency was 0.2 ms for the first 2 s and 10 ms for the next minute. The dead time of the setup was 2 ms.

Supramolecular oscillations experiments. A just redox cycle **PDI-1** solution (i.e., 100, 50 and 25 μM) was tracked with a CCD camera and a diode array spectrometer (Analytikjena, Specord S600) under continuous influx of a 400 mM $Na_2S_2O_4$ solution at constant stirring rate (1000 rpm) in a photography studio (in order to avoid light fluctuations) for 12 hours. Different flow rates (typically from 0.5 μL/min to 0.9 μL/min) were studied in order to map the phase space. Red, green and blue channels were recorded by taking 10 frames per second with matlab interface (see appendix). UV-Vis spectra were recorded from 400 to 900 nm in 2 seconds, spectre were taken every 10 seconds.

Supramolecular wave experiments. A just cycled **PDI-1** solution (800 μL, 100 μM) was poured in a 3D printed chip. The chip contains two glass cover slips separate them by 1mm, the solution can be injected from two sides of the chip. **PDI-1** seeds (30 μL, aged for 1 hour after 1 redox cycle) were injected from one part of the chip. Images were acquired using a CCD camera attached to a stereomicroscope (Nikon SMZ7457), frames were recorded every 10 sec for 1 hour.

3.8. References

1. Fialkowski, M. *et al.* Principles and Implementations of Dissipative (Dynamic) Self-Assembly. *J. Phys. Chem. B* **110,** 2482–2496 (2006).
2. Council, N. R. *Inspired by Biology: From Molecules to Materials to Machines*. (2008). DOI: 10.17226/12159
3. Heinen, L. & Walther, A. Celebrating Soft Matter's 10th Anniversary: Approaches to program the time domain of self-assemblies. *Soft Matter* **11,** 7857–7866 (2015).
4. Merindol, R. & Walther, A. Materials learning from life: concepts for active, adaptive and autonomous molecular systems. *Chem. Soc. Rev.* (2017). DOI: 10.1039/C6CS00738D
5. Epstein, I. R. & Pojman, J. A. *An Introduction to Nonlinear Chemical Dynamics: Oscillations, Waves, Patterns, and Chaos*. (Oxford University Press, 1998).
6. Kondepudi, D. & Prigogine, I. *Modern Thermodynamics: From Heat Engines to Dissipative Structures*. (Wiley, 2014).
7. Roekel, H. W. H. van *et al.* Programmable chemical reaction networks: emulating regulatory functions in living cells using a bottom-up approach. *Chem. Soc. Rev.* **44,** 7465–7483 (2015).
8. Alberts, B. *et al. Molecular Biology of the Cell*. (Garland Science, 2002).
9. Gallego, M. & Virshup, D. M. Post-translational modifications regulate the ticking of the circadian clock. *Nat. Rev. Mol. Cell Biol.* **8,** 139–148 (2007).
10. Ko, C. H. & Takahashi, J. S. Molecular components of the mammalian circadian clock. *Hum. Mol. Genet.* **15,** R271–R277 (2006).
11. Guillaumond, F., Dardente, H., Giguère, V. & Cermakian, N. Differential Control of Bmal1 Circadian Transcription by REV-ERB and ROR Nuclear Receptors. *J. Biol. Rhythms* **20,** 391–403 (2005).
12. Mohawk, J. A., Green, C. B. & Takahashi, J. S. Central and Peripheral Circadian Clocks in Mammals. *Annu. Rev. Neurosci.* **35,** 445–462 (2012).
13. Reppert, S. M. & Weaver, D. R. Coordination of circadian timing in mammals. *Nature* **418,** 935–941 (2002).
14. Yoo, S.-H. *et al.* PERIOD2::LUCIFERASE real-time reporting of circadian dynamics reveals persistent circadian oscillations in mouse peripheral tissues. *Proc. Natl. Acad. Sci. U. S. A.* **101,** 5339–5346 (2004).
15. Mandelkow, E. M., Lange, G., Jagla, A., Spann, U. & Mandelkow, E. Dynamics of the microtubule oscillator: role of nucleotides and tubulin-MAP interactions. *EMBO J.* **7,** 357–365 (1988).
16. Mandelkow, E.-M. & Mandelkow, E. Microtubule oscillations. *Cell Motil. Cytoskeleton* **22,** 235–244 (1992).
17. Lange, G., Mandelkow, E.-M., Jagla, A. & Mandelkow, E. Tubulin oligomers and microtubule oscillations. *Eur. J. Biochem.* **178,** 61–69 (1988).
18. Sept, D., Limbach, H. J., Bolterauer, H. & Tuszynski, J. A. A Chemical Kinetics Model for Microtubule Oscillations. *J. Theor. Biol.* **197,** 77–88 (1999).
19. Marx, A. & Mandelkow, E. A model of microtubule oscillations. *Eur. Biophys. J.* **22,** 405–421 (1994).
20. Bowne-Anderson, H., Zanic, M., Kauer, M. & Howard, J. Microtubule dynamic instability: A new model with coupled GTP hydrolysis and multistep catastrophe. *BioEssays* **35,** 452–461 (2013).
21. Caplow, M. & Shanks, J. Evidence that a single monolayer tubulin-GTP cap is both necessary and sufficient to stabilize microtubules. *Mol. Biol. Cell* **7,** 663–675 (1996).
22. Howard, J. *Mechanics of Motor Proteins and the Cytoskeleton*. (Sinauer Associates, Publishers, 2001).
23. BELOUSOV, B. A periodic reaction and its mechanism. *Ref Radiats Med* (1958).
24. Zaikin, A. N. & Zhabotinsky, A. M. Concentration Wave Propagation in Two-dimensional Liquid-phase Self-oscillating System. *Nature* **225,** 535–537 (1970).
25. Epstein, I. R. & Xu, B. Reaction-diffusion processes at the nano- and microscales. *Nat. Nanotechnol.* **11,** 312–319 (2016).

26. Rabai, G., Beck, M. T., Kustin, K. & Epstein, I. R. Sustained and damped pH oscillation in the periodate-thiosulfate reaction in a continuous-flow stirred tank reactor. *J. Phys. Chem.* **93,** 2853–2858 (1989).
27. Frerichs, G. A., Mlnarik, T. M., Grun, R. J. & Thompson, R. C. A New pH Oscillator: The Chlorite−Sulfite−Sulfuric Acid System in a CSTR. *J. Phys. Chem. A* **105,** 829–837 (2001).
28. Kovacs, K., McIlwaine, R., Gannon, K., Taylor, A. F. & Scott, S. K. Complex Behavior in the Formaldehyde−Sulfite Reaction. *J. Phys. Chem. A* **109,** 283–288 (2005).
29. Kovacs, K., McIlwaine, R. E., Scott, S. K. & Taylor, A. F. An Organic-Based pH Oscillator. *J. Phys. Chem. A* **111,** 549–551 (2007).
30. Semenov, S. N. *et al.* Autocatalytic, bistable, oscillatory networks of biologically relevant organic reactions. *Nature* **537,** 656–660 (2016).
31. Urban, M. W. *Handbook of Stimuli-Responsive Materials*. (John Wiley & Sons, 2011).
32. Yoshida, R. Self-Oscillating Gels Driven by the Belousov–Zhabotinsky Reaction as Novel Smart Materials. *Adv. Mater.* **22,** 3463–3483 (2010).
33. Yoshida, R. & Ueki, T. Evolution of self-oscillating polymer gels as autonomous polymer systems. *NPG Asia Mater.* **6,** e107 (2014).
34. Lagzi, I., Wang, D., Kowalczyk, B. & Grzybowski, B. A. Vesicle-to-Micelle Oscillations and Spatial Patterns. *Langmuir* **26,** 13770–13772 (2010).
35. Ueki, T., Shibayama, M. & Yoshida, R. Self-oscillating micelles. *Chem. Commun.* **49,** 6947–6949 (2013).
36. Lagzi, I., Kowalczyk, B., Wang, D. & Grzybowski, B. A. Nanoparticle Oscillations and Fronts. *Angew. Chem. Int. Ed.* **49,** 8616–8619 (2010).
37. Wang, G. *et al.* The non-equilibrium self-assembly of amphiphilic block copolymers driven by a pH oscillator. *Colloids Surf. Physicochem. Eng. Asp.* **529,** 808–814 (2017).
38. Tamate, R., Ueki, T., Shibayama, M. & Yoshida, R. Effect of substrate concentrations on the aggregation behavior and dynamic oscillatory properties of the self-oscillating block copolymers. *Phys. Chem. Chem. Phys.* (2017). DOI: 10.1039/C7CP03969G
39. Murase, Y., Maeda, S., Hashimoto, S. & Yoshida, R. Design of a Mass Transport Surface Utilizing Peristaltic Motion of a Self-Oscillating Gel. *Langmuir* **25,** 483–489 (2009).
40. Murase, Y., Hidaka, M. & Yoshida, R. Self-driven gel conveyer: Autonomous transportation by peristaltic motion of self-oscillating gel. *Sens. Actuators B Chem.* **149,** 272–283 (2010).
41. Pal, A. *et al.* Controlling the Structure and Length of Self-Synthesizing Supramolecular Polymers through Nucleated Growth and Disassembly. *Angew. Chem. Int. Ed.* **54,** 7852–7856 (2015).
42. Carnall, J. M. A. *et al.* Mechanosensitive Self-Replication Driven by Self-Organization. *Science* **327,** 1502–1506 (2010).
43. Smulders, M. M. J. *et al.* How to Distinguish Isodesmic from Cooperative Supramolecular Polymerisation. *Chem. – Eur. J.* **16,** 362–367 (2010).
44. De Greef, T. F. A. *et al.* Supramolecular Polymerization. *Chem. Rev.* **109,** 5687–5754 (2009).
45. Sorrenti, A., Leira-Iglesias, J., J. Markvoort, A., Greef, T. F. A. de & M. Hermans, T. Non-equilibrium supramolecular polymerization. *Chem. Soc. Rev.* (2017). DOI: 10.1039/C7CS00121E
46. Kulkarni, C., Meijer, E. W. & Palmans, A. R. A. Cooperativity Scale: A Structure–Mechanism Correlation in the Self-Assembly of Benzene-1,3,5-tricarboxamides. *Acc. Chem. Res.* (2017). DOI: 10.1021/acs.accounts.7b00176
47. Nic, M. *IUPAC goldbook*. (IUPAC, 2006).
48. Korevaar, P. A. *et al.* Pathway complexity in supramolecular polymerization. *Nature* **481,** 492–496 (2012).
49. Mo, J. M., Holtzer, M. E. & Holtzer, A. Kinetics of self-assembly of alpha alpha-tropomyosin coiled coils from unfolded chains. *Proc. Natl. Acad. Sci.* **88,** 916–920 (1991).
50. Uhrich, K. E., Cannizzaro, S. M., Langer, R. S. & Shakesheff, K. M. Polymeric Systems for Controlled Drug Release. *Chem. Rev.* **99,** 3181–3198 (1999).
51. Ulery, B. D., Nair, L. S. & Laurencin, C. T. Biomedical applications of biodegradable polymers. *J. Polym. Sci. Part B Polym. Phys.* **49,** 832–864 (2011).

52. Tamada, J. A. & Langer, R. Erosion kinetics of hydrolytically degradable polymers. *Proc. Natl. Acad. Sci.* **90,** 552–556 (1993).
53. Marcon, R. O. & Brochsztain, S. Highly Stable 3,4,9,10-Perylenediimide Radical Anions Immobilized in Robust Zirconium Phosphonate Self-Assembled Films. *Langmuir* **23,** 11972–11976 (2007).
54. Cohen, S. I. A. *et al.* Nucleated polymerization with secondary pathways. I. Time evolution of the principal moments. *J. Chem. Phys.* **135,** 065105 (2011).
55. Ayass, M. M., Al-Ghoul, M. & Lagzi, I. Chemical Waves in Heterogeneous Media. *J. Phys. Chem. A* **118,** 11678–11682 (2014).
56. Kapral, R. & Showalter, K. *Chemical Waves and Patterns*. (Springer Science & Business Media, 2012).
57. Lovrak, M. *et al.* Free-standing supramolecular hydrogel objects by reaction-diffusion. *Nat. Commun.* **8,** 15317 (2017).
58. *Calcium Signaling*. **740,** (Springer Netherlands, 2012).
59. Grzybowski, B. A. *Chemistry in Motion: Reaction-Diffusion Systems for Micro- and Nanotechnology*. (John Wiley & Sons, 2009).
60. Bishop, K. J. M. & Grzybowski, B. A. Localized Chemical Wave Emission and Mode Switching in a Patterned Excitable Medium. *Phys. Rev. Lett.* **97,** 128702 (2006).
61. Scott, S. K. *Oscillations, Waves, and Chaos in Chemical Kinetics*. (Oxford University Press, Incorporated, 1994).
62. Scott, S. K. & Showalter, K. Simple and complex propagating reaction-diffusion fronts. *J. Phys. Chem.* **96,** 8702–8711 (1992).
63. Horváth, D., Petrov, V., Scott, S. K. & Showalter, K. Instabilities in propagating reaction-diffusion fronts. *J. Chem. Phys.* **98,** 6332–6343 (1993).

3.9. Appendix

3.9.1. Cooperative polymerization model

The set of differential equations were used to explain the cooperative polymerization of **PDI-1**. The model takes into account the nucleation and the elongation steps permitting to know the different constant kinetics and also the size of the nucleus. The polymer length up to the nucleus is of length *x*, and the elongated part of length *y* (i.e., leading to a total polymer length of *x+y*). The differential equations obtained are:

Nucleation phase:

Monomer species (Y_1):

$$\frac{dY_1}{dt} = -k_{fn} * \left(2 * Y_1 + \sum_{2}^{x-1} Y_i\right) + k_{rn} * (2 * Y_2 + \sum_{3}^{x} Y_i) - k_{fe} * Y_1 * \sum_{x}^{x+y-1} Y_i + k_{re} * \sum_{x+1}^{x+y} Y_i$$

From dimer (Y_2) to nucleus minus one (Y_{x-1}) monomer:

$$\frac{dY_i}{dt} = k_{fn} * (Y_1 * Y_{i-1}) - k_{rn} * Y_i - k_{fn} * (Y_1 * Y_i) + k_{rn} * Y_{i+1}$$

Nucleus itself (Y_x)

$$\frac{dY_x}{dt} = k_{fn} * (Y_1 * Y_{x-1}) - k_{rn} * Y_x - k_{fe} * (Y_1 * Y_x) + k_{re} * Y_{x+1}$$

Elongation phase:

From first elongated species (Y_{x+1}) to last but one elongated species (Y_{x+y-1}):

$$\frac{dY_i}{dt} = k_{fe} * (Y_1 * Y_{i-1}) - k_{re} * Y_i - k_{fe} * (Y_1 * Y_i) + k_{re} * Y_{i+1}$$

Last monomer on the polymer (Y_{x+y}):

$$\frac{dY_{x+y}}{dt} = k_{fe} * \left(Y_1 * Y_{x+y+1}\right) - k_{re} * Y_{x+y}$$

Matlab code:

```
% THIS MODEL DESCRIBES COOPERATIVE SUPRAMOLECULAR POLYMERIZATION (nuc. size x, elong.
size y)
% ########################################################################
% ########################################################################

tic
%% constants
x = 10; % size nuc.
y = 3000; % size. elong.
C0M = 25e-6;
```

```
C0N = 0; %C0M/(15*x);

Y0 = zeros(x+y,1); % define initial conc. vector (first x vals, then y vals)
Y0(1)=C0M; % initial conc. M (monomer)
Y0(x)=C0N; % initial conc. N (nuclei)
rates(1)=kfn; % forward kf for M
rates(2)=krn; % backward kr for M
rates(3)=kfe; % forward kf for N
rates(4)=kre; % backward kr for N
mwm=1; % molecular weigth monomer m
mwn=1; % molecular weight monomer n

%% time interval
% t_range = linspace(0,500,100000);
% t_range = logspace(0,6,10000)'; % better sampling since most event happen early on
t_range = t; % better sampling since most event happen early on

%% solver
options = odeset('RelTol',1e-10,'AbsTol',1e-10);
[t_val,Y_val]=ode15s(@diffeqsC,t_range,Y0,options,x,y,rates);
% [t_val,Y_val]=ode23s(@diffeqsC,t_range,Y0,options,x,y,rates);

Alpha = 1-((Y_val(:,1))./(C0M+C0N*x)); % alpha vs time including monomers in nucleus
% Alpha = 1-((Y_val(:,1))./(C0M)); % alpha vs time

% %% check conservation of mass
% A = linspace(1,x+y,x+y); % col 1 monomer, col 2 dimer, etc.
% B = repmat(A,size(Y_val,1),1); % fill matrix of size Y_val with A
% C = Y_val.*B;
% Ctot = sum(C,2); % total concentration of species

% % % %% ####### See J.Chem.Edu, 78, 554-555, 2001 (Wen-Shyan Sheu)
% % %
% % % for i = 1:x+y
% % %     fi(:,i) = Y_val(:,i)./(sum(Y_val(:,1:x+y),2)); % matrix of probabilities  (sum all fi = 1)
% % % end
% % %
% % % naxm = linspace(1,x+y,x+y); % to make x-axis with number of monomers in polymer
% % % mwi = mwm * naxm; % vector of polymer molecular weights
% % % Mn1 = zeros(size(Y_val,1),x+y); % pre-allocate
% % % Mw1 = zeros(size(Y_val,1),x+y); % pre-allocate
% % % for i = 1:size(Y_val,1); % for each row (i.e., time) of Y_val
% % %     Mn1(i,:) = fi(i,:).*mwi;
% % %     Mw1(i,:) = fi(i,:).*mwi.*mwi;
% % % end
% % % Mnm = sum(Mn1,2); % number average molecular weight
% % % Mnmend = Mnm(end);
% % % Mw2 = sum(Mw1,2);
% % % Mw = Mw2./Mnm; % weigth average moleculear weight
% % % PDIm = Mw./Mnm; % polydispersity index
% % % PDIendm = PDIm(end); % at eq. (assuming solution converged)
% % % Alphaendm = 1-((Y_val(end,1))./(C0M)); % final degree of polym.
```

```
% % % clear mwi Mn1 Mw1 Mn Mw2 Mw fi
toc


function dYdt = diffeqsC(t,Y,x,y,rates)
% this function defines the rates of all species in a cooperative
% polymerization model - THOMAS HERMANS 27 FEB 2017

%% rate constants
kfn  = rates(1); %
krn  = rates(2); %
kfe  = rates(3); %
kre  = rates(4); %

%% initial rates zero
dYdt = zeros(size(Y)); % zero rate for all species

%% ### FOR NUCLEATION PHASE ###
% i = 1 (monomer M)
dYdt(1) = -kfn*Y(1) * (2*Y(1)+sum(Y(2:x-1))) + krn * (2*Y(2) + sum(Y(3:x))) - kfe*Y(1)*sum(Y(x:x+y-1))
+ kre*sum(Y(x+1:x+y));

% 2 <= i < x-1 (from dimer to nucleus minus one)
for i=2:x-1
   dYdt(i) = kfn*Y(1)*Y(i-1) - krn*Y(i) -kfn*Y(1)*Y(i) + krn*Y(i+1);
end

% i = x (for nucleus itself)
dYdt(x) = kfn*Y(1)*Y(x-1) - krn*Y(x) - kfe*Y(1)*Y(x) + kre*Y(x+1);

%% ### FOR ELONGATION PHASE ###
% x+1 <= j <= x+y-1 (from first elongated species N3 to one but last elongation y-1)
for j=(x+1):(x+y-1)
   dYdt(j) = kfe*Y(1)*Y(j-1) - kre*Y(j) - kfe*Y(1)*Y(j) + kre*Y(j+1);
end

% last monomer on chain (x + y)
dYdt(x+y) = kfe*Y(1)*Y(x+y-1) - kre*Y(x+y);
```

3.9.2. Colorimetric measurements

Matlab code:

```
function realVideo()

% Define frame rate
NumberFrameDisplayPerSecond=15;

% Open figure
hFigure = figure(1);

% Choose webcam video input
vid = videoinput('winvideo', 1);

% Set ROI
vid.ROIPosition = [662 576 51 29]; % [X-Offset Y-Offset Width Height]
src.Exposure = -5;

% Set parameters for video
% Acquire only one frame each time
set(vid,'FramesPerTrigger',1);
% Go on forever until stopped
set(vid,'TriggerRepeat',Inf);
% Get a grayscale image
set(vid,'ReturnedColorSpace','rgb');
triggerconfig(vid, 'Manual');

% set up timer object
TimerData=timer('TimerFcn',
{@FrameRateDisplay,vid},'Period',1/NumberFrameDisplayPerSecond,'ExecutionMode','fixedRate','B
usyMode','drop');

% Start video and timer object
start(vid);
start(TimerData);

% We go on until the figure is closed
uiwait(hFigure);

% Clean up everything
stop(TimerData);
delete(TimerData);
stop(vid);
delete(vid);
% clear persistent variables
clear functions;

% This function is called by the timer to display one frame of the figure

function FrameRateDisplay(obj, event,vid)
persistent IM;
```

```
persistent TrueColor;
persistent blueChannel;
persistent greenChannel;
persistent redChannel;
persistent handlesRaw;
persistent TrueInt;
persistent BlueInt;
persistent GreenInt
persistent RedInt;

trigger(vid);

IM = getdata(vid,1,'uint8');

TrueColor = IM(:,:,:);
redChannel = IM(:,:,1);
greenChannel = IM(:,:,2);
blueChannel = IM(:,:,3);

% blueRatio = uint8(((100 * double(IM(:,:,3)))./(1+double(IM(:,:,1))+double(IM(:,:,2)))) .*
(256./(1+double(IM(:,:,3))+double(IM(:,:,1))+double(IM(:,:,2)))));
% redRatio = uint8(((100 * double(IM(:,:,1)))./(1+double(IM(:,:,1))+double(IM(:,:,2)))) .*
(256./(1+double(IM(:,:,3))+double(IM(:,:,1))+double(IM(:,:,2)))));

if isempty(handlesRaw)
  % if first execution, we create the figure objects
  subplot(5,1,1);
  handlesRaw = image(IM);
  title('CurrentImage');

  % Plot first value
  IntensityTrue = mean(IM(:));
  subplot(5,1,2);
  TrueInt = plot(IntensityTrue);
  title('True Color');
  xlabel('Frame number');
  ylabel('Average value (au)');
  axis tight;

  IntensityBlue = mean(blueChannel(:));
  subplot(5,1,3);
  BlueInt = plot(IntensityBlue);
  title('Blue Channel');
  xlabel('Frame number');
  ylabel('Average value (au)');
  axis tight;

  IntensityGreen = mean(greenChannel(:));
  subplot(5,1,4);
  GreenInt = plot(IntensityGreen);
  title('Green Channel');
  xlabel('Frame number');
```

```
  ylabel('Average value (au)');
  axis tight;

  IntensityRed = mean(redChannel(:));
  subplot(5,1,5);
  RedInt = plot(IntensityRed);
  title('Red Channel');
  xlabel('Frame number');
  ylabel('Average value (au)');
  axis tight;

else
  % We only update what is needed
  set(handlesRaw,'CData',IM);

  IntensityTrue = mean(TrueColor(:));
  TrueData = get(TrueInt,'YData');
  set(TrueInt,'YData',[TrueData IntensityTrue]);

  IntensityBlue = mean(blueChannel(:));
  BlueData = get(BlueInt,'YData');
  set(BlueInt,'YData',[BlueData IntensityBlue]);

  IntensityGreen = mean(greenChannel(:));
  GreenData = get(GreenInt,'YData');
  set(GreenInt,'YData',[GreenData IntensityGreen]);

  IntensityRed = mean(redChannel(:));
  RedData = get(RedInt,'YData');
  set(RedInt,'YData',[RedData,IntensityRed]);


  save('JLI230.mat','TrueData','BlueData','GreenData','RedData'); % save('your file name','value you
want to save',...);
end
```

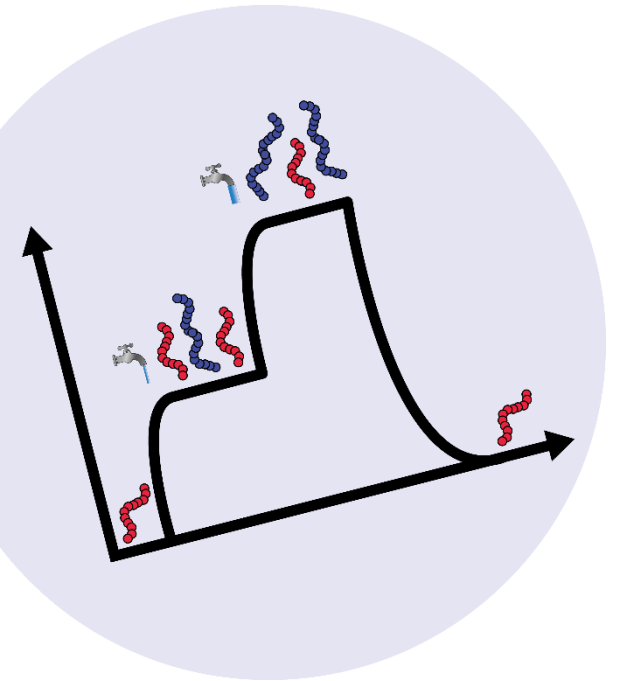

Non-equilibrium steady states in supramolecular polymerization

Abstract: Fuel-driven supramolecular polymers are ubiquitous in living systems. For example, adenosine triphosphate (ATP) is used to control the (de)polymerization of actin filaments. Cell compartmentalization is used to supply fresh ATP to the cytosol and remove waste products. Artificial dissipative polymers have been developed recently, but keeping them in sustained non-equilibrium steady states (NESS) has proven challenging. Herein, we show a supramolecular polymer that can be kept in NESS, inside a membrane reactor (open system) by constant inflow of ATP and outflow of chemical waste. Assembly and disassembly of our polymer is regulated by phosphorylation and dephosphorylation, respectively. Waste accumulation poisons the system causing the reaction cycle to stop. Inside the open system, however, waste can be removed leading to different NESS.

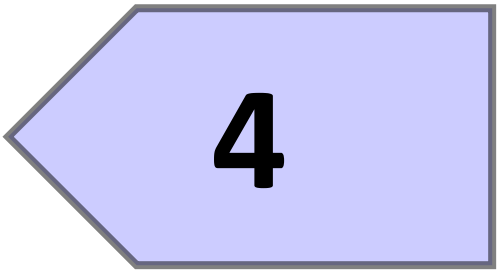

This work has been published:
***Sorrenti A., Leira-Iglesias J., Sato A., Hermans T.M. Non-equilibrium steady states in supramolecular polymerization. *Nature Communications*, **8**, 15899 (2017).

4.1. Introduction

The cell is a kind of factory in which different functions and reactions occur in different places or compartments allowing the control of basic processes of life.[1] For example, the synthesis of all proteins begins in the nucleus and the ribosomes. Once they are ready, sorting signals control the delivery of proteins to the different locations of the cell. Therefore, transport of the different molecules is crucial to connect the different parts of the cell. All cellular functions require large consumption of energy and it is estimated that this value for an average person (50 to 75 kg) is closed to 75 kg of adenosine triphosphate (ATP) per day![2] Without this energy consumption the cell cannot keep its dynamics and structures and in the end, would die.[3] Therefore, ATP recycling is an important task that keeps the cell alive.[4] Specifically, ATP is produced in the mitochondria (eukaryotic cells). The process involves the transport of electrons (derived from the oxidation of food molecules) along the membrane releasing energy in order to pump protons outside the mithocondria. Afterwards, protons flow back down through an enzyme called ATP synthase which uses the proton gradient to produce ATP from adenosine diphosphate (ADP) and inorganic phosphate (P_i), see figure 4.1.[4,5] In addition, this process also triggers other membrane protein machines that activates other functions. Finally, mitochondria store ATP and release ATP to the cytosol to perform other functions. If the mitochondria are blocked, the "power" of the cell would decrease stopping all the driven processes and leading to the death of the cell. The latter stresses the importance of ATP in the cell. For that reason, ATP is recycled more than once per minute in the human body permitting to keep a concentration of ATP ten times higher than the ADP concentration.[4]

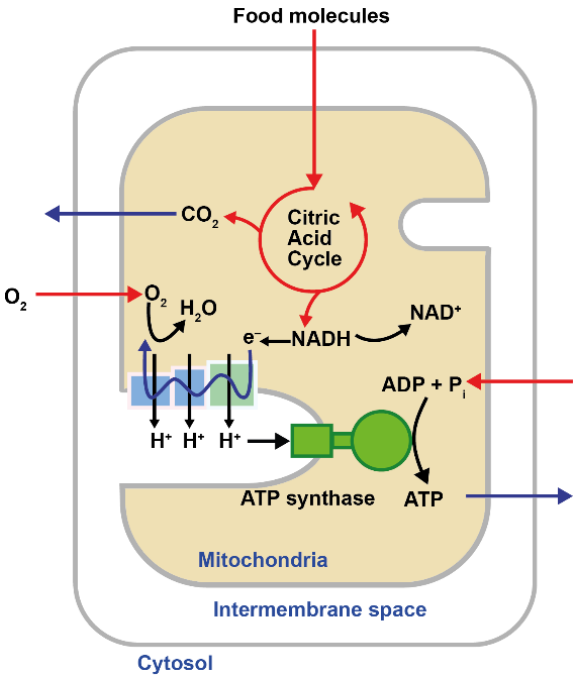

Figure 4.1. Production of ATP in the cell. ATP synthase produces ATP in the mithocondria. Reproduced from Ref. 4.

Enzymes are macromolecules that drive many biological functions. They are important for signal transduction and cell regulation (kinases and phosphatases play an important role).[6] Specifically, they drive unfavourable cellular processes by coupling with the hydrolysis of ATP (energetically favourable).[7,8]

Interestingly, dissipative self-assembly processes such as used by microtubules and actin filaments are sustained by constant addition of chemical fuels (GTP and ATP, respectively), see chapter 1. In addition, microtubule-associated proteins (MAPs) bind to the microtubule and stabilize their polymerization. MAPs also mediate in the interaction between microtubules and other components of the cell. Specifically, phosphorylation of MAPs (hydrolysis of ATP) by different protein kinases is involved in the regulation of the microtubule dynamics leading the structures to the desired place in the cell. Stabilization of actin filaments is performed by a protein called tropomyosin, which prevents the interaction of the actin filament with different kinds of proteins. The latter is important in muscle contraction.[9,10] On the other hand, there are proteins that help to destabilize the polymerization of microtubules or actin filaments leading to depolymerization of both structures in which ATP hydrolysis also occurs in the process.[4,7] In addition, it has been found that some of these proteins together with supramolecular structures are involved in diseases such as Alzheimer's.[11] However, it is not yet clear how this is related with the disease.[4]

Therefore, enzymes are involved in the stabilization and destabilization of the different dissipative supramolecular structures in which ATP hydrolysis drives many of these processes. Understanding these processes is of key importance to develop new synthetic supramolecular system that mimic life-like supramolecular systems. In the recent years, supramolecular chemists have developed artificial supramolecular assemblies that can polymerize/depolymerize by direct chemical modification[12,13], by enzymes[14–17] or mediated by chelation of nucleobases[18–21] upon the addition of a chemical fuel (see chapter 1) leading to transient formation of supramolecular assemblies (monomers are switched from assembling to non-assembling or vice-versa). The lifetime of the assemblies can be tuned depending on the input the system receives. In addition, refuelling of these systems have been shown resulting in a new transient assembly (also called batch excursion).[12,13,15,20–22] However, waste accumulation impedes the repetition of consecutive cycles due to the poisoning of the systems.

In this chapter, we develop a biosynthetic supramolecular system that is kept in various sustained non-equilibrium steady states (NESS) by constant addition of a biologically relevant chemical fuel (ATP) and removing of waste. The latter approach mimics cell compartmentalization where constant inflow and outflow of chemical fuel permit to keep the systems under non-equilibrium conditions.

4.2. Model system: switchable supramolecular polymer (PDI-2)

We designed a symmetric peptide derivative of 3,4,9,10-perylene diimide **PDI-2** (Figure 4.2). The peptide moiety was prepared by solid phase peptide synthesis (SPPS) containing the specific sequence LRRASL for protein kinase A (PKA)[23] followed by peptide coupling with oligoethyleneglycol solubilizing moieties. L-alanine was attached to the core by imidization with perylene-3,4,9,10-tetracarboxylic acid dianhydride yielding the desired core. Finally, a peptide coupling between the peptide derivative and the core was performed leading to the final compound **PDI-2** (see Section 4.9 for further details). **PDI-2**

can be phosphorylated at both serine residues in the presence of PKA upon addition of ATP (chemical fuel) yielding first **p-PDI-2** and then **p2-PDI-2** (Figure 4.2). Dephosphorylation of **p2-PDI-2** is carried out by λ protein phosphatase (λPP) leading to first **p-PDI-2** and finally, **PDI-2**. In addition, a phosphorylation/dephosphorylation cycle produces two equivalents of both ADP and P_i as waste (Figure 4.2). As mentioned above, hydrolysis of ATP is of key importance in living systems. Specifically, phosphorylation of serine/threonine residues is used to control chromatin structures and signal transduction. For that reason, kinases have been target studies in biology and chemistry. They have been previously used in supramolecular chemistry to control the self-assembly of polymeric assemblies[24] or supramolecular hydrogelators[14,15]. In chapter 1 we introduced PDIs, perylene diimides tend to self-assemble in water due to π-π stacking, electrostatic interactions and the hydrophobic effect.[25,26] Specifically, the phosphorylation of **PDI-2** (introduction of two phosphate groups) affects the overall charge of our molecule (4^+ for **PDI-2** versus nearly zwitterionic $4^+/3.3^-$ for **p2-PDI-2**) and thus, changing the structure and stability of their supramolecular polymers.

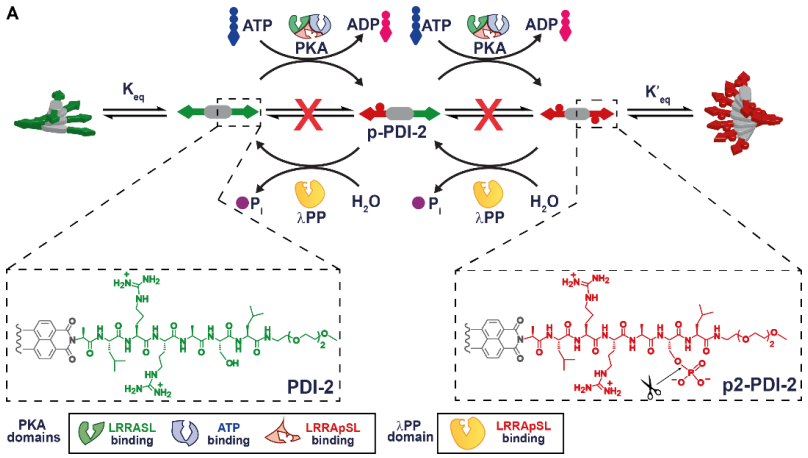

Figure 4.2. Enzyme-controlled supramolecular polymerization. Peptide–perylenediimide derivative **PDI-2** (half is shown) is phosphorylated on the serine residue by protein kinase A (PKA) to give monophosphorylated **p-PDI-2**, and further diphosphorylated **p2-PDI-2**, fuelled by ATP to ADP hydrolysis (one eq. per phosphate introduced). Phosphate hydrolysis (scissors) by λ-protein phosphatase (λPP) yields inorganic phosphate Pi as waste. Both **PDI-2** and **p2-PDI-2** can self-assemble to form equilibrium supramolecular polymers. PKA has three binding sites: for ATP (blue), for the LRRASL peptide (green) and for LRRApSL (red). Reproduced from ref. *** (see page 79) with permission from Nature Research.

The building-block is activated and deactivated via different chemical pathways, that is, mediated by two different enzymes that are working at the same time (summarize in Figure 4.2, cf. Figure 4.17 in appendix), satisfying one of the requirements that has been argued to obtain non-equilibrium steady states (NESS).[27] Therefore, all species (**PDI-2**, **p-PDI-2** and **p2-PDI-2**) are converted through irreversible enzyme-catalysed reactions. The final composition is dictated by the kinetics of phosphorylation and dephosphorylation reactions and not by the thermodynamic stability and thus, the three species are not in chemical equilibrium (red crosses in Figure 4.2). In addition, it is of key importance that deactivation of the building block occurs rapidly and reversibly in order to reach NESS and not stop the reaction cycle (**PDI-2** → **p-PDI-2** → **p2-PDI-2** → **p-PDI-2** → **PDI-2**) after several repetitions. To avoid this, we decided to introduce tryethylene glycol in the peptide moiety

to enhance the water solubility and diminish bundling and/or gelation, which has previously hindered the access of enzymes to different target sites.[14,16]

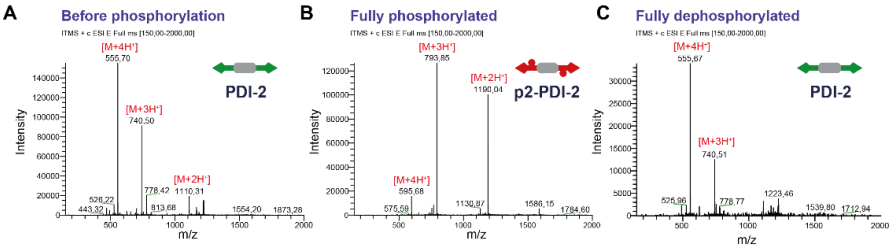

Figure 4.3. Phosphorylation and dephosphorylation of PDI-2. LC-MS spectra of a 1 mM **PDI-2** solution (injection: 4 μM) in the presence of ATP (2 mM, 2eq.), (A) before phosphorylation, (B) and after complete phosphorylation to **p2-PDI-2** (~ 4h) triggered by the addition of 0.13 μM PKA. (C) 200 μM **p2-PDI-2** solution was prepared by phosphorylating **PDI-2** with ATP (400 μM, 2 eq.) and PKA (0.065 μM), afterwards, complete dephosphorylation to **PDI-2** was triggered by the addition of λPP (0.065 μM). Reproduced from ref. *** (see page 79) with permission from Nature Research.

In first place, the phosphorylation was studied by liquid chromatography-mass spectrometry (LC-MS) and ^{31}P-nuclear magnetic resonance. Specifically, quantitative phosphorylation of **PDI-2** was confirmed upon addition of two equivalents of ATP (Figure 4.3A,B and Figure 4.18 in the Appendix). Afterwards, dephosphorylation of both phosphate groups was performed upon addition of λPP phosphatase yielding back the non-phosphorylated **PDI-2** compound (Figure 4.3C). In fact, even if phosphatase are generally non-specific, we have found that Alkaline phosphatase enzyme (Calf intestine, CIP), our first choice, could not dephosphorylate **p2-PDI-2**. Specifically, to completely understand why CIP cannot dephosphorylate **p2-PDI-2**. We studied the phosphorylation of the model non-assembling peptide H-LRRASL-TEG (M_1) (that exactly matches with the **PDI-2** arm) compared to the commercially available Kemptide H-LRRAASLG-OH (M_2). Both peptides can be phosphorylated upon addition of 1 equivalent of ATP (per molecule) in the presence of PKA (Figure 4.4A). However, addition of CIP phosphatase results only in the dephosphorylation of H-LRRAApSLG-OH (pM_2) whereas H-LRRASL-TEG (pM_1) remained unchanged in solution even for days demonstrating that the TEG tail inhibits CIP phosphatase.

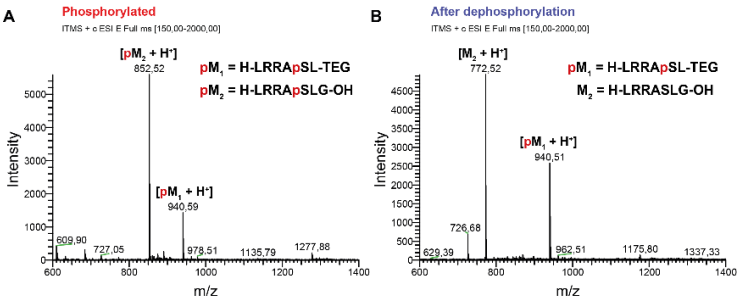

Figure 4.4. Optimizing the phosphatase enzyme. (A) LC-MS spectrum of a 200 μM 1:1 mixture of H-LRRApSL-TEG (pM_1) and H-LRRApSLG-OH (pM_2) prepared by phosphorylation with ATP (200 μM, 1 eq) and PKA (0.065 μM). (B) LC-MS spectrum of the same solution after the addition of CIP (1.4 μM), and incubation 90 min, showing the complete dephosphorylation of only pM_2. Reproduced from ref. *** (see page 79) with permission from Nature Research.

In addition, we had to optimize the experimental conditions at which both enzymes could be used at similar speeds. Namely, both enzymes work at different buffer composition, pH and substrate concentrations. The optimized buffer takes into account the optimal environment for both enzymes and will be referred as the "reaction buffer" (see Section 4.8).

Along this chapter, we will show that we can obtain a stepwise response of **PDI-2** (Figure 4.5A) similar to traditional stimuli-responsive materials.[28] Then, the system shows transient supramolecular behaviour between the different states (Figure 4.5B) and finally, we show that the system can be kept in different NESS using a membrane reactor (Figure 4.5C).

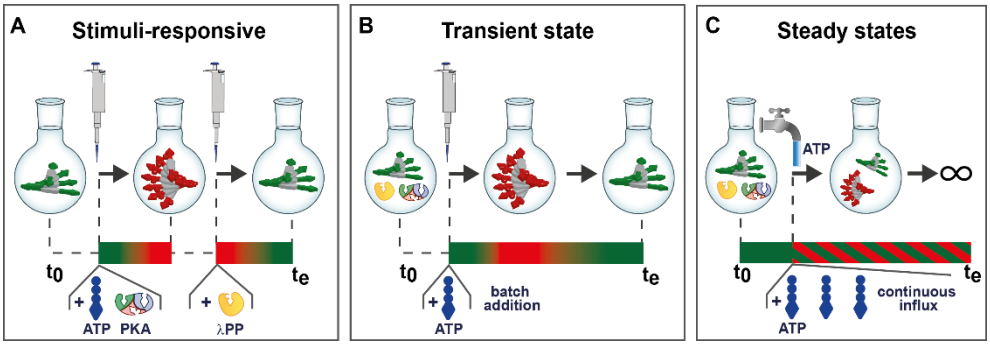

Figure 4.5. From stimuli-responsive to NESS conditions. (A) Stimuli responsiveness: the addition of ATP and PKA to a solution of **PDI-2** results in **p2-PDI-2** and a consequent change of the supramolecular structure of the polymer. A second stimulus, i.e., the addition of λPP, is needed to reset the polymer to its original non-phosphorylated state. (B) Transient state: a single input, i.e., the addition of ATP to a solution of **PDI-2**, in the presence of PKA and λPP, leads to a transient change of the supramolecular structure and chirality of the polymer. (C) Supramolecular non-equilibrium steady-states (NESS). The system is kept in a dissipative steady-state by continuous influx of ATP. Depending on the level of the chemical fuel supplied, different dissipative steady-states can be accessed. Reproduced from ref. *** (see page 79) with permission from Nature Research.

4.3. Effect of phosphorylation on the self-assembly of PDI-2

Once we know that **PDI-2** can be phosphorylated upon addition of ATP and PKA and dephosphorylated upon addition of λPP. We decided to study the self-assembly behaviour of both species (**PDI-2** and **p2-PDI-2**) separately. **PDI-2** dissolves promptly in the reaction buffer (even in the mM range) leading to cherry-red solutions that are stable for months. UV-Vis spectroscopy of a 200 μM **PDI-2** solution shows a broad absorption band from 400 to 620 nm due to S0 → S1 electronic transitions of the core with maxima at 504 and 540 nm (A_{504nm} and A_{540nm}), see Figure 4.6A. Specifically, the lack of the characteristic vibronic progression of monomeric PDIs (ratio A_{504nm}/A_{540nm} of 0.65, Figure 4.6C) and the ratio A_{504nm}/A_{540nm} of 1.46 indicate that **PDI-2** self-assembles into helical stacks through π-π stacking (H-aggregation).[25,26,29] The addition of PKA (0.13 μM) and ATP (400 μM, 2 equivalents) to a **PDI-2** solution (200 μM) was followed by UV-Vis spectroscopy. An increase of the ratio A_{504nm}/A_{540nm} was observed for 100 min up to a plateau at 1.65 (Figure 4.6B). Moreover, LC-MS experiment of the solution confirmed that **PDI-2** was completely converted to **p2-PDI-2**. The increase of the ratio and the overall decrease in intensity suggest that **p2-PDI-2** assemblies grow into bigger structures. In addition, no changes of the

ratio A_{504nm}/A_{540nm} were observed when only ATP was added to a **PDI-2** solution (negative control).

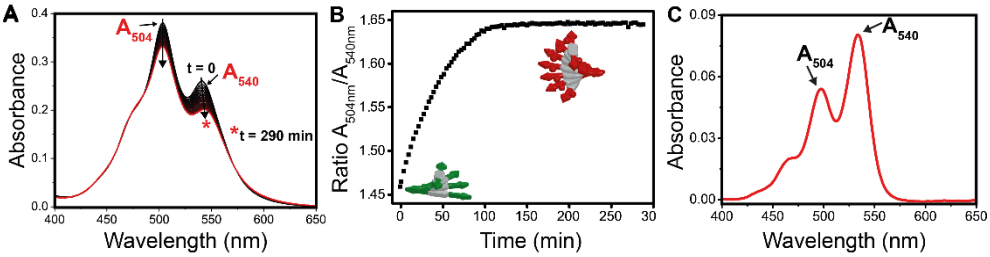

Figure 4.6. Phosphorylation induces changes in the supramolecular polymerization. (A) UV-Vis spectra of a 200 μM **PDI-2** solution (optical path 1 mm) during phosphorylation triggered by the addition of PKA (0.13 μM) and ATP (400 μM), showing the evolution of the two main peaks (A_{504nm}, A_{540nm}) (black arrows). (B) Time course A_{504nm}/A_{540nm} during phosphorylation, extracted from spectra in panel A. (C) UV-Vis spectrum of a 5 μM **PDI-2** solution in the reaction buffer at 85°C. Optical path: 10 mm. Reproduced from ref. *** (see page 79) with permission from Nature Research.

Temperature-dependent UV-Vis experiments were performed to better understand the thermodynamic stability of both supramolecular polymers **PDI-2** and **p2-PDI-2**. A decrease in the ratio A_{504nm}/A_{540nm} was observed for both **PDI-2** and **p2-PDI-2** upon heating from 283 to 368 K indicating partial disassembly of both polymers (Figure 4.7A,B).[30] In addition, consecutive heating-cooling runs of 230 μM solutions (4 consecutive heating/cooling measurements at 1 K/min) were completely reversible suggesting that polymerization for both assemblies occurs under thermodynamic equilibrium with fast exchange dynamics (on the second timescale). The ratio A_{504nm}/A_{540nm} vs temperature (Figure 4.7B) could be described with a T-dependent isodesmic (equal-K_{eq}) polymerization model.[31,32] The following equation can be derived from the model:

$$R_{obs}(T) = \frac{R_{pol}}{1+exp\left[-0.0908\Delta H\frac{T-T_m}{RT_m^2}\right]} + \left(1 + \frac{1}{1+exp\left[-0.0908\Delta H\frac{T-T_m}{RT_m^2}\right]}\right) * R_{mon} \qquad (1)$$

where $R_{obs}(T) = A_{504nm}/A_{540nm}$ at a given temperature (T), R_{pol} corresponds to the ratio $(A_{504nm}/A_{540nm})_{pol}$ for the fully polymerized **PDI-2** or **p2-PDI-2** (that we got from the fitting), R_{mon} corresponds to the ratio $(A_{504nm}/A_{540nm})_{mon}$ for monomeric **PDI-2** or **p2-PDI-2** (set to 0.65) and R is the gas constant. Equation 1 was used to fit the experimental data and obtain the ΔH (the molar enthalpy related to the formation of the non-covalent interactions in the supramolecular polymerization) and the T_m (concentration dependent melting temperature, defined as the temperature for which the degree of aggregation α is 0.5), see Table 4.1.

Table 4.1. Thermodynamics parameters for PDI-1 and p2-PDI-2. Thermodynamic parameters for **PDI-2** and **p2-2PDI-2** supramolecular polymerization in reaction buffer.

Sample	ΔH (kJ·mol^{-1})	T_m (K)	DP_n (298 K)	K_{eq} (10^4 M^{-1}),
PDI-2 (230 μM)	-36.96 ± 0.23	358.5 ± 0.11	2.77	2.14
p2-PDI-2 (230 μM)	-42.54 ± 0.2	368.9 ± 0.10	3.50	3.81

In addition, the degree of aggregation can be calculated using the following equation:

$$\alpha = \frac{R_{obs} - R_{mon}}{R_{pol} - R_{mon}} \quad (2)$$

Equation 2 was used to calculate the degree of aggregation that was plotted vs temperature (Figure 4.7C). The latter can be used to obtain the degree of polymerization DP_N (average stack length) and the equilibrium constant (K_{eq}) at 298 K (Table 4.1) with equations (3) and (4), respectively:

$$DP_N(T) = \frac{1}{\sqrt{1-\alpha(T)}} \quad (3)$$

$$K_{eq}(T) = \frac{[(2DP_N - 1)^2 - 1]}{4C_T} \quad (4)$$

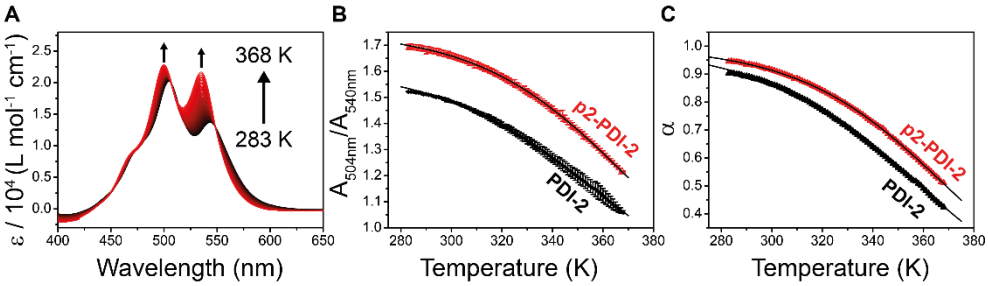

Figure 4.7. Thermodynamics of supramolecular polymerization. (A) Temperature dependent UV-Vis spectra of a 230 μM **PDI-2** solution in the reaction buffer and in the presence of ATP (920 μM, 4 eq.) recorded between 283 and 368 K at 1 K interval (heating rate 1 K min^{-1}, optical path 1 mm). The arrows indicate the evolution of the two main peaks (A_{504nm}, A_{540nm}). (B) Ratio A_{504nm}/A_{540nm} as a function of temperature for **PDI-2** (black points) and **p2-PDI-2** (red points) calculated as the average of four consecutive heating/cooling runs. Error bars show standard deviations. The solid lines correspond to the fitting. (C) Temperature-dependent degree of aggregation, $\alpha(T)$, for **PDI-2** (black points) and **p2-PDI-2** (red points) corresponding to the curve in panel B, calculated by using equation 2. The solid black lines represent the theoretical $\alpha(T)$ for the isodesmic model calculated by using the values of ΔH and *Tm* obtained from the previous fitting. Reproduced from ref. *** (see page 79) with permission from Nature Research.

The results obtained (Table 4.1) indicate that **p2-PDI-2** polymers (K_{eq} = 3.8 x 10^4 M^{-1} and T_m = 368.9 ± 0.1 K) are more aggregated as compared with **PDI-2** polymers (K_{eq} = 2.1 x 10^4 M^{-1} and T_m = 358.5 ± 0.1 K). Previous examples have shown that PDIs tend to form one dimensional columnar assemblies.[25,26,33] When phosphorylated **p2-PDI-2** where drop cast on mica, bundles of long fibers (Figure 4.8B and Figure 4.19 appendix) were detected by atomic force microscopy (AFM). Moreover, shorter fibers could be also shown by transmission electron microscopy (TEM), see Figure 4.20 in the appendix. In addition, dynamic light scattering (DLS) was used to assess the differences between both polymers **PDI-2** and **p2-PDI-2** in solution. The normalized cross correlation function $g^{(1)}$ (τ) indicates that **p2-PDI-2** forms bigger assemblies (R_H = 690 ± 40 nm) than **PDI-2** (R_H = 440 ± 10 nm), see Figure 4.8A. The corresponding relaxation Γ showed a slope of 2 versus scattering vector squared q^2 (log-log insert in Figure 4.8A), confirming that these processes are diffusive.

Finally, we decided to study our system by circular dichroism (CD) spectroscopy. **PDI-2** displays an asymmetric positive couplet at the main absorption band of the chromophore (black line spectrum in Figure 4.8C) characteristic of right-handed P-helical assemblies.[34–36] Moreover, phosphorylation to **p2-PDI-2** triggers the inversion of CD

spectrum to a negative couplet indicating the formation of left-handed M-helical assemblies (Figure 4.8C).[34–36] Interestingly, we found that **PDI-2** and **p2-PDI-2** polymers coexist in solution. Specifically, self-sorting experiments were performed by CD spectroscopy in which linear combinations of the molar fractions of **PDI-2** and **p2-PDI-2** polymers were found indicating that both species do not form mixed assemblies (Figure 4.21 in the Appendix).[37,38] Therefore, phosphorylation yields self-sorted **p2-PDI-2** that has a higher degree of polymerization and opposite helicity.

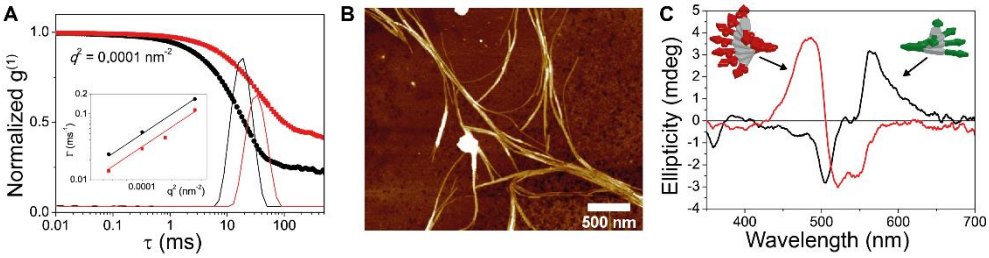

Figure 4.8. PDI-2 and p2-PDI-2 supramolecular polymers. (A) DLS measurements: normalized cross correlation function ($g^{(1)}(\tau)$) of 1 mM **PDI-2** (black dotted line) and **p2-PDI-2** (red dotted line) solutions, showing a shift to higher lag-time τ upon phosphorylation. The corresponding distribution of the relaxation times for **PDI-2** (black solid line) and **p2-PDI-2** (red dotted line). The insert: relaxation Γ versus the square of the scattering vector q^2. (B) AFM image of 2 μM **p2-PDI-2** drop cast on mica. Scale bar 500 nm. (C) CD spectra of 200 μM **PDI-2** (black line) and **p2-PDI-2** (red line) solutions (optical path 1 mm). Reproduced from ref. *** (see page 79) with permission from Nature Research.

So far, we have shown that **PDI-2** was phosphorylated upon addition of ATP and PKA inducing further aggregation of **p2-PDI-2** polymers and leading to bigger and more stable polymers. The latter can be explained due to the changes in the overall charge of the monomer. The polyzwitter-ionic character $4^+/3.3^-$ of **p2-PDI-2** decreases the solubility and the electrostatic repulsions inducing further polymerization. Moreover, an inversion in the helicity of the polymers was observed upon phosphorylation.

4.4. Stepwise phosphorylation and dephosphorylation

The differences in the CD spectra between both **PDI-2** and **p2-PDI-2** assemblies allow us to follow the phosphorylation and dephosphorylation by time-dependent CD measurements in a stepwise way. In first place, the phosphorylation of a **PDI-2** solution (200 μM) containing ATP solution (400 μM) was followed by CD spectra upon addition of PKA (0.13 μM) causing a progressive change of the CD spectra (Figure 4.9A). An increase of the ellipticity at 479 nm was observed (Figure 4.9B). A plateau was reached over time indicating that phosphorylation was finished and thus, the formation of **p2-PDI-2** was completed (confirmed by LC-MS). Afterwards, the addition of λPP to **p2-PDI-2** solution results in a prompt decrease of the ellipticity to the starting value and an inversion of the CD spectra up to the characteristic **PDI-2** spectrum (checked by LC-MS). Stepwise dephosphorylation was performed in the absence of ATP since it was completely consumed in the previous phosphorylation step.

Up to here, we have shown that we can perform stepwise reversibly phosphorylation/dephosphorylation causing a change in the polymerization of both **PDI-2**

and **p2-PDI-2**. Specifically, phosphorylation yields longer and more stable **p2-PDI-2** polymers with opposite chirality that coexist with non-phosphorylated **PDI-2** assemblies.

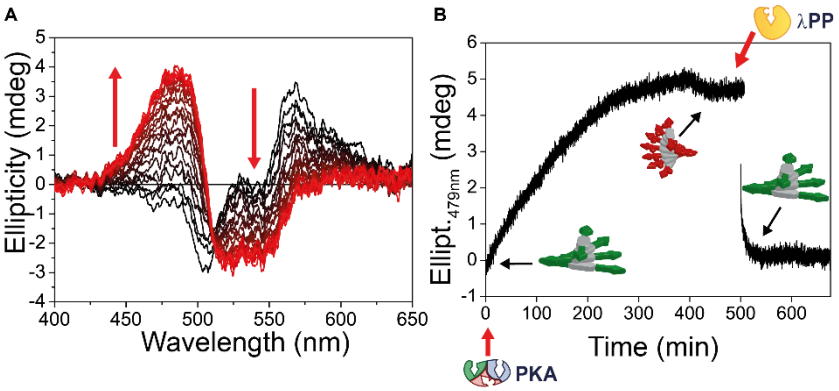

Figure 4.9. Stepwise phosphorylation/dephosphorylation. (A) Time evolution of the CD spectrum (from black to red) during the phosphorylation triggered by addition of PKA (0.11 μM) and ATP (400 μM) to a 200 μM **PDI-2** solution in the reaction buffer at 25°C. Spectra recorded each 6 min, optical path 1 mm. The arrows show the progressive inversion of the CD spectrum. (B) Time course CD measurements (ellipticity at 479 nm vs. time) of a 200 μM **PDI-2** solution during stepwise phosphorylation/dephosphorylation (optical path 1 mm, 400 μM ATP, 0.13 μM PKA, followed by 0.3 μM λPP at *t* = 500 min.). Reproduced from ref. *** (see page 79) with permission from Nature Research.

4.5. Transient self-assembly

Once, stepwise phosphorylation/dephosphorylation was well-stablished, we decided to study the system in a batch reactor. ATP was added to a **PDI-2** solution (containing PKA and λPP) leading to a full cycle (**PDI-2** → **p-PDI-2** → **p2-PDI-2** → **p-PDI-2** → **PDI-2**). LC-MS permits to obtain the molar fraction of each species over time. A transient formation in the molar fraction of **p2-PDI-2** was observed. A fast increase followed by a slower decrease in the molar fraction of **p2-PDI-2** occurs upon addition of a shot of ATP (1 mM) to a **PDI-2** solution (100 μM) containing PKA (0.13 μM) and λPP (0.3 μM), see Figure 4.10A. Interestingly, monophosphorylated **p-PDI-2** shows a complex behaviour with two maxima over the transient formation of **PDI-2** (blue line in Figure 4.10A). To explain what was occurring during the transient experiment, we developed a mathematical model of the enzymatic network that describes the mass action dynamics using differential equations (see section 4.11.5 in the appendix). The model takes into account the kinetics of the phosphorylation/dephosphorylation (two (de)phosphorylation sites per molecule) and all the inhibiting reactions that play a role in the enzymatic network. The species involved in the global process are: PKA catalyses the transfer of a phosphate group from ATP to the peptide sequence producing ADP (in its active site) and λPP cleavages the phosphate group from the peptide sequence producing P_i (inorganic phosphorus) in its active site. The next assumptions were taken: the peptide sequence (LRRASL) and ATP bind randomly to PKA active site, LRRASL and ADP can also bind to PKA's site for ATP (competitive inhibition), LRRASL can also bind to PKA's site for non-competitive inhibitors, λPP dephosphorylates via single-substrate mechanism, P_i can bind to λPP's site (competitive inhibition) and λPP cannot hydrolyse ATP. The latter results in a network of 55 chemical species and an equal number of differential equations (Figure 4.17 in the appendix). The majority of the PKA rates considered into the model have been reported previously.[39,40] However, we consider other

enzymatic rates since we optimized the reaction buffer to have similar PKA and λPP rates. A global minimization of the model was performed in order to fit the reaction rates according with our experimental conditions (see section 4.11.5 in the Appendix). The latter can explain the changes in the concentration of **PDI-2**, **p-PDI-2** and **p2-PDI-2** (solid lines in Figure 4.10A) and agrees with the experimental observations (points in Figure 4.10A). In addition, the model can also explain the complex behaviour of **p-PDI-2** in which the competition between the two phosphorylation reactions **PDI-2** → **p-PDI-2** and **p-PDI-2** → **p2-PDI-2** leads to the first maximum and the competition between the dephosphorylation and the phosphorylation reactions of **p2-PDI-2**, that is, **p2-PDI-2** → **p-PDI-2** and **p-PDI-2** → **p2-PDI-2** leads to the second maximum (Figure 4.23 in Appendix).

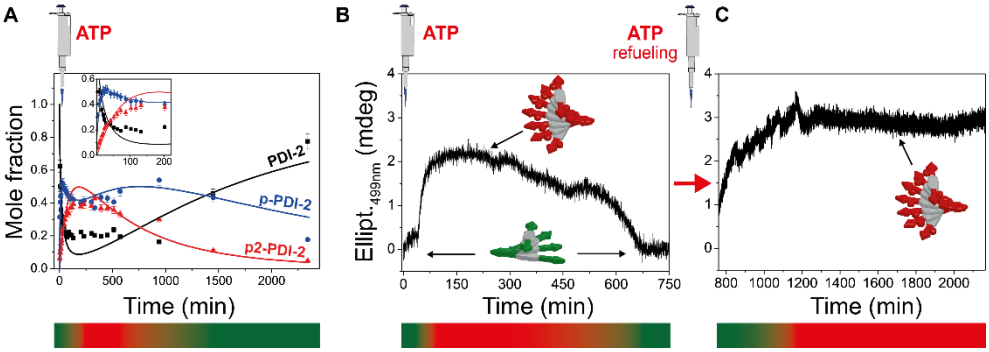

Figure 4.10. Transient state and refueling. (A) Molar fraction of **PDI-2**, **p-PDI-2**, and **p2-PDI-2** versus time by LC-MS (points), following the batch addition of ATP (1 mM), PKA (0.13 μM) and λPP (0.3 μM) to a 100 μM **PDI-2** solution. The solid lines are the fits of the ODE model. The insert is a zoom at the short times. (B) Time course CD measurements (monitored at 499 nm, optical path 1 mm) following the batch addition of ATP (2 mM) to a 200 μM **PDI-2** solution containing PKA (0.13 μM) and λPP (0.2 μM). The colored bar at the bottom of panels A and B indicate the transient formation/disappearance of **p2-PDI-2** (red color) starting from **PDI-2** (green color). (C) Time course CD measured after refueling the same solution as in panel B with a second shot of ATP (2 mM). In this case **p2-PDI-2** accumulates. Reproduced from ref. *** (see page 79) with permission from Nature Research.

Transient self-assembly experiments were also studied by CD measurements, which show first an increase of the ellipticity at 499 nm followed by a slowly decrease to its original value (Figure 4.10B). This indicates that the transient formation of supramolecular species (i.e., transient formation of **p-PDI-2** and **p2-PDI-2**) and the inversion of the helicity are driven by ATP in the reaction buffer and thus, the energy is dissipated. Moreover, once ATP is stopped the system relaxes back to its thermodynamic state **PDI-2**. In addition, the transient self-assembly formation of **p2-PDI-2** is controlled by the rates of phosphorylation and dephosphorylation, which are dictated by the complex dynamics of the network. The model also helps to obtain an extensive vision of the phase space as a function of concentration of PKA, λPP and ATP (Figure 4.24 in Appendix). Previous studies have shown the possibility of obtaining multiple transient self-assembly cycles by refuelling the system.[12,15,19,20] We decided to perform a second addition of ATP to the same solution (Figure 4.10B) to obtain a second transient formation of **p2-PDI-2**. However, we could only obtain phosphorylation but not dephosphorylation back to the initial **PDI-2** state (Figure 4.10C). From the enzymatic network (Figure 4.17 in Appendix), we can deduct that a full cycle (**PDI-2** → **p-PDI-2** → **p2-PDI-2** → **p-PDI-2** → **PDI-2**) produces two equivalents of ADP and P_i by consuming two equivalents of ATP. It is known that P_i is a potent inhibitor of λPP phosphatase[41] and thus, P_i hampers the dephosphorylation of **p2-PDI-2** meaning that the

accumulation of waste leads to poisoning of the system. The latter is a general issue in artificial fuelled supramolecular systems when they are studied in semi(batch) reactors. [12,15,19,20] Interestingly, the poisoning problem was solved by dialysing the solution against fresh buffer (Figure 4.10C, t = 2160 min). A dialysis membering with a molecular weight cut-off (MCWO = 2kD) was chosen allowing only ATP, ADP and P_i to go through but not **PDI-2** (Figure 4.11A). We confirmed that it was possible to remove the waste and go back to the non-phosphorylated **PDI-2** state by checking the solution by LC-MS and CD (Figure 4.11B). In addition, we confirmed that both enzymes can work together and do not deactivate one another since the system keep working perfectly for days.

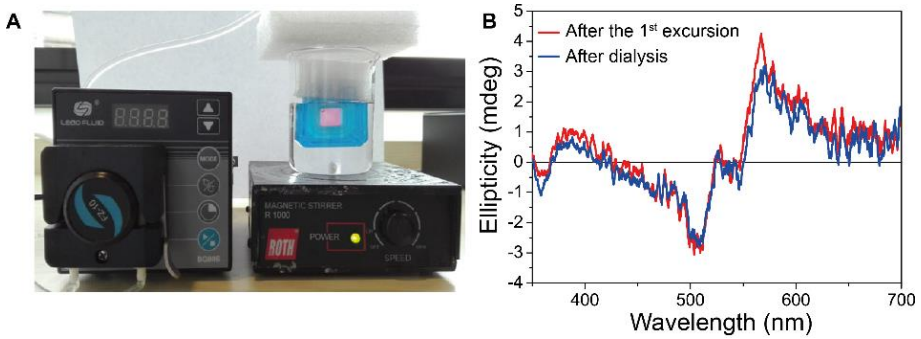

Figure 4.11. Dialysis to get rid of the waste (ADP + P_i). (A) The pink solution (300 μL) coming from the ATP refuelling experiment at 2160 min (see Figure 4.10C), which contained only **p2-PDI-2** (as checked by LC-MS), was put in a Slide-A-Lyzer™ dialysis cassette with a molecular weight cut-off, MWCO = 2 kD, and dialyzed against fresh reaction buffer overnight, continuously replenished by a peristaltic pump. (B) CD spectra of the above solution after overnight dialysis (blue line) as compared with the CD spectrum of the same solution recorded just after the first transient self-assembly (red line), i.e. recorded at 750 min in the experiment reported in Figure 4.10B. Reproduced from ref. *** (see page 79) with permission from Nature Research.

4.6. Non-equilibrium steady-states

As mentioned above, compartmentalization is of key importance in living systems. The latter allows to deliver molecules to different parts of the cell and to remove the chemical waste.[42] For example, dissipative supramolecular systems (e.g., actin filaments) are kept under non-equilibrium by constant fuel/waste exchange and compartmentalization. Encouraged by our last results, we decided to mimic this approach. A continuous flow device was built. A dialysis cassette (MWCO = 2 kD) was flanked by two silicon spacers and quartz windows (Figure 4.12A,B) permitting to keep **PDI-2, p2-PDI-2** and both enzymes (PKA and λPP) inside the central chamber and constantly exchange ATP and the waste (ADP and P_i) within the central chamber (small fluid volume ~ 400 μL) and the reservoirs (Figure 4.12A,B).

Specifically, **PDI-2** was injected into the central chamber, aliquots were taken at different times and tracked by LC-MS allowing to obtain the molar fractions of the solution (See section 4.8). Constant inflow of 1 mM ATP solution (first tap in Figure 4.12C) leads to the first NESS (#1 in Figure 4.12C) in which all the three species (**PDI-2, p-PDI-2** and **p2-PDI-2)** are present in solution with a molar fraction of ~ 0.35, 0.45 and 0.2, respectively (cf. Figure 4.25A in the Appendix). Interestingly, we could keep the first NESS for more than 20 hours (plateau #1 in Figure 4.12C). It is important to say that reaction cycles (phosphorylation and dephosphorylation reactions) are continuously occurring while ATP is

consumed. A second NESS (#2 in Figure 4.12C) was reached by increasing the ATP concentration to 2.5mM (second tap in Figure 4.12C) in which **p2-PDI-2** is mostly present in solution (Figure 4.25B in the Appendix). Then, the non-phosphorylated state was reached by flowing fresh buffer (without ATP, third tap in Figure 4.12C) into both reservoirs (#3 in Figure 4.12C), which has **PDI-2** as the majority species (Figure 4.25C in the Appendix). The latter confirms that phosphorylation only occurs when ATP is present and dephosphorylation keeps going only while phosphorylated species are still in solution. This clearly demonstrates that ATP is needed to maintain different steady states and push the system out of equilibrium in analogy with living systems. Finally, by flowing again ATP solution (5 mM, fourth tap in Figure 4.12C), a different NESS (#4 in Figure 4.12C) was reached characterized by mostly **p2-PDI-2** assemblies (Figure 4.25D in Appendix) indicating the reversibility of our supramolecular open system and thus, preventing the poisoning of system. We can reach different supramolecular steady states by switching the inflow of chemical fuel, and thus mimic living systems. In addition, we can estimate that phosphorylation and dephosphorylation cycles can be repeated at least 8 times per serine residue during the entire experiment in Figure 4.12C.

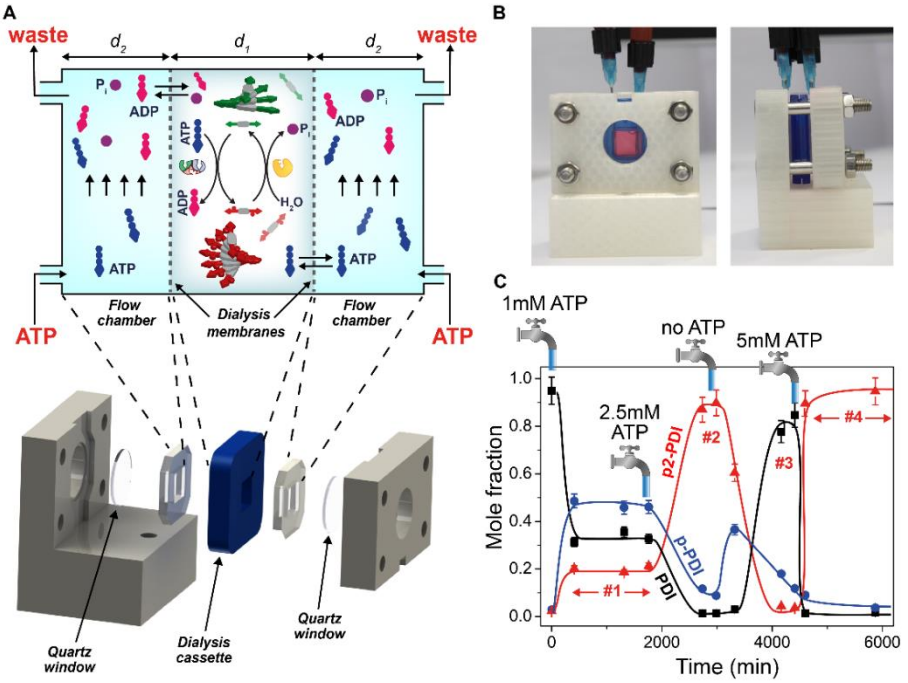

Figure 4.12. Continuous flow device and supramolecular non-equilibrium steady states. (A) Principle of operation and CAD design of the continuous flow device based on a clamped dialysis cassette. The average gap between the membranes d_1 is 1.9 mm, the width of the flow chambers d_2 5.1 mm. (B) Front and side view of the 3D printed device, also showing the inlet and outlet needles inserted through the silicon spacers. (C) Different NESS (plateau regions, #1–4), characterized by different molar fractions of the three species **PDI-2**, **p-PDI-2**, and **p2-PDI-2** (by LC-MS analysis), can be obtained using the continuous flow device, depending on the influx of the fuel ATP. Solid lines are drawn to guide the eye. The taps are placed in correspondence of the time(s) at which we changed the ATP concentration of the solution. For all NESS experiments: 0.085 μM PKA and 0.097 μM λPP. The error bars were set to 6% of the corresponding value. The latter is the maximum error observed in the determination of the molar fraction when injecting 3 times in LC-MS solutions of know composition. Reproduced from ref. *** (see page 79) with permission from Nature Research.

Le chatelier vs NESS

We know that there is not a general consensus in the field of non-equilibrium systems and dissipative self-assembly systems. In this section, we want to clarify that Le Chatelier's principle cannot be applied to our NESS conditions.

Le Chatelier's principle is defined as[43]: *"A system at equilibrium, when subjected to a disturbance, responds in a way that tends to minimize the effect of the disturbance."*

This principle is well-known in chemistry and can explain how a reversible reaction (in equilibrium, $\Delta G = 0$) will evolve after the system is perturbed. As an example, let's focus on a simple reaction: $A \leftrightharpoons B + C$. Once the reaction starts, it will go spontaneously to the thermodynamic equilibrium (ΔG = 0). Afterwards, let's imagine that now we add *C* to our system. Based on Le chatelier's principle we can predict that more reactant will be formed up to a certain point. However, what happens if now we remove constantly *C* from our system. Le Chatelier predicts that the system will shift to the product site. In fact, the principle can be applied since there is a microscopy reversibility of the reaction. The latter perturbation can look similar to our transient self-assembly experiment at first glance. However, the microscopic reversibility is lacking in our system. Phosphorylation is catalyzed by PKA and dephosphorylation is catalyzed by λPP and therefore, both reactions are irreversible.

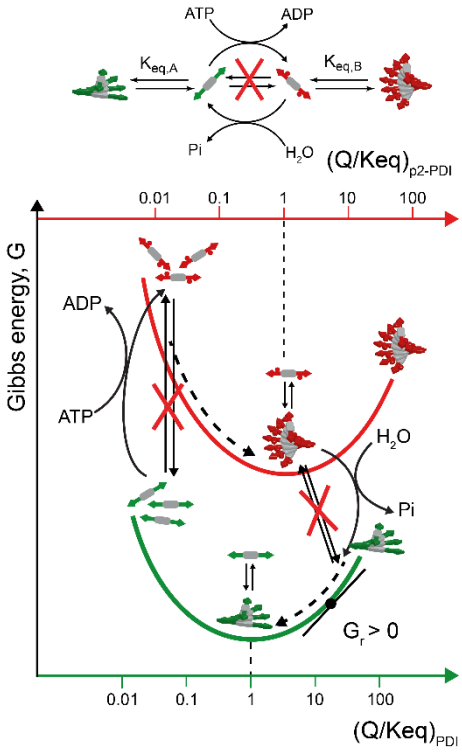

Figure 4.13. Le chatelier vs NESS. Energy landscape of **PDI-2** (green) and **p2-PDI-2** (red) system. Double arrows show microscopic reversibility (equilibria); curved arrows show irreversible reactions.

Now, let's focus on what is happening in our system. **PDI-2** and **p2-PDI-2** are different molecules with different energy landscapes (green and red curves, respectively in Figure 4.13) that can be interconverted in one another by irreversible reactions (solid arrows in Figure 4.13). In addition, Le Chatelier can be applied in the self-assembly of **PDI-2** to **PDI-2** polymers and also, for the polymerization of **p2-PDI-2**. However, the principle can not support our system as a whole since there are irreversible chemical reactions between **PDI-2** and **p2-PDI-2** and therefore, the system does not equilibrate. Moreover, our system operates in open system conditions in which the final composition depends on the rates of the enzymatic reactions (i.e., fuelled kinetics) and how hard the system is driven and not according to the thermodynamics of the species. Finally, as stated by I. Prigogine and D. Kondepudi[44]: *"Le Chatelier's principle only describes the response of a system in thermodynamic equilibrium; it says nothing about the response of a system that is maintained in a non-equilibrium state."*

We want to stress that our NESS conditions cannot be explained as just simple shifting chemical equilibria as described by Le Chatelier's principle (see box above). Specifically, the three species in our system are not in equilibrium and can only interconvert in the presence of ATP and both enzymes. In general, when in a fuelled self-assembly system the assembly kinetics is faster than the reaction kinetics, the assemblies are in a local equilibrium state (apparently accomplishing Le Chatelier's principle) and therefore, the average monomer concentration is changed while the assemblies are dictated by the thermodynamics of the system (i.e., Gibbs energy, concentration, temperature, etc.). In other words, the assemblies just follow the available amount of monomers, which depends on the chemical fuel provided to the system. On the other hand, when the reaction kinetics is faster than the assembly kinetics, the assemblies cannot equilibrate (into a local equilibrium) and the system will be guided by the reaction kinetics of the fuelled reactions.

4.7. Conclusions

In this chapter, we have shown for the first time that is possible to obtain non-equilibrium steady states (NESS) in an artificial supramolecular system. Different steady states can be achieved depending on the influx of chemical fuel (ATP) supplied to the system and outflux of chemical waste (ADP and P_i). The latter was performed in an open reactor allowing to exchange chemical fuel (ATP) and waste and to keep both **PDI-2** and **p2-PDI-2** polymers and both enzymes PKA and λPP. In addition, the amount of ATP determines the steady state reached and the distance to the thermodynamic equilibrium.

We believe that this strategy will be interesting to implement in other self-assembly systems in which so far only transient formation of assembled species have been observed. Different steady states could be reached depending on how hard the system is driven. Moreover, as we have explained in chapter 3, emergent behaviour can be obtained by keeping the system out of equilibrium. In general, our device can be used to drive the system out of equilibrium in which emergent behaviour can be observed such as oscillations and patterns. Our work mimics cell compartmentalization and opens the avenue to develop life-like supramolecular materials that can adapt and perform complex functions like in living systems.

4.8. Experimental section

General. The detailed synthesis and characterization of **PDI-2** and intermediates is shown in Section 4.9. The study of phosphorylation by ^{31}PNMR, more AFM and TEM images, self-sorting experiment, the mathematical model of the enzyme network, as well as the mass spectra corresponding to the NESS of Figure 4.12C are provided in the Appendix.

Experimental conditions. The enzymatic reactions were performed, when not differently specified, in 50 mM Tris-HCl buffer (pH 7.5) containing 10 mM $MgCl_2$, 1 mM $MnCl_2$, 2 mM dithiothreitol (DTT) and 0.1 mM EDTA, at 25°C. We chose to prepare a customized buffer, instead of using the standard buffers supplied by the vendor with the enzymes, because the latter contain 0.01% of the polyethylene glycol surfactant Brij 35, which is likely to affect the self-assembly of our molecules. The addition of $MnCl_2$ was required for the activity of λPP that is a Mn^{2+}-dependent phosphatase. We refer to this buffer as the reaction buffer. Typically, stock 1 mM **PDI-2** solutions, in freshly prepared reaction buffer, were prepared by accurate weighing, and used to obtain the diluted (100-400 μM) **PDI-2** solutions used in the experiments. The stock solutions were freshly prepared the same day of the experiment.

Phosphorylation/dephosphorylation. In a typical phosphorylation experiment, an aliquot of freshly prepared ATP (1-4 μL, 20-50 mM in the reaction buffer) was added to the **PDI-2** solution (200-400 μL, 200 μM), followed by the addition of PKA (1-3 μL of the supplied 13 μM solution) and gentle shaking. The equivalents of ATP are with respect to **PDI-2** molecules (i.e., 2 eq. of ATP correspond to 1 eq. per phosphorylation site). The dephosphorylation was triggered by the addition of an aliquot of λPP (1-3 μL of the supplied 20 μM solution) to a **p2-PDI-2** solution, prepared as described above, in the absence of unreacted ATP. The enzymatic reactions were performed in screw cap sample vial equipped with a glass insert (when followed by LC-MS), or in a 1 mm quartz cuvette (when followed spectroscopically by UV-Vis or CD).

UV-Vis measurements. UV-Vis spectroscopy was used to follow (in time) the changes in aggregation upon phosphorylation (Figure 4.6A,B), as well as to study the thermodynamics of supramolecular polymerization by heating/cooling cycles (Figure 4.7). To this end, we recorded the absorption spectra of **PDI-2** (or **p2-PDI-2**) solutions versus time (or temperature), from which we calculated the ratio of the two maxima at 504 and 540 nm (A_{504nm} and A_{540nm}). Note that the absorbances of the real maxima were considered to calculate A_{504nm}/A_{540nm} (i.e. taking into account the peak shift).

CD measurements. CD spectroscopy was used to study the changes in supramolecular chirality upon (de)phosphorylation both in the step-wise (Figure 4.9) and batch (Figure 4.10) experiments, as well as to study the self-sorting of **PDI-2** and **p2-PDI-2** assemblies (Figure 4.21 in the Appendix). For the time course CD measurements, the phosphorylation was triggered by the fast addition of small aliquots (~ 2 μL) of PKA and ATP solutions to 200 μL of a **PDI-2** solution contained in a 1 mm quartz cuvette, followed by gentle shacking. Afterwards the CD signal at a fixed wavelength was monitored versus time with time steps of 5 s.

LC-MS measurements. Liquid chromatography mass spectrometry (ESI-Ion trap) was used both to check qualitatively the (de)phosphorylation, as well as to calculate the fraction of the three species **PDI-2**, **p-PDI-2**, and **p2-PDI-2** in the batch and steady-state experiments reported in Figure 4.10A and Figure 4.12C. For the latter, the reconstructed ion chromatogram (RIC) was obtained for the three species taking account their characteristic ions (m/z ± 2), from which their relative mole fraction were calculated.

Dynamic light scattering (DLS). A 1 mM **PDI-2** solution in the reaction buffer was split in two parts, and ATP (4 mM, 4 eq.) was added to both the resulting solutions. After that the **p2-PDI-2** sample was prepared by adding PKA to one of the two solutions. After complete phosphorylation (checked by LC-MS) both samples were measured by DLS. The intensity crosscorrelation functions $g^{(2)}(q,\tau) \equiv \langle I_1(q,0)I_2(q,\tau)\rangle / \langle I_1(q,0)\rangle\langle I_2(q,0)\rangle$ were measured on a home-built light scattering setup with an ALV7002 digital correlator using a laser diode at λ = 639 nm at variable scattering vectors $q = \frac{4\pi n}{\lambda} sin\left(\frac{\theta}{2}\right)$, where *n* is the refractive index of the solution. The relaxation dynamics were analysed by the inverse Laplace transformation $g^{(1)}(\tau) = \int_0^\infty H(\Gamma)e^{-\Gamma t}d\Gamma$, where $g^{(1)} = \sqrt{g^{(2)} - 1}$. The translational diffusion coefficient *D* was calculated with the slope of Γ/q^2 obtained from experimental $g^{(1)}$. Hydrodynamic radii R_H were then calculated using the Stokes-Einstein relation $R_H = k_B T/(6\pi\eta D)$, where $D = 1/(\tau q^2)$.

Continuous flow experiments. The cassette holder in the continuous flow device (Figure 4.12A,B), was 3D printed in polylactic acid (PLA). A commercial Slide-A-Lyzer™ dialysis cassette with a molecular weight cut-off, MWCO = 2kD was used as membrane reactor. Two needles connected to microfluidic tubing by Luer lock connectors were inserted through each silicon spacer as the inlet and outlet of two flow chambers flanking the dialysis cassette (Figure 4.12A,B). The inlet needle was pushed down to the bottom of the flow chamber while the outlet was kept at the top (visible in Figure 4.12A), so to ensure that the chamber was always full and the entire surface of the dialysis membrane was in contact with the ATP solution. The inlet was connected to the ATP (or buffer) reservoir and the outlet going to the waste. Each flow chamber has a volume of ~ 800 μL. In a typical experiment 400 μL of a 200 μM **PDI-2** solution containing PKA (0.085 μM) and λPP (0.10 μM) were injected in the dialysis cassette, and remaining air was carefully removed. After that, the 1 mM ATP solution was flowed through the chambers by using a pressure driven pump (Elveflow). We started flowing ~ 20 ml at a flow rate of ~ 4 mL min^{-1}, after that we set the flow rate at ~ 150 μL min^{-1}. At defined times small samples (~ 40 μL) of the reaction solution were taken from the cassette, analysed by LC-MS (5 μL injection), and the remaining part put back in the cassette. At each change of the ATP concentration, the flow chambers were washed with the new solution by flowing at least ~ 25 ml at a flow rate of ~ 5 mL min^{-1}, before setting the flow at ~ 150 μL min^{-1}.

4.9. Synthesis of PDI-2

Synthesis of the perylene-L-alanine core, [N,N'-di(L-alanine)-perylene-3,4:9,10-tetracarboxylic acid diimide], 1

Perylene-3,4,9,10-tetracarboxylic acid bisanhydride (700 mg, 1.78 mmol), L-alanine (380 mg, 4.27 mmol, 2.4 eq) and imidazole (5 g, 73 mmol, 41 eq) were purged with N_2 in a 250 mL double neck round-bottom flask for 15 min. Then, the reaction mixture was heated up to 130 ºC and left stirring 30 min under N_2 atm. Afterwards, the mixture was cooled down to 90 ºC and 100 mL of water was added. The resulting solution was filtered and the filtrate was added dropwise to 300 mL of isopropanol giving a red precipitate. The red solid was collected by filtration and dried under vacuum affording compound **1** (800 mg, 85 %). ^{1}H NMR (400 MHz, DMSO-d6): δ 8.07 (s, 8H), δ 5.56 (dd, *J* = 7.0 Hz, 2H), 1.68 (d, *J* = 7.0 Hz, 6H).

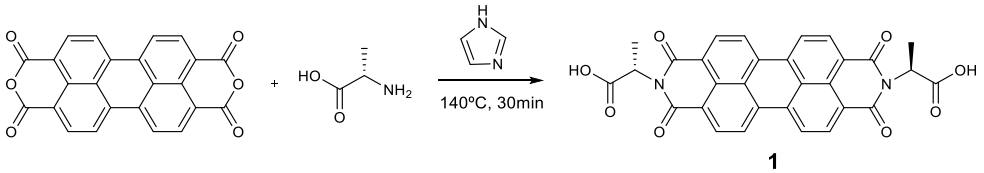

Figure 4.14. Synthesis of the core. Preparation of the perylene-L-alanine core. Reproduced from ref. *** (see page 79) with permission from Nature Research.

Synthesis of Fmoc-LR(Pbf)R(Pbf)AS(tBu)L-OH peptide, 2

Peptide **2** was prepared by manual Fmoc solid phase peptide synthesis, SPPS (Figure 4.15), starting from 2-chlorotrityl resin loaded with L-leucine (200-400 mesh, 0.79 mmol/g capacity, typically 1 g). This is a highly acid labile resin that requires only mild conditions for the final cleavage, which allowed to obtain fully protected **2** (i.e. Fmoc protected at the N-terminus, as well as at the sensitive side chains). The typical protocol involved: a) swelling of the resin (DMF); b) activation of the new amino acid at the carboxylate (with HBTU, 1 eq., HOBt, 1 eq., in the presence of DIPEA, 2 eq. for 10 min); c) coupling reaction (3 eq. of activated amino acid with respect to resin capacity) for 50 min followed by 10 washes with DMF to get rid of the excess of reactants; d) Fmoc deprotection to liberate the *N*-terminus of the growing peptide (piperidine/DMF 1:4, 2 x 20 min) plus 10 washes with DMF. The synthesis cycle b – d was repeated for the different amino acids (Fmoc deprotection was not done at the last cycle). The activation step b was not performed in the case of arginine, to avoid the possible formation of an intermolecular δ-lactame that would decrease the coupling yield.[45] Finally, the fully protected target peptide **2** was cleaved off the resin by treatment with 1% TFA in dichloromethane for 1h. Then **2** was dissolved in dichloromethane and washed with 1 M aqueous HCl to remove traces of piperidine coming from the SPPS. The latter was a necessary step in order to avoid the formation of unwanted acyl-piperidine derivatives in the next coupling reactions. HRMS (ESI+) Calculated Mass for $C_{75}H_{109}N_{12}O_{16}S_2$ [M+H$^+$]: 1497.7520. Found: 1497.7368.

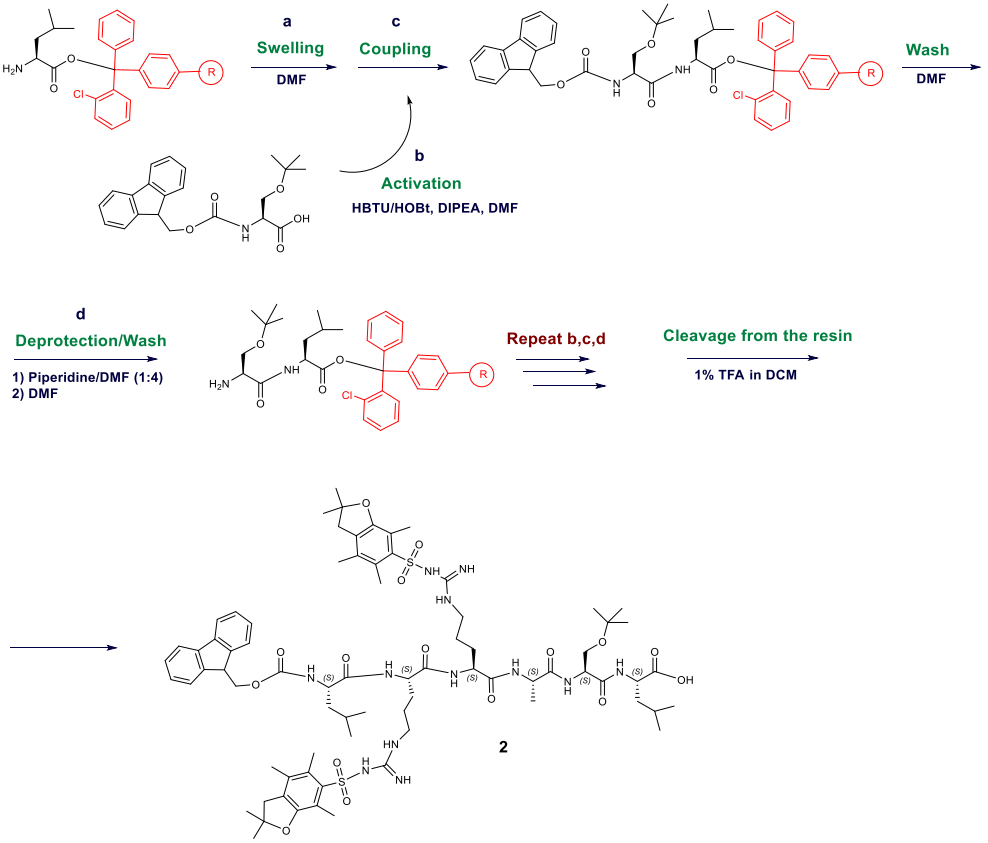

Figure 4.15. Solid phase synthesis. Fmoc solid phase peptide synthesis using the highly acid labile 2-chlorotrityl resin. The fully protected peptide Fmoc-LR(Pbf)R(Pbf)AS(tBu)L-OH was obtained with yields > 90%. Reproduced from ref. *** (see page 79) with permission from Nature Research.

Synthesis of H- LR(Pbf)R(Pbf)AS(tBu)L-TEG, 5

HBTU (137 mg, 0.36 mmol, 1.2 eq) and DIPEA (157 µL, 0.9 mmol, 3 eq) were added to a solution of peptide **2** (450 mg, 0.3 mmol, 1 eq) in 8 mL DMF under N_2 atm. After 5 min, TEG-amine 3 (58.9 mg, 0.36 mmol, 1.2 eq) dissolved in 4 mL DMF was added to this solution and the mixture left stirring overnight (compound **3** was prepared according to a reported procedure[46]). Then, the reaction was quenched by the addition of 100 mL dichloromethane, and the organic phase was washed with saturated $NaHCO_3$ and brine, dried over anhydrous $MgSO_4$ and concentrated to give **4**. Afterwards, the Fmoc protecting group was removed by treating compound **4** with 5 mL of a piperidine/DMF 1:4 mixture during 30 min. After this time, the solvent was evaporated and the crude re-dissolved in 100 mL MeOH. The obtained solution was washed with heptane (5x100 mL) and concentrate to afford **5** (380 mg, 89% yield) as a sticky solid. HRMS (ESI+) Calculated Mass for $C_{67}H_{114}N_{13}O_{16}S_2$ $[M+H^+]$: 1420.7942. Found: 1420.7786.

Synthesis of PDI-2

HBTU (64 mg, 0.17 mmol, 2.4 eq) and DIPEA (125 µL, 0.72 mmol, 9 eq) were added to a solution of **1** (38 mg, 0.07 mmol, 1 eq) in 8 mL DMF under N_2 atm. After 5 min, **5** (220 mg, 0.15 mmol, 2.2 eq) dissolved in 4 mL DMF was added and the reaction mixture was left stirring overnight. The reaction was quenched by the addition of 50 mL dichloromethane, and the organic phase was washed with saturated $NaHCO_3$ and brine, dried over anhydrous $MgSO_4$ and concentrated. The reaction crude was purified by flash chromatography using CH_2Cl_2/MeOH (gradient from 100:0 to 80:20) as eluent to give **6**. Finally, the deprotection of the side chain protecting groups were carried out under strong acid conditions by treatment with TFA/H_2O, 9/1(4 mL) for 4h. The latter solution was poured into 70 mL of diethyl ether resulting in the precipitation of a red solid, that was filtered, washed with diethyl ether, and dried affording **PDI-2** (75 mg, 40%). ^{1}H NMR (400 MHz, D_2O) δ 8.14 (m, 6H), 5.65 (s, 2H), 4.36 (m, 10H), 4.00 – 3.51 (m, 24H), 3.38 (m, 18H), 1.62 (m, 48H), 0.91 (m, 28H), 0.46 (s, 4H). HRMS (ESI$^+$) for $C_{104}H_{164}N_{28}O_{26}$ [M+4H$^+$]: calculated 555.3087; found: 555.3115. [M+3H$^+$]: calculated 740.0759; found: 740.0778. [M+2H$^+$]: calculated 1109.6102; found: 1109.6053.

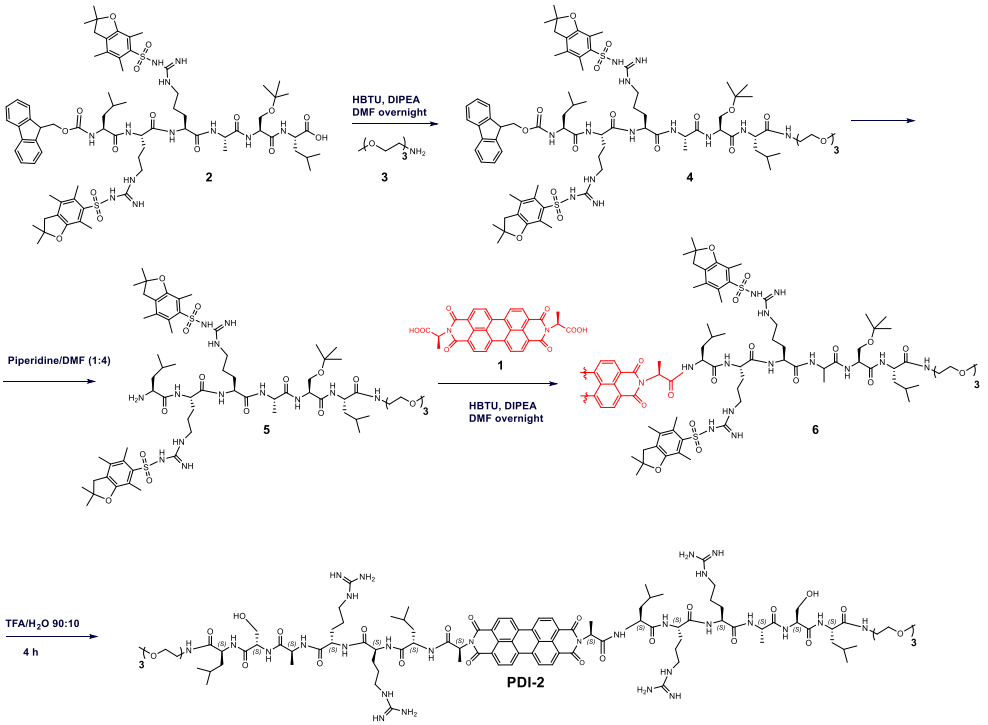

Figure 4.16. Target molecule PDI-2. Preparation of the final target **PDI-2**. Reproduced from ref. *** (see page 79) with permission from Nature Research.

4.10. References

1. Goodsell, D. S. *The Machinery of Life*. (Springer Science & Business Media, 2009).
2. Epstein, I. R. & Xu, B. Reaction-diffusion processes at the nano- and microscales. *Nat. Nanotechnol.* **11,** 312–319 (2016).
3. Rogers, K. *The Cell*. (The Rosen Publishing Group, 2011).
4. Alberts, B. *et al. Molecular Biology of the Cell*. (Garland Science, 2002).
5. Ernster, L. & Schatz, G. Mitochondria: a historical review. *J. Cell Biol.* **91,** 227s–255s (1981).
6. Hunter, T. Protein kinases and phosphatases: The Yin and Yang of protein phosphorylation and signaling. *Cell* **80,** 225–236 (1995).
7. D. R. A. H. (Ph, Harvey, R. A. & Ferrier, D. R. *Biochemistry*. (Lippincott Williams & Wilkins, 2011).
8. Garrett, R. H. & Grisham, C. M. *Biochemistry*. (Cengage Learning, 2016).
9. Kandel, E. *Principles of Neural Science, Fifth Edition*. (McGraw Hill Professional, 2013).
10. Widmaier, E. P., Raff, H., Vander, A. J. & Strang, K. T. *Vander's Human Physiology: The Mechanisms of Body Function*. (McGraw-Hill, 2011).
11. McNeil, C. *Alzheimer's Disease*. (DIANE Publishing, 1997).
12. Boekhoven, J. *et al.* Dissipative Self-Assembly of a Molecular Gelator by Using a Chemical Fuel. *Angew. Chem.* **122,** 4935–4938 (2010).
13. Boekhoven, J., Hendriksen, W. E., Koper, G. J. M., Eelkema, R. & Esch, J. H. van. Transient assembly of active materials fueled by a chemical reaction. *Science* **349,** 1075–1079 (2015).
14. Webber, M. J., Newcomb, C. J., Bitton, R. & Stupp, S. I. Switching of self-assembly in a peptide nanostructure with a specific enzyme. *Soft Matter* **7,** 9665 (2011).
15. Debnath, S., Roy, S. & Ulijn, R. V. Peptide Nanofibers with Dynamic Instability through Nonequilibrium Biocatalytic Assembly. *J. Am. Chem. Soc.* **135,** 16789–16792 (2013).
16. Yang, Z., Liang, G., Wang, L. & Xu, B. Using a Kinase/Phosphatase Switch to Regulate a Supramolecular Hydrogel and Forming the Supramolecular Hydrogel in Vivo. *J. Am. Chem. Soc.* **128,** 3038–3043 (2006).
17. Hirst, A. R. *et al.* Biocatalytic induction of supramolecular order. *Nat. Chem.* **2,** 1089–1094 (2010).
18. Kumar, M. *et al.* A dynamic supramolecular polymer with stimuli-responsive handedness for *in situ* probing of enzymatic ATP hydrolysis. *Nat. Commun.* **5,** 6793 (2014).
19. Pezzato, C. & Prins, L. J. Transient signal generation in a self-assembled nanosystem fueled by ATP. *Nat. Commun.* **6,** 7790 (2015).
20. Maiti, S., Fortunati, I., Ferrante, C., Scrimin, P. & Prins, L. J. Dissipative self-assembly of vesicular nanoreactors. *Nat. Chem.* **8,** 725–731 (2016).
21. Dhiman, S., Jain, A. & George, S. J. Transient Helicity: Fuel-Driven Temporal Control over Conformational Switching in a Supramolecular Polymer. *Angew. Chem.* **129,** 1349–1353 (2017).
22. Wood, C. S., Browne, C., Wood, D. M. & Nitschke, J. R. Fuel-Controlled Reassembly of Metal–Organic Architectures. *ACS Cent. Sci.* **1,** 504–509 (2015).
23. Kemp, B. E. & Pearson, R. B. Protein kinase recognition sequence motifs. *Trends Biochem. Sci.* **15,** 342–346 (1990).
24. Ku, T.-H. *et al.* Controlling and Switching the Morphology of Micellar Nanoparticles with Enzymes. *J. Am. Chem. Soc.* **133,** 8392–8395 (2011).
25. Görl, D., Zhang, X. & Würthner, F. Molecular Assemblies of Perylene Bisimide Dyes in Water. *Angew. Chem. Int. Ed.* **51,** 6328–6348 (2012).
26. Würthner, F. *et al.* Perylene Bisimide Dye Assemblies as Archetype Functional Supramolecular Materials. *Chem. Rev.* **116,** 962–1052 (2016).
27. Mattia, E. & Otto, S. Supramolecular systems chemistry. *Nat. Nanotechnol.* **10,** 111–119 (2015).
28. Urban, M. W. *Handbook of Stimuli-Responsive Materials*. (John Wiley & Sons, 2011).
29. Seibt, J. *et al.* On the geometry dependence of molecular dimer spectra with an application to aggregates of perylene bisimide. *Chem. Phys.* **328,** 354–362 (2006).
30. Görl, D. & Würthner, F. Entropically Driven Self-Assembly of Bolaamphiphilic Perylene Dyes in Water. *Angew. Chem. Int. Ed.* **128,** 12273–12277 (2016).

31. De Greef, T. F. A. *et al.* Supramolecular Polymerization. *Chem. Rev.* **109,** 5687–5754 (2009).
32. Smulders, M. M. J. *et al.* How to Distinguish Isodesmic from Cooperative Supramolecular Polymerisation. *Chem. Eur. J.* **16,** 362–367 (2010).
33. Zhang, X., Görl, D., Stepanenko, V. & Würthner, F. Hierarchical Growth of Fluorescent Dye Aggregates in Water by Fusion of Segmented Nanostructures. *Angew. Chem. Int. Ed.* **53,** 1270–1274 (2014).
34. Würthner, F. *et al.* Supramolecular p−n-Heterojunctions by Co-Self-Organization of Oligo(p-phenylene Vinylene) and Perylene Bisimide Dyes. *J. Am. Chem. Soc.* **126,** 10611–10618 (2004).
35. Rehm, T. H. *et al.* Interaction of spermine-alanine functionalized perylene bisimide dye aggregates with ds-DNA/RNA secondary structure. *Chem. Sci.* **3,** 3393 (2012).
36. Berova, N., Nakanishi, K. & Woody, R. *Circular Dichroism: Principles and Applications*. (John Wiley & Sons, 2000).
37. Onogi, S. *et al.* In situ real-time imaging of self-sorted supramolecular nanofibres. *Nat. Chem.* **8,** 743–752 (2016).
38. Hirst, A. R., Huang, B., Castelletto, V., Hamley, I. W. & Smith, D. K. Self-Organisation in the Assembly of Gels from Mixtures of Different Dendritic Peptide Building Blocks. *Chem. Eur. J.* **13,** 2180–2188 (2007).
39. Sims, P. C. *et al.* Electronic Measurements of Single-Molecule Catalysis by cAMP-Dependent Protein Kinase A. *J. Am. Chem. Soc.* **135,** 7861–7868 (2013).
40. Lew, J., Taylor, S. S. & Adams, J. A. Identification of a Partially Rate-Determining Step in the Catalytic Mechanism of cAMP-Dependent Protein Kinase: A Transient Kinetic Study Using Stopped-Flow Fluorescence Spectroscopy. *Biochemistry (Mosc.)* **36,** 6717–6724 (1997).
41. Reiter, N. J., White, D. J. & Rusnak, F. Inhibition of Bacteriophage λ Protein Phosphatase by Organic and Oxoanion Inhibitors. *Biochemistry (Mosc.)* **41,** 1051–1059 (2002).
42. Reece, J. B. *Campbell Biology*. (Benjamin Cummings / Pearson, 2011).
43. Atkins, P. & Paula, J. de. *Atkins' Physical Chemistry*. (OUP Oxford, 2014).
44. Kondepudi, D. & Prigogine, I. *Modern Thermodynamics: From Heat Engines to Dissipative Structures*. (Wiley, 2014).
45. Isidro-Llobet, A., Álvarez, M. & Albericio, F. Amino Acid-Protecting Groups. *Chem. Rev.* **109,** 2455–2504 (2009).
46. Scherman, O. A., Ligthart, G. B. W. L., Ohkawa, H., Sijbesma, R. P. & Meijer, E. W. Olefin metathesis and quadruple hydrogen bonding: A powerful combination in multistep supramolecular synthesis. *Proc. Natl. Acad. Sci.* **103,** 11850–11855 (2006).
47. Adams, J. A. Kinetic and Catalytic Mechanisms of Protein Kinases. *Chem. Rev.* **101,** 2271–2290 (2001).
48. Whitehouse, S., Feramisco, J. R., Casnellie, J. E., Krebs, E. G. & Walsh, D. A. Studies on the kinetic mechanism of the catalytic subunit of the cAMP-dependent protein kinase. *J. Biol. Chem.* **258,** 3693–3701 (1983).
49. Zhuo, S., Clemens, J. C., Hakes, D. J., Barford, D. & Dixon, J. E. Expression, purification, crystallization, and biochemical characterization of a recombinant protein phosphatase. *J. Biol. Chem.* **268,** 17754–17761 (1993).

4.11. Appendix

4.11.1. Overview of the enzyme controlled supramolecular polymerization

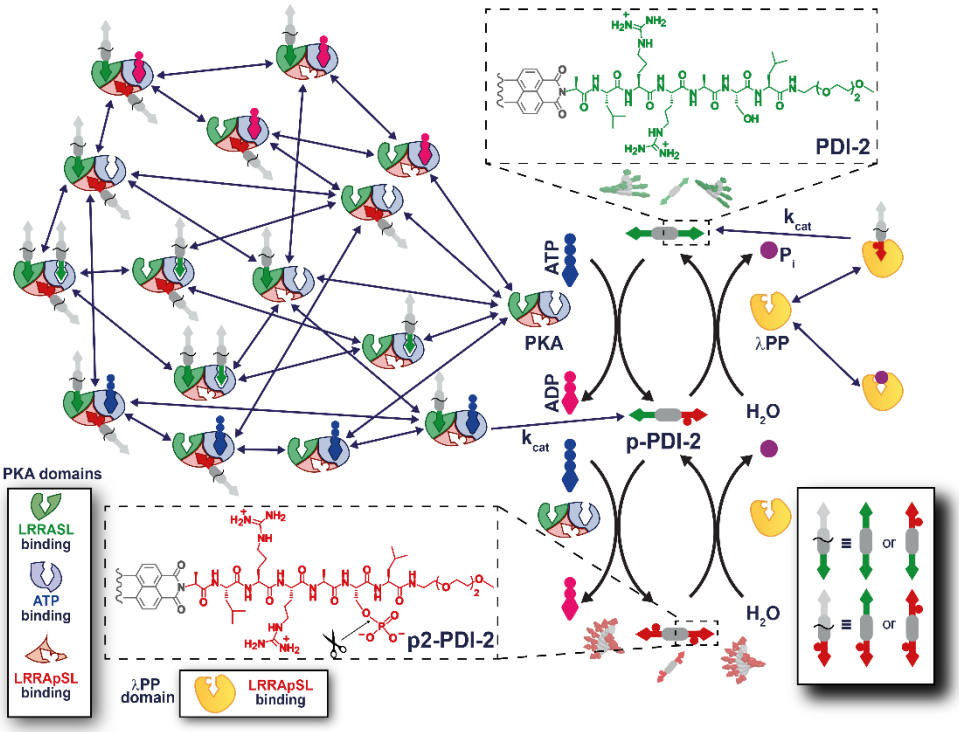

Figure 4.17. General overview of the biomimetic enzyme-controlled supramolecular system. The self-assembling peptide-perylenediimide derivative **PDI-2** (half molecule is shown) can be phosphorylated on the serine residue by Protein Kinase A (PKA) to give monophosphorylated **p-PDI-2**, and further diphosphorylated **p2-PDI-2**, fueled by ATP to ADP hydrolysis (one eq. per phosphate introduced). Diphosphorylated **p2-PDI-2** can in turn be dephosphorylated back to give **PDI-2** (scissors) by Lambda Protein Phosphatase (λPP), which yields inorganic phosphate Pi as waste. The two enzymes work simultaneously, so that the chemical composition of the solution (molar fraction of **PDI-2**, **p-PDI-2**, and **p2-PDI-2**) is determined by the rates of competing phosphorylation and dephosphorylation pathways, but not by chemical equilibrium. This allowed us to push the system into dissipative non-equilibrium steady states (NESS), when working in a membrane reactor, i.e. open system (cfr. Figure 4.12). A schematic representation of the enzyme network(s) is reported. The nodes in the PKA (and λPP) network represent the enzyme-substrate complexes. The edges (double-headed arrows) represent the binding reactions. PKA has three binding sites: i) for ATP (blue), ii) for the LRRASL peptide (green), and iii) for LRRApSL (red). Both **PDI-2** and **p2-PDI-2** self-assemble to give supramolecular polymers with different structure and stability (see main text). Reproduced from ref. *** (see page 79) with permission from Nature Research.

4.11.2. Phosphorylation of PDI-2 using PKA

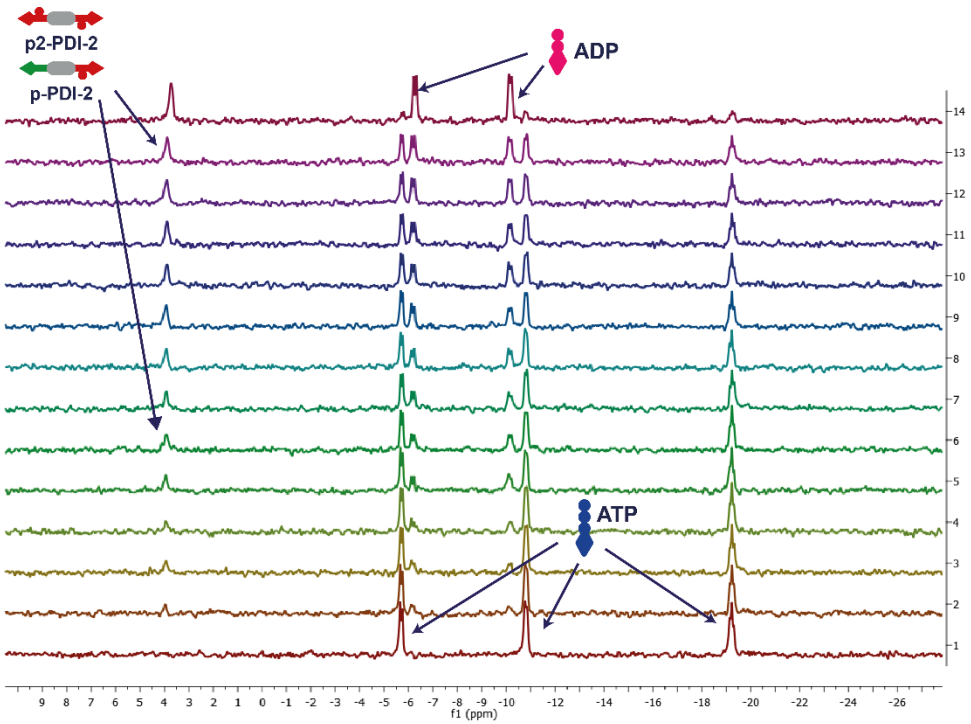

Figure 4.18. NMR experiments. ^{31}P-NMR spectra recorded each 10 min during the phosphorylation of a 0.5 mM **PDI-2** solution in Tris buffer (+ 20% D_2O) in the presence of ATP (1 mM, 2 eq.), triggered by the addition of PKA (0.04 μM). The peak of phosphoserine (LRRApSL in both **p-PDI-2**, and **p2-PDI-2**) increases with time, along with the clear conversion of ATP to ADP. Reproduced from ref. *** (see page 79) with permission from Nature Research.

4.11.3. AFM and TEM images

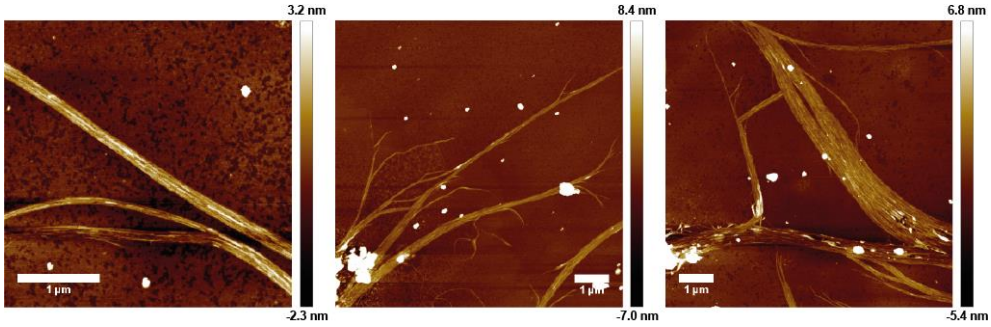

Figure 4.19. Further AFM experiments. AFM images of **p2-PDI-2** aggregates on mica. The sample was prepared by diluting 100 times a 200 μM solution of **p2-PDI-2** in the reaction buffer with MQ water, followed by drop casting on mica. Reproduced from ref. *** (see page 79) with permission from Nature Research.

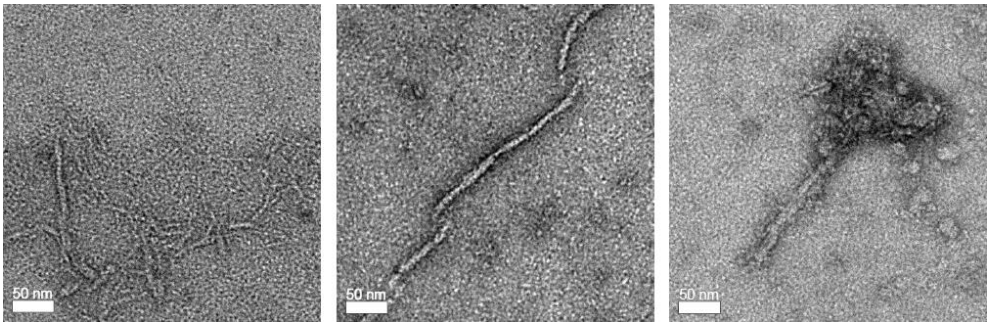

Figure 4.20. TEM experiments. TEM images of **p2-PDI-2** assemblies adsorbed on a carbon film and negatively stained with a 2% uranyl acetate solution. The specimen was adsorbed for 90 min on a small piece of carbon partially floated off a mica sheet at the surface of a Teflon well containing 37 μL of a 80 μM **p2-PDI-2** solution in the reaction buffer. The carbon film was then transferred on an EM copper grid covered by a perforated carbon film (homemade holey grid). Reproduced from ref. *** (see page 79) with permission from Nature Research.

4.11.4. Self-sorting experiments

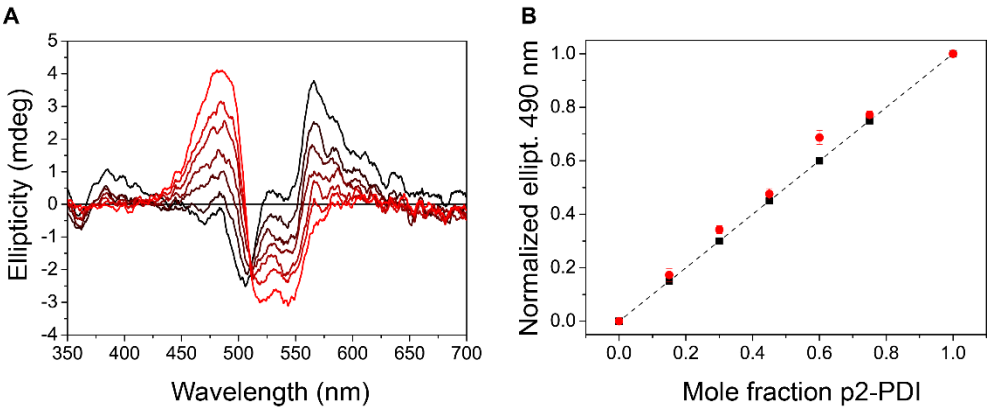

Figure 4.21. Self-sorting experiments. (A) CD spectra of **PDI-2**/**p2-PDI-2** mixtures at different molar ratios from 0:1 (i.e. pure PDI, black spectrum) to 1:0 (i.e. pure **p2-PDI-2**, light red spectrum), at a total concentration (**PDI-2** + **p2-PDI-2**) of 200 μM in the reaction buffer (optical path 1mm). (B) Normalized CD intensities at 490 nm, extracted by the CD spectra in panel a, plotted versus the corresponding molar fraction of **p2-PDI-2** (red circles). The data represent the average and standard deviation (error bars) calculated from two independent experiments. The dashed black line represents the theoretical values of the CD intensity at 490 nm as a function of the mixture composition for a completely self-sorted system (i.e. calculated as linear combination of the CD intensities of each component weighted on the corresponding molar fractions). The black squares highlight the theoretical value of the CD intensity at 490 nm for the specific compositions we investigated experimentally. Reproduced from ref. *** (see page 79) with permission from Nature Research.

The samples for the self-sorting experiments were prepared by mixing different volumes of 200 μM **PDI-2** and **p2-PDI-2** solutions in the reaction buffer. **p2-PDI-2** was previously prepared by phosphorylation triggered by ATP (400 μM, 2 eq.) and PKA (0.065 μM). The mixed samples were incubated for 10 min at room temperature before the CD measurements. No changes of the spectra were observed for longer incubation times (e.g., overnight).

4.11.5. Mathematical modelling of the enzyme network

Description of the model

A set of ordinary differential equation ODEs describing the network formed by the two enzymes Protein Kinase A (PKA) and Lambda Protein Phosphatase (λPP) was built using mass action kinetics. The enzyme PKA catalyses the transfer of the gamma phosphate of ATP to the LRRASL sequence (e.g. present in **PDI-2** and **p-PDI-2**) giving ADP and the phosphorylated peptide LRRApSL (i.e. **p-PDI-2** or **p2-PDI-2**) as products. PKA is modelled as "exiy" (Figure 4.22), where "x" represents the binding site for ATP, "y" is that for LRRASL, and "i" is the binding site for non-competitive inhibitors.

λPP is a Mn^{2+}-dependent protein phosphatase that catalyses the cleavage of the phosphate group from phosphorylated serine (e.g. present in **p-PDI-2** or **p2-PDI-2**), giving non-phosphorylated peptide (i.e. **PDI-2**) and inorganic phosphate (Pi) as products. The latter involve a single-substrate mechanism, so we modelled λPP as "px" (Figure 4.22), where "x" represents the binding site for the phosphopeptide. The model takes into account:

1) A random sequential BiBi kinetic mechanism for PKA, in which both the substrates (ATP and LRRASL) bind, in no obligatory order, before the products are released.[47]
2) The presence of two (de)phosphorylation sites in each **PDI-2** molecule (Figure 4.22)
3) The competitive (substrate) inhibition by LRRASL (present in **PDI-2** and **p-PDI-2**) that can bind to PKA's site for ATP (Figure 4.22, green arrow in blue pocket, "ebiy", "eqiy", "ebqy", "ebry", "ebib", "ebiq", "eqqy", "eqry", "eqib", "eqiq", "ebqb", "ebqq", "ebrb", "ebrq", "eqqb", "eqqq", "eqrb", "ebrq").
4) The competitive (product) inhibition by ADP that can bind to the PKA's site for ATP[48] (Figure 4.22, ADP in the blue pocket, "epiy", "epqy", "epry", "epib", "epiq", "epqb", "epqq", "eprb", "eprq").
5) The noncompetitive (product) inhibition by LRRApSL (present in **p-PDI-2** and **p2-PDI-2**) that can bind to PKA's site for non-competitive inhibitors[48] (Figure 4.22, red arrow in red pocket, "exqy", "exry", "eaqy", "eary", "ebqy", "ebry", "epqy", "epry", "eqqy", "eqry", "exqb", "exqq", "exrb", "exrq", "eaqb", "eaqq", "earb", "earq", "ebqb", "ebqq", "ebrb", "ebrq", "epqb", "epqq", "eprb", "eprq", "eqqb", "eqqq", "eqrb", "eqrq").
6) A single-substrate mechanism, for λPP.
7) The competitive (product) inhibition by Pi that can bind to the λPP's site for the phosphopeptide,[41] (Figure 4.22, "pk").
8) λPP does not feature any ATP hydrolytic activity.[49]

The latter results in a network of 55 chemical species (including free enzymes, substrates and products, and the various enzyme-substrate complexes) that are depicted in Figure 4.22. In Table 4.2 the binding equilibria and the conversion reactions, i.e. the edges of the network, are reported together with the corresponding rate equations based on mass-action kinetics. From the latter, the 55 ODEs describing the enzyme network (i.e. one for each species) were derived as reported in Table 4.3. The set of ODEs were implemented in MATLAB and integrated numerically, using available solvers, in order to obtain the temporal evolution of the concentration of all the species, starting from a set of initial conditions that correspond to the experimental conditions to simulate.

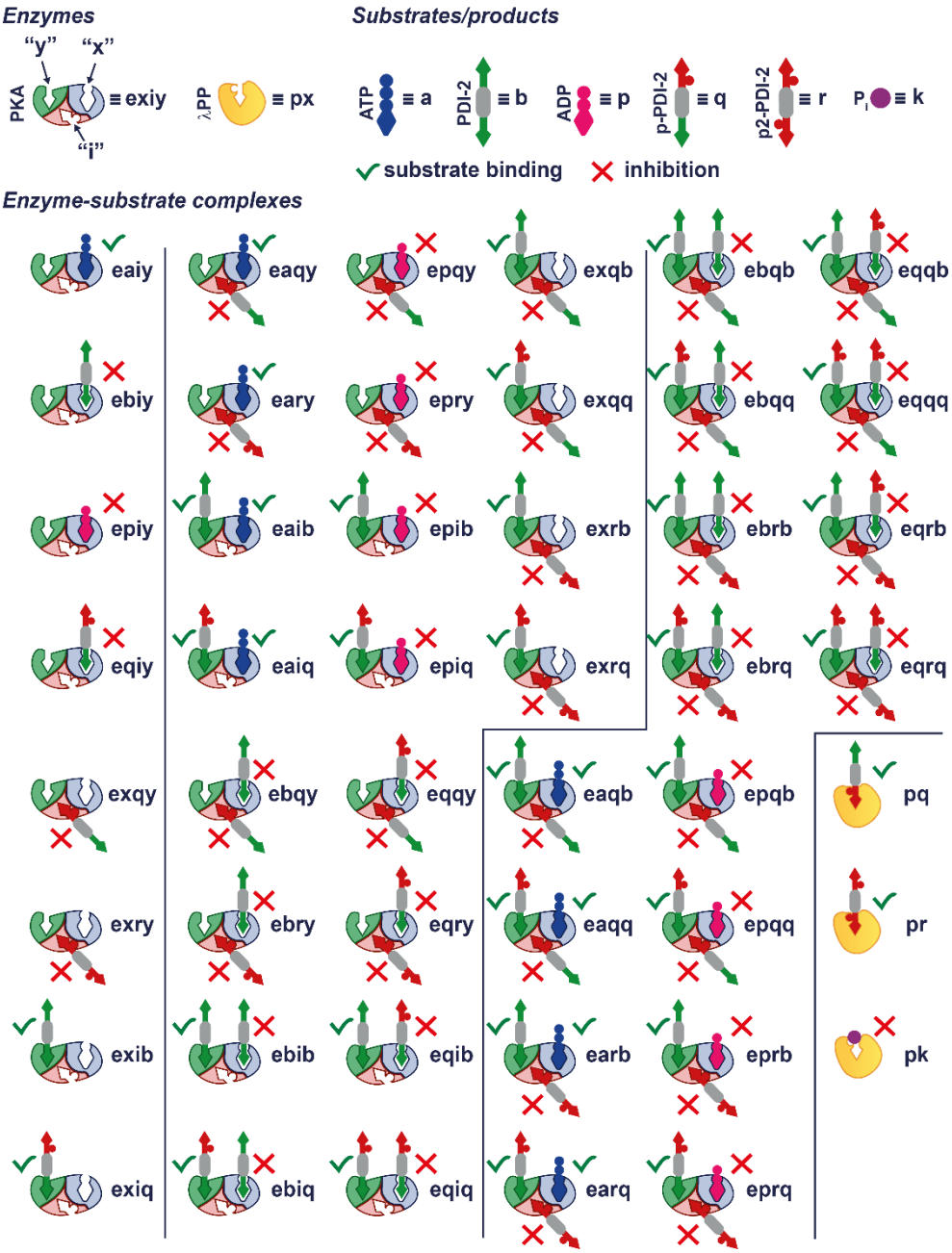

Figure 4.22. Overview of the species comprising the enzyme network (the nodes). The latter include: free enzymes, substrates and products, and the enzyme-substrate complexes. PKA has three binding sites: "x" for ATP (blue), "y" is that for LRRASL, and "i" for non-competitive inhibitor LRRApSL (red). The PKA enzyme-substrate complexes can have one (first column), two (second column) or three (third column) binding sites occupied. The green ticks indicate the substrate binding, the red crosses indicate the binding of inhibitors. Reproduced from ref. *** (see page 79) with permission from Nature Research.

Table 4.2. Reaction network. Overview of the involved binding and conversion reactions with the corresponding rate equations based on mass action kinetics.

Reaction	Rate equation
Zero binding (PKA)	
1) $exiy + a \rightleftarrows eaiy$	$R1 = kiaf * c\_exiy * c\_a - kiar * c\_eaiy$
2) $exiy + b \rightleftarrows ebiy$	$R2 = ksibf * c\_exiy * c\_b - ksibr * c\_ebiy$
3) $exiy + p \rightleftarrows epiy$	$R3 = kpipf * c\_exiy * c\_p - kpipr * c\_epiy$
4) $exiy + q \rightleftarrows eqiy$	$R4 = ksiqf * c\_exiy * c\_q - ksiqr * c\_eqiy$
5) $exiy + q \rightleftarrows exqy$	$R5 = kncqf * c\_exiy * c\_q - kncqr * c\_exqy$
6) $exiy + r \rightleftarrows exry$	$R6 = kncrf * c\_exiy * c\_r - kncrr * c\_exry$
7) $exiy + b \rightleftarrows exib$	$R7 = kibf * c\_exiy * c\_b - kibr * c\_exib$
8) $exiy + q \rightleftarrows exiq$	$R8 = kiqf * c\_exiy * c\_q - kiqr * c\_exiq$
One binding (PKA)	
9) $eaiy + q \rightleftarrows eaqy$	$R9 = kncqf * c\_eaiy * c\_q - kncqr * c\_eaqy$
10) $eaiy + r \rightleftarrows eary$	$R10 = kncrf * c\_eaiy * c\_r - kncrr * c\_eary$
11) $eaiy + b \rightleftarrows eaib$	$R11 = kbf * c\_eaiy * c\_b - kbr * c\_eaib$
12) $eaiy + q \rightleftarrows eaiq$	$R12 = kqf * c\_eaiy * c\_q - kqr * c\_eaiq$
13) $ebiy + q \rightleftarrows ebqy$	$R13 = kncqf * c\_ebiy * c\_q - kncqr * c\_ebqy$
14) $ebiy + r \rightleftarrows ebry$	$R14 = kncrf * c\_ebiy * c\_r - kncrr * c\_ebry$
15) $ebiy + b \rightleftarrows ebib$	$R15 = kbf * c\_ebiy * c\_b - kbr * c\_ebib$
16) $ebiy + q \rightleftarrows ebiq$	$R16 = kqf * c\_ebiy * c\_q - kqr * c\_ebiq$
17) $epiy + q \rightleftarrows epqy$	$R17 = kncqf * c\_epiy * c\_q - kncqr * c\_epqy$
18) $epiy + r \rightleftarrows epry$	$R18 = kncrf * c\_epiy * c\_r - kncrr * c\_epry$
19) $epiy + b \rightleftarrows epib$	$R19 = kbf * c\_epiy * c\_b - kbr * c\_epib$
20) $epiy + q \rightleftarrows epiq$	$R20 = kqf * c\_epiy * c\_q - kqr * c\_epiq$
21) $eqiy + q \rightleftarrows eqqy$	$R21 = kncqf * c\_eqiy * c\_q - kncqr * c\_eqqy$
22) $eqiy + r \rightleftarrows eqry$	$R22 = kncrf * c\_eqiy * c\_r - kncrr * c\_eqry$
23) $eqiy + b \rightleftarrows eqib$	$R23 = kbf * c\_eqiy * c\_b - kbr * c\_eqib$
24) $eqiy + q \rightleftarrows eqiq$	$R24 = kqf * c\_eqiy * c\_q - kqr * c\_eqiq$
25) $exqy + a \rightleftarrows eaqy$	$R25 = kiaf * c\_exqy * c\_a - kiar * c\_eaqy$
26) $exqy + b \rightleftarrows ebqy$	$R26 = ksibf * c\_exqy * c\_b - ksibr * c\_ebqy$
27) $exqy + p \rightleftarrows epqy$	$R27 = kpipf * c\_exqy * c\_p - kpipr * c\_epqy$
28) $exqy + q \rightleftarrows eqqy$	$R28 = ksiqf * c\_exqy * c\_q - ksiqr * c\_eqqy$
29) $exqy + b \rightleftarrows exqb$	$R29 = kibf * c\_exqy * c\_b - kibr * c\_exqb$
30) $exqy + q \rightleftarrows exqq$	$R30 = kiqf * c\_exqy * c\_q - kiqr * c\_exqq$
31) $exry + a \rightleftarrows eary$	$R31 = kiaf * c\_exry * c\_a - kiar * c\_eary$
32) $exry + b \rightleftarrows ebry$	$R32 = ksibf * c\_exry * c\_b - ksibr * c\_ebry$
33) $exry + p \rightleftarrows epry$	$R33 = kpipf * c\_exry * c\_p - kpipr * c\_epry$
34) $exry + q \rightleftarrows eqry$	$R34 = ksiqf * c\_exry * c\_q - ksiqr * c\_eqry$
35) $exry + b \rightleftarrows exrb$	$R35 = kibf * c\_exry * c\_b - kibr * c\_exrb$

36) $exry + q \rightleftarrows exrq$	$R36 = kiqf*c\_exry*c\_q - kiqr*c\_exrq$
37) $exib + a \rightleftarrows eaib$	$R37 = kaf*c\_exib*c\_a - kar*c\_eaib$
38) $exib + b \rightleftarrows ebib$	$R38 = ksibf*c\_exib*c\_b - ksibr*c\_ebib$
39) $exib + p \rightleftarrows epib$	$R39 = kpipf*c\_exib*c\_p - kpipr*c\_epib$
40) $exib + q \rightleftarrows eqib$	$R40 = ksiqf*c\_exib*c\_q - ksiqr*c\_eqib$
41) $exib + q \rightleftarrows exqb$	$R41 = kncqf*c\_exib*c\_q - kncqr*c\_exqb$
42) $exib + r \rightleftarrows exrb$	$R42 = kncrf*c\_exib*c\_r - kncrr*c\_exrb$
43) $exiq + a \rightleftarrows eaiq$	$R43 = kaf*c\_exiq*c\_a - kar*c\_eaiq$
44) $exiq + b \rightleftarrows ebiq$	$R44 = ksibf*c\_exiq*c\_b - ksibr*c\_ebiq$
45) $exiq + p \rightleftarrows epiq$	$R45 = kpipf*c\_exiq*c\_p - kpipr*c\_epiq$
46) $exiq + q \rightleftarrows eqiq$	$R46 = ksiqf*c\_exiq*c\_q - ksiqr*c\_eqiq$
47) $exiq + q \rightleftarrows exqq$	$R47 = kncqf*c\_exiq*c\_q - kncqr*c\_exqq$
48) $exiq + r \rightleftarrows exrq$	$R48 = kncrf*c\_exiq*c\_r - kncrr*c\_exrq$
Two binding (PKA)	
49) $eaqy + b \rightleftarrows eaqb$	$R49 = kbf*c\_eaqy*c\_b - kbr*c\_eaqb$
50) $eaqy + q \rightleftarrows eaqq$	$R50 = kqf*c\_eaqy*c\_q - kqr*c\_eaqq$
51) $eary + b \rightleftarrows earb$	$R51 = kbf*c\_eary*c\_b - kbr*c\_earb$
52) $eary + q \rightleftarrows earq$	$R52 = kqf*c\_eary*c\_q - kqr*c\_earq$
53) $ebqy + b \rightleftarrows ebqb$	$R53 = kbf*c\_ebqy*c\_b - kbr*c\_ebqb$
54) $ebqy + q \rightleftarrows ebqq$	$R54 = kqf*c\_ebqy*c\_q - kqr*c\_ebqq$
55) $ebry + b \rightleftarrows ebrb$	$R55 = kbf*c\_ebry*c\_b - kbr*c\_ebrb$
56) $ebry + q \rightleftarrows ebrq$	$R56 = kqf*c\_ebry*c\_q - kqr*c\_ebrq$
57) $epqy + b \rightleftarrows epqb$	$R57 = kbf*c\_epqy*c\_b - kbr*c\_epqb$
58) $epqy + q \rightleftarrows epqq$	$R58 = kqf*c\_epqy*c\_q - kqr*c\_epqq$
59) $epry + b \rightleftarrows eprb$	$R59 = kbf*c\_epry*c\_b - kbr*c\_eprb$
60) $epry + q \rightleftarrows eprq$	$R60 = kqf*c\_epry*c\_q - kqr*c\_eprq$
61) $eqqy + b \rightleftarrows eqqb$	$R61 = kbf*c\_eqqy*c\_b - kbr*c\_eqqb$
62) $eqqy + q \rightleftarrows eqqq$	$R62 = kqf*c\_eqqy*c\_q - kqr*c\_eqqq$
63) $eqry + b \rightleftarrows eqrb$	$R63 = kbf*c\_eqry*c\_b - kbr*c\_eqrb$
64) $eqry + q \rightleftarrows eqrq$	$R64 = kqf*c\_eqry*c\_q - kqr*c\_eqrq$
65) $eaib + q \rightleftarrows eaqb$	$R65 = kncqf*c\_eaib*c\_q - kncqr*c\_eaqb$
66) $eaib + r \rightleftarrows earb$	$R66 = kncrf*c\_eaib*c\_r - kncrr*c\_earb$
67) $eaiq + q \rightleftarrows eaqq$	$R67 = kncqf*c\_eaiq*c\_q - kncqr*c\_eaqq$
68) $eaiq + r \rightleftarrows earq$	$R68 = kncrf*c\_eaiq*c\_r - kncqr*c\_earq$
69) $ebib + q \rightleftarrows ebqb$	$R69 = kncqf*c\_ebib*c\_q - kncqr*c\_ebqb$
70) $ebib + r \rightleftarrows ebrb$	$R70 = kncrf*c\_ebib*c\_r - kncrr*c\_ebrb$
71) $ebiq + q \rightleftarrows ebqq$	$R71 = kncqf*c\_ebiq*c\_q - kncqr*c\_ebqq$
72) $ebiq + r \rightleftarrows ebrq$	$R72 = kncrf*c\_ebiq*c\_r - kncrr*c\_ebrq$
73) $epib + q \rightleftarrows epqb$	$R73 = kncqf*c\_epib*c\_q - kncqr*c\_epqb$
74) $epib + r \rightleftarrows eprb$	$R74 = kncrf*c\_epib*c\_r - kncrr*c\_eprb$

75) $epiq + q \rightleftarrows epqq$	$R75 = kncqf * c\_epiq * c\_q - kncqr * c\_epqq$
76) $epiq + r \rightleftarrows eprq$	$R76 = kncrf * c\_epiq * c\_r - kncrr * c\_eprq$
77) $eqib + q \rightleftarrows eqqb$	$R77 = kncqf * c\_eqib * c\_q - kncqr * c\_eqqb$
78) $eqib + r \rightleftarrows eqrb$	$R78 = kncrf * c\_eqib * c\_r - kncrr * c\_eqrb$
79) $eqiq + q \rightleftarrows eqqq$	$R79 = kncqf * c\_eqiq * c\_q - kncqr * c\_eqqq$
80) $eqiq + r \rightleftarrows eqrq$	$R80 = kncrf * c\_eqiq * c\_r - kncrr * c\_eqrq$
81) $exqb + a \rightleftarrows eaqb$	$R81 = kaf * c\_exqb * c\_a - kar * c\_eaqb$
82) $exqb + b \rightleftarrows ebqb$	$R82 = ksibf * c\_exqb * c\_b - ksibr * c\_ebqb$
83) $exqb + p \rightleftarrows epqb$	$R83 = kpipf * c\_exqb * c\_p - kpipr * c\_epqb$
84) $exqb + q \rightleftarrows eqqb$	$R84 = ksiqf * c\_exqb * c\_q - ksiqr * c\_eqqb$
85) $exqq + a \rightleftarrows eaqq$	$R85 = kaf * c\_exqq * c\_a - kar * c\_eaqq$
86) $exqq + b \rightleftarrows ebqq$	$R86 = ksibf * c\_exqq * c\_b - ksibr * c\_ebqq$
87) $exqq + p \rightleftarrows epqq$	$R87 = kpipf * c\_exqq * c\_p - kpipr * c\_epqq$
88) $exqq + q \rightleftarrows eqqq$	$R88 = ksiqf * c\_exqq * c\_q - ksiqr * c\_eqqq$
89) $exrb + a \rightleftarrows earb$	$R89 = kaf * c\_exrb * c\_a - kar * c\_earb$
90) $exrb + b \rightleftarrows ebrb$	$R90 = ksibf * c\_exrb * c\_b - ksibr * c\_ebrb$
91) $exrb + p \rightleftarrows eprb$	$R91 = kpipf * c\_exrb * c\_p - kpipr * c\_eprb$
92) $exrb + q \rightleftarrows eqrb$	$R92 = ksiqf * c\_exrb * c\_q - ksiqr * c\_eqrb$
93) $exrq + a \rightleftarrows earq$	$R93 = kaf * c\_exrq * c\_a - kar * c\_earq$
94) $exrq + b \rightleftarrows ebrq$	$R94 = ksibf * c\_exrq * c\_b - ksibr * c\_ebrq$
95) $exrq + p \rightleftarrows eprq$	$R95 = kpipf * c\_exrq * c\_p - kpipr * c\_eprq$
96) $exrq + q \rightleftarrows eqrq$	$R96 = ksiqf * c\_exrq * c\_q - ksiqr * c\_eqrq$
Product formation (PKA)	
97) $eaib \rightarrow exiy + p + q$	$R97 = kcat * c\_eaib$
98) $eaiq \rightarrow exiy + p + r$	$R98 = kcat * c\_eaiq$
One binding (λPP)	
99) $px + q \rightleftarrows pq$	$R99 = kpqf * c\_px * c\_q - kpqr * c\_pq$
100) $px + r \rightleftarrows pr$	$R100 = kprf * c\_px * c\_r - kprr * c\_pr$
101) $px + k \rightleftarrows pk$	$R101 = kpikf * c\_px * c\_k - kpikr * c\_pk$
Product formation (λPP)	
102) $pq \rightarrow px + b + k$	$R102 = kcatp * c\_pq$
103) $pr \rightarrow px + q + k$	$R103 = kcatp * c\_pr$

Table 4.3. Differential equations. Overview of the differential equations describing the concentration versus time of the 55 species depicted in Figure 4.22. The rates R1-R103 are defined in Table 4.2.

Differential equations (ODEs)
$\frac{d[a]}{dt} = -R1 - R25 - R31 - R37 - R43 - R81 - R85 - R89 - R93$
$\frac{d[b]}{dt} = -R2 - R7 - R11 - R15 - R19 - R23 - R26 - R29 - R32 - R35 - R38 - R44 - R49 - R51 - R53$
$-R55 - R57 - R59 - R61 - R63 - R82 - R86 - R90 - R94 + R102$
$\frac{d[p]}{dt} = -R3 - R27 - R33 - R39 - R45 - R83 - R87 - R91 - R95 + R97 + R98$
$\frac{d[q]}{dt} = -R4 - R5 - R8 - R9 - R12 - R13 - R16 - R17 - R20 - R21 - R24 - R28 - R30 - R34 - R36$
$-R40 - R41 - R46 - R47 - R50 - R52 - R54 - R56 - R58 - R60 - R62 - R64 - R65 - R67 - R69$
$-R71 - R73 - R75 - R77 - R79 - R84 - R88 - R92 - R96 + R97 - R99 + R103$
$\frac{d[r]}{dt} = -R6 - R10 - R14 - R18 - R22 - R42 - R48 - R66 - R68 - R70 - R72 - R74 - R76 - R78$
$-R80 + R98 - R100$
$\frac{d[k]}{dt} = -R101 + R102 + R103$
$\frac{d[exiy]}{dt} = -R1 - R2 - R3 - R4 - R5 - R6 - R7 - R8 + R97 + R98$
$\frac{d[eaiy]}{dt} = +R1 - R9 - R10 - R11 - R12$
$\frac{d[ebiy]}{dt} = +R2 - R13 - R14 - R15 - R16$
$\frac{d[epiy]}{dt} = +R3 - R17 - R18 - R19 - R20$
$\frac{d[eqiy]}{dt} = +R4 - R21 - R22 - R23 - R24$
$\frac{d[exqy]}{dt} = +R5 - R25 - R26 - R27 - R28 - R29 - R30$
$\frac{d[exry]}{dt} = +R6 - R31 - R32 - R33 - R34 - R35 - R36$
$\frac{d[exib]}{dt} = +R7 - R37 - R38 - R39 - R40 - R41 - R42$
$\frac{d[exiq]}{dt} = +R8 - R43 - R44 - R45 - R46 - R47 - R48$
$\frac{d[eaqy]}{dt} = +R9 + R25 - R49 - R50$
$\frac{d[eary]}{dt} = +R10 + R31 - R51 - R52$

$$\frac{d[eaib]}{dt} = +R11 + R37 - R65 - R66 - R97$$

$$\frac{d[eaiq]}{dt} = +R12 + R43 - R67 - R68 - R98$$

$$\frac{d[ebqy]}{dt} = +R13 + R26 - R53 - R54$$

$$\frac{d[ebry]}{dt} = +R14 + R32 - R55 - R56$$

$$\frac{d[ebib]}{dt} = +R15 + R38 - R69 - R70$$

$$\frac{d[ebiq]}{dt} = +R16 + R44 - R71 - R72$$

$$\frac{d[epqy]}{dt} = +R17 + R27 - R57 - R58$$

$$\frac{d[epry]}{dt} = +R18 + R33 - R59 - R60$$

$$\frac{d[epib]}{dt} = +R19 + R39 - R73 - R74$$

$$\frac{d[epiq]}{dt} = +R20 + R45 - R75 - R76$$

$$\frac{d[eqqy]}{dt} = +R21 + R28 - R61 - R62$$

$$\frac{d[eqry]}{dt} = +R22 + R34 - R63 - R64$$

$$\frac{d[eqib]}{dt} = +R23 + R40 - R77 - R78$$

$$\frac{d[eqiq]}{dt} = +R24 + R46 - R79 - R80$$

$$\frac{d[exqb]}{dt} = +R29 + R41 - R81 - R82 - R83 - R84$$

$$\frac{d[exqq]}{dt} = +R30 + R47 - R85 - R86 - R87 - R88$$

$$\frac{d[exrb]}{dt} = +R35 + R42 - R89 - R90 - R91 - R92$$

$$\frac{d[exrq]}{dt} = +R36 + R48 - R93 - R94 - R95 - R96$$

$$\frac{d[eaqb]}{dt} = +R49 + R65 + R81$$

$$\frac{d[eaqq]}{dt} = +R50 + R67 + R85$$

$$\frac{d[earb]}{dt} = +R51 + R66 + R89$$

$$\frac{d[earq]}{dt} = +R52 + R68 + R93$$

$$\frac{d[ebqb]}{dt} = +R53 + R69 + R82$$

$$\frac{d[ebqq]}{dt} = +R54 + R71 + R86$$

$$\frac{d[ebrb]}{dt} = +R55 + R70 + R90$$

$$\frac{d[ebrq]}{dt} = +R56 + R72 + R94$$

$$\frac{d[epqb]}{dt} = +R57 + R73 + R83$$

$$\frac{d[epqq]}{dt} = +R58 + R75 + R87$$

$$\frac{d[eprb]}{dt} = +R59 + R74 + R91$$

$$\frac{d[eprq]}{dt} = +R60 + R76 + R95$$

$$\frac{d[eqqb]}{dt} = +R61 + R77 + R84$$

$$\frac{d[eqqq]}{dt} = +R62 + R79 + R88$$

$$\frac{d[eqrb]}{dt} = +R63 + R78 + R92$$

$$\frac{d[eqrq]}{dt} = +R64 + R80 + R96$$

$$\frac{d[px]}{dt} = -R99 - R100 - R101 + R102 + R103$$

$$\frac{d[pq]}{dt} = +R99 - R102$$

$$\frac{d[pr]}{dt} = +R100 - R103$$

$$\frac{d[pk]}{dt} = +R101$$

Optimization of the rate constants by using experimental data

The microscopic rate constants have been chosen at the beginning based on the values reported in literature for the rates of PKA,[39,40] as well as on the knowledge of the binding constants of substrates and inhibitors to PKA and λPP.[41,48] However, to match the model description to our experimental data, that we collected under different conditions (reaction buffer), we performed an optimization of the rate constants by a global minimization procedure. First we built a function in MATLAB whose output is the distance (summed square of residuals) between the concentration versus time profiles for the three species **PDI-2**, **p-PDI-2** and **p2-PDI-2** determined experimentally and those calculated by numerical integration for a given set of parameters (rate constants) and fixed initial conditions (the same as in the experiment). Secondly, we looked for the lowest minimum of the above nonlinear multivariable function (i.e. its global minimum) by using the Global Search option (with fmincon solver) within the MATLAB Global Optimization Toolbox. By inputting an initial set of rate constants (Table 4.4) as the starting point for the optimization problem, together with suitable upper and lower bounds, we got an optimized set of rate constants which correspond to the best match between the calculated and experimental temporal evolutions of **PDI-2**, **p-PDI-2** and **p2-PDI-2.** Remarkably, the Global Search algorithm was found to converge to practically the same solution even when starting quite far away from the minimum, e.g. with rate constants 3 of 4 orders of magnitude different from the optimized ones.

Table 4.4. Rate constants.

Constants	Initial	Optimized	Units	Description
kiaf	$1.6\cdot10^5$	$9.29\cdot10^6$	$M^{-1}\ s^{-1}$	Binding *a* to *exiy*, forward (*a* first to bind)
kiar	$2.0\cdot10^2$	$6.84\cdot10^1$	s^{-1}	Binding *a* to *exiy*, reverse (*a* first to bind)
kaf	$5.0\cdot10^5$	$1.57\cdot10^7$	$M^{-1}\ s^{-1}$	Binding *a* to *exiy*, forward (*a* second to bind)
kar	$3.5\cdot10^2$	$4.29\cdot10^2$	s^{-1}	Binding *a* to *exiy*, reverse (*a* second to bind)
kibf	$5.9\cdot10^6$	$1.27\cdot10^7$	$M^{-1}\ s^{-1}$	Binding *b* to *exiy*, forward (*b* first to bind)
kibr	$5.6\cdot10^2$	$1.21\cdot10^1$	s^{-1}	Binding *b* to *exiy*, reverse (*b* first to bind)
kbf	$1.0\cdot10^7$	$2.81\cdot10^6$	$M^{-1}\ s^{-1}$	Binding *b* to *exiy*, forward (*b* second to bind)
kbr	$3.5\cdot10^2$	$3.83\cdot10^2$	s^{-1}	Binding *b* to *exiy*, reverse (*b* second to bind)
kpqf	$1.0\cdot10^6$	$1.14\cdot10^3$	$M^{-1}\ s^{-1}$	Binding *q* to *px*, forward
kpqr	$1.0\cdot10^3$	$2.30\cdot10^2$	s^{-1}	Binding *q* to *px*, reverse
ksibf	$1.0\cdot10^7$	$1.57\cdot10^7$	$M^{-1}\ s^{-1}$	Subst. inhib. *b* binding to x-site of *exiy*, forward
ksibr	$1.0\cdot10^4$	$1.99\cdot10^5$	s^{-1}	Subst. inhib. *b* binding to x-site of *exiy*, reverse

ksiqf	$5.9 \cdot 10^{6}$	$3.66 \cdot 10^{7}$	$M^{-1}\ s^{-1}$	Subst. inhib. *q* binding to x-site of *exiy*, forward
ksiqr	$5.9 \cdot 10^{3}$	$8.50 \cdot 10^{4}$	s^{-1}	Subst. inhib. *q* binding to x-site of *exiy*, reverse
kncqf	$1.0 \cdot 10^{7}$	$3.31 \cdot 10^{7}$	$M^{-1}\ s^{-1}$	Noncomp. inhib. of *q* versus *exiy* forward
kncqr	$1.0 \cdot 10^{4}$	$4.24 \cdot 10^{4}$	s^{-1}	Noncomp. inhib. of *q* versus *exiy* reverse
kpipf	$5.0 \cdot 10^{5}$	$9.00 \cdot 10^{7}$	$M^{-1}\ s^{-1}$	Prod. inhib. *p* binding to x-site of *exiy*, forward
kpipr	$5.0 \cdot 10^{2}$	$5.55 \cdot 10^{1}$	s^{-1}	Prod. inhib. *p* binding to x-site of *exiy*, reverse
kpikf	$1.0 \cdot 10^{6}$	$7.93 \cdot 10^{4}$	$M^{-1}\ s^{-1}$	Prod. inhib. *k* binding to *px*, forward
kpikr	$1.0 \cdot 10^{3}$	$2.29 \cdot 10^{3}$	s^{-1}	Prod. inhib. *k* binding to *px*, reverse
kcat	3.0	2.93	s^{-1}	Reaction rate of kinase
kcatp	$1.0 \cdot 10^{2}$	$4.75 \cdot 10^{1}$	s^{-1}	Reaction rate phosphatase
Constraints[1]				
kiqf = kibf/2				Binding *q* to *exiy* (*q* first to bind), forward
kiqr = kibr				Binding *q* to *exiy* (*q* first to bind), reverse
kqf = kbf/2				Binding *q* to *exiy* (*q* second to bind), forward
kqr = kbr				Binding *q* to *exiy* (*q* second to bind), reverse
*kprf = kpqf*2*				Binding *r* to *px*, forward
kprr = kpqr;				Binding *r* to *px*, reverse
*kncrf = kncqf*2*				Noncomp. inhib. of *r* versus *exiy* forward
kncrr = kncqr				Noncomp. inhib. of *r* versus *exiy* reverse

[1]Based on statistical arguments due to the presence of one or two sites of (de)phosphorylation.

Analysis of the reaction rates

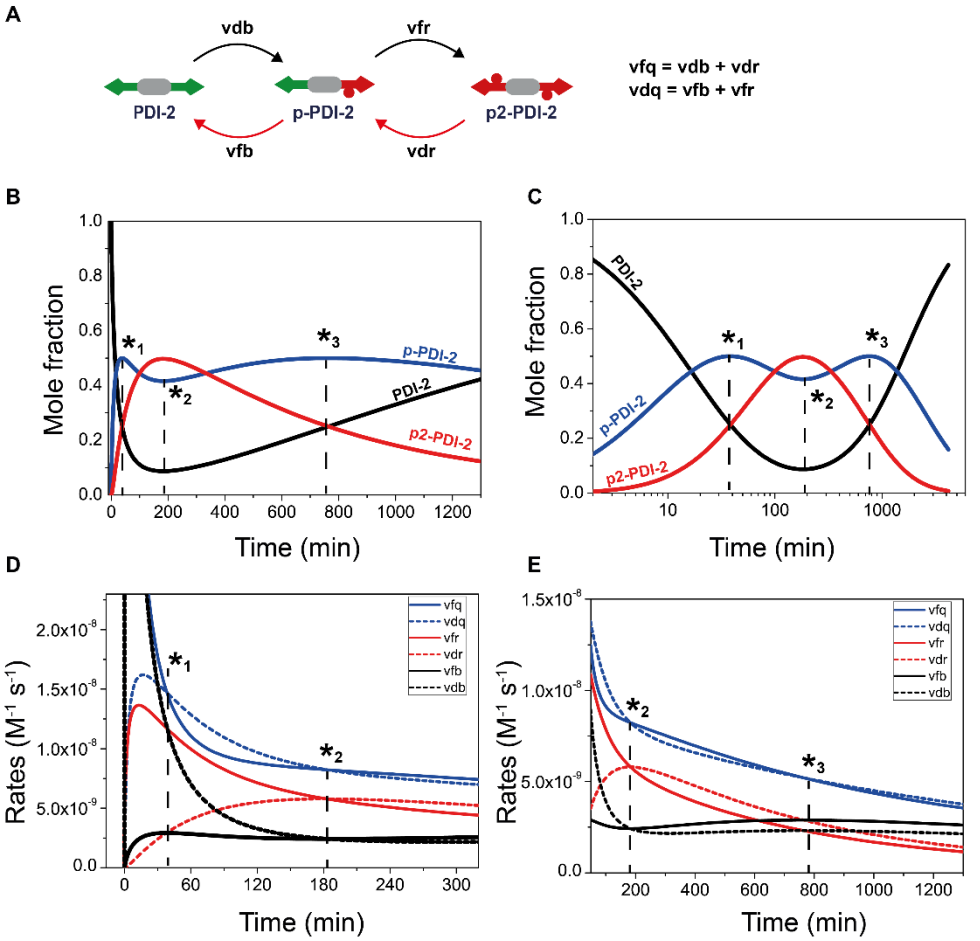

Figure 4.23. Reaction rates. (A) Rates of formation and disappearance of **PDI-2**, **p-PDI-2**, and **p2-PDI-2**, due to their interconversion. (B) Simulation of the transient assembly reported in Figure 4.10A of the main text, with **PDI-2** = 100 μM, ATP = 1 mM, PKA = 0.13 μM, and λPP = 0.3 μM, as initial concentrations and using the optimized kinetic constants reported in Supplementary Table 4.4. (C) The same plot as panel (B) reported in semilog scale to better appreciate the maxima. (D) Change with time of the rates defined in panel (A) during the transient assembly reported in panel (B): zoom at shorter times; (E) Same data as (D) but zoomed at longer times. Reproduced from ref. *** (see page 79) with permission from Nature Research.

From the mathematical model (Figure 4.22) it is possible to calculate the rates of formation and disappearance of the three species, **PDI-2**, **p-PDI-2**, **p2-PDI-2**, due to their interconversion (Figure 4.23A), where vdb = R97; vfr = R98; vdr = R103; vfb = R102; vfq = R97+R103; vdq = R98+R102, as defined in Table 4.2.

We used these values to rationalize the behaviour observed for monophosphorylated **p-PDI-2**, during the transient assembly, reported in Figure 4.10A of the main text, with two maxima observed at around 37 and 180 min (Figure 4.23 and Figure 4.24).

At the beginning the rate of **PDI-2** disappearance (vdb) due to the first phosphorylation **PDI-2** → **p-PDI-2** is the highest (dashed black), which yields a fast accumulation of **p-PDI-2** (high vfq, blue solid). The latter occurs until the first maximum of **p-PDI-2** concentration (37 min, *1) is reached, at which the velocity of **p-PDI-2** disappearance (vdq, dashed blue) matches that of its formation (vfq, solid blue). From this point, and until 183 min (*2) the concentration of **p-PDI-2** starts to decrease (vdq > vdf), which is mainly due to the fact that the rate of formation of **p2-PDI-2** overcame that of disappearance of **PDI-2** (vfr > vdb) or, in other words, the phosphorylation **p-PDI-2** → **p2-PDI-2** is faster than **PDI-2** → **p-PDI-2**. Note that so far the concentration profiles are mainly dominated by the reactions of PKA. Beyond 180 min the concentration of **p-PDI-2** starts to increase again (vdf > vdq) until a new maximum at around 750 min (*3). The latter occurs because the disappearance of **p2-PDI-2** becomes faster than its formation (vdr < vfr), i.e. the dephosphorylation **p2-PDI-2** → **p-PDI-2** is faster than the phosphorylation **p-PDI-2** → **p2-PDI-2**. Note that in this time interval, also **p-PDI-2** → **PDI-2** is faster than **PDI-2** → **p-PDI-2**, (vfb > vdb) that would consume **p-PDI-2**, but the absolute value of these rates are lower than the former. Finally beyond 750 min, the concentration of **p-PDI** starts to slowly decay, which is due to the fact that the dephosphorylation **p-PDI-2** → **PDI-2** become faster than the dephosphorylation **p2-PDI-2** → **p-PDI-2** (vfb > vdr), and remains the fastest reaction until the end of the transient assembly.

Simulation arrays of enzymatic ODE model

In addition to performing a global optimization to obtain more accurate rate constants (cf. Figure 4.10A in the main text), we performed simulations over a wide range of PKA (10^{-3} to 10^{-8} M), λPP (10^{-3} to 10^{-8} M), and ATP (10^{-4} to $10^{-0.5}$ M) concentrations (Figure 4.24). In this way, we use the enzymatic ODE model (see above) to establish the time and amplitude of a transient excursion in **p2-PDI-2** (in a closed system). In other words, depending on the concentrations we can determine at what time the most **p2-PDI-2** is present in the solution. Starting from the experimental conditions (cf. Figure 4.10A) we obtain a transient change in **p2-PDI-2** concentration with a maximum fraction of **p2-PDI-2** of ~0.5 (i.e., half of all initial **PDI-2** has been di-phosphorylated), occurring at ~10^4 s (=183 min.), shown in inset #1 (Figure 4.24). If the concentration of λPP is increased significantly, the amplitude of the excursion is lowered (~0.01, Figure 4.24A,B, #2), but it happens much faster (74 s, Figure 4.24C,D #2). To get a fast and large transient change, we can increase all concentrations (#3), leading to a max. frac. **p2-PDI-2** of ~0.93 after only 127 s. In short, these simulations show that both the amplitude and timescale of the transient change can be changed at will. The (competitive and non-competitive) inhibition pathways in the system (see above) do make the timescale of the excursion (Figure 4.24C,D) quite non-trivial.

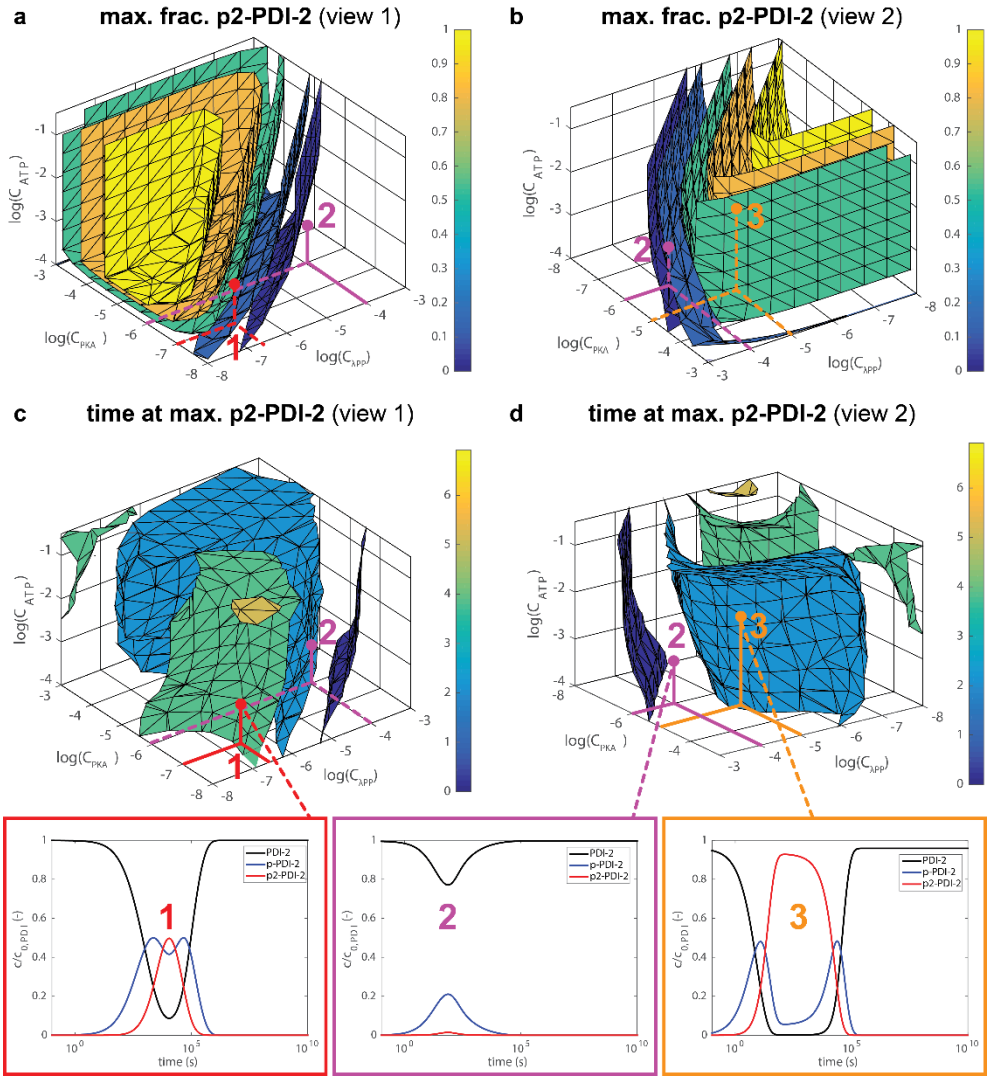

Figure 4.24. Phase Space. Numerical simulations of enzymatic ODE model (100 µM **PDI-2**) as a function of concentration of PKA, λPP, and ATP. Two characteristics are plotted: the maximum fraction of **p2-PDI-2** reached during the transient change (i.e., concentration **p2-PDI-2** divided by the initial **PDI-2** concentration), and ii) the time at which the maximum fraction of **p2-PDI-2** occurs. (A) Max. frac. **p2-PDI-2** (linear color scale: blue is 0, yellow is 1). (B) The same plot as panel a rotated 180° about the z-axis. (C) Time at max. **p2-PDI-2** (logarithmic color scale: blue is 1 s, yellow is 10^7 s). (D) The same plot as panel c rotated 180° about the z-axis. Insets (1–3) show the concentrations of **PDI-2**, **p-PDI-2**, and **p2-PDI-2** at different PKA, λPP, and ATP concentrations. Inset 1 (cf. Figure 4.10A): PKA (0.13 µM), λPP (0.3 µM), ATP (1 mM). Inset 2: PKA (1 µM), λPP (0.1 mM), ATP (1 mM), showing only a very small fraction of **p2-PDI-2** at the maximum. Inset 3: PKA (10 µM), λPP (10 µM), ATP (10 mM), resulting in a very high transient change in **p2-PDI-2** fraction. Reproduced from ref. *** (see page 79) with permission from Nature Research.

4.11.6. NESS experiments

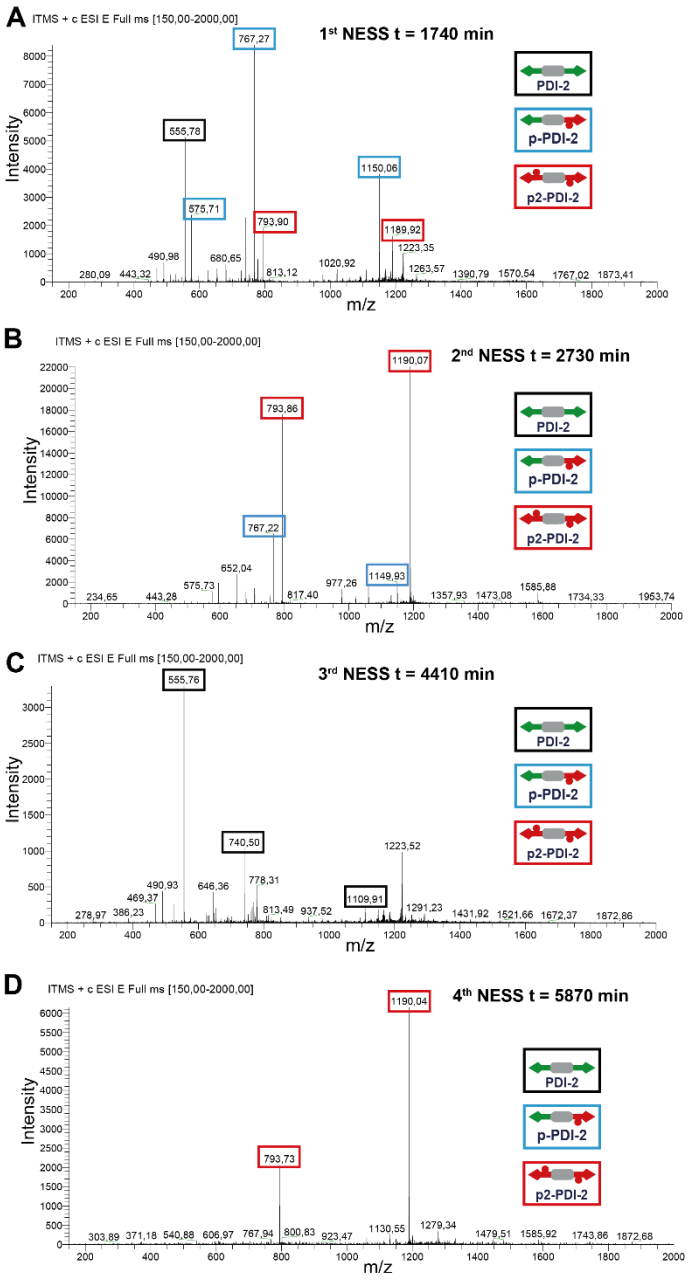

Figure 4.25. Molar fractions at different NESS. LC-MS spectra measured (A) along the first NESS obtained by flowing continuously 1 mM ATP (#1 in Figure 4.12C, sampled at t = 1740 min), (B) along the second NESS obtained by flowing 2.5 mM ATP (#2 in Figure 4.12C, sampled at t = 2730 min), (C) along the third NESS obtained by flowing only buffer without ATP (#3 in Figure 4.12C, sampled at t = 4410 min) and (D) along the fourth NESS obtained by flowing 5 mM ATP (#4 in Figure 4.12C, sampled at t = 5870 min). Reproduced from ref. *** (see page 79) with permission from Nature Research.

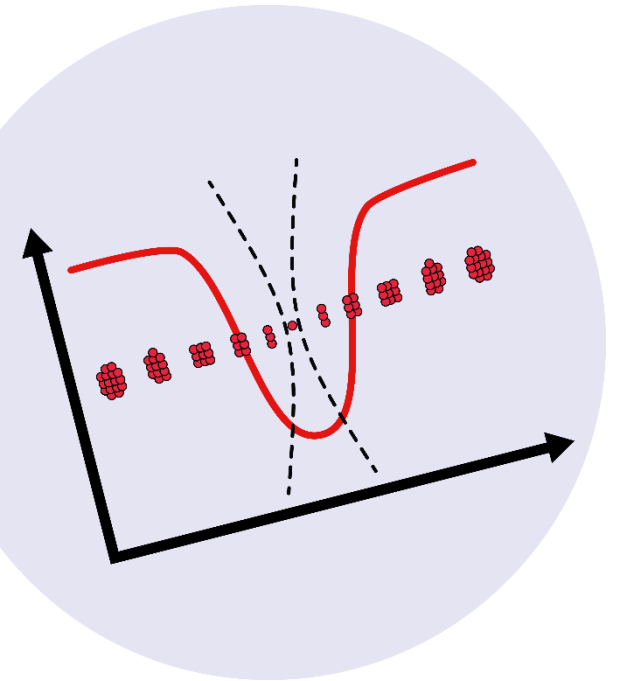

Pushing supramolecular polymerization out of equilibrium by thermophoresis

Abstract: Some biological diseases involve protein aggregation and precipitation. Understanding their mechanism and the interactions that are involved is a crucial task. Microscale thermophoresis (MST) has been introduced recently in biophysics to study biological relevant interactions. Herein, we demonstrate the supramolecular polymerization of a perylene diimide derivative and the applicability of the MST technique to study the self-assembly behaviour under non-equilibrium conditions. We believe that this will help to obtain kinetics insights of different self-assembly mechanisms.

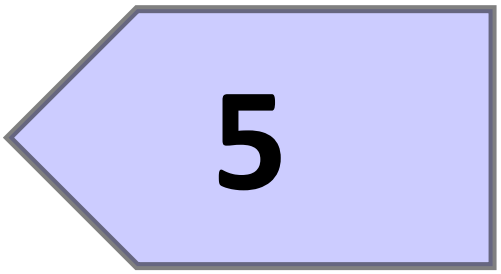

5.1. Introduction

Some biological diseases such as Alzheimer and Parkinson involve protein aggregation and precipitation of amyloid fibrils.[1–3] Small molecules may produce the precipitation of amyloid fibres and play an important role in the disease.[4–7] The fundamental knowledge of the general mechanism of these diseases is lacking, as well as, the interactions between the proteins and the small molecules. The latter has led to develop experimental techniques that could be used to study and identify the interactions involved in the diseases, but many of them are limited by sample concentration or sensitivity. Thermophoresis is the directed motion of particles along a temperature gradient. In other words, a temperature gradient in space induces not only a heat flow but also a net flux of molecules. The latter is also known as the Ludwig-Soret effect.[8,9] Typically, molecules deplete from the regions with elevated temperatures (known as positive thermophoresis), however, the opposite behaviour can be also observed (i.e., negative thermophoresis).[10,11] After some time the molecular concentration reaches a steady state due to the simultaneous and opposite effects of thermal diffusion and (D_T) and standard (Fickian) diffusion (D) when a stationary temperature gradient is applied.[10,12] A combination of local equilibrium and non-equilibrium effects can be used to describe the concentration profile that follows an exponential distribution: $C/C_0 = \exp(-S_T \Delta T)$, where $S_T = D_T/D$ is the Soret coefficient.[13,14] Thermophoresis can be used to probe size, charge and solvation of molecules. Based on local equilibrium conditions the Soret coefficient can be expressed as:

$$S_T = \frac{A}{k_B T} \left(-s_{hyd} + \frac{\beta \sigma_{eff}^2}{4\, \varepsilon \varepsilon_0 T} \times \lambda_{DH} \right)$$

where k_B is Boltzmann constant, T is temperature, λ_{DH} is Debye length, ε is dielectric constant, Q_{eff} is the effective charge, σ_{eff} is effective surface charge, and β is a factor related to the temperature derivative of the dielectric constant.

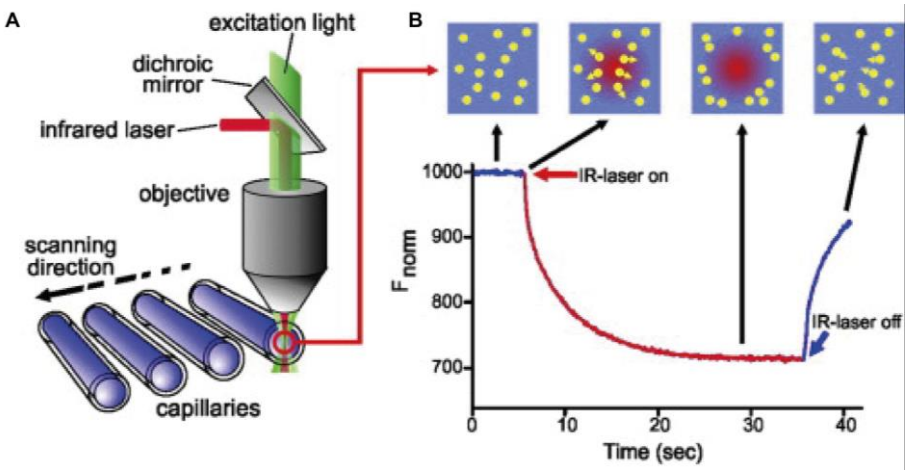

Figure 5.1. Basics of microscale thermophoresis (MST). (A) In a MST experiment: solutions are heated by an IR laser in small glass capillaries. The concentration profile is quantified by following the fluorescence in the tryptophan region. (B) A normal experiment shows a starting fluorescence. Molecules deplete from the hot region to the cold one (positive thermophoresis) after switching on the IR laser. Finally, particles relax back once the IR is switched off again. Reproduced from Ref. 10 with permission from Elsevier.

In the last decade, microscale thermophoresis (MST, a technique based on the Soret coefficient) has become relevant to study different aspects of biomolecular functions.[8,10,13] MST has been used to study the binding constants of macromolecules.[8,15–18] Binding usually induces changes in the size, charge or conformation of the host and thus, changes the Soret coefficient. In a typical MST experiment, thermophoresis is measured by following the fluorescence of a solution contained inside small glass capillaries (Figure 5.1A). A temperature gradient of about 2-6 °C is produced by an infrared laser (IR) in a volume of about 50 μm (in diameter). The changes in the concentration induced are followed by measuring the fluorescence of the solution (Figure 5.1B). In a normal experiment, the starting fluorescence is measured for a few seconds (Figure 5.1B, first plateau). Afterwards the IR is switched on inducing the depletion of particles (decay in Figure 5.1B, red line). A plateau indicates the formation of a steady state. Finally, the IR is off and particles relax back to the original starting point (increase in Figure 5.1B, blue line).[8,10] Specifically, for the commercially available "label free" Nanotemper machine the emission and excitation matches that of tryptophan (an essential amino acid in living systems).[10] The MST technique has been employed in the analysis of bio-molecular interactions such as oligonucleotide-interactions[15,19], protein-DNA interaction[20,21], protein-protein interactions[22–24], protein-small molecule interactions[16,25,26] and protein-liposome interactions[27,28]. In addition, MST can be also used to study the thermodynamics of biomolecular interactions, protein folding or enzyme kinetics.[29–33]

Recently, Buell and co-workers[13] demonstrated that different assembled species such as oligomers and fibrillar proteins show different thermophoretic behaviour. This allows to discriminate between aggregates of proteins of different sizes. The latter opens the avenue to study ligand binding to supramolecular structures such as amyloid fibrils. This can be used for the development of diagnostic and therapeutic strategies against diseases. So far, there are no examples in which MST is used to study artificial supramolecular assemblies. Encouraged by Buell and co-worker's results we hypothesize that MST can be used to study kinetics insights of supramolecular systems. Specifically, supramolecular polymers with polydispersity ~ 2.0 (at equilibrium) will show different size of aggregates in solution (first dashed circle in Figure 5.2). When the building-clock shows positive thermophoresis, the bigger assemblies will deplete faster than the smaller ones upon switching on the IR laser and thus, perturb the equilibrium. The larger assemblies will travel more distance with respect to the focal center inducing a change in the concentration and species distribution. If the thermophoresis is negative, the behaviour will be the opposite (second bottom process in Figure 5.2). Once the IR is off, assemblies will relax back to their original place (cf. Figure 5.2). We believe that the relaxation of the molecules can be used to elucidate k_{on} and k_{off} of polymerization, similarly to a concentration jump experiment.

In this chapter, we will show preliminary results of the applicability of MST to study the self-assembly insights of a model system, a perylene diimide derivative building-block. In the first place, we studied the thermophoretic behaviour of a model molecule that is monomeric in solution. Next, the supramolecular polymerization of the model self-assembling building-block was well-characterized by different techniques. Finally, we studied the thermophoretic behaviour of the model self-assembling building-block.

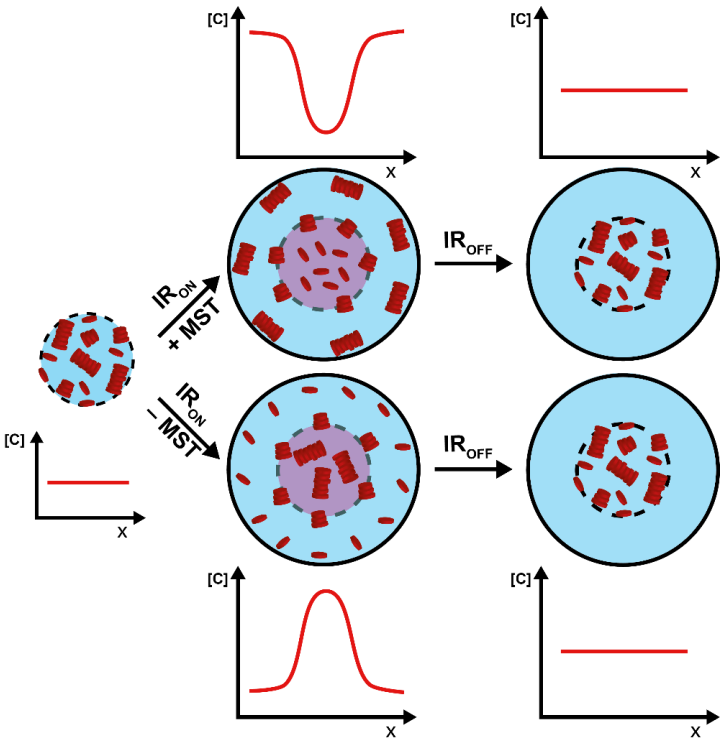

Figure 5.2. Pushing supramolecular polymerization out-of-equilibrium by MST. A starting solution will show a characteristic polydispersity in solution (i.e., different aggregate sizes). MST allows to discriminate between sizes after switching on the IR laser (i.e., bigger assemblies deplete faster than smaller ones) inducing a change in the concentration profile for both positive and negative thermophoresis. Assemblies will relax back after switching off the IR laser allowing to measure the kinetics insights (k_{on} and k_{off} of polymerization) of distinct supramolecular systems.

5.2. MST measurements of the non-assembly model: umbelliferone

First of all, we decided to study the thermophoretic behaviour of umbelliferone (also known as 7-hydroxycoumarin). Umbelliferone shows a fluorescence emission in the tryptophan region and thus, the thermophoretic behaviour can be explored with our MST device. In addition, the solvent has to be carefully chosen, it has to contain an O–H bond (e.g., water, methanol, ethanol, etc.) since the IR laser hits one of the characteristic vibronic bands of the O–H bond (at 1480 nm). Umbelliferone is promptly dissolved in methanol up to the mg/mL range yielding a transparent solution. The thermophoretic behaviour of a 60 μM solution was studied at different IR laser powers (from 10 to 90 %, i.e., the maximum laser power is 120mW). Umbelliferone shows positive thermophoretic behaviour when the solution is heated up with the IR laser meaning that the center is depleted (decay of the fluorescence in Figure 5.3A). Afterwards, molecules diffuse back to the original volume once the IR laser was switched off (recovery of the fluorescence in Figure 5.3A). Higher IR powers show higher thermophoretic behaviour of umbelliferone solution, which induces a larger depletion of molecules and thus, a higher change in the fluorescence intensity when the IR laser is on. Moreover, the relaxation time is longer when the IR laser value is higher indicating that when molecules are depleted farther it takes more time for the molecules

to relax back (Figure 5.3A). Therefore, umbelliferone shows a normal thermophoretic behaviour.

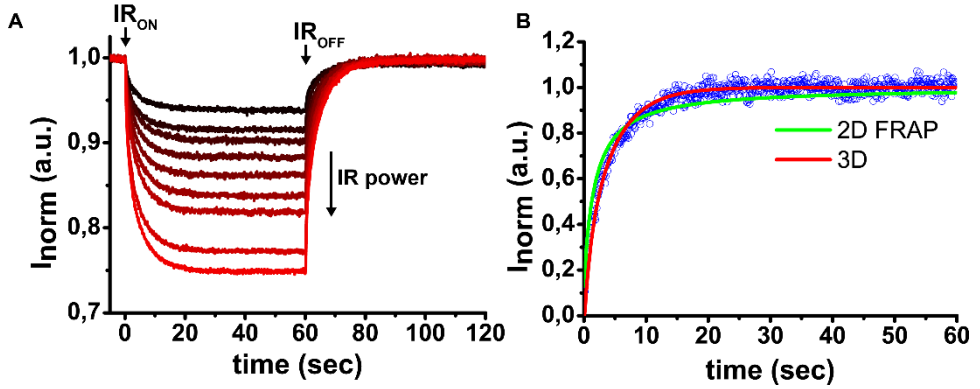

Figure 5.3. MST measurements of umbelliferone. (A) MST measurements of 60 μM umbelliferone (7-hydroxycoumarin) in methanol, thermophoresis is measured for 60 s at different IR laser powers (i.e., from 10 to 90), afterwards, relaxation back is measured for 60 s at 19.9 ˚C. LED power of 2 % and IR power of 10-90 % (12-108 mW. (B) Relaxation process of the same umbelliferone solution. The data is fitted with a 2D FRAP model (blue line) and a 3D home-built model (green line).

Next, we explore the back-diffusion profile in order to obtain the diffusion coefficient of umbelliferone. The model considers the Fickian diffusion of molecules into a sphere (3D model) assuming that only a small sphere is observed in the center of the depletion sphere (i.e., the confocal volume of detection is smaller than the IR depleted one). The model was numerically integrated in MATLAB and fitted to the experimental data. The model shows a good fit with the experimental data (red line in Figure 5.3B). In addition, fluorescence recovery after photobleaching (FRAP) 2D model was also considered as previously used in the literature,[8,34,35] but the fit was much worse (green line in Figure 5.3B). The 3D model has only one fitting parameter, the diffusion coefficient. The diffusion coefficient is calibrated with the value obtained from DOSY NMR. Surprisingly, the 3D model fits the data well even if the initial assumptions are not very accurate: the confocal volume in reality is ellipsoidal and not spherical, and the initial concentration depletion is not exactly Gaussian (note: from personal communication with Nanotemper GmbH). Now that we understand a general thermophoretic behaviour we decided to move on and study the polymerization of our model self-assembly system by traditional techniques. Later on, we study the thermophoretic behaviour of our self-assembling system.

5.3. Model self-assembly system: PDI-3

We designed a symmetric 3,4,9,10-perylene diimide derivative **PDI-3** containing tryptophan moieties in order to measure the thermophoretic behaviour in our MST device (Figure 5.4A). The oligoethyleneglycol derivative of gallic acid was prepared following the same protocol as in chapter 2. Afterwards, peptide coupling between the gallic derivative and a mono-protected ethylenediamine was performed yielding the corresponding protected amine, which was deprotected by TFA. Afterwards, L-tryptophan was incorporated into the core by imidization with perylene-3,4,9,10-tetracarboxylic acid dianhydride yielding the tryptophan perylene diimide core. Finally, a peptide coupling

between the core and the gallate derivative was done leading to the target molecule **PDI-3** (Figure 5.4A, for further details see section 5.7).

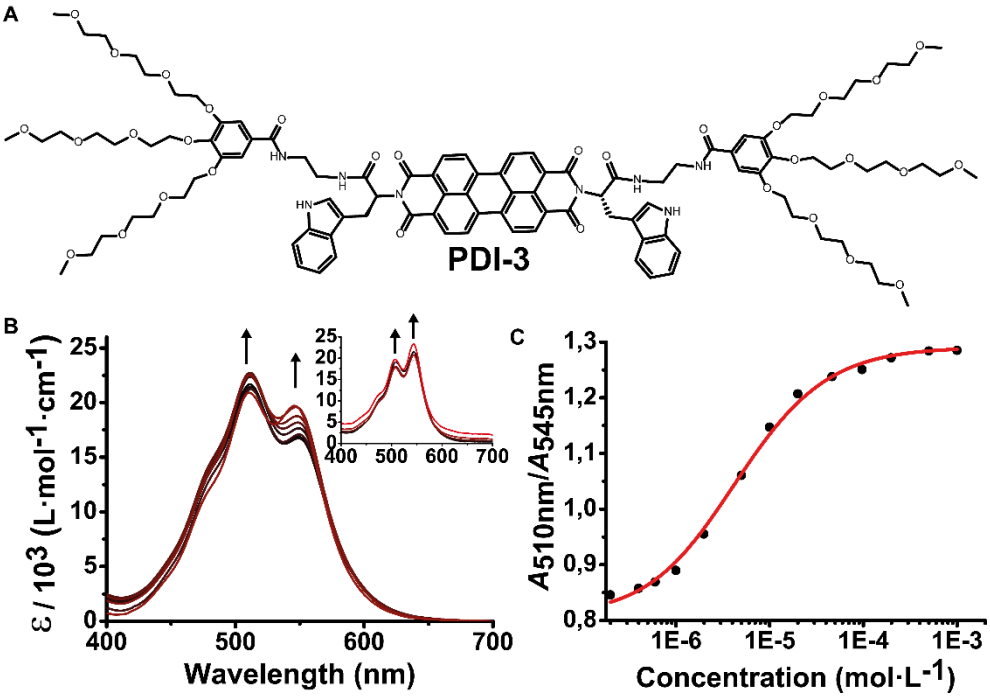

Figure 5.4. Model self-assembly PDI-3. (A) Chemical structure of **PDI-3**. (B) UV-Vis spectroscopy of **PDI-3** at different concentrations. The arrows indicate disassembly of **PDI-3** upon dilution. The inset shows UV-Vis spectra at lower concentrations, the arrows indicate again the direction of disassembly. (C) Ratio A_{510nm}/A_{545nm} as a function of concentration.

PDI-3 was promptly dissolved in aqueous borate 50 mM solution (pH 8) up to the mM range yielding pinkish solutions. UV-Vis spectroscopy of a 1 mM **PDI-3** solution shows a broad absorption band from 400 to 600 nm (black spectrum in Figure 5.4B) due to the S0 → S1 electronic transition of the chromophore with maxima at 510 and 545 nm (A_{510nm} and A_{545nm}, respectively). The ratio between both peaks 1.28 and the lack of the characteristic vibronic progression of monomeric PDIs ratio (A_{510nm}/A_{545nm} = 0.65) strongly indicates the formation of H-aggregates due to π-π stacking of the chromophores.[36–39] The ratio A_{510nm}/A_{545nm} starts to decrease upon dilution of **PDI-3** solution (Figure 5.4C) indicating the loss of the π-π stacking. Specifically, the relative increase of the intensity of A_{545nm} with respect to the A_{510nm} band indicates disassembly of **PDI-3** (inset in Figure 5.4B). However, the ratio A_{510nm}/A_{545nm} at lower concentration indicates that **PDI-3** was not completely disassembled in borate buffer solution. The supramolecular polymerization of **PDI-3** can be described with an isodesmic polymerization. The same model developed in Chapter 2 was used to fit the A_{510nm}/A_{545nm} ratio upon dilution of **PDI-3** solution yielding a K_{eq} = 1.3 x 10^5 M^{-1} and a $R^2 > 0.99$. Moreover, UV-Vis spectroscopy also shows a peak at 280 nm due to the absorption of tryptophan substituents (see appendix). The latter remained unchanged upon dilution of **PDI-3** indicating that tryptophan absorption is not affected by the supramolecular polymerization of **PDI-3**.

To further study the aggregation behaviour of **PDI-3**, we explored the assembly behaviour of 50 μM **PDI-3** solution in different mixtures of borate buffer and tetrahydrofuran (THF). UV-Vis spectra blue shift upon increasing the fraction of THF (φ_{THF}) due to the decrease in polarity of the solvent (Figure 5.5A). In addition, the spectra shows a better resolved vibronic progression of the chromophore with maxima at 495 and 530 nm and a third maximum appear at 465 nm characteristic of the 0-2 vibronic transition (Figure 5.5A). Moreover, the increase of the extinction coefficient (i.e., 0-1 and 0-0 vibronic transitions), together with the decrease of the ratio (Figure 5.5B, different maxima were considered for the different fractions of THF) upon increasing the amount of THF indicates that disassembly of **PDI-3** occurs progressively. Interestingly, **PDI-3** was molecularly dissolved (ratio 0.65) for $\varphi_{THF} > 0.6$. On the other hand, no progression can be observed of the characteristic absorption band of tryptophan upon increment of φ_{THF} suggesting that tryptophan is not affected by the aggregation of **PDI-3** as it was observed upon dilution of **PDI-3** in buffer solutions (See Appendix).

.

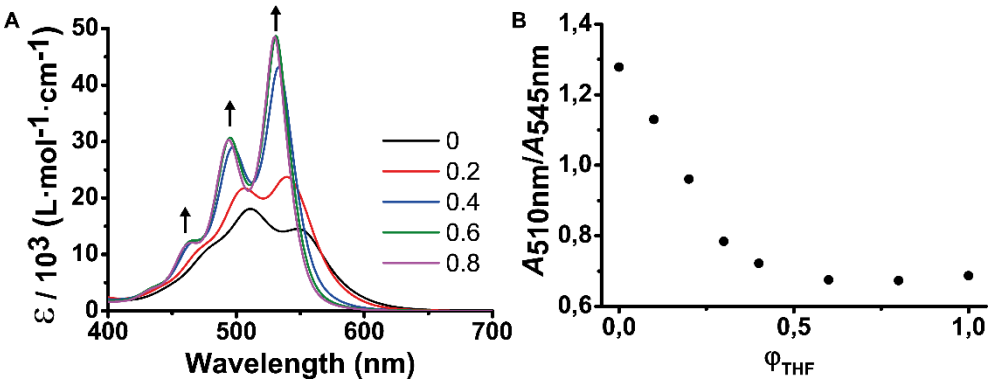

Figure 5.5. PDI-3 in mixtures of borate buffer and THF. (A) UV-Vis spectra of a 50 μM **PDI-3** solution in different mixtures of borate buffer and THF. Arrows indicate changes upon increasing the fraction of THF (φ_{THF}). (B) Ratio of the corresponding maxima for the 0-0 and 0-1 vibronic transitions as a function of φ_{THF}.

Fluorescence spectroscopy of **PDI-3** was also studied in borate buffer and in mixture of borate buffer and THF. In buffer, **PDI-3** emission shows a broad band from 330 to 500 nm with a maximum at 345 nm due to the tryptophan moieties, and a shoulder at 475 nm (red line in Figure 5.6A) suggesting an electronic coupling between the core and the tryptophan residue of **PDI-3**. In addition, the emission spectrum of just L-tryptophan as a control in borate buffer (red line in Figure 5.6B) shows a single band from 300 to 450 nm with maximum at 360 nm (no shoulder was observed). Moreover, the intensity of tryptophan was 65 times higher compared with the intensity of **PDI-3** spectrum indicating that fluorescence of the tryptophan moiety was quenched due to the aggregation of **PDI-3**. On the other hand, emission of **PDI-3** could not be observed indicating that aggregation completely quenches the fluorescence of the PDI core. The fluorescence was also studied in mixtures of borate buffer and THF (Figure 5.6C). Interestingly, the increase of the intensity upon increasing the fraction of THF by a factor of 20 indicates that the addition of THF disassembles **PDI-3** aggregates (Figure 5.6C).

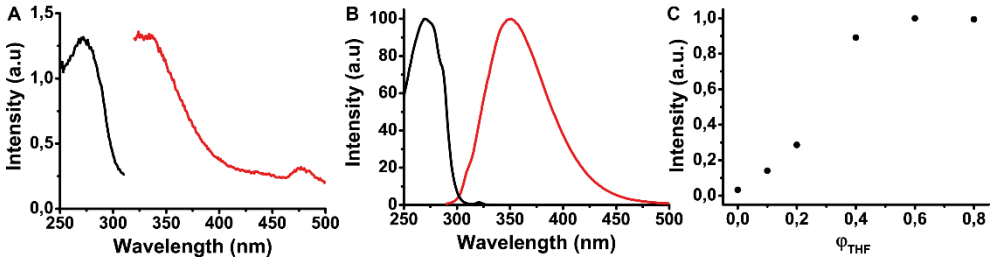

Figure 5.6. Fluorescence of PDI-3. Excitation (black) and emission (red) spectra of (A) **PDI-3** (50 μM) and (B) L-tryptophan (10 μM). Excitation and emission at 280 and 360 nm, respectively. (C) Maximum intensity in the emission of **PDI-3** (50 μM) in mixtures of borate buffer and THF. Excitation at 280 nm.

To completely understand **PDI-3** polymerization, we studied the self-assembly behaviour by dynamic light scattering (DLS) of a 500 μM **PDI-3** solution in borate buffer and also in borate buffer and THF mixtures (0.2 and 0.4 φ_{THF}). Specifically, DLS measurements of **PDI-3** in borate buffer solution show a bimodal distribution of assemblies with two different sizes (i.e., hydrodynamic radii R_H = 82 ± 14 and 598 ± 125 nm), see Figure 5.7A. Interestingly, **PDI-3** borate buffer/THF solutions (φ_{THF} = 0.2 and 0.4) shows lower scattering intensity as compared with pure buffer solution. Two species were also observed at φ_{TFH} = 0.2 with R_H = 59 ± 8 and 650 ± 200 nm (Figure 5.7B) and larger aggregates (R_H = 1.02 ± 0.14 μm) were observed at φ_{TFH} = 0.4. The lower scattering intensity (3 times lower as compared with pure buffer **PDI-3** solutions) suggest that the addition of THF induces disassembly of **PDI-3** assemblies as observed by UV-Vis and fluorescence spectroscopy. However, the size of the assemblies remained unchanged. For φ_{TFH} = 0.4, preliminary studies have shown apparently larger aggregates, but this could be due to contaminations with dust particles. More studies are needed.

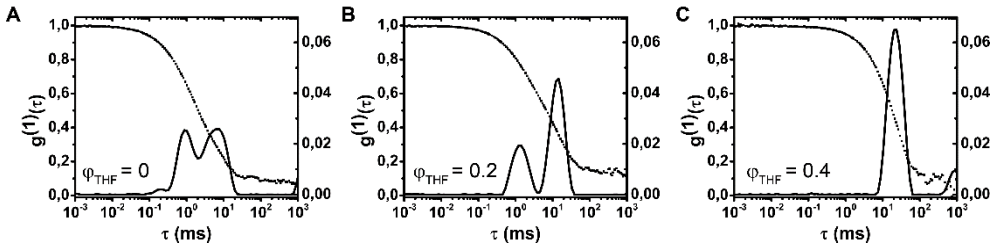

Figure 5.7. DLS measurements. The intensity autocorrelation function of 500 μM **PDI-3** solution in (A) buffer solution, (B) 0.2 φ_{THF} and (C) 0.4 φ_{THF} at 25 ºC.

So far, we have seen that **PDI-3** forms H-aggregates through π-π stacking in borate buffer solutions. Dilution induced partial disassembly of **PDI-3**. In addition, **PDI-3** consecutively disassembled upon addition of THF. DLS measurements confirm that **PDI-3** is assembled in borate buffer solutions. In addition, the scattering intensity of mixtures of borate buffer and THF solution was lower as compared with pure buffer solutions indicating that THF promotes disassembly of **PDI-3**. However, further investigations are needed to finally confirm our results.

5.4. MST measurements on PDI-3

In this section, we will show the thermophoretic behaviour of L-tryptophan (i.e., the control molecule) in borate buffer solution and **PDI-3** in buffer solution. Specifically, the fluorescence intensity is followed at the tryptophan region. L-tryptophan shows positive thermophoretic behaviour when the IR laser was switched on (Figure 5.8A) meaning that molecules were depleted from the hotter regions. Once the IR was switched off, L-tryptophan relaxed back to its original volume. However, the signal did not completely recover to its starting value due to photobleaching. The latter was confirmed when an exponential decrease of the intensity was observed without applying a temperature gradient (i.e., IR laser off during the entire measurement, see black line in Figure 5.8A). In addition, higher IR powers (from 10 to 70 %) induce further depletion of L-tryptophan molecules due to the consecutive increment in the temperature gradients (Figure 5.8A) and thus, higher temperature gradients lead to larger concentration gradients.

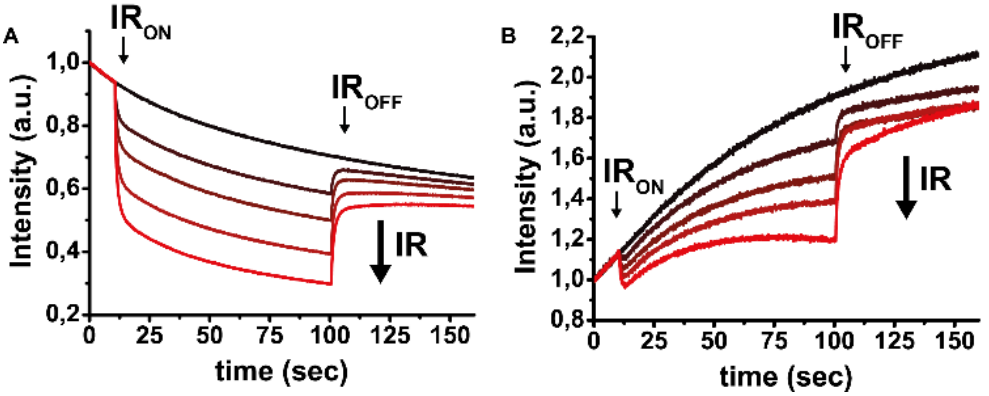

Figure 5.8. MST measurements. MST measurements of (A) L-tryptophan (10 μM) and (B) **PDI-3** (50 μM) in borate buffer. Arrows indicate change upon generating a larger temperature gradient. LED power of 30%, IR power of 0-70% (0-84 mW).

When a 50 μM **PDI-3** solution was studied by MST, we found that the starting fluorescence emission intensity of **PDI-3** was 20 times lower as compared to L-tryptophan in agreement with fluorescence spectrometry experiments (see above). When the IR laser was not switched on (no temperature gradient), a continuous increase of the intensity was observed (top curve in Figure 5.8B). The increase in intensity was unexpected since perylene diimides are very photo-stable, and photo-bleaching would not lead to higher signals. This result may indicate that the excitation light is affecting the assembly behaviour of **PDI-3**. The increase of the intensity could suggest that the concentration of **PDI-3** increases within the irradiated volume over time. However, a higher concentration would lead to more assembly, and thus further quenching of the fluorescence of the tryptophan moiety. Instead, we hypothesise that photo-excitation promotes disassembly of **PDI-3** while the total concentration remains constant over time, perhaps due to photoreduction of the PDI core.[40,41] The increase in fluorescence intensity is in that case due to the presence of more monomeric (and thus more emissive) **PDI-3** species in solution.

A decrease of the fluorescence intensity was observed when the IR laser was switched on indicating depletion of **PDI-3** assemblies from hot to cold regions (positive thermophoretic behaviour), see Figure 5.8B. In addition, as observed for L-tryptophan

molecules, higher IR powers promote larger concentration gradients and thus, higher depletion of **PDI-3** assemblies (Figure 5.8B). When the IR laser was turned off, **PDI-3** assemblies diffuse back to their original volume. However, up to now extracting useful information such as k_{on} or k_{off} from these measurements has proven difficult. Especially, due to the unexpected excitation light-induced increase in fluorescence. Currently we are building a new setup where we couple MST to a fluorescence microscope. The setup will allow us to see what is occurring inside the capillaries. Moreover, the IR laser will be of a wavelength capable of heating organic solvents, which will allow us to study a more simple (isodesmic and/or cooperative) supramolecular polymerization process (e.g., in n-heptane or methylcyclohexane). As many others have found before us, self-assembly in aqueous environments is complicated. The fact that the UV dilution experiments (cf. Figure 5.4B) were in good agreement with the isodesmic model was promising. The DLS data, however, shows a bimodal size distribution, which is not expected for a simple 1D isodesmic polymerization. Further studies have to show whether MST will become a useful tool in the field of supramolecular chemistry, beyond measuring simple guest-host interactions.

5.5. Conclusions

In this chapter, we reported the supramolecular polymerization of a perylene diimide derivative (**PDI-3**) containing tryptophan moieties as a model to measure the thermophoresis. We have shown that **PDI-3** is assembled through π-π stacking (H-aggregation) in borate buffer solution even in the μM range. Addition of THF promotes disassembly of **PDI-3** in solution permitting to achieve molecularly dissolved **PDI-3** solutions. Importantly, we found that the fluorescence of the tryptophan moiety was quenched upon aggregation of **PDI-3**.

In addition, we demonstrated the applicability of microscale thermophoresis to study supramolecular systems under non-equilibrium conditions. **PDI-3** shows thermophoretic depletion of molecules when the temperature gradient was applied. Interestingly, our hypothesis is that photo-excitation possibly promotes further disassembly of **PDI-3** increasing the amount of monomeric species in solution. In other words, **PDI-3** reaches different steady states when different temperature gradients are applied. We believe that this fact can be applied to study the kinetic insights of different self-assembly systems. However, further studies are needed in order to completely understand the thermophoretic behaviour of different systems.

Now, we are working on the development of a mathematical model to understand the thermophoretic behaviour of different systems and also, we are trying to combine MST with fluorescence microscopy in order to really observe what is occurring in the solution. We hope that this studies will bring a new technique that allow to study supramolecular system under non-equilibrium conditions.

5.6. Experimental section

Sample preparation. Samples were prepared in mixtures of borate buffer (0.5 M, pH-value of 8) and/or tetrahydrofuran, and sonicated for 30 s at room temperature.

UV/Vis spectroscopy. Absorption spectra were recorded on a Jasco V-670 spectrophotometer. Samples were held in cuvettes of quartz with path lengths of 1.0 and 10.0 mm for concentrations ranging from 100 μM to 1 mM and from 5 to 50 μM respectively. In addition, experiments were performed at lower concentrations of 0.02 to 2 μM using a home-made cell with a path length of 10.0 cm, which was constructed from a 3D-printed cassette and two windows of quartz. The absorption coefficient (ε) was determined according to the Beer–Lambert law, *i.e.* $\varepsilon = A/(c \cdot l)$ where *A, c,* and *l* are the absorption, concentration and path length respectively.

Fluorescence spectroscopy. Emission and excitation spectra were recorded on a Horiba Fluorolog-3 spectrofluorometer in right angle detection mode. Samples were held in cuvettes of quartz with a path length of 10.0 mm. Wavelengths of emission and excitation, and concentrations are specified in the captions of figures.

Dynamic light scattering. Experiments were performed on a home-built setup with an ALV7002 digital correlator using a laser diode with a wavelength of 639 nm. The absolute scattering intensity (I_q) was computed according to

$$I_q = \frac{I_s - I_{sol}}{I_{tol}} \left(\frac{n_{sol}}{n_{tol}}\right)^2 R_\theta$$

where I_s, I_{sol}, and I_{tol} are the measured scattering intensities of the sample, the solvent, and toluene respectively, with the refractive indices n_{sol} (= 1.33) and n_{tol} (= 1.49), and Rayleigh ratio (R_θ = 9.8 x 10^{-6} cm^{-1} at 639 nm). Intensity cross-correlation functions ($g^2(\tau)$) were measured at scattering vectors ($q = (4 \cdot \pi \cdot n/\lambda) \sin(\vartheta/2)$) ranging from 0.006 to 0.022 nm^{-1}. Sequentially, the electric field cross-correlation function ($g^{(1)}(\tau)$) were calculated according to $g^{(1)}(\tau) = \sqrt{(g^{(2)}(\tau) - 1)}$, and analysed with CONTIN algorithm to determine distributions of the relaxation time (τ_D). The relaxation time corresponding to the maximum value of the distribution was used to determine the diffusion coefficient ($D = (\tau \cdot q^2)^{-1}$). Subsequently, the hydrodynamic radius (R_h) was determined using the Stokes-Einstein relationship, *i.e.* $R_h = k_B \cdot T / (6 \cdot \pi \cdot \eta \cdot D)$ where k_B, T, and η are the Boltzmann constant, temperature, and viscosity respectively.

Microscale thermophoresis. Experiments were performed on a NanoTemper Monolith NT.LabelFree. Samples were prepared at a concentration of 500 μM in borate buffer solution and at a concentration of 50 μM in borate buffer and THF mixtures, measured at a temperature of 22 °C, and held in capillaries (PolyMicro) with an inner diameter of 102 μm. The coating of the capillaries was burned off using a Bunsen burner and the capillaries were sealed with wax. LED and MST power are specified in the caption of figures.

5.7. Synthesis of PDI-3

L-Tryptophan was purchased from Bachem. *N*-(*tert*-Butoxycarbonyl)-1,2-diaminoethane was purchased from Tokyo Chemical Industry. Methyl gallate derivative was previously prepared (see chapter 2). All other reactants, reagents and solvents were purchased from Sigma-Aldrich.

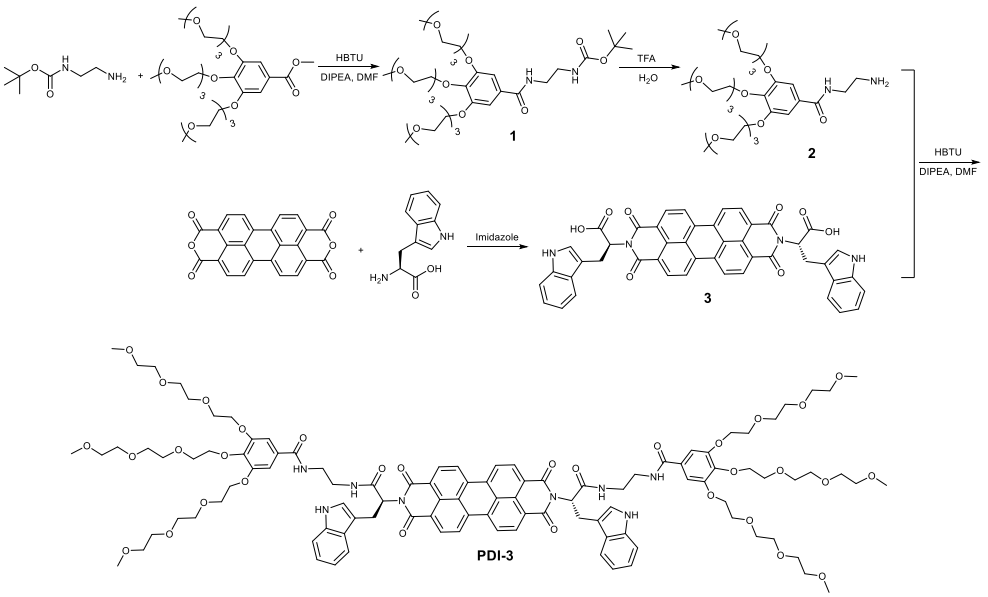

Figure 5.9. Synthesis of PDI-3. Synthetic route followed to obtain **PDI-3**.

***N*-(*N*-(*tert*-Butoxycarbonyl)-2-aminoethyl)-3,4,5-tris(2-(2-(2methoxyethoxy) ethoxy)ethoxy)benzamide (1).** 3,4,5-tris(2-(2-(2-Methoxyethoxy)ethoxy)ethoxy)benzoid acid (497 mg, 0.82 mmol) and HBTU (372 mg, 0.98 mmol) were mixed in DMF (6 mL) and the reaction flask was affixed with a balloon filled with nitrogen gas. DIPEA (0.43 mL, 2.47 mmol) was added dropwise, followed by *N*-(*tert*-butoxycarbonyl)-1,2-diaminoethane (4) (0.16 mL, 1.01 mmol) and the reaction mixture was stirred at room temperature (20-25 °C) overnight (18-24 h). Then $CHCl_3$ (12 mL) was added and the reaction mixture was washed with an aqueous solution of sodium bicarbonate (saturated, 2 x 18 mL), followed by an aqueous solution of sodium chloride (saturated, 2 x 18 mL) and dried over anhydrous $MgSO_4$. Tthe solvent was removed by rotatory evaporation to give compound **2** as a yellow oil (593 mg). ^{1}H-NMR (400 MHz, DMSO-d_6): δ (ppm) = 7.19 (s, 2H), 4.22 (t, 6H), 3.87-3.80 (t, 6H), 3.71-3.52 (m, 26H), 3.44 (t, 2H), 3.34 (s, 9H), 1.42 (s, 9H); MS (ESI-TOF): m/z = 773.87 calculated for $[M{\cdot}Na]^+$, 773.45 observed.

***N*-(2-Aminoethyl)-3,4,5-tris(2-(2-(2-methoxyethoxy)ethoxy)ethoxy)benzamide (2).** Compound **1** (0.59 g, 0.79 mmol) was placed in a round-bottom flask. Distilled water (0.3 mL) was added, followed by trifluoroacetic acid (TFA) (2.0 mL) and the reaction mixture was stirred at room temperature (20-25 °C) overnight (18-24 h). Then diethyl ether (40 mL) was added and the solvent was removed by rotatory evaporation to give compound **3** as a

yellow oil (0.85 g). ^{1}H-NMR (400 MHz, DMSO-d_6): δ (ppm) = 7.13 (s, 2H), 4.19 (t, 6H), 3.86-3.79 (t, 6H), 3.70-3.52 (m, 26H), 3.36 (s, 9H), 3.19 (t, 2H); MS (ESI-TOF): m/z = 651.77 calculated for $[M{\cdot}H]^+$, 651.47 observed.

***N,N'*-bis(L-Tryptophan)perylene-3,4,9,10-tetracarboxylic diimide (3).** Perylene-3,4,9,10-tetracarboxylic dianhydride (251 mg, 0.64 mmol), L-tryptophan (291 mg, 1.43 mmol) and imidazole (1.0 g) were placed in a round-bottom flask. The flask was purged with nitrogen gas for 15 min. The reaction mixture was stirred at 120 °C under nitrogen atmosphere (reflux) for 30 min. Then the reaction mixture was cooled to room temperature (20-25 °C) and distilled water (50 mL) was added. The precipitate was removed by filtration under vacuum, and the filtrate was acidified with HCl (12 M, 3 mL) to precipitate the product. The precipitate was collected by filtration under vacuum, washed with distilled water (5 x 9 mL) and dried at 40 °C under vacuum to give compound **3** as a purple solid (448 mg, 91%). ^{1}H-NMR (400 MHz-DMSO-d_6): δ (ppm) = 10.87 (s, 2H), 8.0 (bs, 4H), 7.63 (d, 2H), 7.25-7.15 (d, 4H), 6.98-6.91 (d, 4H), 6.06 (t, 2H), 3.69 (d, 4H).

***N,N'*-bis(3,4,5-tris(2-(2-(2-Methoxyethoxy)ethoxy)ethoxy)benzoylaminoethyl-L-tryptophan)perylene-3,4,9,10-tetracarboxylic diimide (PDI-3).** Compound **3** (81.5 mg, 0.11 mmol) and HBTU (95.5 mg, 0.25 mmol) were mixed in DMF (8 mL) and the reaction flask was affixed with a balloon filled with nitrogen gas. DIPEA (0.16 mL, 0.92 mmol) was added dropwise, followed by a solution of compound **2** (192.5 mg, 0.25 mmol) in DMF (3.0 mL) and the reaction mixture was stirred at room temperature (20-25 °C) for 4 h. Then $CHCl_3$ (70 mL) was added and the reaction mixture was washed with an aqueous solution of sodium bicarbonate (saturated, 2 x 80 mL), followed by an aqueous solution of sodium chloride (saturated, 2 x 80 mL) and dried over anhydrous $MgSO_4$. The solvent was removed by rotatory evaporation and the reaction mixture was purified by preparative liquid chromatography using distilled water/acetonitrile as eluent and dried under vacuum to give **PDI-3** as a red solid (31.3 mg, 14%). ^{1}H-NMR (400 MHz DMSO-d_6): δ (ppm) = 8.10 (b), 7.67 (b), 7.18 (b), 7.04 (b), 6.93 (b), 6.25 (b), 4.07 (b), 3.67-3.45 (b), 3.37 (s); MS (ESI-TOF): m/z = 1016.23 calculated for $[M{\cdot}2H]^{2+}$, 1015.74 observed.

5.8. References

1. Knowles, T. P. J., Vendruscolo, M. & Dobson, C. M. The amyloid state and its association with protein misfolding diseases. *Nat. Rev. Mol. Cell Biol.* **15,** 384–396 (2014).
2. Mietelska-Porowska, A., Wasik, U., Goras, M., Filipek, A. & Niewiadomska, G. Tau Protein Modifications and Interactions: Their Role in Function and Dysfunction. *Int. J. Mol. Sci.* **15,** 4671–4713 (2014).
3. Brunden, K. R., Trojanowski, J. Q. & Lee, V. M.-Y. Advances in Tau-focused drug discovery for Alzheimer's disease and related tauopathies. *Nat. Rev. Drug Discov.* **8,** 783–793 (2009).
4. Chang, E. *et al.* Modulation and Detection of Tau Aggregation with Small-Molecule Ligands. *Curr. Alzheimer Res.* **6,** 409–414 (2009).
5. Cisek, K., L. Cooper, G., J. Huseby, C. & Kuret, J. Structure and Mechanism of Action of Tau Aggregation Inhibitors. *Curr. Alzheimer Res.* **11,** 918–927 (2014).
6. Rojo, L. E., Alzate-Morales, J., Saavedra, I. N., Davies, P. & Maccioni, R. B. Selective Interaction of Lansoprazole and Astemizole with Tau Polymers: Potential New Clinical Use in Diagnosis of Alzheimer's Disease. *J. Alzheimers Dis.* **19,** 573–589 (2010).
7. Watanabe, H., Ono, M. & Saji, H. Novel PET/SPECT Probes for Imaging of Tau in Alzheimer's Disease. *The Scientific World Journal* (2015). doi:10.1155/2015/124192
8. Jerabek-Willemsen, M., Wienken, C. J., Braun, D., Baaske, P. & Duhr, S. Molecular Interaction Studies Using Microscale Thermophoresis. *ASSAY Drug Dev. Technol.* **9,** 342–353 (2011).
9. Soret, C. Archives des Sciences Physiques et Naturelles de Genève, 48-61 (1879).
10. Jerabek-Willemsen, M. *et al.* MicroScale Thermophoresis: Interaction analysis and beyond. *J. Mol. Struct.* **1077,** 101–113 (2014).
11. Duhr, S. & Braun, D. Thermophoretic Depletion Follows Boltzmann Distribution. *Phys. Rev. Lett.* **96,** 168301 (2006).
12. Duhr, S. & Braun, D. Why molecules move along a temperature gradient. *Proc. Natl. Acad. Sci.* **103,** 19678–19682 (2006).
13. Wolff, M. *et al.* Quantitative thermophoretic study of disease-related protein aggregates. *Sci. Rep.* **6,** srep22829 (2016).
14. Braibanti, M., Vigolo, D. & Piazza, R. Does Thermophoretic Mobility Depend on Particle Size? *Phys. Rev. Lett.* **100,** 108303 (2008).
15. Wienken, C. J., Baaske, P., Rothbauer, U., Braun, D. & Duhr, S. Protein-binding assays in biological liquids using microscale thermophoresis. *Nat. Commun.* **1,** ncomms1093 (2010).
16. Seidel, S. A. I. *et al.* Label-Free Microscale Thermophoresis Discriminates Sites and Affinity of Protein–Ligand Binding. *Angew. Chem. Int. Ed.* **51,** 10656–10659 (2012).
17. Fisher, E. *et al.* Detection and Characterization of Small Molecule Interactions with Fibrillar Protein Aggregates Using Microscale Thermophoresis. *ACS Chem. Neurosci.* (2017). DOI: 10.1021/acschemneuro.7b00228
18. Entzian, C. & Schubert, T. Studying small molecule–aptamer interactions using MicroScale Thermophoresis (MST). *Methods* **97,** 27–34 (2016).
19. Baaske, P., Wienken, C. J., Reineck, P., Duhr, S. & Braun, D. Optical Thermophoresis for Quantifying the Buffer Dependence of Aptamer Binding. *Angew. Chem. Int. Ed.* **49,** 2238–2241 (2010).
20. Doetsch, M. *et al.* Study of E. coli Hfq's RNA annealing acceleration and duplex destabilization activities using substrates with different GC-contents. *Nucleic Acids Res.* **41,** 487–497 (2013).
21. Schubert, T. *et al.* Df31 Protein and snoRNAs Maintain Accessible Higher-Order Structures of Chromatin. *Mol. Cell* **48,** 434–444 (2012).
22. Wilson, S. M. *et al.* Inhibition of Transmitter Release and Attenuation of Anti-retroviral-associated and Tibial Nerve Injury-related Painful Peripheral Neuropathy by Novel Synthetic Ca^{2+} Channel Peptides. *J. Biol. Chem.* **287,** 35065–35077 (2012).
23. Xiong, X. *et al.* Receptor binding by a ferret-transmissible H5 avian influenza virus. *Nature* **497,** 392–396 (2013).

24. Arbel, N., Ben-Hail, D. & Shoshan-Barmatz, V. Mediation of the Antiapoptotic Activity of Bcl-xL Protein upon Interaction with VDAC1 Protein. *J. Biol. Chem.* **287,** 23152–23161 (2012).
25. Shang, X. *et al.* Small-molecule inhibitors targeting G-protein–coupled Rho guanine nucleotide exchange factors. *Proc. Natl. Acad. Sci.* **110,** 3155–3160 (2013).
26. Gaffarogullari, E. C., Krause, A., Balbo, J., Herten, D.-P. & Jäschke, A. Microscale thermophoresis provides insights into mechanism and thermodynamics of ribozyme catalysis. *RNA Biol.* **10,** 1815–1821 (2013).
27. Bogaart, G. van den, Meyenberg, K., Diederichsen, U. & Jahn, R. Phosphatidylinositol 4,5-Bisphosphate Increases Ca^{2+} Affinity of Synaptotagmin-1 by 40-fold. *J. Biol. Chem.* **287,** 16447–16453 (2012).
28. van den Bogaart, G. *et al.* Synaptotagmin-1 may be a distance regulator acting upstream of SNARE nucleation. *Nat. Struct. Mol. Biol.* **18,** 805–812 (2011).
29. Schramm, V. L. Enzymatic Transition States, Transition-State Analogs, Dynamics, Thermodynamics, and Lifetimes. *Annu. Rev. Biochem.* **80,** 703–732 (2011).
30. Baron, R. & McCammon, J. A. Molecular Recognition and Ligand Association. *Annu. Rev. Phys. Chem.* **64,** 151–175 (2013).
31. Kunitz, M. Crystalline Desoxyribonuclease: I. Isolation and General Properties Spectrophotometric Method for the Measurement of Desoxyribonuclease Activity. *J. Gen. Physiol.* **33,** 349–362 (1950).
32. Vanecko, S. & Laskowski, M. S. Studies of the Specificity of Deoxyribonuclease I. Hydrolysis of Oligonucleotides Carrying a Monoesterified Phosphate on Carbon 3'. *J. Biol. Chem. US* **236,** (1961).
33. Uverskiĭ, V. N. & Ptitsyn, O. B. [Three-stage equilibrium unfolding of small globular proteins by denaturing agents. I. Carboanhydrase B]. *Mol. Biol. (Mosk.)* **30,** 1124–1134 (1996).
34. Sperling, R. A. *et al.* Size Determination of (Bio)conjugated Water-Soluble Colloidal Nanoparticles: A Comparison of Different Techniques. *J. Phys. Chem. C* **111,** 11552–11559 (2007).
35. Axelrod, D., Koppel, D. E., Schlessinger, J., Elson, E. & Webb, W. W. Mobility measurement by analysis of fluorescence photobleaching recovery kinetics. *Biophys. J.* **16,** 1055–1069 (1976).
36. Würthner, F. *et al.* Perylene Bisimide Dye Assemblies as Archetype Functional Supramolecular Materials. *Chem. Rev.* **116,** 962–1052 (2016).
37. Görl, D., Zhang, X. & Würthner, F. Molecular Assemblies of Perylene Bisimide Dyes in Water. *Angew. Chem. Int. Ed.* **51,** 6328–6348 (2012).
38. Seibt, J. *et al.* On the geometry dependence of molecular dimer spectra with an application to aggregates of perylene bisimide. *Chem. Phys.* **328,** 354–362 (2006).
39. Chen, Z. *et al.* Photoluminescence and Conductivity of Self-Assembled π–π Stacks of Perylene Bisimide Dyes. *Chem. – Eur. J.* **13,** 436–449 (2007).
40. Ghosh, I., Ghosh, T., Bardagi, J. I. & König, B. Reduction of aryl halides by consecutive visible light-induced electron transfer processes. *Science* **346,** 725–728 (2014).
41. Tauber, M. J., Kelley, R. F., Giaimo, J. M., Rybtchinski, B. & Wasielewski, M. R. Electron Hopping in π-Stacked Covalent and Self-Assembled Perylene Diimides Observed by ENDOR Spectroscopy. *J. Am. Chem. Soc.* **128,** 1782–1783 (2006).

5.9. Appendix

UV-Vis Spectra of tryptophan moiety

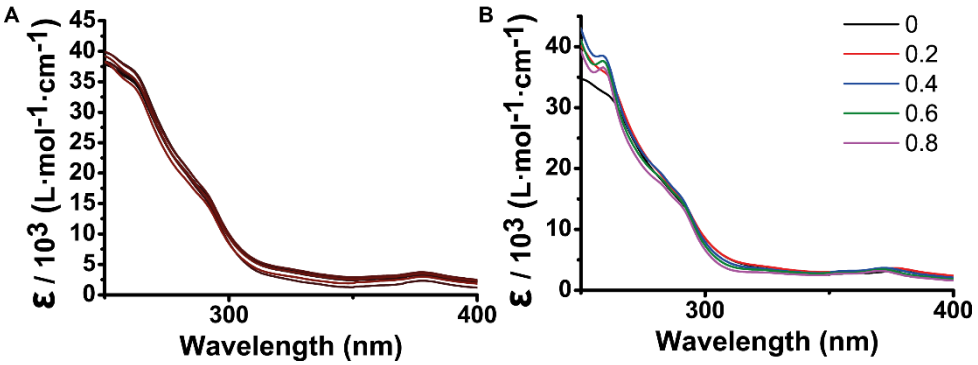

Figure 5.10. UV-Vis spectra of tryptophan moiety. UV-Vis spectra of **PDI-3** solutions in (A) borate buffer at various concentrations, which were prepared by way of dilution, and (B) mixtures of borate buffer and tetrahydrofuran (THF) at various volume fractions of THF.

Epilogue

Evolution of life combines self-organizing, self-assembly, reaction-diffusion processes, compartmentalization, communication and motion.[1] Will it be possible to create artificial life? What do we need to understand and integrate all these processes together? Cells use all of these processes to perform complex functions. Specifically, dissipative supramolecular systems are coupled to reaction diffusion processes endowing the cell adaptable properties in order to perform functions at a precise time and location. To this end, supramolecular systems are regulated by chemical fuels and occur under non-equilibrium conditions. Perfect spatiotemporal control over the self-assembly is obtained upon the incorporation of feedback loops and signalling. For example, microtubules are highly dynamic structures but at the same time very stiff structures because they are operating under non-equilibrium conditions.

In the past, supramolecular chemists have developed sophisticated systems in which the final shape or size can be previously determined. For example, DNA origami can give almost any desired structure.[2–4] However, unexpected structures can also appear. Smart preparation protocols have been developed to tune the self-assembly permitting different outcomes at the same final conditions. In chapter 2, we show a new approach to perform pathway selection mediated by chemical fuels, which allows to control the outcome of the self-assembly. It will be interesting to see if this approach can also be applied to other systems.

As a step further, artificial supramolecular systems have been shown in which the system is kept under non-equilibrium conditions for a certain period of time leading to a transient formation of assembled structures. In chapter 4, we have shown for the first time that sustained non-equilibrium steady states can be achieved in an open membrane reactor, allowing continuous inflow and outflow of chemical fuel and waste, respectively. The latter approach mimics compartmentalization in the cell, which controls different vital processes. In addition, it is well known that emergent behaviour can appear under non-equilibrium conditions in the presence of (delayed) feedback. Oscillations have been found in soluble chemical reaction networks but so far, there are no examples in which supramolecular polymers themselves are the oscillator in analogy with microtubules. In chapter 3, we have shown a first attempt at making an artificial supramolecular oscillator. The feedback from size-dependent disassembly combined with cooperative supramolecular polymerization produced artificial supramolecular oscillations.

However, we are far from understanding dissipative systems. For that reason, new techniques must be incorporated to study the systems under non-equilibrium conditions. In chapter 5, we studied whether thermophoresis can be used as a tool to follow supramolecular polymerization under non-equilibrium conditions. The complications of self-assembly in water together with unexpected light-induced phenomena will take some time to be resolved.

In addition, kinetic models have proven to be invaluable in the understanding the systems presented in this thesis. In chapter 3, we have built a model that provides a first entry into explaining the observed artificial supramolecular oscillations. Interestingly, the model shows oscillatory behaviour taking into account only minimal conditions, that is, the cooperative growth of the assemblies and the reduction and oxidation of our system. Exploring a multi-dimensional phase-space is, however, time consuming and further studies

are needed. In chapter 4, the enzymatic network together with the polymerization of our system was taken into account. Here it turned out that the typical Michaelis-Menten approach used for enzymes generally could not be used. We were using full conversion of the substrate and concentrations beyond the linear response. It was satisfying that simple mass action laws did provide quantitative agreement with the experiments.

We believe that our results are stepping stone to explain and develop more dissipative supramolecular polymerization systems. Many other challenges remain, like how to anchor such non-equilibrium polymers to defined objects in order to exert mechanical forces, or how to combine catalytic activity and self-assembly in a single building block (i.e., like the tubulin heterodimer). More in general, understanding the behaviour of such systems will open the avenue to develop more life-like materials with impressive properties such as self-healing, self-repairing, self-adaptability or even allowing to control motion of different systems. Maybe, these kinds of materials help us to understand the origin of life, to control the fate of the cell, or even to treat and understand different diseases.

1. Alberts, B. *et al. Molecular Biology of the Cell*. (Garland Science, 2002).
2. Endo, M., Yang, Y. & Sugiyama, H. DNA origami technology for biomaterials applications. *Biomater. Sci.* **1,** 347–360 (2013).
3. Kuzuya, A. & Komiyama, M. DNA origami: Fold, stick, and beyond. *Nanoscale* **2,** 309–321 (2010).
4. Tørring, T., Voigt, N. V., Nangreave, J., Yan, H. & Gothelf, K. V. DNA origami: a quantum leap for self-assembly of complex structures. *Chem. Soc. Rev.* **40,** 5636–5646 (2011).

Dissipative supramolecular polymerization mediated by chemical fuels

Summary

Supramolecular chemistry aims to develop complex structures through non-covalent intermolecular interactions. So far, the majority of the artificial supramolecular structures that have been developed reside in the thermodynamic equilibrium state. The most stable configuration is found when reversible non-covalent interactions are involved. However, when strong non covalent interactions play a role, the self-assembly process can be determined by the kinetics of the system leading to metastable or kinetically trapped states. The final assembly state depends on sample preparation and experimental protocols, and the latter is an important factor in the preparation of supramolecular materials with functional properties. Biological systems continuously consume energy to keep the system in dissipative non-equilibrium states. Assembly/disassembly of microtubules is an excellent example of a dissipative system where a chemical fuel (GTP) is constantly provided to the system to keep it out of equilibrium. Energy consumption allows spatiotemporal control over the microtubule structures permitting the cell to perform actions such as cell division, motility and intracellular transport. Recently, supramolecular chemist have developed dissipative self-assembly systems, however, only few examples have been reported. In addition, only transient formation of supramolecular structures has been performed, since waste accumulation results in poisoning of the system impeding long term dissipative systems. Exploiting dissipative self-assembly can lead to obtain emergent behaviour such as non-equilibrium steady-states, oscillations or patterns. In this thesis, we have developed different dissipative supramolecular systems that are kept under non-equilibrium conditions by constant addition of chemical fuels.

In chapter 2, we synthetized a water soluble perylene diimide derivative (**PDI-1**) that can be easily reduced in a stepwise process to the dianion **PDI-1**$^{2-}$ via radical anion (**PDI-1**$^{\bullet-}$) formation upon addition of $Na_2S_2O_4$. **PDI-1** can be easily dissolved in borate buffer giving a reddish solution. **PDI-1** forms large colloidal aggregates that precipitate overnight. Upon addition of $Na_2S_2O_4$, a change in colour was observed from red to purple, indicative of the formation of **PDI-1**$^{2-}$. Surprisingly, **PDI-1**$^{2-}$ was partially assembled in solution (equilibrium between monomeric and small assembled species), despite that it is charged. Oxidation back to the neutral **PDI-1** state was performed under exposure to air. Next, we studied the effect of 1 redox cycle (1 reduction/oxidation step). Interestingly, **PDI-1** assemblies grow for a defined time via cooperative polymerization after a redox cycle. Seeding experiments (seeds were obtained by performing one redox cycle and waiting 1 hour) eliminate the lag phase of the polymerization, and enhance the growth rate, thus confirming the cooperative polymerization of **PDI-1**. In addition, the effect of multiple redox cycles was studied. Interestingly, a progressive evolution of the system was observed when performing more than one redox cycle at a certain frequency. In other words, the final supramolecular structure is determined by the frequency, number of cycles and starting conditions.

In chapter 3, we decided to study our redox-switchable **PDI-1** supramolecular system under continuous influx of $Na_2S_2O_4$ in a stirred semi-batch reactor. Remarkably, we

found an oscillating window by exploring different flow rates of $Na_2S_2O_4$. The (redox) reaction kinetics of our supramolecular oscillator were studied by performing stopped-flow experiments. Interestingly, a size-dependent reduction of **PDI-1** assemblies was found. In other words, the reduction rate depends on the size of the supramolecular assemblies. The latter acts as the negative feedback that in general makes oscillations more likely to be found. Moreover, a mathematical model was developed in order to explain the observed behaviour. Preliminary analyses on the model have shown damped oscillations, even in the absence of length dependence. This means that damped oscillations could be introduced more generally in cooperative polymerization systems, when they are coupled to a fuel-driven disassembly step. Preliminary simulations including the length dependent reduction rate showed an increase in oscillation amplitude indicating that additional negative feedback increases the oscillations. In addition, spatiotemporal behaviour was studied to understand reaction-diffusion processes. A thin layer (to avoid convection) of freshly reduced/oxidized **PDI-1** solution was seeded with an 1 hour old reduced/oxidized seeds in a Petri dish leading to a travelling wave of the supramolecular assemblies through the dish.

In chapter 4, we designed a perylene diimide peptide derivative (**PDI-2,** see fig. 3a) that can be phosphorylated by a kinase enzyme on its serine residues upon addition of adenosine triphosphate (ATP). After phosphorylation, **p2-PDI-2** can be dephosphorylated by a phosphatase enzyme. First of all, we confirmed the stepwise phosphorylation/ dephosphorylation of our molecule. Next, we studied the self-assembly behaviour of both aggregates (**PDI-2** and **p2-PDI-2**). The studies indicate that **p2-PDI-2** is more aggregated in solution. An inversion of the CD spectrum after phosphorylation points to right handed assemblies for **PDI-2** and left-handed assemblies for **p2-PDI-2**. In other words, phosphorylation leads to larger self-assemblies that have opposite supramolecular chirality as compared to the non-phosphorylated molecules. A transient formation of **p2-PDI-2** assembly was achieved by adding a shot of ATP in a batch reactor (i.e., substrate and both enzymes in the buffer solution). A fast formation of **p2-PDI-2** followed by a slow conversion back to the **PDI-2** was observed. However, only phosphorylated **PDI-2** was observed when a second shot of ATP was performed, suggesting poisoning of our system due to the accumulation of waste. It was possible to remove the waste of the system by dialyzing the solution against buffer. In order to mimic living systems where non-equilibrium steady-states (NESS) are reached by continuous exchange of fuel/waste and compartmentalization by membranes, we designed an open system that allows the exchange of ATP/waste between a central chamber and two reservoirs (situated on each side of the central chamber and separated by dialysis membranes). Different non-equilibrium steady-states (NESS) were obtained depending of the inflow of ATP. The reaction cycle **PDI-2 → p2-PDI-2 → PDI-2** can run (in principle) infinitely long under NESS conditions, whereas in batch it would cycle only once.

In chapter 5, we studied the thermophoretic effect on the polymerization of a perylene diimide derivative with a tryptophan moiety (**PDI-3**). We have seen that **PDI-3** forms H-aggregates through π-π stacking in borate buffer solutions. **PDI-3** can be partially disassembled upon dilution. In addition, **PDI-3** consecutively disassembled upon addition of THF. The light scattering intensity of mixtures of borate buffer and THF solution was lower as compared with pure buffer solutions suggesting that THF promotes disassembly of **PDI-3**. Next, the thermophoretic behaviour of our system was studied by microscale thermophoresis (MST). A typical MST experiment shows a fast decrease of the fluorescence intensity after switching on the IR laser due to the depletion of molecules. Once the steady-

state is reached (characterized by a plateau) the IR laser is switched off and the fluorescence intensity returns to the starting value due to the back-diffusion of the molecules and assemblies. **PDI-3** is quenched upon aggregation. When the IR laser was switched on, we observed a fast depletion of molecules followed by a prompt increase of the fluorescence intensity while the laser was still on. We hypothesise that photo-excitation promotes disassembly of **PDI-3** while the total concentration remains constant over time. The increase in fluorescence intensity is in that case due to the presence of more monomeric **PDI-3** species in solution. However, up to now relevant information on the supramolecular polymerization (such as k_{on} or k_{off}) from these measurements has proven difficult. Currently, we are working on a new setup where we couple MST to a fluorescence microscope. The setup will allow us to observe what is occurring inside the capillaries, and will provide more insight.

In general, our work has demonstrated different ways to push and keep supramolecular polymerization out of equilibrium, using chemical fuels or thermal gradients. Depending on how hard the system is driven, emergent behaviour such as oscillations or waves were obtained. In parallel with the experiments, mathematical models were developed in order to better understand this complex behaviour. We believe that the studies presented in this thesis will help to develop more life-like supramolecular materials that can perform complex functions such as self-repairing, self-adaptability, etc.

Polymérisation supramoléculaire dissipative sous carburant chimique

Résumé

1. Introduction

Les processus d'auto-assemblages sont la pierre angulaire du vivant et lui permettent notamment de remplir des fonctions complexes telles que la signalisation ou le transport cellulaire. De ce fait, le design de briques moléculaires en mesure d'interagir et de s'assembler avec précision en structures supramoléculaires sous l'action d'un stimulus (pH, force ionique, lumière, etc.) s'est vu revêtir une importance toute particulière au cours des dernières années.[1,2] Au jour d'aujourd'hui, la plupart des architectures supramoléculaires développées en laboratoire se trouvent être à l'équilibre thermodynamique (#1, Figure 1) correspondant à la configuration supramoléculaire la plus stable.[3] L'équilibre thermodynamique semble être favorisé lorsque les briques moléculaires interagissent faiblement les unes avec les autres. En revanche, lorsque ces interactions ont des énergies plus conséquentes, le comportement du système a souvent tendance à être dicté par sa cinétique permettant d'accéder à des états thermodynamique métastables ou « piégés cinétiquement » (respectivement #2 & #3, Figure 1). L'état thermodynamique dans lequel un assemblage supramoléculaire résidera dépend donc du design moléculaire initial mais aussi du protocole expérimental utilisé dont les subtiles variations peuvent parfois permettre d'accéder à différents états thermodynamiques pouvant ainsi donner accès à une large palette d'architectures supramoléculaires.[3]

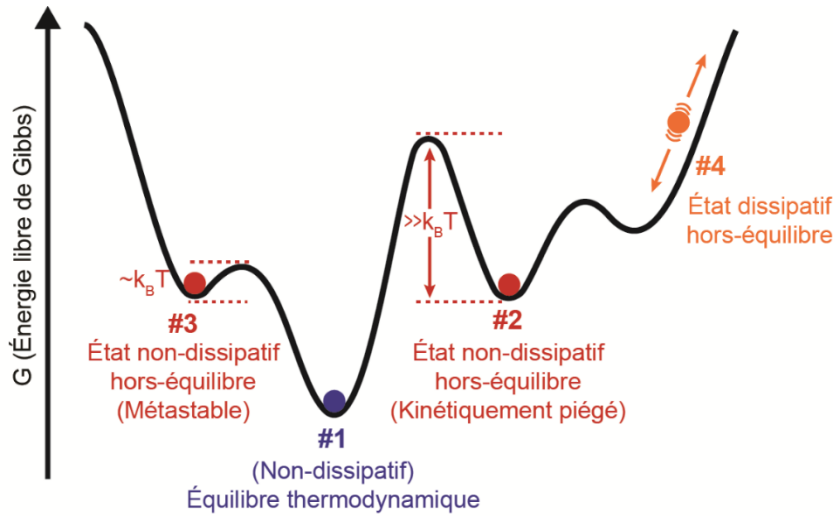

Figure 1. Schéma permettant d'identifier les différents états thermodynamiques accessibles par un assemblage supramoléculaire. Diagramme énergétique de Gibbs schématique.

Le vivant, en revanche, opère loin de l'équilibre, et l'on parle alors d'état dissipatif hors-équilibre (#4, Figure 1). Ces systèmes prélèvent de l'énergie dans leur milieu en continu afin de la dissiper pour maintenir une structure fonctionnelle et adaptive. Les microtubules incarnent le parfait exemple d'assemblage dissipatif hors-équilibre. Les dimères de tubuline s'assemblent et se désassemblent au gré de l'hydrolyse de la guanosine triphosphate (GTP) en guanosine diphosphate (GDP). L'apport constant de GTP aux microtubules leur permet de se maintenir hors-équilibre et de se réarranger au besoin. Ce contrôle spatiotemporel dicté par l'apport en énergie permet à la cellule de se diviser ou encore de se déplacer.[4] Séduits par cette facette du vivant, les chimistes supramoléculaires se sont récemment employé à faire le design de systèmes supramoléculaires dissipatifs. Néanmoins, seuls quelques systèmes supramoléculaires dissipatifs ont pu être amenés à maturité qui sont malheureusement empoisonnés par leur propre production de déchets.[5-7] Ils ne peuvent donc dissiper de l'énergie que sur une courte période et nous les qualifions pour la suite de « systèmes dissipatifs transitoires » (Figure 2A).[8]

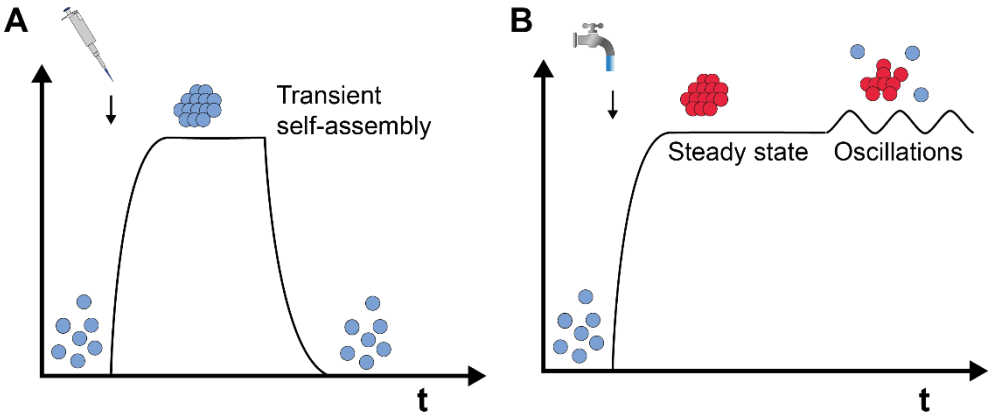

Figure 2. Systèmes auto-assemblés dissipatifs. (A) L'addition d'un équivalent de carburant chimique permet la formation transitoire d'espèces auto-assemblées. (B) Un comportement émergent peut être observé lors de l'addition constante de ce même carburant. Le système supramoléculaire dissipe alors de l'énergie en continu ce qui lui permet de rester loin de l'équilibre thermodynamique (régime permanent, oscillations,…)

Le but de cette thèse fut d'explorer les différentes stratégies permettant d'obtenir un control spatiotemporel sur différents assemblages supramoléculaires en les faisant « travailler » loin de l'équilibre, dans un état dissipatif, dans le but d'assister, sur le long terme, à l'émergence de structures supramoléculaire aux propriétés égalant celles trouvées dans la nature (Figure 2B).

2. Résultats et discussions

Les Perylènes diimides (PDIs) sont des briques moléculaires de choix en chimie supramoléculaire. Leur propension à s'auto-assembler (π-π stacking) et leur propriétés spectroscopiques déjà bien connues en font un système plus qu'indiqué pour l'élaboration d'objets supramoléculaires dissipatifs.[9] Au cours de ces trois années, nous avons donc usé de divers stimulus (réactions oxydo-réductantes ou enzymatiques, champs magnétiques ou encore effet thermophorétique) sur des architectures supramoléculaires à base de PDI dans le but d'en modifier la structure.

2.1. Sélection du chemin supramoléculaire par réaction redox

Un dérivé de perylène diimide (**PDI-1**) soluble dans l'eau a d'abord dû être synthétisé. Ce dernier peut facilement être réduit en dianion (**PDI-1**$^{2-}$) en présence de dithionite ($Na_2S_2O_4$, Figure 3A). **PDI-1** peut aisément être dissout dans une solution tampon borate en une solution rouge. L'agrégation de **PDI-1** en objets colloïdaux a pu être mise en évidence par UV-Vis et microscopie confocale (ces agrégats précipitent en 12h). Lors de la réduction sous addition de dithionite, la solution passe du rouge (**PDI-1**) au violet (**PDI-1**$^{2-}$). Là encore, la présence du di anion a été attestée par UV-Vis. Des analyses par diffusion dynamique de la lumière (DLS) ont néanmoins pu montrer que **PDI-1**$^{2-}$ ne s'auto-assemble que partiellement en solution. Une exposition à l'air libre de la solution de **PDI-1**$^{2-}$ permet de l'oxyder et d'y retrouver l'espèce neutre (Figure 3A). Il a ensuite été décidé d'étudier l'effet d'un cycle redox sur la structure de l'assemblage supramoléculaire (Figure 3B). Un suivi cinétique par UV-Vis juste après avoir réalisé un cycle redox montre que la structure supramoléculaire résultante évolue, et ce de façon auto-catalytique (i.e. nucléé, Figure 3C). Cette hypothèse a pu être vérifiée en effectuant un ensemencement d'une solution fraîche de **PDI-1** avec d'autres ayant subi un cycle redox (1 heure après), ensemencement à l'issue duquel le temps de latence a pu être diminué de façon significative (caractéristique des systèmes auto-catalytiques). De surcroît, lorsque des semences (vieilles d'une heure) sont passées au sonicateur pendant 5 minutes avant d'être introduites dans une solution de **PDI-1** (ayant subi 1 cycle), le procédé atteint un plateau bien plus tôt ce qui indique que l'assemblage de **PDI-1** est plus rapide (Figure 3C). Ces résultats sont caractéristiques d'une polymérisation supramoléculaire auto-catalytique (après un cycle redox, Figure 3C)).

Forts de ce constat, il a ensuite été décidé d'évaluer l'effet de plusieurs cycles redox successifs sur le système supramoléculaire. Pour ce faire, la croissance auto-catalytique de **PDI-1** a été suivie par diffusion dynamique de la lumière (DLS) et par UV-Vis après chaque cycle redox (7 cycles espacés de 20 minutes chacun). Une nette hausse de l'intensité (scattering R_{vv}/c, DLS) peut alors être observée, après un premier cycle suggérant la présence de plus d'assemblage en solution. Les cycles subséquents entrainent quant à eux une diminution progressive de l'intensité (DLS) et une diminution globale du rayon hydrodynamique des espèces en solution (Figure 3D) suggérant des changements structuraux progressifs. Il est à noter qu'à l'issue du 3ème ou 4ème cycle, les agrégats restent globalement les mêmes (Rh= 628 ± 83 nm), Figure 3D.

Il est alors apparu que les conditions initiales, le nombre de cycles ainsi que la fréquence avec laquelle ils sont effectués sont tous les trois des paramètres influençant la structure supramoléculaire (Figure 2B). Entre autre, ce projet nous a permis de montrer qu'il était possible de naviguer le long du paysage énergétique du processus d'assemblage

de **PDI-1** sans le modifier chimiquement mais à l'aide d'un carburant chimique (i.e. Cycles redox).[10]

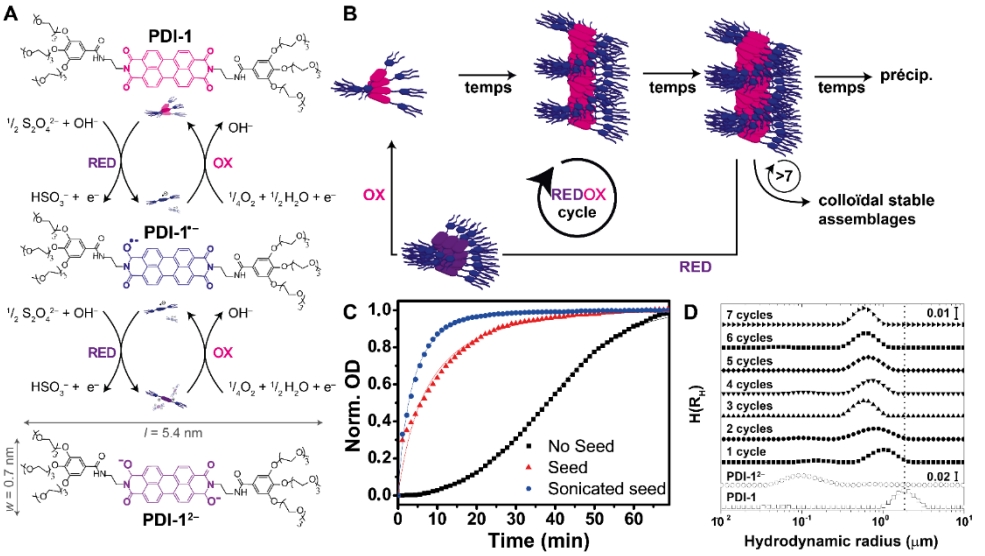

Figure 3. Système modèles et « pathway selection » (A) La molécule de PDI peut être réduite en dianion par addition de dithionite et peut être de nouveau oxyder en espèce neutre à l'air libre. (B) Le nombre et la fréquence des cycles redox affectent la structure supramoléculaire résultante**.** (C) Densité optique normalisée (OD) à 528 nm en fonction du temps après 1 cycle redox d'une solution de **PDI-1** à 10 μM (carrés noirs) ainsi que pour une solution de **PDI-1** ensemencée avec des « seeds » de **PDI-1** agées d'une heure (triangles rouges) ou ensemencée avec des « seeds » passées au sonicateur (cercles bleus). La courbe en S est caractéristique d'un processus auto-catalytique. (D) Rayon hydrodynamique (R_H) mesuré pour une solution fraichement préparée de **PDI-1** (carrés creux), pour **PDI-1**$^{2-}$ (cercles vides) et pour **PDI-1** ayant subi jusqu'à 7 cycles redox. Il est à noter que la taille des assemblages ne change plus après 3 cycles.

2.2. Vagues et oscillations supramoléculaires

Les oscillations sont monnaie courante dans les systèmes vivants tels que les filaments d'actine ou les microtubules. Dans tous ces systèmes, le cycle de réactions qui les caractérise comprend un feedback positif (processus auto catalytique) et un feedback négatif (processus inhibiteur). L'apparition de motifs spatiotemporels repose sur les inhomogénéités de la solution (i.e. pas d'agitation ou transport moléculaire).[8] L'un des oscillateurs les plus célèbres, la réaction de Belousov-Zhabotinsky, permet d'observer des oscillations dans un système ouvert sous agitation (en contraste avec les motifs spatiotemporels observés lorsqu'il n'y a aucune agitation dans un système fermé). Jusqu'à maintenant, les oscillateurs ont pu être couplés à des systèmes supramoléculaires mais jamais encore une oscillation ne s'est vue attribuée pour origine la cinétique non linéaires de son système supramoléculaire associé.[11,12]

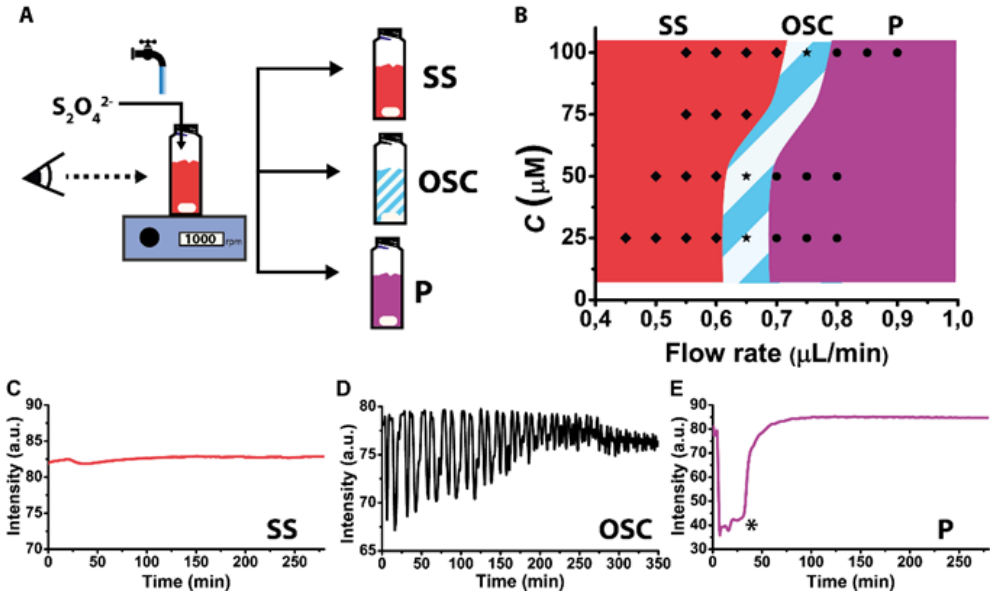

Figure 4. Diagramme de phase des différents comportements de PDI-1 (A) Le diagramme de phase a été établi dans un réacteur « semi-batch » sous un flux constant de $Na_2S_2O_4$ et sous agitation continue. (B) Le diagramme de phase a été construit avec différente concentration de **PDI-1** et différents débits de $Na_2S_2O_4$. Trois différents comportements ont pu être mis en exergue : (C) une régime permanent (zone rouge du panel B), (D) une fenêtre oscillatoire (zone bleu/blanche) et (E) une plage de débit débouchant sur une précipitation (zone violette).

Dans ce contexte, nous avons décidé d'explorer les possibilités d'auto-assemblages de **PDI-1** en lui fournissant en continu de l'énergie à dissiper. Pour ce faire, nous avons décidé d'y apporter un flux continu de carburant chimique et en laissant la solution agitée à l'air libre. En modifiant le flux de $Na_2S_2O_4$, nous avons pu découvrir une fenêtre de débit pour laquelle la structure s'assemble (**PDI-1**) et se désassemble (**PDI-1**$^{2-}$) de façon oscillatoire. C'est, à notre connaissance le premier système supramoléculaire en mesure d'osciller de lui-même. Les cinétiques des cycles redox ont pu être étudié par méthode de « stopped-flow » et ont révélé que le taux de réduction était proportionnel à la taille des espèces supramoléculaire présentes en solution : plus les assemblages sont gros, plus il est difficile de les réduire. En somme, si la nucléation de l'auto-assemblage agit comme un feedback positif, l'inhibition du taux de réduction elle agit comme un feedback négatif: toutes les conditions sont alors remplies pour le système pour osciller.

L'espace de phases du système a pu être balisé par UV-Vis, diffusion dynamique/statique de la lumière (DLS et SLS) ainsi qu'avec des mesures colorimétriques (Figure 4A). Le diagramme de phase de cet oscillateur supramoléculaire a été construit en faisant varier la concentration de **PDI-1** comme celle du carburant chimique (Figure 4B). Cela a notamment permis de mettre en lumière 3 différents régimes. (SS, OSC et P, Figure 4C-E). Le premier régime est un régime permanent (SS) et est atteint pour des faibles débits de carburant chimique ($Na_2S_2O_4$) où l'intensité de couleur suggère que **PDI-1** est l'espèce prédominante en solution (figure 4C, zone rouge de la Figure 4B). Nous pensons que le taux d'oxydation est plus grand que celui de réduction rendant de ce fait le désassemblage impossible. Une fenêtre oscillatoire (OSC) peut être atteinte en augmentant le débit de carburant (Figure 4D, zone bleue/blanche). Si l'on augmente la concentration de **PDI-1** le débit en carburant nécessaire pour pouvoir rester dans cette fenêtre oscillatoire augmente

également ce qui est naturel dans la mesure où plus de réducteurs doivent être utilisés pour réduire plus de molécules. Le dernier régime exploré (P, zone violette, figure 4E) est atteint en augmentant d'avantage le débit en carburant et correspond à la précipitation du système au bout de quelques minutes. Les espèces majoritaires y sont **PDI-1**$^{\bullet-}$ et **PDI-1**$^{2-}$. Cette précipitation pourrait être du fait que l'espèce radicalaire **PDI-1**$^{\bullet-}$ s'auto-assemble en solution bien plus rapidement que son homologue neutre **PDI-1** provoquant la formation de plus gros agrégats ne pouvant rester en solution. Autant que l'on sache, ces travaux mettent en lumière le tout premier exemple d'oscillateur supramoléculaire en solution. L'intérêt d'un tel système vient du fait que la croissance supramoléculaire affecte directement les cinétiques de réduction créant de ce fait un « retour d'information » affectant à son tour l'auto-assemblage étudié et lui permettant d'atteindre des régimes particuliers inatteignables à l'équilibre thermodynamique.

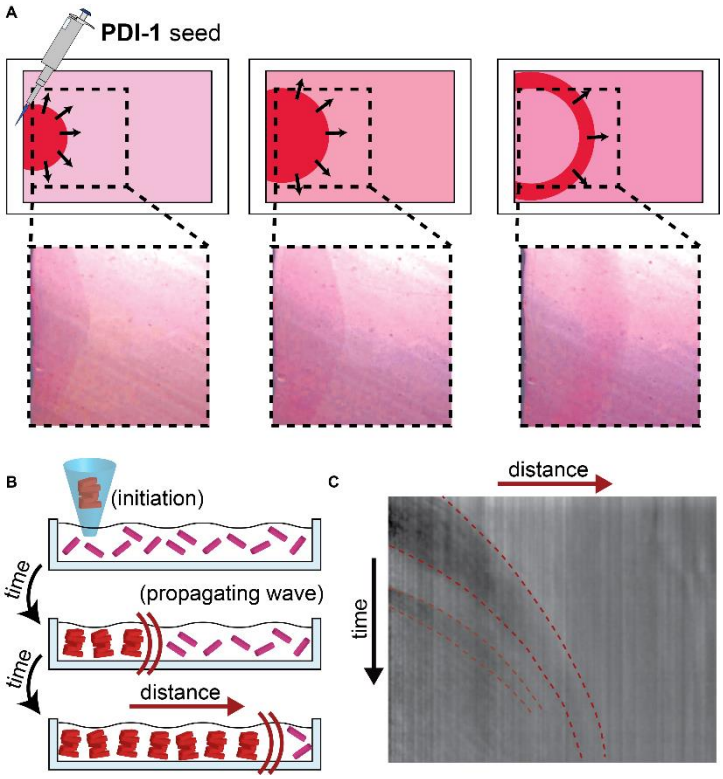

Figure 5. Vagues supramoléculaires en couche fine liquide (A,B) Une solution de **PDI-1** ayant tout juste subi un cycle redox est déposée dans un récipient imprimé en 3D surmonté d'une lame en verre de façon à confiner le liquide en une couche mince et à limiter les mouvements de convection. Des semences de PDI-1 (vieilles d'une heure) y sont ensuite déposées entrainant la formation subséquente d'une vague supramoléculaire. (C) Le kymographe correspondant montre que la célérité de cette vague n'est pas constante. Une seconde vague supramoléculaire peut être observée peu de temps après le passage de la première.

De surcroît, nous avons pu développer un modèle mathématique en mesure de prévoir les oscillations du système en fonction des vitesses de réactions en jeu. Enfin, après avoir poussé ce système dans un état dissipatif caractérisé par ces oscillations, nous avons décidé d'en étudier le comportement spatiotemporel pour comprendre les mécanismes de ce système à réaction-diffusion. Pour ce faire, une fine couche (épaisse d'un millimètre afin

d'éviter toute forme de convection) de solution de **PDI-1** ayant juste subit un cycle redox fut ensemencée avec une plus vieille, donnant naissance à une onde supramoléculaire traversant la solution (Figure 5A,B). Deux des faces étant en verre transparent, il nous a été possible d'imager la solution à l'aide d'un stéréoscope. Des semences de **PDI-1** vieilles d'une heure y sont ensuite déposés (figure 5A,B). Comme mentionné précédemment, une solution fraîche de **PDI-1** et des semences plus vieilles ont une couleur légèrement différente ce qui permet de visualiser les phénomènes en jeu à l'intérieur de cette couche mince (Figure 5A). Il est intéressant de s'apercevoir que peu de temps après l'ensemencement, une bande rose (plus sombre que la solution de **PDI-1** initiale) se forme et traverse la couche mince dans sa longueur (Figure 5C). La propagation de cette bande suggère une auto-amplification des assemblages de **PDI-1**. La solution ensemencée est nucléée par les semences permettant la formation de nouveaux assemblages supramoléculaire de **PDI-1** et ce sous forme de bande mouvante traversant ce film de solution de **PDI-1**.

2.3. Etats dissipatifs supramoléculaires hors-équilibre

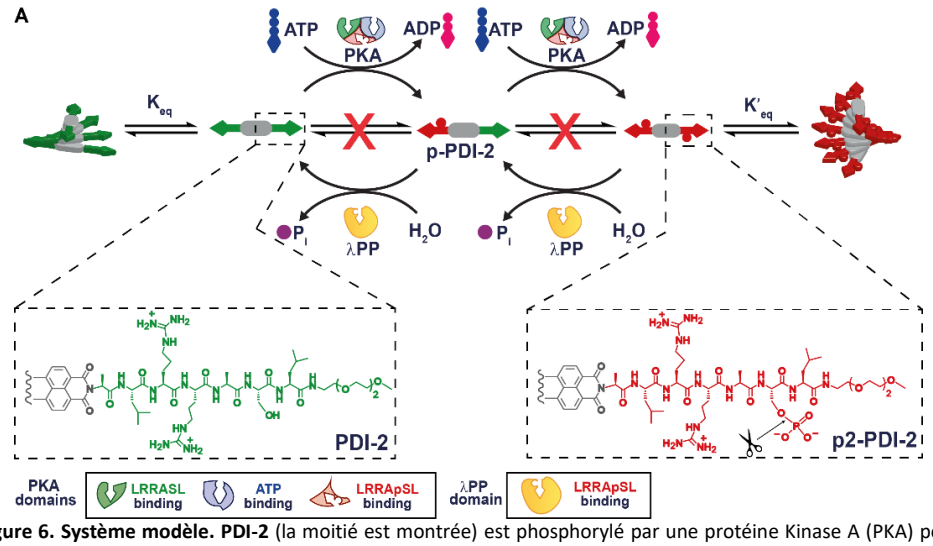

Figure 6. Système modèle. PDI-2 (la moitié est montrée) est phosphorylé par une protéine Kinase A (PKA) pour donner **p2-PDI-2**, en présence d'ATP. L'hydrolyse du groupement phosphate (ciseaux) est effectuée par une protéine lambda phosphatase (lambdaPP). **PDI-2** comme **p2-PDI-2** peuvent s'auto-assembler pour former, à l'équilibre, des polymères supramoléculaires. PKA possède 3 sites de liaison : un pour l'ATP (bleu), un pour le peptide LRRASL (vert) et un pour le LRRApSL (rouge).

Nous avons également voulu pousser un second système supramoléculaire dans un état dissipatif. Il s'agit cette fois d'un dérivé peptidique de pérylène (**PDI-2**). Cette brique moléculaire est en mesure d'être phosphorylée en **p2-PDI-2** par une kinase sur un résidu sérine présent sur sa structure sous addition d'adénosine triphosphate (ATP). Après phosphorylation, **p2-PDI-2** peut être déphosphorylé par une phosphatase (Figure 6). Dans un premier temps, nous avons décidé d'étudier les étapes de phosphorylation et de déphosphorylation de notre molécule, qui peuvent être mise en évidence par LC-MS et par des mesures de dichroïsme circulaire. Nous nous sommes ensuite intéressés à son processus d'auto-assemblage. Les agrégats supramoléculaires ont pu être mis en lumière

par UV-Vis, microscopie à transmission électronique (TEM) ainsi que par des mesures DLS. Ces mesures ont notamment pu montrer que **p2-PDI-2** était plus agrégé que son homologue **PDI-2** mais toujours stable en solution. Une inversion dichroïque montre que **PDI-2**, originellement de type hélice droite, se réorganise sous forme d'hélice gauche lorsque la phosphorylation est effectuée pour donner **p2-PDI-2**. Nous avons ensuite laissé la kinase et la phosphatase en présence de **PDI-2** sous addition de d'ATP. Après l'addition, le signal dichroïque trahit la formation des agrégats supramoléculaires à base de **p2-PDI-2** pour ensuite laisser place à un retour à **PDI-2** (Figure 7A). Une seconde addition d'ATP déclenche la formation de **p2-PDI-2** et de son assemblage supramoléculaire associé mais aucune reconversion en **PDI-2** ne peut être observée (Figure 7B). Le système est en réalité empoisonné par la production de déchets.

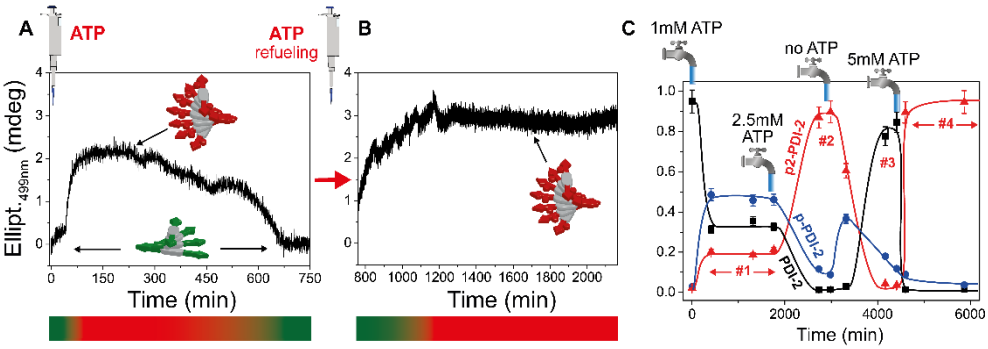

Figure 7. Etats transitoires et NESS. (A) Mesure dichroïque dans le temps permettant de suivre l'addition « batch » de l'ATP (2mM) dans une solution de **PDI-2** à 200 μM et contenant PKA à 0.13 μM ainsi que λPP à 0.2 μM. Les barres de couleurs des panels A et B représentent la formation/disparition (dans le temps) de **p2-PDI-2** (rouge) en partant de **PDI-2** (vert). (B) Mesure dichroïque similaire après un second shot d'ATP (2mM). Dans ce cas précis, **p2-PDI-2** s'accumule. (C) Différents NESS (régions de plateau #1-4), caractérisés par différentes fractions molaires de **PDI-2**, **p-PDI-2**, et **p2-PDI-2** (par LC-MS) peuvent être obtenus à l'aide d'un réacteur à flux continu et dépendent du débit en ATP. Les lignes sont là pour guider les yeux. Les dessins de robinets sont là pour indiquer le moment où la concentration en ATP dans la solution est changée.

Afin de pouvoir également pousser ce système supramoléculaire dans un état dissipatif, il a été décidé de construire une chambre microfluidique (par impression 3D) composée de 3 compartiments séparés par des membranes de dialyse : une chambre principale, ou sont stockés les molécules de **PDI-2** et **p2-PDI-2** ainsi que les enzymes nécessaires aux cycles de phosphorylation et deux réservoirs. Les membranes permettent de confiner les réactions dans la chambre tout en permettant à l'ATP de pénétrer dans la chambre et d'alimenter le travail des enzymes (Figure 7C). Les déchets eux aussi peuvent alors être évacués par la membrane, permettant cette fois la découverte de régimes permanents en faisant varier le débit d'ATP dans la chambre. Le premier état stationnaire a pu être obtenu avec un flux constant d'ATP à 1mM, caractérisé par la présence de toutes les espèces en solutions, dont les fractions peuvent varier en fonction du régime permanent associé (Figure 7C). Le cycle de phosphorylation peut être maintenu en théorie indéfiniment lorsqu'il opère en régime permanent (état dissipatif), alors qu'en système « batch », une seule oscillation pouvait être observée. Cette méthode peut être appliquée à d'autres assemblages supramoléculaires répondants à des stimulus pour pouvoir les garder hors-équilibre.[13]

Nous avons montré qu'il était possible d'obtenir une réponse par étape de **PDI-2** (Figure 8A) à la manière des traditionnels matériaux sensibles aux stimuli. Nous avons ensuite pointé le comportement supramoléculaire transitoire de ce système entre différents états thermodynamique (Figure 8B). Enfin, nous avons pu naviguer entre différents NESS (Non-equilibrium state) à l'aide d'un réacteur à membrane (Figure 8C).

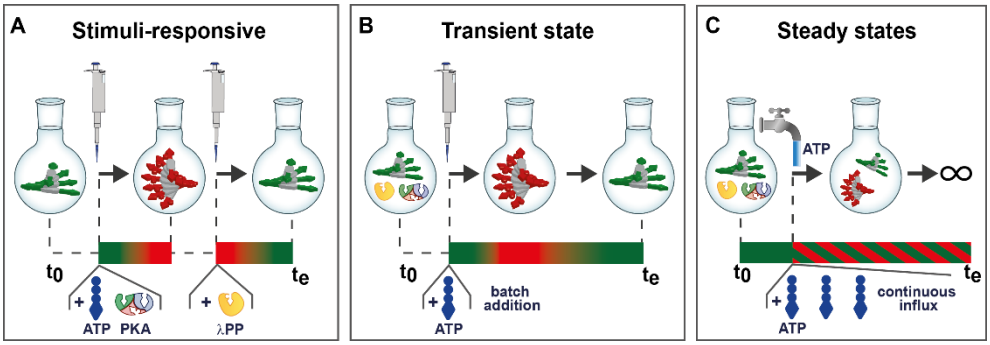

Figure 8. D'une réponse à un stimuli aux conditions NESS. (A) réponse à un stimuli: l'addition d'ATP et de PKA à une solution de **PDI-2** entraîne la formation de **p2-PDI-2** et donc à la formation de nouveaux types d'agrégats supramoléculaires. Un second stimuli (i.e. : addition de λPP) est nécessaire pour permettre à l'assemblage supramoléculaire de retourner dans son état originel. (B) Etat transitoire : Un unique stimuli (i.e. : l'addition d'ATP à une solution de **PDI-2** en présence de PKA et λPP, mène à un changement transitoire de la structure supramoléculaire en solution caractérisé par un inversement de la chiralité supramoléculaire. (C) Le système supramoléculaire est maintenu dans un état dissipatif hors-équilibre (NESS) à l'aide d'un apport constant en ATP. Faire varier le débit de carburant permet d'accéder à différents états thermodynamique hors-équilibre.

2.4. Les effets de la thermophérèse sur la polymérisation supramoléculaire

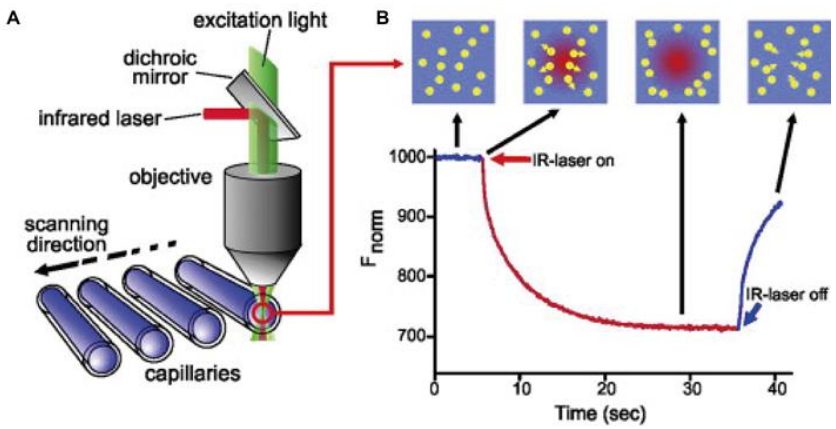

Figure 9. Les bases de la MST (MicroScale Thermophoresis). (A) Dans une expérience type, les solutions sont chauffées par un laser IR à l'intérieur de petits capillaires en verre. La concentration locale est suivie par fluorescence (tryptophan region) (B) Une expérience type est caractérisée par une fluorescence de départ. Dès que le laser IR est allumé, on observe une déplétion locale des molécules qui migrent du chaud vers le froid (thermophérèse positive). Enfin, lorsque l'IR est éteint, les molécules diffusent de nouveau dans le volume qu'elles venaient de quitter.

Lorsque l'on applique un gradient de température a des molécules en solution, ces molécules vont migrer le long de ce gradient : c'est la thermophérèse (ou effet Soret).[14,15]

Cet effet peut être décrit par la motilité thermophoretique et le coefficient de diffusion des particules en solutions. La « Microscale thermophoresis » (MST) est une technique d'analyse basée sur cet effet Soret largement utilisée les constantes d'associations de macromolécules (des changements en taille, en charge ou de conformation font varier le coefficient de Soret). Au cours d'une analyse MST, de petits changements de concentration due au gradient de température (un laser infra-rouge excite la bande vibronique des liaisons OH ce qui réchauffe la solution de 2 à 6°C) peuvent être détectés dans de petits capillaires (pour éviter tout mouvement convectif) grâce à des changements en fluorescence (Figure 9A,B).[16]

Nous pensons que la thermophérèse peut être utilisée pour l'étude de cinétiques supramoléculaires. De façon plus spécifique, un polymère supramoléculaire avec une polydispersité de 2 en solution à l'équilibre présentera différente tailles d'aggrégats en solution (premier cercle pointillé, Figure 10). En cas de thermophérèse positive, les plus gros agrégats migreront plus vite que les plus petits en dehors de la région irradiée par IR ce qui va de ce fait perturber l'équilibre. La concentration locale changeante va modifier avec elle la distribution en taille des espèces en solution. En cas de thermophérèse négative cette fois-ci, le comportement sera opposé (second procédé, Figure 10). Dès lors que le laser IR est éteint, les assemblages vont s'adapter à un nouveau changement de concentration locale (retour aux conditions d'équilibre). Nous pensons que l'étude de la relaxation des molécules peut nous apporter des informations sur les constante d'association/désassemblage k_{on} et k_{off} des assemblages supramoléculaires étudiés.

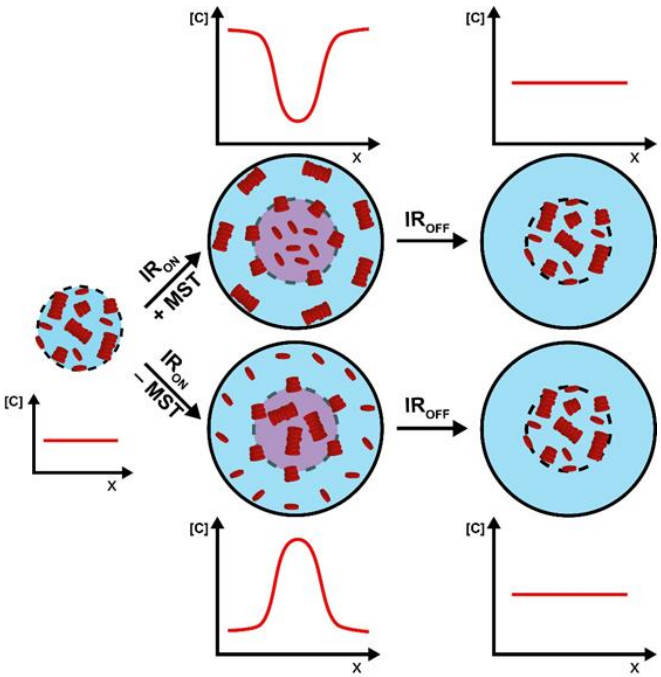

Figure 10. La MST comme outil permettant de pousser un assemblage loin de son équilibre thermodynamique. Une solution supramoléculaire initiale possédant une polydispersité caractéristique. La thermophérèse permet de « trier » les agrégats par tailles suite à leur déplétion différentielle. La relaxation diffusive (lorsque le laser IR est éteint) permet de mesurer les constante d'association/désassemblage k_{on} et k_{off}.

Là encore, nous avons décidé de synthétiser un dérivé de perylène possédant un groupement tryptophane (**PDI-3**, Figure 11A). Une fois la polymérisation supramoléculaire de **PDI-3** étudiée, nous avons décidé d'étudier ce système par MST. Au cours d'une expérience typique, L-tryptophan montre un thermophérèse positive après allumage du laser IR (figure 11B) ce qui se traduit par une migration des molécules hors de la zone illuminée. Dès lors que le laser est éteint, les molécules diffusent de nouveau dans la zone d'observation. La fluorescence ne retrouve néanmoins pas son niveau initial à cause d'un photo-blanchiment. Ce processus a d'ailleurs pu être mis en évidence grâce à l'observation d'une chute exponentielle de la fluorescence sans application d'un gradient de température. Dans le cas de **PDI-3**, lorsque le laser IR est allumé, on observe comme dans le cas général une rapide diminution de la fluorescence mais suivie cette fois par une rapide augmentation avant même d'atteindre un plateau. Nous pensons que lors de ce chauffage, les molécules de **PDI-3** se désassemblent partiellement, menant à un quenching moins important de la fluorescence (Figure 11C). Ces résultats préliminaires appellent à d'autres investigations afin de comprendre les mécanismes d'auto-assemblage de molécules soumises à un gradient de température.

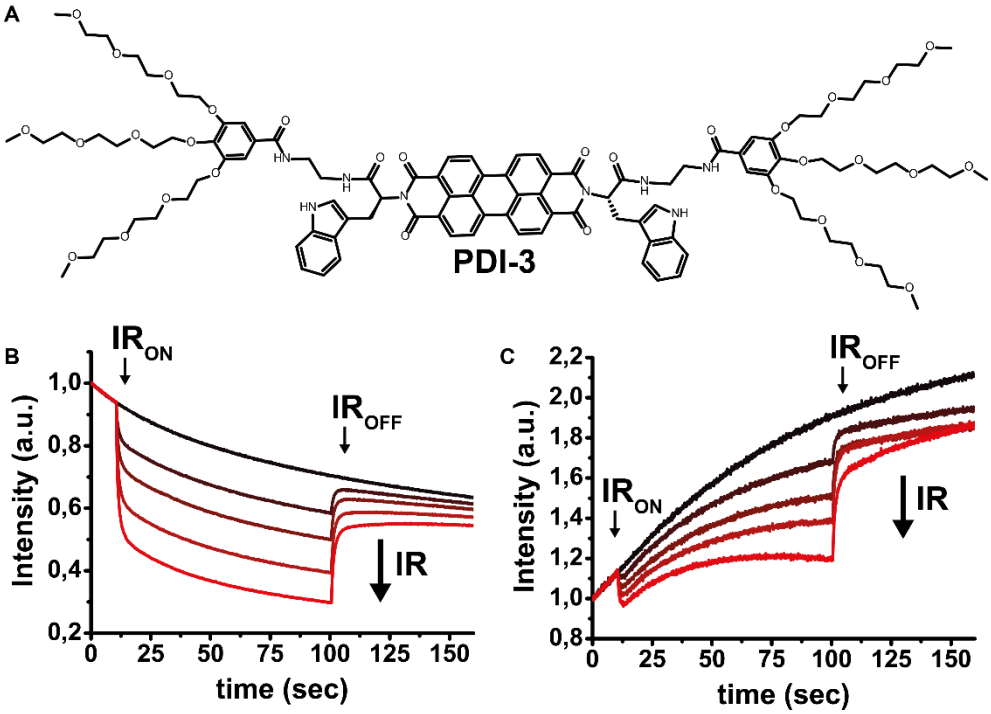

Figure 11. Mesures MST. (A) **PDI-3**. (B,C) Mesures MST de B) L-tryptophan (10 μM) et (C) **PDI-3** (50 μM) dans un tampon borate. Les flèches indiquent un changement de la puissance du laser IR, induisant un plus grand gradient de température. La LED est à 30%, l'IR passe de 0 à 70% (0 à 84 mW).

3. Conclusion générale

En conclusion, nous avons pu montrer au cours de ces trois années qu'il était possible d'obtenir un contrôle spatiotemporel supramoléculaire à l'aide de différent stimulus. Prodiguer au système un apport continu en énergie lui permet parfois de faire émerger un nouveau comportement (oscillations, régimes permanents loin de l'équilibre,…). En parallèle de ce travail expérimental, nous avons développé des modèles mathématiques capables d'expliquer et de prédire le comportement de systèmes supramoléculaires en état dissipatif loin de l'équilibre. Nous avons également pu adapter une technique d'analyse MST à l'étude des assemblages supramoléculaires qui s'avère être un outil nouveau et prometteur pour la caractérisation de système supramoléculaires. Nous espérons que tous ces projets combinés nous permettront un jour de poser la première pierre vers le développement de systèmes supramoléculaires « vivants » capables d'effectuer des tâches complexes, de se réparer ou de s'adapter.

4. Références

1. Lehn, J.-M. *Proc. Natl. Acad. Sci.* **99**, 4763–4768 (2002).
2. Aida, T., Meijer, E. W. & Stupp, S. I. *Science* **335**, 813–817 (2012).
3. Sorrenti, A., Leira-Iglesias, J., J. Markvoort, A., Greef, T. F. A. de & Hermans, T. M. *Chem. Soc. Rev.* (2017). DOI: 10.1039/C7CS00121E
4. Alberts, B., Johnson, A., Lewis, J., Raff, M., Roberts, K. & Walter, P. Molecular Biology of the Cell. (*Garland Science*, 2002).
5. Boekhoven, J., Brizard, A. M., Kowlgi, K. N. M., Koper, G. J. M., Eelkema, R. & Van Esch, J. H. *Angew. Chem.* **122**, 4935–4938 (2010).
6. Debnath, S., Roy, S. & Ulijn, R. V. *J. Am. Chem. Soc.* **135**, 16789–16792 (2013).
7. Maiti, S., Fortunati, I., Ferrante, C., Scrimin, P. & Prins, L. J. *Nat. Chem.* **8**, 725–731 (2016).
8. Epstein, I. R. & Pojman, J. A. An Introduction to Nonlinear Chemical Dynamics: Oscillations, Waves, Patterns, and Chaos. (*Oxford University Press*, 1998).
9. Würthner, F., Saha-Möller, C. R., Fimmel, B., Ogi, S., Leowanawat, P. & Schmidt, D. *Chem. Rev.* **116**, 962–1052 (2016).
10. Leira-Iglesias, J., Sorrenti, A., Sato, A., Dunne, P. A. & Hermans, T. M. *Chem Commun* **52**, 9009–9012 (2016).
11. Lagzi, I., Wang, D., Kowalczyk, B. & Grzybowski, B. A. *Langmuir* **26**, 13770–13772 (2010).
12. Lagzi, I., Kowalczyk, B., Wang, D. & Grzybowski, B. A. *Angew. Chem. Int. Ed*. **49**, 8616–8619 (2010).
13. Sorrenti, A., Leira-Iglesias, J., Sato, A. & Hermans, T.M. *Nat. communications*, accepted.
14. Astumian, R. D. *Proc. Natl. Acad. Sci.* **104**, 3–4 (2007).
15. Braibanti, M., Vigolo, D. & Piazza, R. *Phys. Rev. Lett*. **100**, 108303 (2008).
16. Jerabek-Willemsen, M., Wienken, C. J., Braun, D., Baaske, P. & Duhr, S. *ASSAY Drug Dev. Technol.* **9**, 342–353 (2011).

Acknowledgments

Firstly, I would like to thank my advisor Dr. Thomas Hermans for giving me the opportunity to do my PhD in this fantastic University and Institute. I couldn't imagine a better place to do the PhD. It has been 3 wonderful years with lots of nice experiences. I really appreciate all the support and motivation you gave me. I could never do what we achieved without your support, knowledge and help with the experiments. I want to thank you all for your advice and help you gave inside and outside the lab. It is amazing all the things you know and how hard you work to deal with all the stuff that occurs in the group. You are one of the role models for my future career. You fuelled my interest for continuing in academia and for non-equilibrium systems (even if the topic is too complicated). I think it is amazing all the things that will come from this field in the future and I would really like to be part of this future. Estoy muy agradecido por todo el apoyo y la oportunidad que me has dado. Muchas gracias por todo y le deseo lo mejor a tu familia!!

Alessandro merece una mención especial. Sin él no hubiera conseguido muchas de las cosas que he hecho en estos tres años. Es increíble la cantidad de información que conoces y todo lo que he podido aprender de ti. Has tenido paciencia en todo momento y siempre has intentado animarme y apoyarme en todo lo que hemos hecho juntos a lo largo de estos dos años y medio que hemos sido compañeros. Sin tu supervisión y ayuda no hubiera sido lo mismo. También quiero agradecerte toda la ayuda y el cariño recibido por tu parte y Francesca fuera del laboratorio. Sin vosotros la vida Estrasburgo habría sido más difícil. Espero que en el futuro te vaya muy bien y tengas mucha suerte y espero seguir aprendiendo mucho de ti!!

I would like to thank Dr. Akihiro Sato for all his support and help in and outside the lab. He is the world expert of DLS and without him many things would have never been possible. I really enjoy the time we spend together during this 3 years. All the best for your future and your family (Rio and your future baby)!!

I really appreciate the help of Dr. Michael Stich and I would like to thank him for the work done on the oscillator model. I really appreciate the week you spend in the lab and all the knowledge you transferred to me. Many thanks for your contribution and for being part of my mid-thesis committee. Muchas gracias!

I would like to thank Dr. Boekhoven, Dr. Escuder and Dr. Palmans for being part of my committee and all the time they spent with my thesis.

I want to thank Dr. Peter Dunne for his help in the lab and the CV measurements. Also, for the nice discussions and time we spend together. I want to thank Dr. Takuji Adachi for the help with the 3D printer and the nice discussions we have in the lab. I really enjoy our time together in the lab. Also, I would like to thank Dr. Vincent Marichez for his help in the lab, the translations and for the help with French bureaucracy and also for the nice coffee times! I also really appreciate the help and enthusiasm of Lafayette and Mithun. All the best for you future! I would also thank to Annia for all her help and nice moments. And all the friends I made in Strasbourg. Specially, Youssef for all the nice moments and his help for whatever thing I have needed.

También quiero agradecer el apoyo y cariño recibido de mis padres todos estos años. Todo el cariño que mis suegros me han dado desde que forme parte de sus vidas y agradecer todo el cariño que he recibido de mi familia.

No quiero terminar los agradecimientos sin darle las gracias a mi Esposa. María sin tu apoyo, cariño y comprensión no hubiera sido posible estar aquí en Estrasburgo. Han sido momentos duros. Estar separado después de tantos años juntos pero ha merecido la pena. Estoy contentísimo de haber formado una familia contigo y no puedo esperar para saber que nos deparará el futuro. De momento viene un bebé! Qué más puedo pedir! Solo puedo decir que gracias por todo, por quererme y estar siempre a mi lado. Te quiero!

Abbreviations

Adenosine diphosphate	ADP
Adenosine monophosphate	AMP
Adenosine triphosphate	ATP
Association constant	K_a
Atomic force microscopy	AFM
Belousov-Zhabotinsky reaction	BZ
Boltzmann constant	k_B
Continuous stirring tank reactor	CSTR
Degree of aggregation	α
Degree of polymerization	DP_N
Dichloromethane	DCM
Dimethylformamide	DMF
Dynamic light scattering	DLS
Elongation constant	k_e
Equilibrium constant	K_{eq}
Fickian diffusion	D
Fluorescence recovery after photobleaching	FRAP
Guanosine diphosphate	GDP
Guanosine triphosphate	GTP
Hydrodynamic radius	R_H
Inorganic phosphate	P_i
λ protein phosphatase	λPP
Meso-(4-sulfonatophenyl) porphyrin	H_2TPPS_4
Methylcyclohexane	MCH
Microscale thermophoresis	MST
Microtubule-associated proteins	MAPs
microtubules	MTs
Naphthalene diimide derivative	NDPA
Non-equilibrium steady states	NESS
Nucleation constant	k_n
Oligo(p-phenylenevinylene)	OPV
Optical density	OD
Perylene-3,4,9,10-tetracarboxylic acid diimide	PDI
Protein kinase A	PKA
Room temperature	rt
Temperature	T
Tetrahydrofuran	THF
Thermal diffusion	D_T
Transmission electron microscopy	TEM
Trifluoroacetic acid	TFA

Jorge Leira-Iglesias

Dissipative supramolecular polymerization mediated by chemical fuels

Résumé

Les cellules vivantes ont constamment recours à l'auto-assemblage dissipatif afin de s'adapter et d'effectuer différentes fonctions (translation, transport de masse, etc.). Encore loin d'un tel niveau de complexité, nous avons néanmoins l'ambition d'en étudier en détail les aspects thermodynamiques comme cinétiques afin de mieux comprendre les comportements supramoléculaire résultants. Jusqu'à présent, seul des systèmes dissipatifs transitoires ont pu être mis en évidence. Le design de nouvelles méthodes et de techniques capables de « pousser » des assemblages supramoléculaires hors-équilibre est crucial. Cette thèse énumère et explique en détail les différentes stratégies que nous avons mises en place afin de contrôler et de mieux comprendre les auto-assemblages dissipatifs. Nous avons notamment montré l'importance de « carburants chimiques » ou encore de gradients thermiques dans le maintien d'un système supramoléculaire dans un état hors-équilibre dans l'espoir d'y observer l'émergence de comportements uniques et nouveaux tels que des oscillations ou encore l'apparition de vagues supramoléculaires.

Mots-clés: systèmes dissipatifs supramoléculaires, assemblages supramoléculaires, oscillations, vagues supramoléculaires, carburant chimique.

Résumé en anglais

Living cells use dissipative self-assembly polymerization to quickly adapt and perform different functions (translation, mass transport, etc.). We are far from mimicking such systems. Thermodynamic and kinetic insights are important in order to elucidate the self-assembly behaviour of the different supramolecular systems. So far, only transient dissipative systems have been demonstrated. The design of new methodologies and techniques to bring and keep the system out of equilibrium are needed. In this thesis, we have developed new strategies and methodologies to tune, control and understand dissipative self-assembly. Constant influx of energy by chemical fuels or thermal gradients allows to keep the system under non-equilibrium conditions. This allows us to observe emergent behaviour such as oscillations or waves.

Keywords: supramolecular polymerization, dissipative self-assembly, oscillations, supramolecular waves, chemical fuels.